

This electronic thesis or dissertation has been downloaded from the King's Research Portal at <https://kclpure.kcl.ac.uk/portal/>



Evaluating effects of atrial structure on re-entrant drivers for atrial fibrillation using image-based computational approaches

Roy, Aditi

Awarding institution:
King's College London

The copyright of this thesis rests with the author and no quotation from it or information derived from it may be published without proper acknowledgement.

END USER LICENCE AGREEMENT



Unless another licence is stated on the immediately following page this work is licensed

under a Creative Commons Attribution-NonCommercial-NoDerivatives 4.0 International

licence. <https://creativecommons.org/licenses/by-nc-nd/4.0/>

You are free to copy, distribute and transmit the work

Under the following conditions:

- Attribution: You must attribute the work in the manner specified by the author (but not in any way that suggests that they endorse you or your use of the work).
- Non Commercial: You may not use this work for commercial purposes.
- No Derivative Works - You may not alter, transform, or build upon this work.

Any of these conditions can be waived if you receive permission from the author. Your fair dealings and other rights are in no way affected by the above.

Take down policy

If you believe that this document breaches copyright please contact librarypure@kcl.ac.uk providing details, and we will remove access to the work immediately and investigate your claim.

**Evaluating Effects of Atrial Structure on
Re-entrant Drivers for Atrial
Fibrillation Using Image-Based
Computational Approaches**



Aditi Roy

School of Biomedical Engineering & Imaging Sciences

Faculty of Life Sciences and Medicine

This dissertation is submitted for the degree of

Doctor of Philosophy

London

November 2019

Declaration

I declare that the thesis hereby submitted to King's College London for the degree of Doctor of Philosophy has not been previously submitted for a degree at this, or any other university; that it is my work in design and execution and that all material contained therein has been duly acknowledged.

The research work presented in this thesis has been undertaken by me, with the help of my supervisors, Dr Oleg Aslanidi, Prof Tobias Schaeffter and Dr Marta Varela.

No in-vivo data were collected specifically for the purpose of carrying the studies presented in this thesis, and only existing datasets were used.

The magnetic resonance imaging data used in Chapter 4, 5 and 6 have been collected Dr Henry Chubb and his team at St Thomas' Hospital, London, UK.

Aditi Roy

November 2019

Acknowledgements

I would like to extend my deepest gratitude to my supervisors. To Dr Oleg Aslanidi, for his guidance, availability and unwavering support throughout my PhD. During the most difficult times, when the path was unclear, you have always helped me to see the bigger picture. To Dr Marta Varela, for her patience and motivation. Your depth of knowledge and expertise across a range of topics has always inspired me. To Prof Tobias Schaeffter, for his insights. I have learned a lot from them and achieved a great deal, none of which would be possible without their support and nurturing. I thank them for equipping me with the knowledge and confidence to face greater challenges ahead of me.

I would also like to thank my thesis progression committee members: Dr David Nordsletten, Dr Martin Bishop and Prof Steven Niederer, for their insightful comments and constant encouragement. And I thank Dr Henry Chubb for providing patient imaging data.

The work presented in this thesis was supported by King's College London through the Engineering and Physical Sciences Research Council (EPSRC) [EP/L015226/1] and the Wellcome/EPSRC Centre for Medical Engineering [WT 203148/Z/16/Z]. I benefitted from their environment and I am thankful for their support. I would also like to extend my sincerest thanks to the IT team of the School of Biomedical Engineering and Imaging Sciences, for their uninterrupted support, especially Soba for his constant source of positivity.

My PhD journey wouldn't have been the same without my friends at KCL, Jemma Brown, James Bland, Rainbow Lo, Max Balmus, Elsa-Marie Otoo and Samuel Venin – for all the great times I have had over the last four years. Special thanks go to the undergraduate students who I worked closely with, Ahmed Qureshi, Maria Muffoletto and Ali Tajabadi, who always kept me on my feet and inspired me with new ideas and helped me grow.

Lastly but not least, I would like to thank my parents for their unwavering support and source of inspiration. I wouldn't have been able to arrive here without you.

Abstract

Atrial fibrillation (AF), the most common sustained cardiac arrhythmia, affects over 33 million people worldwide. Catheter ablation (CA) has become a first-line treatment for drug-refractory AF and is particularly effective in paroxysmal AF patients in the early stages of the disease. However, CA has high recurrence rates in patients with chronic forms of the disease. This is due to the empirical nature of the procedure and lack of mechanistic knowledge of optimal ablation sites and strategies in these patients, whose atria is altered by AF-induced electrical and structural remodelling. The purpose of the work presented in this thesis is to investigate the influence of patient-specific atrial structure on electrophysiological function, specifically the dynamics of re-entrant drivers (RDs) of AF, and to establish a mechanistic link between the atrial structure and location of RDs. Establishing such a link would allow for non-invasive identification of the RD locations, which could ultimately guide CA in chronic AF patients.

The first part of the study focused on atrial wall thickness (AWT) and to a lesser extent on atrial fibrosis, both of which can be reconstructed from medical imaging data and have been linked to atrial structural remodelling underlying the progression of AF. The effect of the atrial structure was investigated using two sets of computational models: 1) a simple model of an atrial slab with a step-change in AWT and a synthetic fibrotic patch, and 2) patient-specific atrial models with geometry and fibrosis reconstructed from magnetic resonance imaging (MRI) of 6 AF patients. The simple atrial slab model demonstrated that RDs drift towards and then along the AWT step. Furthermore, in the presence of a fibrotic tissue patch near the step, the RDs were attracted to the patch, and the ultimate RD location was determined by both fibrosis and AWT. In patient-specific 3D atrial models, the behaviour of the RDs was governed by the interaction between AWT and fibrosis in the right atrium (RA), owing to its trabecular structure with large AWT gradients. In the left atrium (LA) with more uniform AWT, the extensive fibrosis distribution played a more prominent role in influencing the RD dynamics.

In the following part, RD locations in LA were investigated by: 1) developing image-based 3D atrial models from patient MRI data, 2) applying the models to dissect the mechanistic links between atrial structure and the RD dynamics and 3) using the modelling outcomes to quantify the ultimate patient-specific RD locations. Simulations in the patient-specific models revealed that the RD dynamics were strongly influenced by the amount and spatial distribution of fibrotic tissue. RDs were typically found at fibrotic regions in AF patients from Utah 3 and 4 categories with high fibrotic burden (>25%), but more often near the pulmonary veins (PVs) in patients from Utah 2 category. The RDs anchored to specific, relatively small regions, labelled as target areas, with a high percentage of target areas located within the fibrotic tissue region in patients from Utah 3 and 4 categories. The patient-specific target areas showed that areas that harboured the RDs were much smaller than the entire fibrotic areas, indicating potential targets for therapy. Finally, CA strategies based on the knowledge of target areas were evaluated in-silico to terminate RDs efficiently. Ablation strategies that connected the target areas with linear lesions to the PVs or the mitral valve have superior anti-fibrillatory effect compared to ablating the target areas alone, as well as compared to clinically applied strategies such as the PV isolation. Thus, the novel image-based modelling workflow presented in this thesis has been applied to dissect multiple effects of atrial structure on the genesis of RDs, providing a deeper understanding of the mechanisms of AF sustenance and paving the way to designing patient-specific CA treatments.

Supporting Publications

The work presented in this dissertation has been published in several journal articles and international conference proceedings listed below.

Chapter 3 & 4

- Roy, A., Varela, M., and Aslanidi, O. Image-Based Computational Evaluation of the Effects of Atrial Wall Thickness and Fibrosis on Re-entrant Drivers for Atrial Fibrillation. *Frontiers in Physiology*. 9, 1352 (2018).
- Roy, A., Varela, M., and Aslanidi, O. Image-based computational evaluation of the competing effect of atrial wall thickness and fibrosis on re-entrant drivers for atrial arrhythmias, *Computing in Cardiology*, 44 (2017).
- Roy, A., Varela, M. and Aslanidi, O. Drivers of right atrial tachycardia anchor to the crista terminalis due to atrial wall thickness gradients, *EP Europace*, 19, iii71–iii72 (2016).

Chapter 5

- Roy, A., Varela, M., Chubb, H., MacLeod, R., Hancox, J., Schaeffter, T., and Aslanidi, O. Identifying Locations of Re-entrant Drivers from Patient-Specific Distribution of Fibrosis in the Left Atrium. *PloS Computational Biology*. (2020).
- Roy, A., Varela, M., and Aslanidi, O. Predicting catheter ablation targets from patient specific fibrosis distribution in the left atrium. *Biophysical Society Thematic Meetings 2019*, pp 88 (2018).

Chapter 6

- Roy, A., Varela, M., Chubb, H. et al., Virtual Catheter Ablation of Target Areas Identified from Image-Based Models of Atrial Fibrillation, *Functional Imaging and Modeling of the Heart*, *Lecture Notes in Computer Science*, vol 11504. Springer, Cham, (2019).
- Muffoletto, M., Fu, X., Roy, A. et al., Development of a Deep Learning Method to Predict Optimal Ablation Patterns for Atrial Fibrillation, *IEEE Conference on Computational Intelligence in Bioinformatics and Computational Biology*, (2019).

Presentations

- Functional Imaging and Modelling of the Heart, Bordeaux, France, June 2019, Poster Presentation.
- Heart by numbers: Integrating theory, computation and experiment to advance cardiology meeting, Biophysical Society, Berlin, Germany, September 2018, Poster Presentation.
- Imaging sciences and Biomedical Sciences Divisional Symposium, London, UK, October 2017, Best Oral Presentation Award.
- Computing in Cardiology International Conference, Rennes, France, September 2017, Oral Presentation.
- ERSRC UK Medical Imaging Summer School, London, UK, September 2017, Best Oral Presentation Award.
- EHRA EUROPACE-CARDIOSTIM Congress organised by the European Society of Cardiology, Vienna, Austria, June 2017, Poster Presentation.

Table of contents

List of Figures	12
List of Tables.....	15
Nomenclature.....	16
Chapter 1 Introduction.....	19
1.1 Motivation and Aims	19
1.2 Thesis Overview	20
Chapter 2 Background.....	22
2.1 Section Outline	22
2.2 The Cardiovascular System	23
2.2.1 The gross anatomy of the heart	23
2.2.2 Atrial structure	25
2.2.3 The flow of blood through the heart	25
2.2.4 The electrical conduction system.....	26
2.3 Cardiac Electrophysiology.....	28
2.3.1 Functional anatomy of cardiac myocyte	28
2.3.2 The cell membrane and ion transporters	29
2.3.3 The cardiac action potential	31
2.3.4 Characterisation of action potentials.....	33
2.3.5 Action potential restitution.....	34
2.3.6 Action potential propagation and excitation-contraction coupling.....	34
2.4 Atrial Fibrillation.....	37
2.4.1 Mechanisms underlying AF	37
2.4.2 Atrial fibrosis	44
2.4.3 Current treatment strategies for AF	48

2.5	Mathematical Modelling and Simulations	53
2.5.1	Modelling atrial electrophysiology	54
2.5.2	Modelling multiscale excitation propagation in the atria.....	60
2.5.3	Numerical solvers	62
2.5.4	Role of modelling and simulations in understanding AF mechanisms.....	66
2.5.5	3D atrial models with patient-specific fibrosis	68
Chapter 3	A Mechanistic Study: Drift of RDs induced by AWT gradients	70
3.1	Section Outline	70
3.2	Introduction and Motivation	70
3.3	Methods	72
3.3.1	Simulating cardiac electrophysiology	72
3.3.2	Study 1a: Influence of AWT step on the RD dynamics.....	73
3.3.3	Study 1b: Comparative influence of fibrosis and AWT step on the RD dynamics	78
3.4	Results.....	80
3.4.1	Study 1a: 3D Atrial Slab with AWT step	80
3.4.2	Study 1b: Comparative effect of AWT and fibrosis on RDs	85
3.5	Discussion.....	87
3.5.1	Influence of the AWT step parameters on the RD dynamics	88
3.5.2	Mechanisms of the AWT step effects on the RD dynamics	89
3.5.1	Competing influence of fibrosis and AWT on RDs.....	91
3.6	Limitations.....	92
3.7	Conclusions.....	93
Chapter 4	Image-Based Computational study: Role of Patient-Specific AWT and Fibrosis	94
4.1	Section Outline	94
4.2	Introduction and Aims	94

4.3	Methods	96
4.3.1	Simulating cardiac electrophysiology	96
4.3.2	Study A: Influence of patient-specific AWT on the RD dynamics	97
4.3.3	Study B: Competing effect of AWT and fibrosis on the RD dynamics.....	98
4.3.4	Simulation protocol for RD initiation	99
4.4	Results.....	100
4.4.1	Study 2: Right Atrial Geometry	100
4.4.2	Study 3: Left Atrial Geometry	103
4.5	Discussion.....	106
4.5.1	Variation of AWT in subject-specific atrial geometries	106
4.5.2	Effect of subject-specific AWT on the RD dynamics.....	107
4.5.3	Competing influence of subject-specific AWT and fibrosis on the RDs..	108
4.6	Limitations.....	109
4.7	Conclusions.....	110
Chapter 5	Predicting Locations of RDs from Patient-Specific Distribution of Fibrosis in the LA.....	112
5.1	Section Outline	112
5.2	Introduction and Motivation	113
5.3	Methods	115
5.3.1	Atrial electrophysiology model.....	115
5.3.2	3D patient-specific LA models	115
5.3.3	AF simulation protocol and data analysis	118
5.4	Results.....	121
5.4.1	Patient-specific fibrosis distribution in 3D atrial models.....	121
5.4.2	Atrial fibrosis influences the distribution of RDs across patient-specific LA models	121
5.4.3	Patient-specific fibrosis determines the RD anchoring locations	123

5.4.4	Targets for ablation identified from patient-specific LA models	127
5.5	Discussion.....	131
5.5.1	Influence of atrial fibrosis on the distribution of RDs	131
5.5.2	Comparison with previous studies of RDs and ablation	132
5.5.3	Limitations	134
5.6	Conclusions.....	135
Chapter 6	Virtual Catheter Ablation of Atrial Fibrillation: Target Areas Identified from Image-Based Models	137
6.1	Section Outline	137
6.2	Introduction and Motivation	137
6.2.1	Model-based ablation strategies.....	138
6.2.2	Challenges of fibrosis imaging in the atria	138
6.3	Methods	139
6.3.1	Virtual ablation of the predicted target areas	139
6.3.2	LGE-MR intensity thresholding and RD locations.....	141
6.4	Results.....	144
6.4.1	Effect of different ablation strategies on the termination of RDs.....	144
6.4.2	Effect of IIR threshold on target areas	147
6.5	Discussion.....	150
6.5.1	Virtual Ablation on the predicted target areas	150
6.5.2	LGE-MR intensity thresholding and RD locations.....	152
6.5.3	Limitations	153
6.6	Conclusions.....	154
Chapter 7	Conclusions	155
7.1	Summary.....	155
7.2	Main Findings.....	155
7.3	Future work.....	157

Chapter 8	Appendix	159
8.1	Numerical Implementation	159
8.1.1	A single cell model	159
8.1.2	3D action potential propagation	160
8.1.3	Implementation for RD Tip Tracking Algorithm	162
8.2	Appendix to Chapter 3	166
8.2.1	RD tip trajectories in 3D slab with varying AWT step	166
8.2.2	Anchoring of RDs in 3D slab with ATW step and fibrotic patch	167
8.3	Appendix to Chapter 5	168
8.3.1	Anchoring of RDs at specific locations inside fibrotic patches	168
8.4	Appendix to Chapter 6	169
References	171

List of Figures

Figure 2.1: The position of the heart in the body	22
Figure 2.2: The gross anatomy of the heart and the cardiovascular system.....	23
Figure 2.3: Internal anatomy of the atria.....	24
Figure 2.4: The cardiac conduction system.....	26
Figure 2.5: Myocardial tissue histology.....	28
Figure 2.6: The cardiac myocyte.....	29
Figure 2.7: The Action Potential.....	31
Figure 2.8: Properties of atrial action potential.....	33
Figure 2.9: Schematic image of excitation-contraction coupling. The arrows indicate the sequence of events (labelled 1 to 4) showing the direction of Ca^{2+} movement. Here, the inner grey compartment is the SR.	36
Figure 2.10: A schematic representation of the major contributors to the genesis of AF, which explains the notion “AF begets AF”	38
Figure 2.11: The three main classical mechanisms proposed for initiation and maintenance of AF.....	39
Figure 2.12: Schematic images of anatomic re-entry formation around an obstacle.....	40
Figure 2.13: Conceptual theories of functional re-entry:	41
Figure 2.14: Increase in the severity of fibrosis with AF disease progression.....	43
Figure 2.15: Different types of fibrosis based on their spatial patterns.....	45
Figure 2.16: Quantification of atrial fibrosis from LGE-MRI.....	46
Figure 2.17: Different types of CA procedures.....	49
Figure 2.18: The Utah classification for atrial fibrosis quantified using LGE-MR images and AF recurrence	51
Figure 2.19: The steps involved in creating mathematical model of cardiac electrophysiology and run simulations.....	53
Figure 2.20: The Hodgkin-Huxley (H-H) model.....	55
Figure 2.21: The atrial Fenton-Karma model.....	57

Figure 2.22: A schematic representation	60
Figure 2.23: Finite difference approximation in a 2D grid.	64
Figure 3.1: Diagram of the 3D atrial tissue setup.....	71
Figure 3.2: The RD initiation protocol in the slab with an AWT step and varying stimulus locations.....	74
Figure 3.3: The steps involved in identifying the tip of the RD.....	75
Figure 3.4: The hypotrochoidal (“flower-like”) pattern traced by the RD tip over time.	76
Figure 3.5: Steps to track the RD core and calculate its drift velocity.....	77
Figure 3.6: CV and APD measured for forward and backward wave propagation directions.	78
Figure 3.7: CV and APD measured on the slab with a step and fibrotic patch.....	79
Figure 3.8: Effects of AWT step on the RD dynamics in atrial slab (Study 1a) with the aFK model.	82
Figure 3.9: Effect of AWT gradients on the drift velocity of RDs in a slab (Study 1a) with aFK model.	83
Figure 3.10: Effect of AWT gradients on the tip velocity of RD as it zig-zagged between the thick and thin region of the atrial slab.	84
Figure 3.11: Effects of AWT step on the RD dynamics in 3D slab with the CRN atrial cell model (Study 1a).	85
Figure 3.12: Competing effects of AWT and fibrosis in the 3D atrial slab (Study 1b).	86
Figure 3.13: Changes in the RD wavefront during propagation at the AWT step.	90
Figure 4.1: Workflow for the image-based atrial modelling (Studies 2 & 3).	96
Figure 4.2: Anchoring of RD to AWT gradient at the CT region in the RA of Person 1.	99
Figure 4.3: Anchoring of RD to AWT gradient at the CT region and the fibrotic patch in the RA of Person 1.	100
Figure 4.4: Effects of AWT on the RD dynamics on the RA.	101
Figure 4.5: Competing effects of AWT and fibrosis in the RA.	102
Figure 4.6: Competing effects of AWT and fibrosis in the LA.	104
Figure 4.7: Competing effects of AWT and fibrosis in the LA.	105
Figure 5.1: A schematic image of the chapter outline.....	112

Figure 5.2: Workflow for identifying patient-specific target areas with the highest probability of harbouring RDs.	115
Figure 5.3: Left atrial fibrosis quantification from LGE-MRI.	117
Figure 5.4: Patient-specific fibrosis distribution in 6 AF patients with Utah scores from 2 to 4.	118
Figure 5.5: AF initiation protocol.	119
Figure 5.6: The pipeline for identifying target areas from the RD probability map. Sim: simulation	120
Figure 5.7: Regions of RD stabilisation in patient-specific LA models.	123
Figure 5.8: The effect of fibrosis on the RD dynamics in a patient-specific LA model.	124
Figure 5.9: The anchoring of RDs to fibrotic patches in patient-specific LA models.	126
Figure 5.10: Identifying RD location maps from patient-specific tip probability maps.	127
Figure 5.11: Patient-specific RD location maps – potential target areas for CA.	128
Figure 5.12: Comparison of the fibrosis burden to target area volume of in each patient-specific LA models.	129
Figure 5.13: Patient-specific RD location maps – catheter ablation targets.	130
Figure 6.1: The workflow for reconstruction of the image-based LA model	139
Figure 6.2: CA strategies tested using virtual ablation platform.	141
Figure 6.3: LGE-MRI intensity thresholding for fibrosis assessment.	142
Figure 6.4: 3D atrial slab with realistic fibrotic patch.	142
Figure 6.5: CA with the clinical used ablation Strategies 1 and 2 failed to terminate AF in the majority of cases.	144
Figure 6.6: Target area guided ablation with Strategy 5 successfully terminated AF.	145
Figure 6.7: The outcome of CA using different strategies in Patient 2 (A) and Patient 3 (B).	146
Figure 6.8: AF inducibility following CA Strategies 3 and 4.	147
Figure 6.9: Effect of the BZ size on the dynamics of RDs in a 3D tissue slab.	148
Figure 6.10: Effect of the BZ size on the dynamics of RDs in the patient-specific LA model.	149

List of Tables

Table 2.1: Parameters of the FK model obtained from Goodman et al. [128], calculated by fitting APD and CV restitution curves from sheep atria.	59
Table 4.1: Effects of AWT and fibrosis of the RD dynamics.	111
Table 5.1: Characteristics of the 6 AF patients whose LA models were used in the study. PsAF: persistent AF, PAR: paroxysmal AF. The patients have been labelled 1 to 6 (column 1), in the decreasing order of their fibrosis burden (column 5) and assigned a Utah score (column 6) in accordance with [69].	116
Table 5.2: Segmentation and modelling of fibrosis. Labelling of voxels in the LA patient geometries according to their LGE-MRI intensity ratio (IIR) relative to the blood pool. Voxels with $IIR > 1.24$ are part of a fibrotic core. $IIR < 1.08$ corresponds to healthy tissue and the intermediate values of IIR form a fibrotic border zone with intermediate properties.	120
Table 5.3: Properties of patient-specific fibrosis distributions. The size of the primary fibrotic patch decreases with the fibrotic burden (FB).	121
Table 6.1: The chosen IIR cut-off values used in Study 1. Column 2 shows the % change in size of the BZ with respect to the control, while columns 3 and 4 present the IIR threshold values used.	143
Table 6.2: The chosen IIR values and resultant FB in Study 2.	143

Nomenclature

AF	Atrial fibrillation
CA	Catheter ablation
PV	Pulmonary veins
LA	Left atrium
RDs	Re-entrant drivers
AWT	Atrial wall thickness
MRI	Magnetic resonance imaging
LGE	Late gadolinium enhancement
AV	Atrioventricular
MV	Mitral valve
RA	Right atrium
RAA	Right atrial appendage
CT	Crista terminalis
LAA	Left atrial appendage
RV	Right ventricle
LV	Left ventricle
SA	Sinoatrial
AP	Action potential
ANS	Autonomic nervous system
BB	Bachmann's bundle
SR	Sarcoplasmic reticulum
V	Transmembrane potential
V_i	Intracellular potential
V_e	Extracellular potential
Na^+	Sodium ion
K^+	Potassium ion
Ca^{2+}	Calcium ion
RMP	Resting membrane potential
I_{Na}	Sodium current

I_{to}	Transient outward current
I_{CaI}	Inward L-type Ca^{+} current
I_{Kr} and I_{Ks}	Outward K^{+} currents
$I_{Na/Ca}$	Sodium calcium exchanger current
APD	Action potential duration
ERP	Effective Refractory Period
Cx	Connexins
ATP	Adenosine triphosphate
BCL	Basic cycle length
PAF	Paroxysmal AF
PsAF	Persistent AF
EADs	Early afterdepolarization
DADs	Delayed afterdepolarization
CV	Conduction velocity
λ	Wavelength
EAM	Electroanatomic mapping
Gd	Gadolinium
IIR	Image intensity ratio
CA	Catheter ablation
AADs	Anti-arrhythmic drugs
TdP	Torsades de Pointes
CFAEs	Complex fractionated electrograms
DF	Dominant frequency
ShEn	Shannon entropy
DECAAF	Delayed-Enhancement MRI (DE-MRI) Determinant of Successful Radiofrequency Catheter Ablation of Atrial Fibrillation
FB	Fibrotic burden
ODEs	Ordinary differential equations
H-H	Hodgkin and Huxley
FN	FitzHugh-Nagumo
FK	Fenton-Karma
I_{fi}	Fast-inward current

I_{so}	Slow outward current
I_{si}	Slow inward current
$\theta(x)$	Heaviside step function
FK-CNTRL	Control FK model
FK-CAF	Chronic FK model
CRN	Courtemanche-Ramirez-Nattel
D	Diffusion coefficient tensor
PDEs	Partial differential equations
FE	forward Euler
FDM	Finite difference method
FEM	Finite elements method
FVM	Finite volume method
dx, dy and dz	Space steps
dt	Time step
BZ	Border zone
FIRM	Focal and impulse rotor modulation
ECGI	Electrocardiographic imaging
PVI	Pulmonary vein isolation
MF	Mean frequency

Chapter 1

Introduction

1.1 Motivation and Aims

Atrial fibrillation (AF), the most common sustained cardiac arrhythmia [1], is characterised by rapid and irregular activations of the upper chambers of the heart [2]. This disrupts the coordinated contraction of the atrial chambers, and as a result, AF patient suffers from significantly decreased cardiac output, which leads to morbidity and poor quality of life and requires long term medical treatment. Moreover, AF is associated with a 5-fold increase in the risk of stroke [3] and is independently associated with a two-fold increase in all-cause mortality, as well as with increased risks of heart failure and cognitive impairment [4]. AF affects about 33.5 million people worldwide, and its prevalence is predicted to rise progressively over the coming decades, bringing with it the increased burden of high morbidity and mortality of the affected population [5].

Catheter ablation (CA) is a well-established clinical therapy for the restoration of normal sinus rhythm in AF patients who do not respond well to anti-arrhythmic drugs, with success rates of up to 70% in patients with episodes of AF lasting less than 1 week (paroxysmal AF). The widely accepted CA strategy is the electrical isolation of pulmonary vein (PV) sleeves in the left atrium (LA), which are believed to be the primary substrate for the generation of the ectopic electrical impulses and/or anchoring of re-entrant drivers (RDs) responsible for triggering and sustaining AF [6–10]. However, approximately 30% of AF patients are asymptomatic, which leads to delayed diagnosis and the development of persistent AF lasting for months and years. In these patients, the success rate of CA drops to about 40% [11], and their therapy often requires repeated ablation procedures. A potential factor for the low efficacy of CA in these patients is the presence of high degrees of electrophysiological and structural remodelling, which alters the AF substrate, making the underlying electrical dynamics more complex and the drivers more difficult to locate and eliminate. Understanding the mechanisms behind the AF drivers and quantifying their locations, and thus changing the focus of CA strategies from anatomy-based

targets (such as the PVs) to patient-specific functional targets (such as the RDs themselves), could lead to significant improvement of the efficiency of CA therapy.

In recent years, advances in catheter and electro-anatomic mapping technologies have enabled the development of more patient-specific CA strategies that complement standard approaches in persistent AF patients, by targeting either the AF drivers or the underlying substrate for AF maintenance. However, such techniques are limited by the challenges of invasive mapping and visualising electrical activity on the surface of the fibrillating atria with sufficiently high resolution. Moreover, they don't contribute to the mechanistic understanding of the AF drivers. Therefore, the success rates of such enhanced CA strategies remain suboptimal.

With the advancement of novel imaging tools, the paradigm is shifting towards non-invasive identification of patient-specific regions where the atrial substrate can be arrhythmogenic [12,13]. The novel imaging data also facilitates the development of patient-specific biophysical models that can be used for both elucidating the mechanisms of AF drivers and identifying their locations. Such image-based models have been successfully applied for investigating physiological and pathological factors that contribute to cardiac arrhythmogenesis [12–16].

The goal of this dissertation is to apply image-based computational modelling of the atria to explore the mechanisms of RDs sustaining AF, and thus identify patient-specific RD locations that can be targeted by CA therapy. This is achieved by designing a series of studies that focus on specific structural features of the atria, which can be quantified from patient imaging. Such features include the atrial wall thickness (AWT) and fibrosis, both of which can be quantified from magnetic resonance imaging (MRI) and integrated into the patient-specific 3D atrial models. The models then enable the investigation of the mechanistic influence of such features on the dynamics of RDs and their ultimate locations in a given patient. Hence, the models will help generate personalised targets for CA, primarily focusing on RDs in LA. Ultimately, this will create an image-based computational platform for guiding CA therapy in AF patients.

1.2 Thesis Overview

The thesis is organised into 6 Chapters, and an outline of the structure is presented below.

Chapter 2 provides the necessary background to the interdisciplinary work presented in the following chapters. First, the basic principles of cardiac anatomy and electrophysiology are introduced. The mechanisms underlying cardiac arrhythmias, AF in particular, are then

discussed, along with the existing treatment options and related challenges. Finally, the theory behind cardiac electrophysiology is outlined, methods used for the construction of biophysical cardiac models are summarised, and the contribution of modelling and simulation to exploring AF is highlighted.

Chapter 3 describes the investigation of the effects of AWT gradients on the dynamics of RDs and compares these effects to other known structural influences, such as those of atrial fibrosis. In this proof-of-concept study, all the simulations are performed using a simple 3D slab representation of the LA wall, allowing us to gain insights into mechanistic links between AWT and the dynamics of RDs.

Chapter 4 builds upon the investigation presented in Chapter 3, extending it to realistic 3D atrial geometries created using imaging data from AF patients. In addition to exploring the effects of patient-specific AWT gradients on the atrial RD dynamics, the comparative effects of such gradients and patient-specific fibrosis distribution on the RDs are evaluated. Thus, the influence of several structural factors on the RD localisation in the atrial is explored.

Chapter 5 focuses on the in-depth investigation of the effects of fibrosis on the RD dynamics in patient-specific LA models. Here a semi-automated image-based computational pipeline is created to construct patient-specific LA models from late gadolinium enhanced (LGE) MR images and then apply the model simulations to generate patient-specific maps of RD locations. Such maps could provide personalised targets areas for guiding CA.

Chapter 6 uses the imaged-based model predictions of the previous chapter and utilises the predicted patient-specific target areas to perform virtual ablation, specifically applying the CA lesions to the target areas. Success rates of such image-based modelling-guided CA are compared to the success of virtual ablations that are based on existing clinical CA strategies. Besides, the sensitivity of this approach to the image-processing and modelling steps is investigated.

Chapter 7 summarises the main conclusions of each chapter and links them together. Moreover, it outlines the clinical implications of this work and future directions.

Chapter 2

Background

2.1 Section Outline

The chapter aims to provide the biomedical and mathematical background needed to understand the work presented in the following chapters. In Section 2.2 and 2.3, details of cardiac anatomy and electrophysiology relevant to atrial fibrillation (AF) are presented. In Section 0, the mechanisms underlying cardiac arrhythmias, AF in particular, are discussed along with the existing treatment options and related challenges. Section 2.5 presents the mathematical background behind cardiac electrophysiology, computational modelling and simulation techniques for AF.

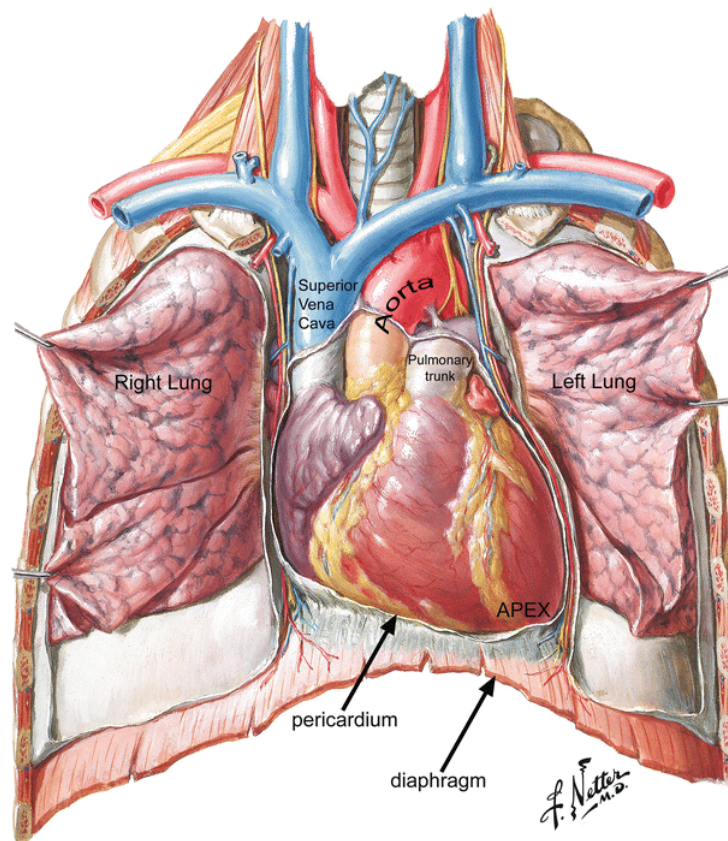


Figure 2.1: The position of the heart in the body, adapted from [17].

2.2 The Cardiovascular System

The heart is the mechanical pump of the body. Together with the network of blood vessels, it constitutes the cardiovascular system, which is responsible for the delivery of nutrients, electrolytes, dissolved gasses and waste products to the entire body and lungs. On average, the heart pumps approximately 7,000 L of blood every day and contracts about 2.5 billion times over its lifetime [18]. It has become one of the most studied organs, because of its crucial importance for the normal function of the body and the increasing morbidity and death rates linked to cardiac diseases. The following sections will provide a brief overview of cardiac anatomy and physiology, whereas more comprehensive details can be found in books [17].

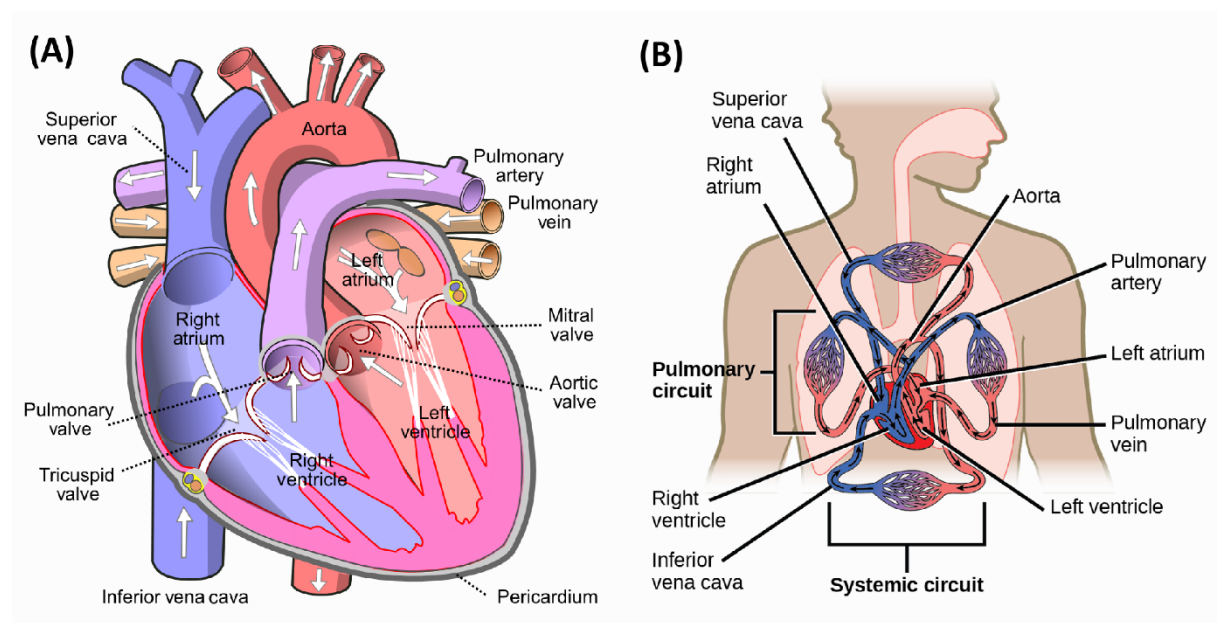


Figure 2.2: The gross anatomy of the heart and the cardiovascular system. (A) Schematic image of the structure of the heart with white arrows indicating the direction of blood flow through the 4 chambers [19]. (B) Schematic image of the blood flow through the circulatory system, where the systemic circulation involves the exchange of blood between the heart and the body [20], while the pulmonary circulation system consists of the exchange of blood between the lungs and the heart. Here the oxygenated and deoxygenated blood is shown in red and blue, respectively.

2.2.1 The gross anatomy of the heart

The heart is a hollow muscular organ situated just to the left of the midline of the thoracic cavity between the lungs (Figure 2.1). The size of an average human heart is approximately the size of a person's closed fist [21]. It is surrounded by a fluid-filled sac-like double layer called the pericardium (Figure 2.2A), which serves to protect this vital organ. A cross-section cut through

the heart walls reveals several layers: the outer protective epicardium, the myocardium and inner endocardium [17].

The heart is composed of four distinct chambers shown in Figure 2.2A. This four-chamber structure of the heart enables the separation of the systemic from the pulmonary circulation system (Figure 2.2B). The former is regulated by the left side of the heart (left atrium and ventricle), which is responsible for the distribution of oxygenated blood throughout the body while bringing deoxygenated blood back to the heart. The right side of the heart, on the other hand, controls the movement of blood between the heart and the lungs for blood oxygenation.

The atria and ventricles are separated, on the epicardial side, by the coronary sulcus, while the left and right halves of the heart are separated via a septum to prevent the mixing of blood. The flow of blood from the atria to the ventricles is regulated by the atrioventricular (AV) valves located on the plane of this sulcus. These consist of the mitral valve (MV) on the left and the tricuspid valve on the right. These valves ensure unidirectional flow of blood between the atria and the ventricles. A cross-section cut through the heart walls reveal several layers: the outer protective epicardium, thick middle myocardium and inner endocardium. Amongst them, the myocardium is the contracting layer of the heart and consists of circularly and spirally arranged network of cells called the cardiac myocyte [17].

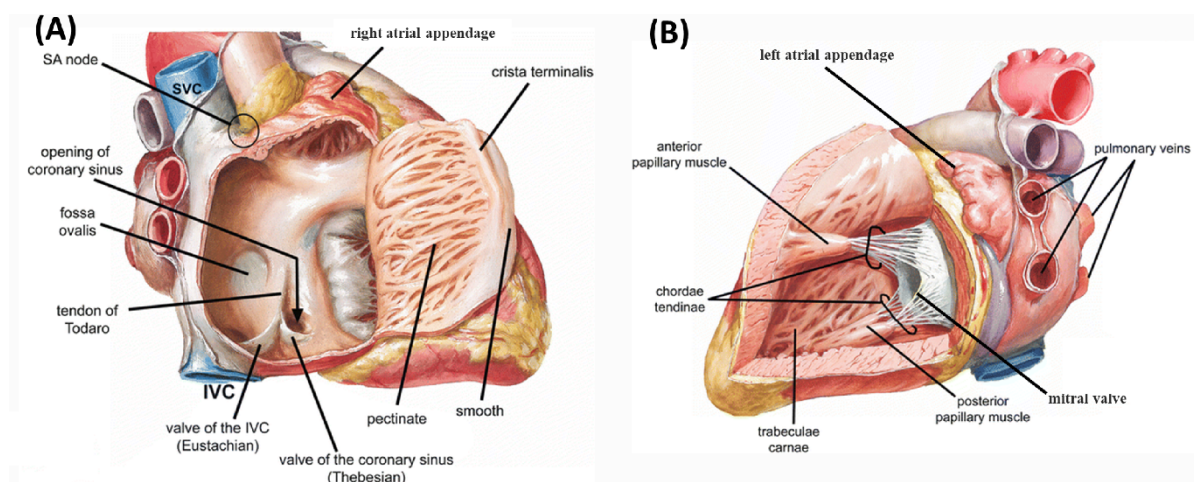


Figure 2.3: Internal anatomy of the atria. On the left, (A) the right atrium has been opened to reveal the internal structure, and on the right, (B) is the left atrium with PVs highlighted. Images adapted from [17].

2.2.2 Atrial structure

The right atrium (RA) is larger in size than the left atrium (LA) (Figure 2.3) [17]. The terminal sulcus, an external groove extending from the superior vena cava to the inferior vena cava separates the RA into two parts: the principal cavity (sinus venarum) and the anteriorly located right atrial appendage (RAA). In the internal surface of the RA shown in Figure 2.3A, this groove is marked by the crista terminalis (CT), a vertical smooth muscular ridge. Behind the CT the atrial surface is smooth, while the front of it resembles a tooth-like structure consisting of muscular fibres called the pectinate muscles. The RA (Figure 2.3A) receives deoxygenated blood from the upper part of the body via the superior vena cava and the inferior part of the body via the inferior vena cava.

Freshly oxygenated blood from the lungs enters the LA through the pulmonary veins (PVs), usually four in number, which opens into the upper posterior surface of the LA shown in Figure 2.3B. The left atrial appendage (LAA) is a finger-shaped extension originating from the main body of the LA with a well-defined narrow orifice. Externally, the LAA appears as a flattened tubular structure with one or more bends and terminating in a pointed tip directed anterosuperiorly [22]. A large variation in the size and shape of the LAA has been reported clinically, and its function in the cardiac cycle has been attributed to increasing the cardiac volume. However, in the presence of cardiac rhythm disorders, LAA is often regarded as the site for thrombus formation due to its reduced contractibility and blood stasis.

2.2.3 The flow of blood through the heart

A schematic image of the blood flow through the chambers of the heart is shown in Figure 2.2A. The deoxygenated blood flows into the RA via the superior vena cava and inferior vena cava from the systemic circuit. As the RA contracts, the deoxygenated blood passes into the right ventricle (RV) via the tricuspid valve. The subsequent contraction of the ventricles forces the tricuspid valve to close and the blood to flow through the pulmonary valves into the right and left pulmonary arteries, transporting it to the lungs. The deoxygenated blood passes through the lung's capillary network, where gas exchange occurs. The freshly oxygenated blood is then returned to the heart via the PVs into the LA. The contraction of the LA results in blood moving into the left ventricle (LV) through the MV. When the LV contracts, the MV closes, and the oxygenated blood is forced into the aorta and distributed throughout the body via arteries and capillaries. In this sequence of events, the right and left side of the heart contracts

simultaneously, which is known as systole, with each side pumping the same volume of blood in each cardiac cycle. The systole is followed by diastole, where the relaxation of the heart muscles allows for the blood to refill the chambers. The heart muscle cannot receive oxygen from the blood within its chambers. Instead, it has its own system of capillaries embedded in the walls, which is known as coronary circulation.

2.2.4 The electrical conduction system

In healthy conditions, during sinus rhythm, electrical impulses follow a regimented route, and the arrival of supra-threshold electrical stimuli results in active contraction of cardiac muscle cells, myocytes. This allows for the coordinated rhythmic contraction of the four chambers of the heart. A schematic image for the cardiac conduction system is shown in Figure 2.4.

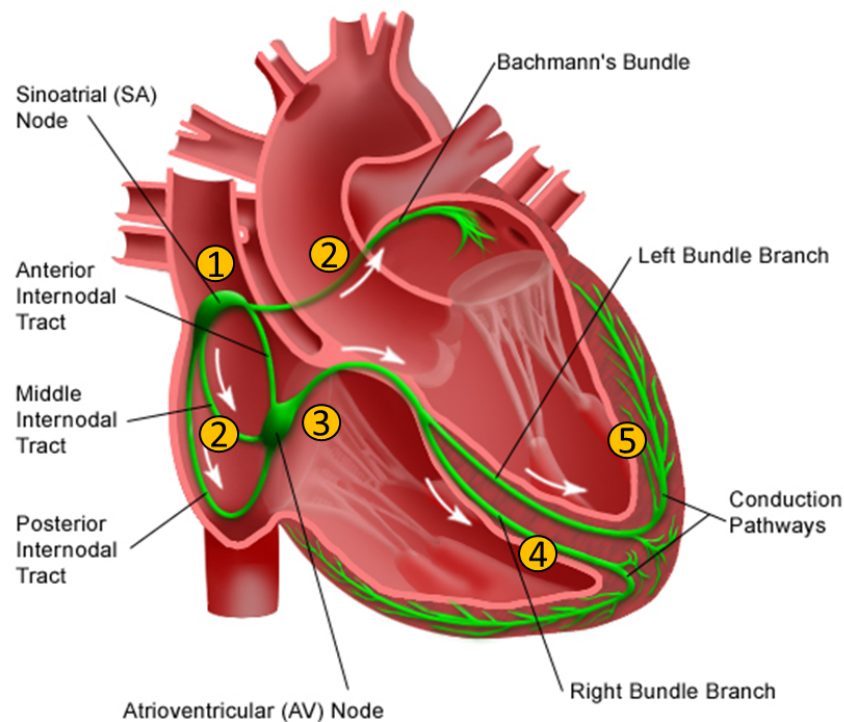


Figure 2.4: The cardiac conduction system. A Schematic image of the electrical conduction system in green with the sequence of events labelled 1-5. Image adapted from [23].

The primary electrical signal is initiated by the sinoatrial node (SA node) located at the base of the superior vena cava in the RA (Figure 2.4, 1). The SA node consists of a small collection of specialised cells that are autonomous electrical oscillators and spontaneously generate electrical impulses known as action potentials (AP) at an intrinsic rate between 60 and 100 beats per

minute (bpm) [24]. Each AP spreads through the cardiac wall and is responsible for the normal heart rhythm of about 60-100 bpm, and hence the SA node is referred to as the pacemaker of the heart. Moreover, the SA node is controlled by the autonomic nervous system (ANS), which can regulate its firing rate, and hence the heart rate [25,26]. The parasympathetic input slows down the firing rate, thereby decreasing the heart rate. The sympathetic input, on the other hand, increases the firing rate, and thus the heart rate [24]. This regulatory system allows the heart to adapt to various physiological stressors, for example during exercise, where the sympathetic system increases the heart rate to meet the body's increased demand in oxygen.

The APs propagate across the RA with fast conduction along the CT and pectinate muscles resulting in the contraction of the RA (Figure 2.4, 2). Trans-septal conduction is facilitated by several fibrous bundles such as the Bachmann's bundle (BB), which is one of the largest collection of fibres in the atria, running from the top of the RA into the anterior surface of the LA (Figure 2.4, 2). As the AP passes from right to left, the LA contracts right after the RA with a slight delay which is usually considered negligible. Here the cardiac impulses can reach the AV node located at the base of the atria (Figure 2.4, 3), which introduces a slight delay before the electrical signal reaches the ventricles. This delay allows for the atria to contract and the ventricles to refill before the conducted AP triggers ventricular contraction. Therefore, the AV node plays an important role in maintaining normal cardiac rhythm. From the AV node, the electrical impulses pass into the intraventricular septum through a specialised collection of fibres called the AV bundle (or the bundle of His), extending into Purkinje fibres (Figure 2.4, 4). The bundle spreads in a tree-like manner, branching into the left and the right bundles throughout the interior of the ventricles (Figure 2.4, 5). The impulses originating from the Purkinje fibres stimulation causes contraction of the ventricular walls in a twisting motion to facilitate blood flow into the aorta and the pulmonary trunk.

2.3 Cardiac Electrophysiology

The myocardium is a highly organised structure comprising of cardiac muscle cells (cardiomyocytes) and fibroblasts, which are involved in the maintenance of the extracellular matrix [27]. Blood vessels (which are part of the coronary system) and nerves can also be found. The fundamental property of the myocardium, which enables it to generate and conduct electrical signals and induce contraction, is through the function of the cardiac myocytes that are the primary constituents of the heart muscle. In the section, we will provide a brief review of cardiac electrophysiology, the study of the electrical activity of the heart. We will discuss the structural components of cardiac myocyte and put them in a functional context to explain their electrophysiological properties.

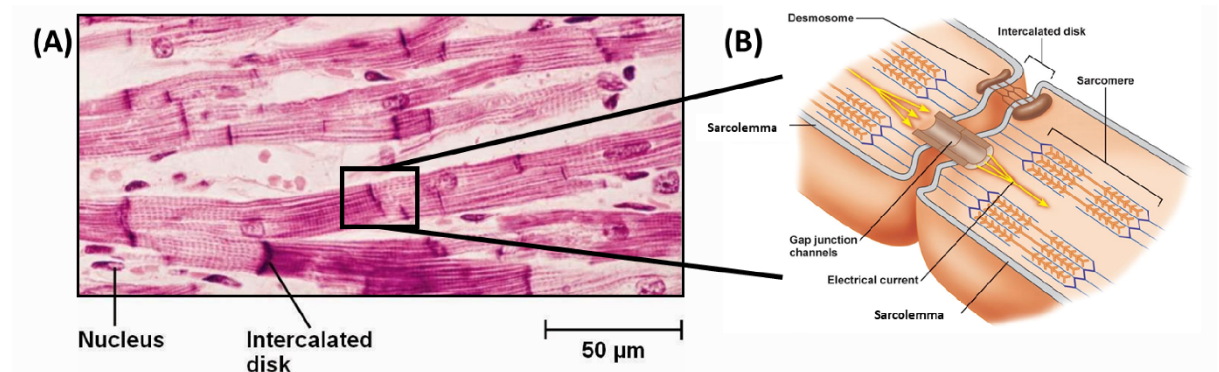


Figure 2.5: Myocardial tissue histology. (A) Strained cardiac tissue showing the arrangement of multiple cardiac myocytes. (B) Schematic image of the junction between two myocytes and some of the intercellular components.

2.3.1 Functional anatomy of cardiac myocyte

The cardiac myocyte is the contractile unit of the myocardium whose primary function is to produce mechanical tension. In mammalian atrial and ventricular tissue, they are approximately cylindrical in shape and roughly 50 – 150 μm in length and about 10 to 20 μm in diameter [27]. Unlike skeletal muscle cells, cardiac myocytes are often single nucleated and branched at the ends (Figure 2.5A). The fluid in the intracellular space of the cardiac myocyte is called the sarcoplasm, which contains various ionic species as well as several biomolecules and organelles [27]. The sarcolemma surrounds each myocyte with a phospholipid bilayer that forms a semi-permeable barrier to the movement of ions between the sarcoplasm and the extracellular space (Figure 2.6B). The movement of ions between inter and extracellular spaces occurs only via specific protein structures embedded in the sarcolemma called ionic channels. The flow of ions

through these channels results in inward and outward currents underlying the generation of AP, the details of which will be discussed in Section 2.3.3. Moreover, specialised structures called intercalated disks form cell-to-cell junction between adjacent cardiac myocytes (Figure 2.5B). This allows for mechanical coupling between cardiomyocytes, as well as providing a passage for the flow of ions between cells for rapid conduction of APs [28].

Among organelles within the myocyte, there are mitochondria, myofibrils, the sarcoplasmic reticulum, the sarcomere and finally, the cytoskeleton holding all the organelles together [27]. The mitochondria are present in abundance, occupying almost 40% of the cell volume, thus emphasising the immense energy demands of the myocyte [28]. Each myocyte composed of bundles of myofibrils that contain myofilaments. The sarcoplasm also contains myofibrils, with distinct repeating unit termed sarcomere, the primary contractile unit of the cell. Each sarcomere is composed of thick and thin filaments (Figure 2.5B). The chemical interactions between these filaments enable the sarcomere to change length during excitation-contraction coupling. Another organelle, the sarcoplasmic reticulum (SR) is an intracellular membrane network which wraps around the myofibrils without touching them. SR acts as calcium (Ca^{2+}) store and plays an important role in calcium homeostasis and contraction-excitation coupling, further discussed in Section 0.

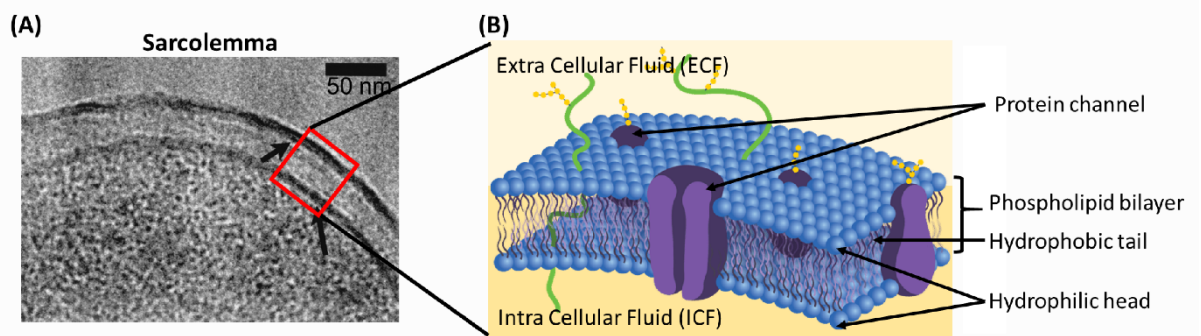


Figure 2.6: The cardiac myocyte. (A) Electron microscopy image of the cell membrane in *E. Coli* bacteria [29] showing the sarcolemma, phospholipid layer. (B) Schematic image of the cell membrane showing the phospholipid bilayer, modified and adapted from [30].

2.3.2 The cell membrane and ion transporters

The cell membrane of the cardiomyocyte, or sarcolemma, is a phospholipid bilayer which encapsulates the sarcoplasm and separates the cell from its extracellular space (Figure 2.6). The fundamental function of the sarcolemma is to provide a barrier for diffusion. Hence, the lipid

molecules are arranged in a specific fashion, such that their hydrophilic heads are facing outward, interacting with the fluid on either side of the membrane. This specific configuration allows the sarcolemma to interact with both the extra and intracellular fluids, while its hydrophobic core renders it impermeable to charged molecules (Figure 2.6B). Moreover, there exists a difference in charge distribution between the extracellular fluids and the intracellular fluids resulting in a potential difference across the sarcolemma. This is referred to as the transmembrane potential,

$$V = V_i - V_e \quad (2.1)$$

Here V_i and V_e denote the intracellular and extracellular potentials.

Embedded within the phospholipid bilayer are different protein structures that are found either bound to the membrane surface (peripheral membrane proteins) or buried within the membrane with domains on one or both side (integral membrane proteins) [31]. Integral proteins spanning the entire phospholipid bilayer, particularly those that form pores and channels, take part in moving molecules between intra and extracellular spaces (Figure 2.6B). These specialised protein structures are responsible for the excitability of the cardiac myocyte.

The opening and closing of these channels are typically dependent on stimuli from either change in the membrane potential, neurotransmitters, ions or mechanical stretch. Moreover, when a channel opens, it only becomes selectively permeable to a restricted set of ions, where the selectivity comes from the specific interactions of the ions with the channel pore. Hence, many different types of ion channels can be found across the membrane. In cardiac myocytes the primary channels are for sodium (Na^+), potassium (K^+) and calcium (Ca^{2+}) ions [32]. Chlorine is involved to a lesser extent. The channels can be further divided into different categories depending on their electrical behaviour determined by their underlying protein structure. Relevant to this context, there are primarily 3 different ion-transporting protein structures, namely channels, exchangers and pumps. Ions pass through channels down their electrochemical gradient without the input of metabolic energy. Other ion-transporter proteins, such as the pumps, move ions against their concentration gradient through active transport using cellular metabolic energy. However, ion exchangers can be classified neither as active nor as passive transporter protein. Instead, they use energy from the ion flowing down the electrochemical gradient to move another ion against it. The role of ionic pumps and exchangers

is critical in the ability of the cell to be excited repeatedly and in preventing the build-up or depletion of ion concentration in the intracellular space.

2.3.3 The cardiac action potential

When a sufficiently large external electrical stimulus is applied to the cell membrane, the transmembrane potential rises above a threshold potential before returning, typically more than 100 ms later, to its original state. This cyclic change in the membrane potential in response to the external stimulus is referred to as the action potential, AP.

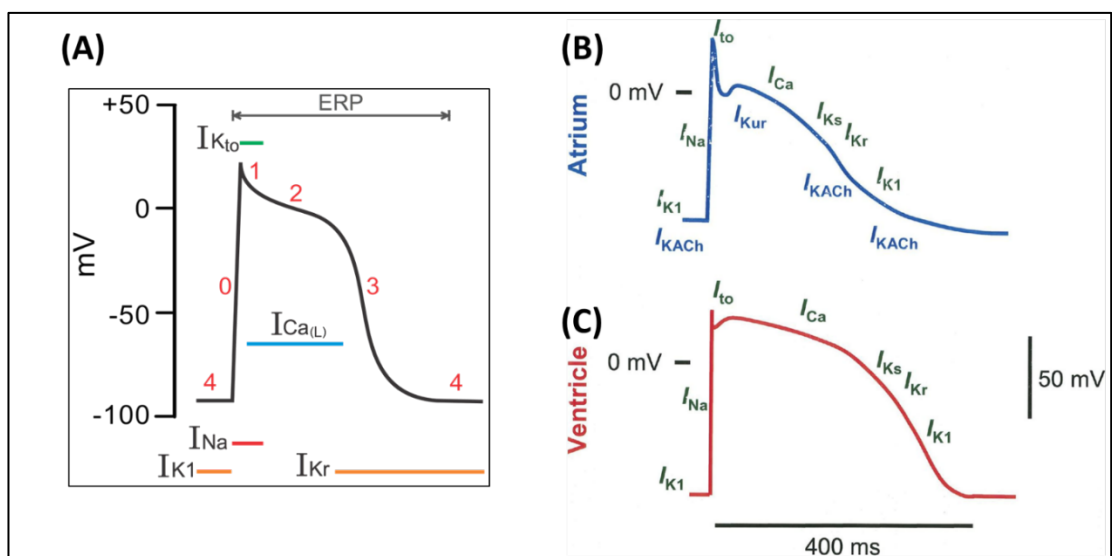


Figure 2.7: The Action Potential. (A) A generic AP morphology with different phases labelled. The shape and currents in the atrial and the ventricular myocyte are shown in panels (B) and (C), respectively. Images replicated with permission from [7].

The AP consists of 5 distinct phases (Figure 2.7, A) where each phase corresponds to the action of one or more ionic channels. A schematic image of the atrial AP with all the phases labelled is shown in Figure 2.7A.

Phase 4: When the cardiac myocyte is at rest, the transmembrane potential is referred to as the resting membrane potential (RMP), which is typically within -65 and -85 mV for atrial cells [33]. This is labelled at Phase 4 of the cardiac AP. The critical balance of background currents determines the RMP.

Phase 0: When the membrane voltage is sufficiently perturbed from the RMP, either by stimulus from an external source or neighbouring cells, after a threshold voltage is reached, the fast Na^+ channels rapidly activate and remains activated for 2-10 ms. During this time, there is

an influx of Na^+ ions from the extracellular to the intracellular space down its electrochemical concentration gradient. As the positive charge flows into the cell, the membrane potential rapidly increases, and the cell depolarizes. This forms the rapid upstroke observed in Phase 0 of the AP. It is important to note that the velocity of AP propagation across the heart is related to this upstroke.

Phase 1: After the inactivation of the Na^+ current (I_{Na}), the transient outward current (I_{to}) becomes active. This is carried mainly by K^+ ions flowing out of the cell and partially repolarizing the membrane. The current is referred to as transient as it inactivates within 30-40 ms, hence giving rise to the characteristic notch observed in Phase 1 of the AP (Figure 2.7).

Phase 2: During this phase, the delicate balance between the inward L-type Ca^+ current (I_{CaL}) and the outward K^+ currents (I_{Kr} and I_{Ks}) results in a plateau phase of the AP, which is critical for the contraction of the myocyte. Moreover, the influx of Ca^{2+} ions in the intracellular space initiates Ca^{2+} induced Ca^{2+} release from Ca^{2+} stores in the SR. The high concentration of Ca^{2+} ultimately causes the myocyte to contract (as discussed further in section 0).

Phase 3: The final phase of AP is marked by the termination of Ca^{2+} current, and a progressive increase in K^+ currents (I_{Kr} and I_{Ks}) to fully repolarize the cell membrane to the RMP. The most critical role in the repolarization is played by an inward rectifier K^+ current, I_{K1} , which is larger than all the other K^+ currents and only activates over a very narrow range of voltage (-30 mV to -80 mV). During this phase, the sodium-calcium exchanger ($I_{\text{Na/Ca}}$) also helps decrease the cytoplasmic Ca^{2+} concentration by exchanging 3 Na^+ ions entering the cell for every 1 Ca^{2+} ion being expelled. This results in an inward current which helps prolong the plateau while slowing repolarization. As the membrane repolarizes and the potential becomes negative, the K^+ channels inactivate, and AP returns to the stable *Phase 0* until another stimulus is applied.

Across the myocardium, a large degree of heterogeneity in the morphologies of the APs can also be found depending on which region of the heart they belong to [34,35]. Typically, the human atrial AP is shorter and presents a more triangular morphology (Figure 2.7, B) compared to the spike and dome-shaped with a prominent longer plateau of the ventricular counterpart (Figure 2.7, C). The differences can be attributed to the distinct ion-channel properties and distribution of the atrial and ventricular myocytes. Furthermore, the atria itself is characterised by variations in AP morphology. Differences in APs between the CT, pectinate muscles, atrial wall, appendage and atrioventricular rings have been reported [36].

2.3.4 Characterisation of action potentials

A standardised framework for characterising APs exists such that it allows for comparing APs from different regions, species and disease state (Figure 2.8). In the following table, some of the key terminology used throughout the thesis has been summarised.

Attribute	Definition
Resting Membrane Potential (RMP)	RMP is potential at which non-pacemaker cells remain at their resting state. In atrial myocytes, it varies between -65 and -80 mV [33].
Peak Amplitude	This is the maximum positive voltage reached during an AP.
Amplitude	It is the difference in voltage between peak and RMP.
Action Potential Duration (APD)	It is defined as the amount of time for which the voltage remains above a specific threshold. Experimentally this threshold is chosen anywhere from 50% to 90% for recovery from the peak to the RMP. In atrial myocytes APD ₉₀ at 1Hz is highly variable, typically ranging from 150 to 500 ms [33].
Effective Refractory Period (ERP)	ERP is a short period of time following an AP when another AP cannot be generated regardless of the size of the stimulus. This is because the Na ⁺ channels are inactivated and remain until repolarization is complete. This helps in prevention of the back propagation of the impulse.

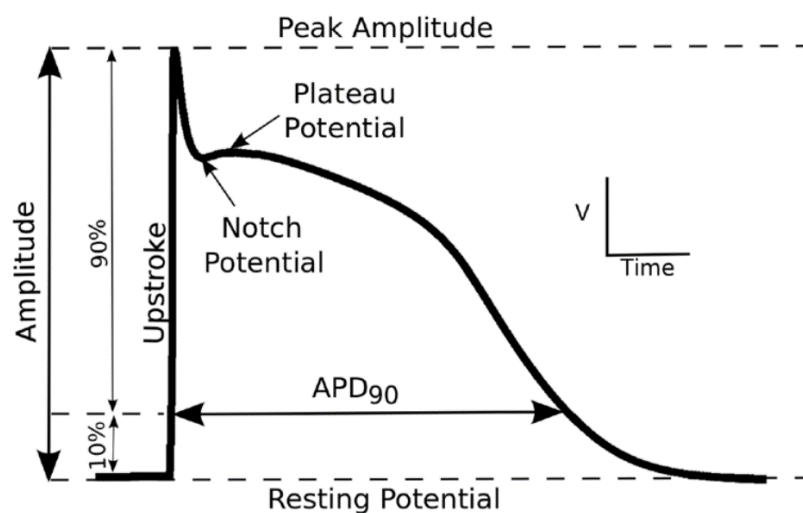


Figure 2.8: Properties of atrial action potential. Image adapted from [37].

2.3.5 Action potential restitution

When myocytes are stimulated at a regular interval, the AP properties such as APD, plateau, amplitude, upstroke velocity, etc. are affected by the size of the interval referred to as the basic cycle length (BCL). In fact, as BCL is decreased, APD becomes shorter and upstroke velocity slower. The relationship between BCL and APD is known as the APD restitution curve. Mechanistically, APD restitution occurs because at fast pacing rate the ion channels involved in AP generation are not fully recovered before the next AP occurs, and therefore generate less current. The ability of the cardiac myocytes to adapt to a faster rate by shortening APD allows for adequate contraction of the heart and pumping of blood under a wide range of physiological conditions.

The APD restitution curve can be constructed by varying BCL using the S1-S2 protocol. When myocytes are stimulated at a regular interval, these are known as the S1 stimuli. In the S1-S2 protocol, however, a number of S1 stimuli is followed by a shortly coupled S2 stimulus. Note that APs cannot be initiated earlier than a refractory period (which roughly corresponds to APD₉₀) because Na⁺ channels are inactivated and remain closed until repolarization is complete. This helps in the prevention of back propagation of AP and puts a limit on the size of S2. The shape and characteristics of the APD restitution curve provide important information about arrhythmogenesis [38]. A sufficiently steep restitution curve could lead to instability [39].

2.3.6 Action potential propagation and excitation-contraction coupling

Cardiac myocytes are electrically coupled to their neighbours through specific protein channels, gap junctions, which are located on the intercalated disks (Figure 2.5B). The flow of ions and electrical impulses occur between cells via these gap junctions. For example, when the first cell is stimulated in a single 1D strand of myocytes, the ions from the intracellular space of this cell flows into the adjacent cell and increase its potential. When the threshold for the activation of Na⁺ current is reached, the cell membrane depolarizes triggering a new AP. This chain of events allows for the propagation of APs through the myocardium.

The proteins constituting the gap junction are known as connexins (Cx). In the cardiac tissue, there are 3 main types of connexions, named based on their molecular weight: Cx40, Cx43, and Cx45, amongst which Cx43 is the most abundant [32] and responsible for the fastest flow of ions between myocytes. Moreover, there exist regional variation in gap junction distribution

between and within the atria and ventricles. Nodal tissue (SA and AV node) lacks Cx43 compared to atrial and ventricular tissue, making conduction there much slower [40,41].

Cardiac myocytes are arranged end to end in a longitudinal manner, forming fibre-like structures. There are more gap junctions along the fibres than across them (at the lateral sides). This results in faster AP conduction along the fibre than in the transverse direction. In normal conditions, the longitudinal conduction velocity in the human atria varies between ~50 and ~120 cm/s [42]. Under pathological conditions like AF, the velocity values could be reduced by ~15% in human [43] and even more in animals. A summary of conduction velocities measured in human tissues reported in the literature can be found in a review paper by Dossel et al. [42]. Note also that myofibres in the atria, have a very complex arrangement, often with different orientations across different transmural layers [44].

As mentioned previously, electrical waves spread across the cardiac myocardium, initiating and regulating contraction. Coupling of the electrical excitation of the heart with its contraction is known as excitation-contraction coupling or EC coupling. Here we will only provide a brief description of the events that lead to the contraction of the myocyte (Figure 2.9).

During Phase 2 of the AP, the L-type Ca^{2+} channels on the membrane activates, resulting in an influx of Ca^{2+} ions into the intracellular space (Figure 2.9, 1). The increase in intracellular calcium concentration triggers the release of Ca^{2+} ions from the SR by binding to the ryanodine receptors (RyR) (Figure 2.9, 2). Following the increase in the intracellular Ca^{2+} concentration, two events occur. First, the intracellular Ca^{2+} ions inactivate the L-type Ca^{2+} channels to prevent further influx of Ca^{2+} ions. Second, the Ca^{2+} ions activate the contractile unit of the myofibrils, resulting in myocyte contraction (Figure 2.9, 3). The myofibrils are composed of filaments known as myofilaments which in cardiac muscle are constructed from proteins, principally actin and myosin. The Ca^{2+} ions bind to troponin, which in turn binds to the actin filament. This binding causes a change in the shape of troponin and exposes areas of the actin. The head of the myosin filament binds to these areas resulting in the formation of a cross-bridge structure. The myosin head utilises adenosine triphosphate (ATP) produced by the mitochondria to move the actin filaments. This results in shortening of the muscle as the actin filament slides across the myosin filament. Following this, the myosin head detaches from the actin and returns to its original position. It then binds to another part of the actin filament to produce another contraction, shortening the muscle even further. This process continues until Ca^{2+} is removed

from the cell. In the absence of Ca^{2+} ions, the troponin changes shape and blocks the binding site of the actin filaments, which causes the muscles to relax. The decrease in Ca^{2+} is driven by Ca^{2+} transporters: (i) the SR Ca^{2+} pump, which transports Ca^{2+} back into the SR, and (ii) the $\text{Na}^+/\text{Ca}^{2+}$ exchanger and the sarcolemma Ca^{2+} pump, which pumps Ca^{2+} ions out of the intracellular fluids and restores intracellular calcium concentration (Figure 2.9, 4). Note that the above description of excitation-contraction coupling is simplified, and further detail can be found elsewhere [45,46].

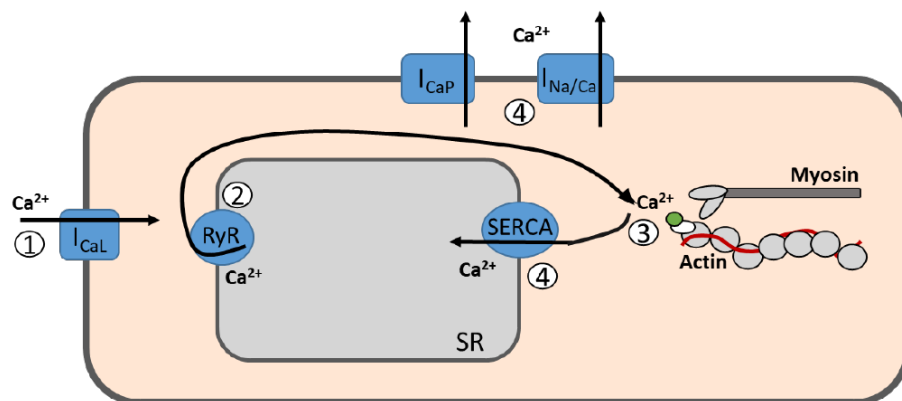


Figure 2.9: Schematic image of excitation-contraction coupling. The arrows indicate the sequence of events (labelled 1 to 4) showing the direction of Ca^{2+} movement. Here, the inner grey compartment is the SR.

2.4 Atrial Fibrillation

Atrial fibrillation (AF) is the most commonly sustained cardiac arrhythmia, characterised by a rapid and irregular rhythm of the atria. During AF, atrial cells fire at a rate of 400 to 600 beats per minute as compared to 60 beats per minute in sinus rhythm [2]. The AV node, owing to its filtering effect, acts as a barrier and prevents all the atrial impulses from conducting to the ventricles. This averts an extremely rapid ventricular rate which could result in compromised cardiac contraction and rapid death. However, the ventricular rate during AF is still high, approximately 150 bpm, and irregular as the SA node no longer regulates it, but instead by the interaction between the AV node and the atrial rate. Although they are sometimes asymptomatic, a short-lived episode of AF in healthy individuals may also result in chest pain, palpitation and light headiness. AF is not directly lethal, but when sustained for a long duration, can result in loss of effective atrial contraction leading to reduced cardiac output, fatigue, morbidity, decreased quality of life and increased risks of stroke and heart failure [47]. In 2010, approximately 33.5 million people worldwide were affected by AF, and in coming decades, studies predict a progressive increase in the prevalence and incidence of AF accompanied by high morbidity and mortality [5]. The clinical risk factors for AF include several cardiac diseases, such as heart failure, and advancing age [48,49].

AF initially presents in paroxysmal (PAF) form, which can self-terminate within 7 days and spontaneously convert to normal sinus rhythm. Persistent AF (PsAF) lasts for more than 7 days and requires pharmacological or direct-current electric cardioversion, while the restoration to sinus rhythm becomes impossible in cases of permanent AF (PerAF) [50,51]. Despite its clinical importance and high prevalence, limited knowledge of the mechanisms responsible for initiation and sustenance of AF have prevented clinicians from treating the arrhythmia efficiently. In the following sections, a brief review of what is known about AF mechanisms and its treatment strategies is presented, along with an overview of challenges that need to be addressed to improve the efficiency of AF treatment and make it more patient-specific.

2.4.1 Mechanisms underlying AF

Mechanisms underlying AF are complex and multifactorial. A schematic image summarising the major factors contributing to the genesis of AF are presented in Figure 2.10. The common factors to AF initiation and maintenance are a trigger and a substrate (Figure 2.10, green boxes). The trigger can act on the substrate to generate re-entrant drivers (RDs) for AF (Figure 2.10,

blue boxes). Such drivers are believed to be the main mechanism underlying AF [51]. During AF, these rapidly discharging drivers can result in irregular electrical activations of the atria wall. Moreover, as AF progresses, it promotes atrial remodelling (Figure 2.10, yellow) which favours the development of triggers and substrate for re-entry, hence further facilitating AF. This self-reinforcing property of AF is described as “AF begets AF”, which highlights the progressive nature of this complex disorder. A detailed review of mechanisms underlying AF can be found elsewhere [2,50–54]. Here, a brief overview of the well-known triggers and substrates for AF, as well as types of atrial remodelling that enhance the vulnerability of the heart to AF, is presented below.

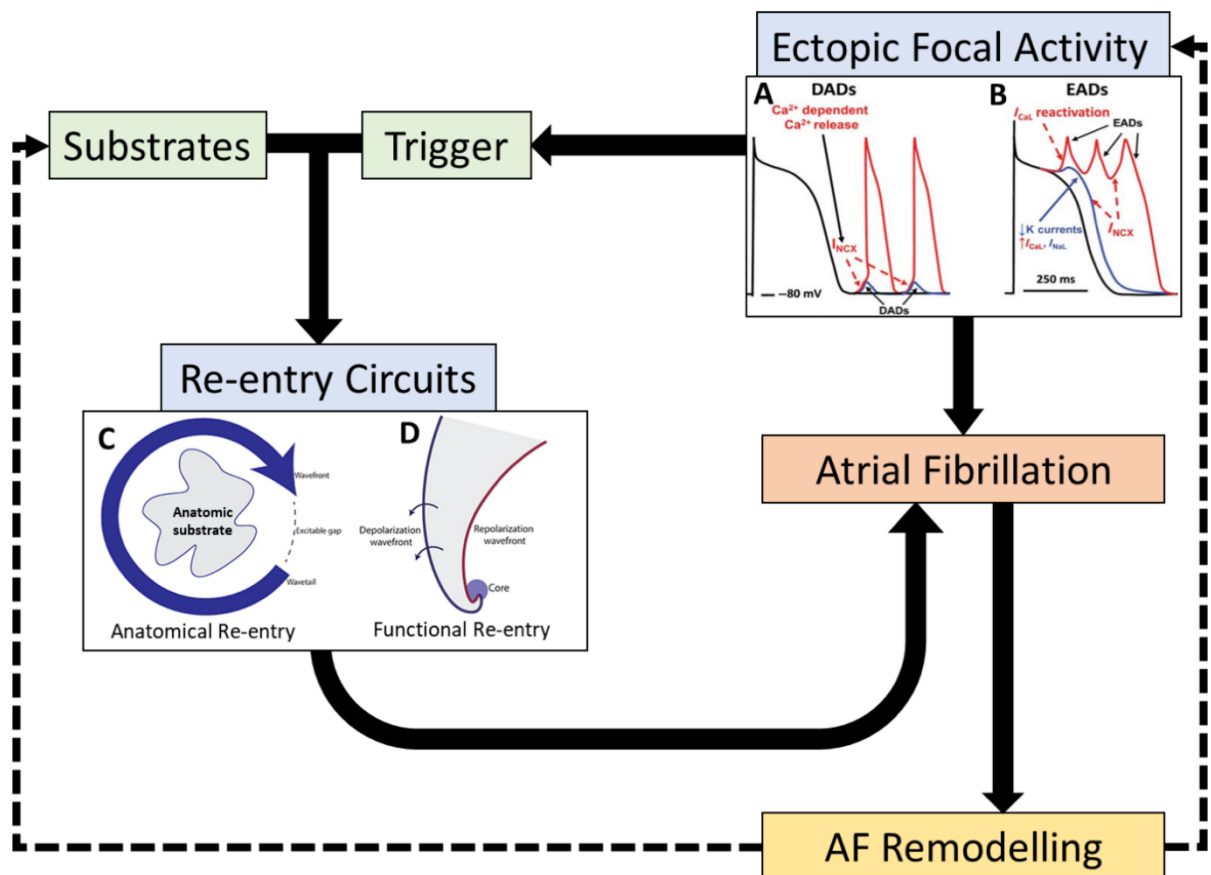


Figure 2.10: A schematic representation of the major contributors to the genesis of AF, which explains the notion “AF begets AF”. The flow diagram shows that once triggered directly by ectopic sources or via re-entrant drivers formed due to interactions of the ectopic with tissue substrates, AF causes atrial remodelling which promotes AF maintenance by generating more triggers and substrates. Electrical remodelling reduces ERP and facilitates re-entry, and also promote further development of ectopic activity. Structural remodelling causes atrial dilation and development of fibrosis, which facilitates slow and heterogeneous AP conduction and more re-entrant drivers.

The three main classical mechanisms proposed since the early 20th century for initiation and maintenance of AF are [52,54]: (i) ectopic AP firing either by a single focus followed by fibrillatory conduction or by multiple simultaneously discharging foci (Figure 2.11, a), (ii) formation of a single localised re-entrant circuit, a “mother rotor” (Figure 2.11, b) or (iii) multiple re-entrant circuits with fibrillatory conduction (Figure 2.11, c). Determining the underlying mechanism could have a profound therapeutic implication, especially for catheter ablation treatment for AF.

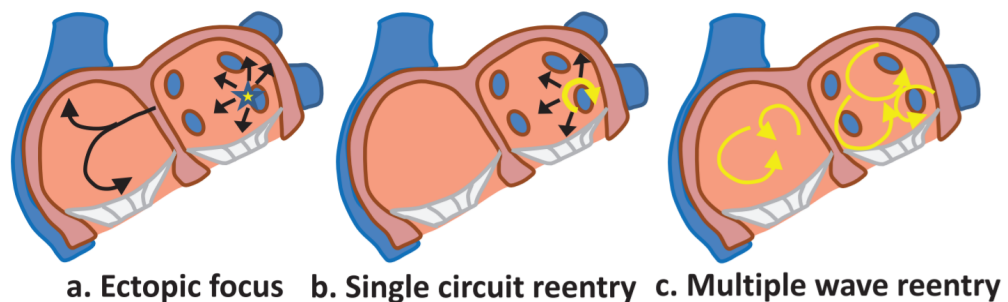


Figure 2.11: The three main classical mechanisms proposed for initiation and maintenance of AF. Image adapted from [52] with permission.

Advance mapping and computational modelling technologies have shed further light into the mechanisms contributing to the genesis of AF [52]. Narayan et al. [55], used high-density invasive mapping in AF patients and showed the presence of small number of stable RDs at fixed locations. However, Haissaguerre et al. [56] and Cochet et al. [13] used non-invasive mapping in combination with modelling to show the existence of transient RDs which localised at fibrotic regions. Endocardial–epicardial dissociation has emerged as a novel AF mechanism. Simultaneous epicardial and endocardial mapping by Van der Does et al. [57], De Groot et al. [58] and Gutbrod et al. [59] showed breakthrough activations at either surface that could facilitate AF perpetuation.

2.4.1.1 AF triggers

Ectopic activity can act as AF trigger, and can also maintain AF when occurring repetitively over a long period of time. Such triggers can arise from micro-re-entry, enhanced automaticity (spontaneous diastolic depolarization) or triggered activity (afterdepolarizations) [60]. A vast majority of triggers are localised at the PV sleeves [10] and are thought to arise from either early afterdepolarizations (EADs) or delayed afterdepolarization (DADs). EADs occur during phases 2-3 of AP, as a result of APD prolongation, which allows for inactivated Ca^{2+} channels

to recover and generate inward Ca^{2+} current leading to secondary depolarization of the cell membrane (Figure 2.10, A). DADs, on the other hand, occur during phases 3-4, as a result of an abnormal increase in diastolic Ca^{2+} concentration, which enhances the activity of the $\text{Na}^+/\text{Ca}^{2+}$ exchanger. The exchanger works by extruding 1 Ca^{2+} ion for 3 extracellular Na^+ ions causing a net inward current which can depolarize the cell membrane [51,54] (Figure 2.10, B). The mechanisms for myocytes developing autonomic activations are not fully understood. However, early experimental studies have shown that blocking autonomic behaviour suppresses AF while promoting DADs by facilitating the release of Ca^{2+} ions from the SR increases AF inducibility [61].

2.4.1.2 Re-entry

RDs are one of the key mechanisms of AF maintenance [62]. The formation of RDs requires a trigger and a suitable tissue substrate. When the substrate is an anatomical obstacle, anatomical re-entry is generated (for example, AV node re-entry tachycardia, typical atrial flutter, etc.). In such cases, ectopic foci act as a trigger, while anatomical obstacles (such as the AV node or PVs) act as substrate sustaining anatomical re-entry. An example of an ectopic focus initiating a single RD around an anatomical obstacle is shown in Figure 2.12.

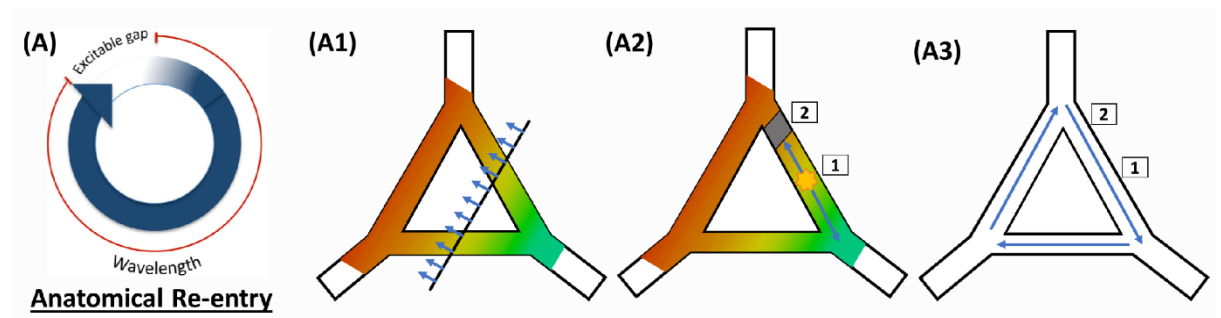


Figure 2.12: Schematic images of anatomic re-entry formation around an obstacle. (A) Anatomical re-entry circuit with an excitable gap. (A1) Depolarization of a triangular junction of several cardiac fibres by an AP propagating in the direction indicated by arrows. (A2) an ectopic focus (\otimes) emerges from location 1, while location 2 is still refractory (grey), which results in conduction block towards location 2. (A3) The AP propagates along an alternative path (clockwise) and reaches location 2 when it is no longer refractory, resulting in the formation of a persistent re-entrant circuit.

The minimum path length required for formation of re-entry around an obstacle is equal to the wavelength (λ) of the AP, which is defined as the distance travelled by the AP with a conduction velocity (CV) over one refractory period [2]:

$$\lambda = \text{ERP} \times \text{CV} \quad (2.2)$$

Hence, substrates that are characterised by lower refractory period and CV are more likely to sustain RDs. Moreover, a shorter λ allows more RDs to fit in the atria and maintain AF [2].

The formation of RDs, however, does not always require an anatomical obstacle. The RDs can be formed when an ectopic wave encounters a transiently refractory region (or a region with heterogeneous ERP) and break downs generating a singularity around which the newly formed RDs can rotate [63,64]. This mechanism is known as functional re-entry (Figure 2.13C).

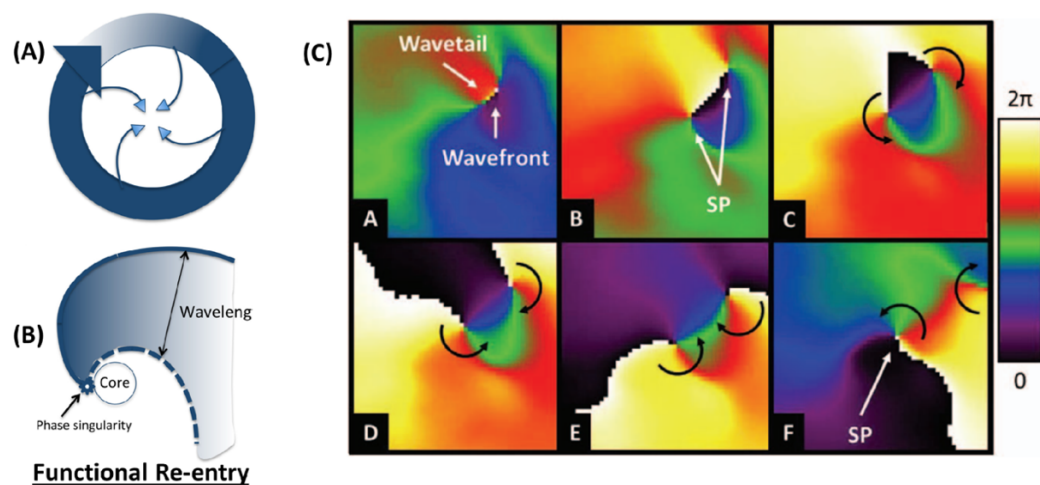


Figure 2.13: Conceptual theories of functional re-entry: (A) Leading circle, (B) Spiral wave. (C) Experimental recording of wave-break resulting in the formation of two RDs, replicated with permission from [64].

Re-entry has been conceptualised by using either the leading circle or the spiral wave theory. Historically, the leading circle model proposed by Allesie et al. [65] in the 1970s suggested that re-entry organises itself in circuits whose circumference is equal to or greater than the wavelength and central region is unexcitable, as it is rendered refractory due to the centripetal excitation wavefront (Figure 2.13, A). However, this concept was later replaced by a widely accepted spiral wave paradigm proposed by Wiener et al. [66], according to which impulses propagate around a functionally unexcitable core (Figure 2.13, B). In a spiral wave, the curved wavefront and wave-tail meet at one point – the tip or phase singularity – which travels around the core. The curvature of the wavefront progressively increases towards the core where it reaches a critical value [67]. The higher the curvature, the slower the wave propagation; therefore, the critically high curvature at the core makes it impossible for the AP to invade the core [68]. In this sense, the core is unexcitable. Currently, the spiral wave paradigm is dominant

in the theory of RDs and fibrillation [69]. It accounts for the wave curvature effects and meandering behaviour of RDs, as observed in experimental recordings [70]. In simulations presented in the dissertation, we used spiral waves to model re-entrant mechanisms of AF. Therefore, in all chapters, RDs will refer to spiral waves.

In cardiac muscle, the spiral wave dynamics is affected by the excitability of the underlying tissue. Excitability is a measure of the stimulus current strength required to excite cardiac tissue. A higher excitability would mean a smaller current is required to initiate an AP and a faster AP propagation, and visa-versa [71]. For instance, fibrotic and ischemic regions would have a significantly lowered excitability compared to healthy myocardium.

Modelling and simulation studies using a wide range of models have shown that the spiral wave tip rotates around a circular core in tissues with lower excitability, whereas complex flower-like meandering pattern with linear core are seen as the tissue excitability is increased (this will be discussed further in Chapter 3 Section 3.4.1). Computational simulations by Krinsky, Efimov and Jalife [72,73] have demonstrated such transitions from circular rotation to hypermeander by altering the fast sodium current conductance. However, the existing cardiac mapping methods do not allow a full characterisation of the meander patterns in a patient with the same resolution as in numerical simulations. Limited experimental studies have identified transient meander patterns of spiral waves with linear core in the normal myocardium [71,73,74].

2.4.1.3 AF-induced atrial remodelling

The generation and maintenance of RDs in the heart can be favoured by the alteration of the electrophysiological and structural properties on the underlying tissue substrate, for example, by reducing the ERP and/or CV. Such an alteration occurs naturally during AF in the form of AF-induced remodelling (see also above in Section 2.4.1), which alters atrial structure and function. Hence, atrial remodelling can be broadly classified into electrical and structural remodelling.

Electrical remodelling alters ion channel expression of the cardiac myocyte in such a way that atrial APD/ERP and wavelength becomes shorter, which promotes the formation of re-entry and helps sustain AF [2,51,54]. Electrical remodelling processes have been extensively reviewed elsewhere [2,51,53]. Briefly, its major determinants of reduced APD are: (i)

downregulation of L-type calcium current (I_{CaL}), which shortens the AP plateau and (ii) upregulation of K^+ currents (such as I_{K1} and acetylcholine-dependent K^+ current), which accelerates AP repolarization. Moreover, remodelling may also cause alterations in the distribution of gap junctions and decrease the amount of the gap junction forming connexins, thus altering atrial CV and anisotropy. Electrical remodelling can, therefore, result not only in wavelength reduction but also in wave-breaks due to increased anisotropy.

Structural remodelling alters atrial size and the underlying atrial tissue properties, down to cellular ultrastructure. This can lead to pathological changes in conduction pathways, which contribute to RD formation and stabilisation. Most notably, structural remodelling is associated with the development of atrial fibrosis which plays an important role in the maintenance of AF. Fibrosis is characterised by the formation of excessive extracellular matrix and collagen deposition in the myocardium [75]. Numerous factors can contribute to the development of fibrosis during AF, such as atrial stretch, neurohumoral activity and oxidative stress.

Importantly, the development of fibrosis is linked to AF itself. Experimental studies in dog hearts [76] have demonstrated a great increase in fibrosis during chronic AF. Conversely, increased AF susceptibility has been reported across numerous animal models that develop atrial fibrosis. Both patient medical imaging and ex-vivo histology of atrial tissue have shown an increase in the amount of fibrosis in PsAF compared to PAF patients and healthy individuals [77] (see in Figure 2.14). This suggests that AF progression itself is among factors that either predispose or contribute to the development of atrial fibrosis.

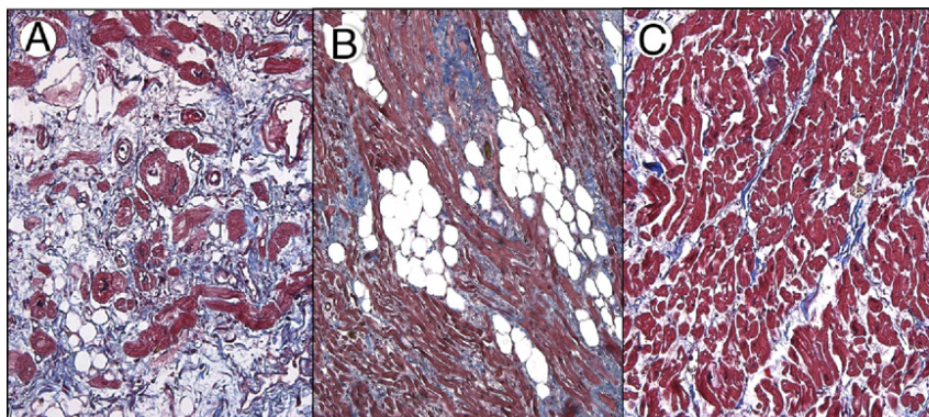


Figure 2.14: Increase in the severity of fibrosis with AF disease progression. Figure reproduced from [77] with permission, shows a light microscopic image of atrial tissue specimens from crista terminalis of patients with, (A)

permanent AF, (B) paroxysmal AF and (C) healthy individual without the history of AF. The myocytes have red stains, and fibrosis is in white. Percentages of fibrotic tissue in A, B and C are 51%, 2% and 5%, respectively.

2.4.2 Atrial fibrosis

In the healthy myocardium, fibroblasts provide a 3D mechanical scaffold which helps in the integration of all the myocytes into an effective pump. However, cell damage from injury, hypertension and AF progression triggers the profibrotic signalling process, which promotes the differentiation of fibroblast to myofibroblast. The latter proliferate rapidly and deposit collagenous extracellular matrix at high rates, allowing for wound healing by scar formation [75]. This auto-protective mechanism of the myocardium is critical for mechanical stability of the heart. However, the increase of the non-conductive collagenous tissue affects electrical conduction by impairing inter-myocyte coupling and often forming conduction barriers. Hence, fibrotic regions facilitate slow conduction or a complete conduction block, which increases the susceptibility to initiation and maintenance of RDs [75]. Additionally, fibroblast and myofibroblasts can be electrically coupled to myocytes, acting and as current sources/sinks and modifying their electrical properties, which can promote automaticity and ectopic activity [78]. In summary, fibrosis is a structural change that promotes arrhythmogenesis in multiple ways, generating a vulnerable substrate for the initiation of RDs and ectopy.

2.4.2.1 Arrhythmogenic potential of fibrosis

Fibrosis has been broadly categorised into compact, diffuse, patchy and interstitial based on distinct patterns observed in histological data, as shown in Figure 2.15 [79]. Compact fibrosis (also refers to as scar) arises from previous infarct or ablation. These regions are composed of collagen and devoid of myocytes, hence electrically non-conductive. Compact fibrotic regions provide obstacles for anatomical macro-re-entry (Figure 2.15, B). However, regions of diffuse, patchy and interstitial fibrosis can generate slow discontinuous conduction because they are a mixture of collagen and conductive tissue, which facilitates the formation of RDs (Figure 2.15, C). Hence, the latter cases of fibrosis present greater arrhythmogenic risk.

In a structurally remodelled atria, all types of fibrosis can exist and be spatially distributed in a patient-specific manner [80]. This makes it extremely challenging to clearly distinguish among different types of fibrosis from imaging data and evaluate their effects on AF.

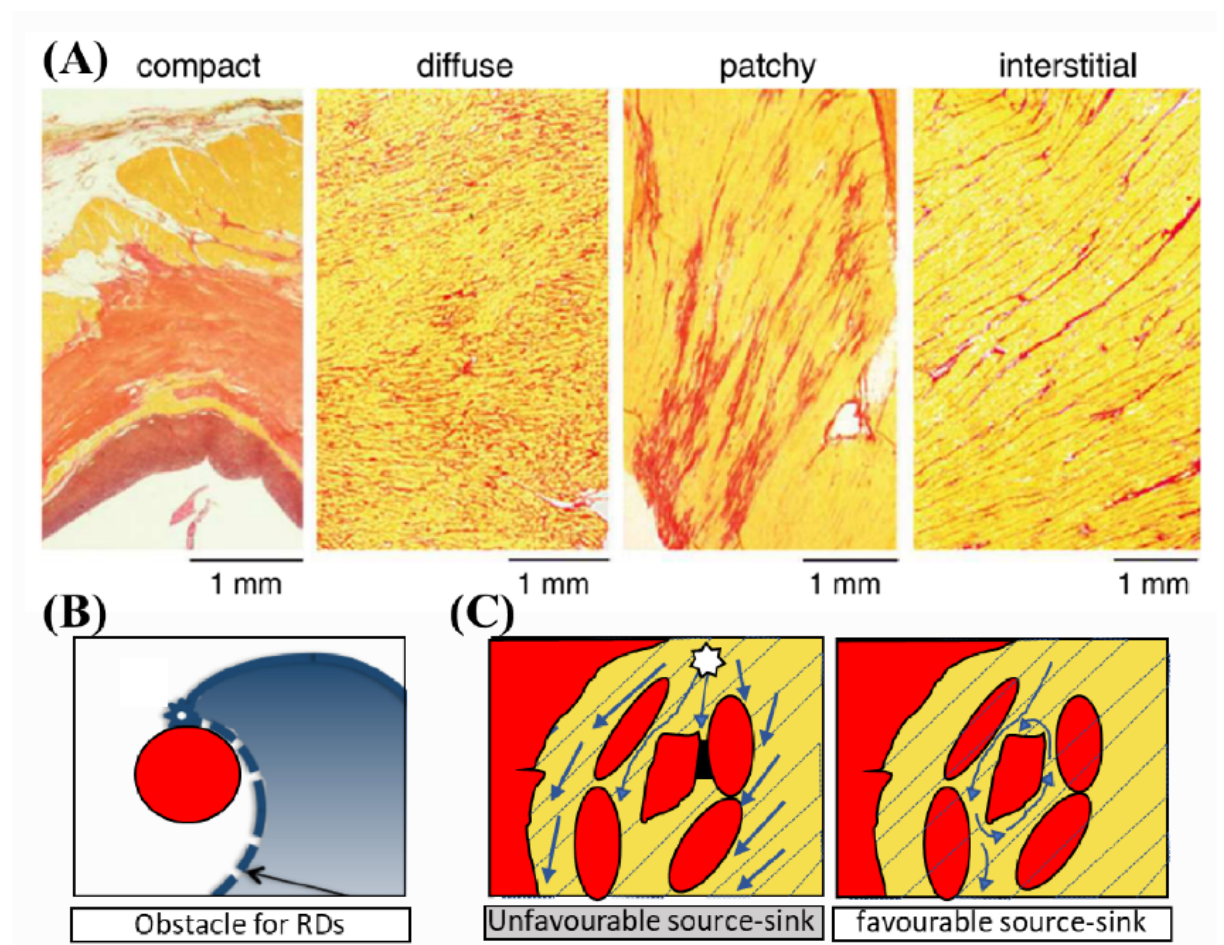


Figure 2.15: Different types of fibrosis based on their spatial patterns. The red and yellow regions denote the collagen and myocardium, respectively. (A) Starting from the left, (i) Compact fibrosis or scar which is devoid of myocytes, (ii) diffuse fibrosis which is uniformly scattered throughout the tissue, (iii) patchy fibrosis with larger infiltrations of collagenous regions present between myocyte bundles and (iv) interstitial fibrosis with long fibrotic strands leading to increased anisotropy [79]. Compact fibrosis generates obstacles for formation of macro-entry (B) while diffuse, patchy and interstitial fibrosis generates heterogeneous conduction (C) giving rise to RDs.

2.4.2.2 Imaging of atrial fibrosis

Traditionally, invasive 3D electroanatomic mapping (EAM) has been used for the assessment of electrical changes in the atria [49]. However, advances in imaging have facilitated the non-invasive assessment of atrial fibrosis. Magnetic resonance imaging (MRI) with late gadolinium enhancement (LGE) is one of the methods used for identification, localisation and quantification of atrial fibrosis [81]. A Gadolinium (Gd) based contrast agent accumulates in the extracellular matrix owing to the slow washout kinetics in the diseased tissue compared to healthy tissue. This results in an increase in signal intensity in the fibrotic areas due to the

abundance of extracellular matrix [82]. Specific MRI protocols have been developed for imaging and quantification of atrial fibrosis, as shown in Figure 2.16, from [81].

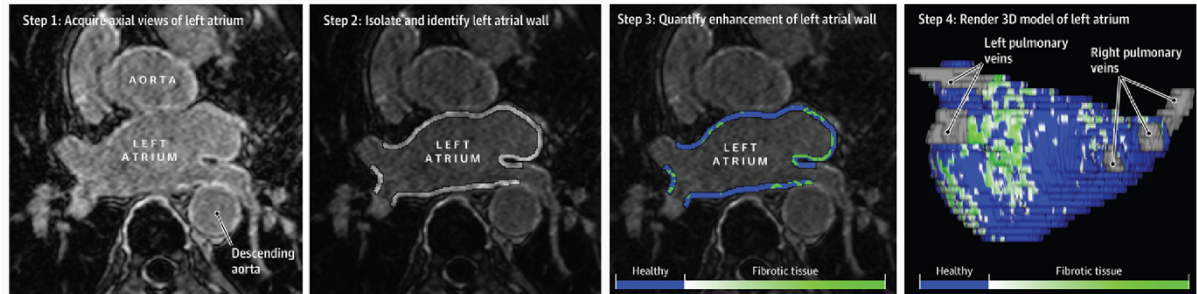


Figure 2.16: Quantification of atrial fibrosis from LGE-MRI. The steps involved are proposed by Marrouche et al. [81]: (i) Step 1 is the acquisition of high resolution 3D LGE-MR images of the LA, (ii) Step 2 is the segmentation of the LA wall from the images, (iii) Step 3 is the quantification of fibrosis based in relative contrast enhancement and finally, (iv) Step 4 is the colour-coded fibrosis map projected on the LA wall.

LGE-images are typically acquired 15-30 min after the injection of the contrast agent, to allow it to accumulate preferentially in fibrotic tissue. The presence of the contrast agent shortens the longitudinal relaxation time constant, T_1 , of the fibrotic tissue, making fibrosis appear brighter than healthy tissue in T_1 -weighted images. The in-plane resolution ranges from 1.2-1.6 mm while, slice thickness ranges from 1.5-4.0 mm.

Image processing is then performed to detect the atrial wall and fibrosis. The wall segmentations are typically carried out manually by clinicians. After the atrial wall has been segmented, thresholding techniques are applied with a cut-off value to distinguish between healthy and fibrotic tissue. However, clinically and experimentally, highly variable image intensity thresholding techniques have been used for defining fibrosis [83]. In particular, histogram-based intensity thresholding is widely used for detection of scar tissue from ablation [84]. Here, the cut-off value is defined as being 2 or 3 standard deviations above a reference value (either atrial wall or blood pool intensity). Recent studies have adopted this approach to detect atrial fibrosis [81,85]. Despite being promising, the reproducibility and reliability of fibrosis assessment with LGE-MRI in the atria is a controversial issue.

The lack of standardised image acquisition and processing protocols result in poor reproducibility across different clinical centres and present the main limitation of LGE-MRI for the assessment of atrial fibrosis. A recent analysis performed by Chubb et al [86], showed that the choice and dose of contrast agent, image acquisition time after administration of the contrast

agent and scanner strength affects the assessment of scar tissue. Moreover, lack of standardisation is also an issue in image processing techniques that are highly operator dependent, especially in identifying patchy fibrosis or inhomogeneous grey LGE areas [83].

Alternative techniques such as image intensity ratio (IIR), which normalises myocardial intensity with the mean blood pool intensity are being developed [87,88]. This allows for reducing intra-patient and inter-scan variability by reducing the confounding effects of physiological parameters (surface to coil proximity, contrast dose, body mass index, etc.) that affect the images globally and are unrelated to the underlying tissue characteristics [87]. Moreover, the IIR threshold to distinguish between healthy tissue, fibrosis and scar are established by assessing the correlation between IIR values and local bipolar voltage recorded via EAM. Although this approach helps in standardisation, the choice of the IIR threshold values to distinguish between healthy and fibrotic myocardium is still an open question.

Another challenge associated with LGE-MRI is the capability of LGE-MRI to reliably detect fibrosis. Gd is not a specific marker for atrial fibrosis and it accumulates in regions with increased volume of extracellular matrix, which could also be linked with other pathological processes, such as inflammation and edema. Most reliable validation would be based on histological analysis, but this is not straightforward to perform in humans and can only be performed in localised areas [89]. An alternative method commonly used for validation is based on comparing image intensity from LGE-MRI with voltage maps from EAM (discussed in Section 2.4.3.3) [85,87]. However, this approach involves high density invasive mapping, which is affected by several technical variables such as the mapping catheter's tip size, shape, orientation and coverage on the atrial surface and lack of consensus on the cut-off voltage to define scar. Moreover, registering atrial shell obtained from EAM with MRI data is very challenging and small miss-alignment can affect the classification of fibrotic regions from non-fibrotic regions [83].

An alternative tool for assessment of atrial fibrosis is post-contrast cardiac MRI atrial T1 mapping [90]. This imaging technique has been shown to reliably index atrial fibrosis which correlates with tissue voltage and outcome of catheter ablation [91]. However, T1 mapping technique does not provide a spatial localisation of fibrosis necessary for guiding treatment. Therefore, LGE remains the most promising tool for the detection of localised and cohesive fibrosis in the atria.

2.4.3 Current treatment strategies for AF

The treatment of AF follows two main strategies, rate control and rhythm control, depending on the patient-specific disease condition and history [4]. Rate control is aimed exclusively towards controlling the ventricular rate despite continuing fibrillation in the atria. It is carried out either using pharmacological agents that slow down the maximum rate of conduction through the AV node (beta-blockers and calcium channel blockers) or by isolation of the AV node with catheter ablation (CA). Rhythm control, on the other hand, aims to restore the sinus rhythm via: electrical or pharmacological cardioversion, the use of either anti-arrhythmic drugs (AADs) or CA. Although the normal atrial function is only restored with rhythm control, clinical trials comparing the rate to rhythm control till date have comparable outcomes [4].

2.4.3.1 Anti-arrhythmic drugs

AADs work by altering cardiac electrical properties to regain sinus rhythm. One of the most common strategies to restore sinus rhythm is by applying class III anti-arrhythmics that block K^+ channels and therefore prolong APD, increasing the wavelength, reducing the excitable gap and terminating RDs. However, APD prolongation could also be pro-arrhythmic, giving rise to a distinct form of ventricular tachycardia known as Torsades de Pointes (TdP) arrhythmias (long QT syndrome) [92]. Therefore, an important side effect of AADs is the risk of severe ventricular arrhythmias which can be life-threatening. It is believed that prolonged APD causes EAD events in Purkinje fibres, which propagate to ventricles and give rise to intraventricular re-entry associated with TdP [93,94]. Moreover, AADs affect more than one ionic channel, making their net effect on the atria and also the ventricles difficult to predict. Computational models are thus being increasingly used to aid the design of safe AADs [95].

CASTLE-AF trial (Catheter Ablation versus Standard Conventional Therapy in Patients with Left Ventricular Dysfunction and Atrial Fibrillation) found CA to result in a lower recurrence rate and better sinus rhythm maintenance compared to AADs in AF patients with heart failure [96]. Another recent clinical trial, CABANA (Catheter Ablation vs Anti-arrhythmic Drug Therapy for Atrial Fibrillation) showed symptomatic AF patients to have a greater quality of life (at 12 months evaluation) when treated with CA compared to AADs [97]. However, there is yet no evidence that it significantly reduces mortality, stroke, bleeding and cardiac arrest compared to medical therapy [98].

2.4.3.2 Radio-frequency catheter ablation

Over recent decades, technical advancements in clinical electrophysiology have brought radio-frequency CA to the forefront of treatment for arrhythmias. CA is an invasive procedure where catheters are used to deliver localised energy to burn tissue around or within arrhythmogenic areas, thus isolating them from the surrounding healthy tissue. Ablation procedures for paroxysmal AF have been successful by isolation of the PVs (Figure 2.17, A), which is believed to be the main source of rapid spontaneous focal activity or local RDs [10]. Therefore, PV isolation has been established as the gold standard of treatment for paroxysmal AF [99].

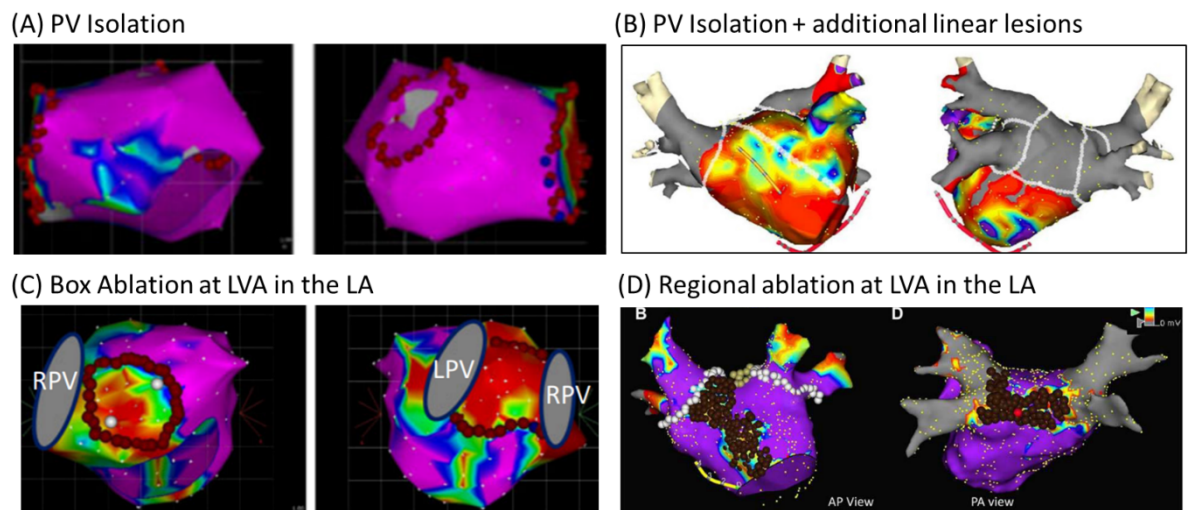


Figure 2.17: Different types of CA procedures. (A) PV isolation with red circles indicating the location of the ablation lesion [100], (B) PV isolation plus additional linear lesions in white [101], (C) Box ablation around low voltage areas [100] and (D) regional ablation across the entire low voltage areas [102]. The LA voltage is colour coded such that red corresponds to voltage $< 0.5\text{ mV}$ and purple – to voltage $> 1.5\text{ mV}$ for panels A, C and D.

In fact, CA may result in conversion of AF to macroreentrant atrial tachycardia in many cases [103,104]. Atrial tachycardia (AT) is a supraventricular tachycardia which causes that atria to beat rapidly (100 - 200 bpm), usually with regular rhythm on the continuum between AF and sinus rhythm [105]. Successful ablation of AT often results in the restoration of sinus rhythm. AT can either be focal or macro-entrant in nature. The former is characterised by radial and centrifugal atrial activation from the point of origin, which can be located anywhere in the atria (PVs, superior vena cava, coronary sinus, etc.) [105]. The mechanism underlying focal discharge could be rapid depolarizations, microreentry or afterdepolarizations. In macroreentrant AT, on the other hand, activation is continuous and uninterrupted due to re-

entrant wavefront rotating around an obstacle formed by anatomical obstacles (venous or valvular orifices), scars, or areas of functional block.

However, despite its high success rates in paroxysmal AF patients, PV isolation has suboptimal outcomes and high AF recurrence rates among long-standing PsAF patients [8,106]. In order to address this, additional strategies to improve the outcome of CA in these patients have been developed over the years. These include such standardised approaches as: (i) creation of additional linear lesions in the LA (Figure 2.17, B) consisting of a roof line connecting left and right superior PV and/or LA isthmus ablation between left inferior PV and the MV [107], (ii) automatic ganglionic plexi ablation [108] and (iii) ablation of the vein of Marshall [109]. Other, more personalised strategies directly target substrate or/and drivers of AF using EAM, which include targeting atrial regions with: (iv) complex fractionated electrograms (CFAEs) [110], high dominant frequency (DF) [111], high Shannon entropy (ShEn) [112]. More recently, (v) direct ablation of AF drivers (ectopic triggers or RDs) identified invasively using basket catheters [113] or non-invasively using body surface electrodes [114] has also been applied.

The lack of consensus is reflected in a lack of reproducibility of such strategies across multicentre trials. For example, the randomised trial STAR-AF II failed to demonstrate any significant reduction in AF recurrence when comparing PVI plus additional linear lesion or CFAE group to PVI group alone [106]. AF driver-guided ablation is also limited by the challenges of mapping and visualising electrical activity on the endocardial surface with sufficiently high resolution [115]. This can explain contradictory outcomes of multicentre trials, where some centres have shown favourable outcomes of AF driver-guided ablation [116], while others have failed to find advantages in this approach compared to PVI [117]. Therefore, despite the low long-term efficiency, PVI is still the primary ablation strategy for PsAF patients.

This brings us the question of why PVI is inefficient in long-standing PsAF patients. This could be because of changes in the complexity of AF mechanisms as it progresses [118]. Initially, AF is driven by localised focal or re-entrant sources clustered in relatively limited atrial region (such as the PVs), which send rapid activations to other regions of the atrial wall [119]. AF progression leads to more and more advanced levels of atrial remodelling, which generates more arrhythmogenic substrates and allows the atria to sustain multiple triggers or/and RDs outside the PV region, whose locations become harder to predict [2]. Therefore, we can hypothesise that the efficacy of CA in PsAF patients could be greatly improved by targeting the

remodelled atrial substrates in addition to PVI. This requires reliable methods for the accurate identification of these arrhythmogenic substrates during AF. Identifying such locations throughout the atria requires a better understanding of the interplay between structural and functional mechanisms underlying various stages of AF in individual patients.

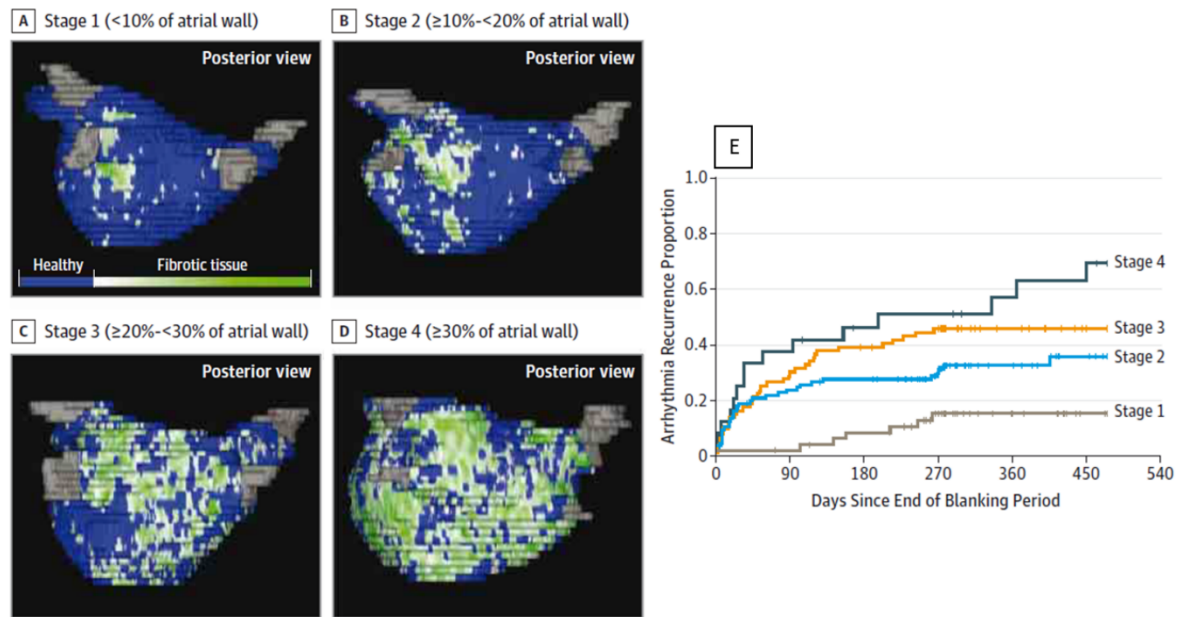


Figure 2.18: The Utah classification for atrial fibrosis quantified using LGE-MR images and AF recurrence [81]. (A-D) Example of left atria with increasing atrial fibrosis (green) burden classified as stages 1-4. (E) The cumulative incidence of AF recurrence after 475 days indicates increasing recurrence proportion in patients with increasing fibrosis burden. The image has been adapted from [81].

2.4.3.3 Ablation strategies targeting atrial fibrosis

There is growing evidence linking AF progression and treatment efficacy with atrial fibrosis. Specifically, a multicentre clinical observation study, DECAAF, has demonstrated that AF recurrence after PVI correlates with fibrotic burden (FB) assessed using LGE-MRI (discussed in Section 2.4.2.2). Briefly, the trial was conducted by Marrouche et al. [81], on a cohort of 272 PAF and PsAF patients undergoing their first PVI. These patients were classified into 4 groups according to their total amount of atrial fibrosis (FB), as shown in Figure 2.18. These groups were: (i) Utah 1 (FB < 10% of the atrial wall), (ii) Utah 2 ($10\% \leq \text{FB} < 20\%$), (iii) Utah 3 ($20\% \leq \text{FB} < 30\%$), and (iv) Utah 4 ($\text{FB} \geq 30\%$). The cumulative incidences of AF recurrence after 475 days of PV isolation (Figure 2.18, B), was 15.3%, 35.8%, 45.9% and 69.4% in Utah 1, 2, 3 and 4, respectively. Furthermore, studies performed by other centres have confirmed these findings, suggesting AF recurrence and CA failure to be more frequent in patients with $\text{FB} \geq$

30% [120]/ 35%[121]. This clearly highlights the arrhythmogenic potential of fibrosis in AF patients and emphasising the importance of fibrosis quantification as a critical tool for patient stratification for CA treatment. Moreover, these outcomes lay the foundation for substrate modification-based ablation strategies in patients with higher FB.

Furthermore, high LGE-MRI intensity has been linked with fibrotic regions identified from histology [89], as well as correlated with low-voltage areas identified from electro-anatomic mapping [85,87], broadly defined as regions with bipolar voltage < 0.5 mV during sinus rhythm [122]. Hence, low voltage areas are often regarded as a surrogate for atrial fibrosis. CA strategies that target low voltage areas in addition to PVI have shown improved success rates [100,102,122–126]. This technique is known as scar homogenization, and the rationale behind is to eliminate low voltage areas within the atrial walls and convert them to electrically non-conductive regions. Even though some studies have shown promising results when comparing this substrate-based ablation strategy to PVI only, others have failed to find the advantage of this procedure over PVI [117,127]. Large scale randomised studies are required to confirm the efficiency of this strategy. Specific challenges related to this approach include its poor standardisation in terms of (i) detection of low voltage areas, which is dependent on the type and resolution of mapping electrode used, (ii) low voltage area ablation protocols that vary across multiple centres. For example, Kottkamp et al. [100] proposed box isolation of fibrotic areas (BIFA) by circumferential isolation of the low voltage areas (Figure 2.17, C). On the other hand, Yamaguchi et al. [102] ablated over the entire low voltage areas (Figure 2.17, D). Second, the extensive ablation at the low voltage areas across the atrial wall has led to a significant decline in left atrial function in these patients [102].

In summary, even though different CA approaches discussed above have led to a reduction in AF recurrence in PsAF compared to PVI, the success and reproducibility across multicentre trials are controversial. This may be due to a lack of knowledge of how structural remodelling influences AF dynamics in PsAF patients. Understanding the latter in a clinical setting is challenging due to the poor resolution of invasive mapping and non-invasive imaging tools that are unable to capture the complex AF dynamics. Moreover, even limited mapping methods require lengthy and often unsafe procedures, further undermining their clinical value.

2.5 Mathematical Modelling and Simulations

Mathematical models of biological systems provide a platform for simulation processes that are difficult to explore in an experimental setting. Over the years such models have been used to explore mechanisms of processes as varied as electrical function of the brain [128] and perfusion in tumour blood vessels [129], proving the effectiveness of the modelling approach. The work presented in this thesis uses this approach to model the electrical activity of the atria (described in section 2.2) and to improve the understanding of AF. Moreover, the developed models can be used as a platform for testing treatment strategies in-silico, which would be impossible to perform with the same level of detail in a clinical setting.

This section will provide a brief overview of the different components required for the construction of a 3D atrial model and discuss the techniques used for the simulation of AF. First, the development of single cell models (Figure 2.19, Step 1 and 2) using an example of the very first mathematical cell model by Hodgkin-Huxley will be discussed. Second, the mathematical formulation of cardiac tissue models, the underlying assumptions and methods for solving the relevant equations numerically are presented. Finally, a brief review of AF simulations performed with 3D atrial models is provided (Figure 2.19, Step 3).

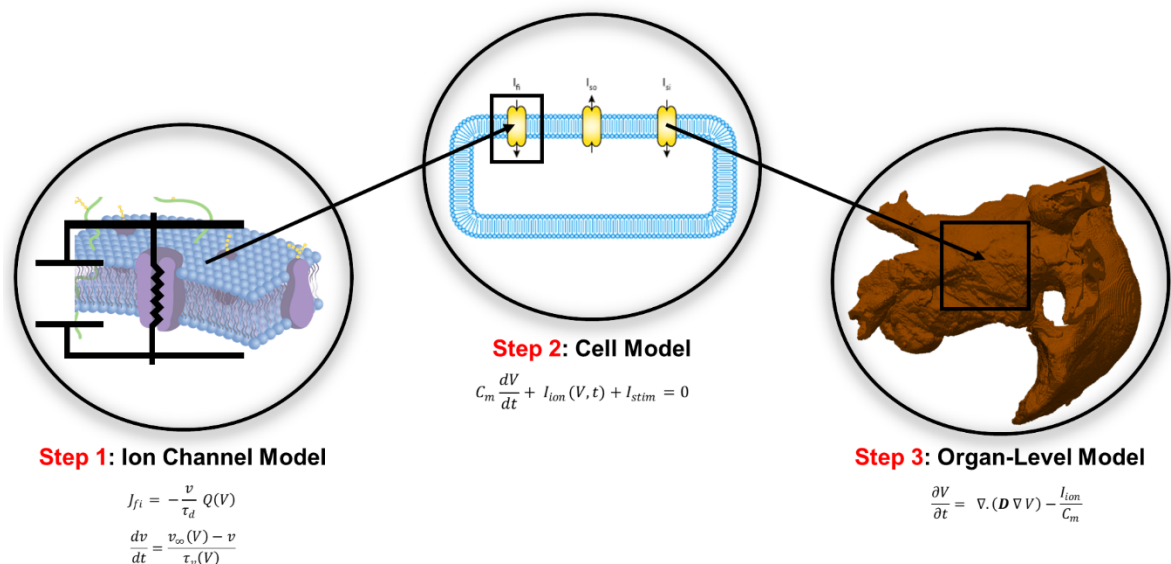


Figure 2.19: The steps involved in creating mathematical model of cardiac electrophysiology and run simulations.

2.5.1 Modelling atrial electrophysiology

Hodgkin and Huxley (H-H) laid the foundation for electrophysiology modelling in 1952 with the publication of the first quantitative model for propagation of electrical impulses along an axon of a squid neuron [130]. In 1962 they were awarded the Nobel Prize in Physiology or Medicine for their work. They modelled the electrical activity of an excitable cell by treating individual components of the cell membrane as elements of an electrical circuit and described its properties using a set of ordinary differential equations. Their work paved the way for the extension of computational modelling studies to cardiac cells. In any such model, the change in transmembrane voltage V can be calculated using the following equations:

$$C_m \frac{dV}{dt} + I_{ion}(V, t) + I_{stim} = 0 \quad (2.3)$$

$$I_{ion}(V, t) = \sum_x I_x = \sum_x G_x (V - V_{x_ion}) \quad (2.4)$$

The derivation of the equations comes from formalism laid down by Hodgkin and Huxley, who modelled the cell membrane as a capacitor connected in parallel with variable resistors and batteries representing the ionic currents (Figure 2.20, *A-B*). Here C_m is the membrane capacitance, V is the membrane potential (Section 2.3.2, equation 2.1) and is defined as the potential difference between intracellular and extracellular spaces, and I_{ion} is the sum of ionic currents flowing through channels, pumps and exchangers across the membrane (equation 2.4).

The different ionic currents I_x that constitute I_{ion} can be computed using the product of their respective conductance G_x and their driving potential, $V - V_{x_ion}$. Here V_{x_ion} is the Nernst (or reversal) potential of the x^{th} type ion, which is defined as the membrane potential at which the ion's rate of movement from one side to other side of the membrane due to the ion's concentration gradient is balanced by the rate of movement in the opposite direction due to the electric fields associated with the transmembrane voltage [131].

Hodgkin and Huxley also introduced the concept of gating to explain the time and voltage dependent behaviour of the ionic channels. According to their model, each ionic channel has one or more gates which can be either in an open or closed position independently of one another. A channel is said to be in their open state when all its gates are open, and vice versa. Therefore, the conductance (G_x) of each ion channel is the product of the gating variables (γ_i)

that describe the open probability of the channels and their respective maximum conductivity (g_x), as shown in equation 2.5-2.6. Here α_{γ_i} and β_{γ_i} are the rate constants that describe the transition of the gates from open to close state and vice versa. Their values can be obtained from fitting experimental voltage clamp data with mathematical functions [132].

$$I_x = g_x \prod_i \gamma_i (V - V_{x_{ion}}) \quad (2.5)$$

$$\frac{d\gamma_i}{dt} = \alpha_{\gamma_i}(1 - \gamma_i) - \beta_{\gamma_i}\gamma_i \quad (2.6)$$

By solving equations 2.3-2.6 numerically, we can reproduce the resulting AP due to application of a stimulating current, I_{stim} , to a single cell (solution shown in Figure 2.20C) and the behaviour of individual gating variables (Figure 2.20D).

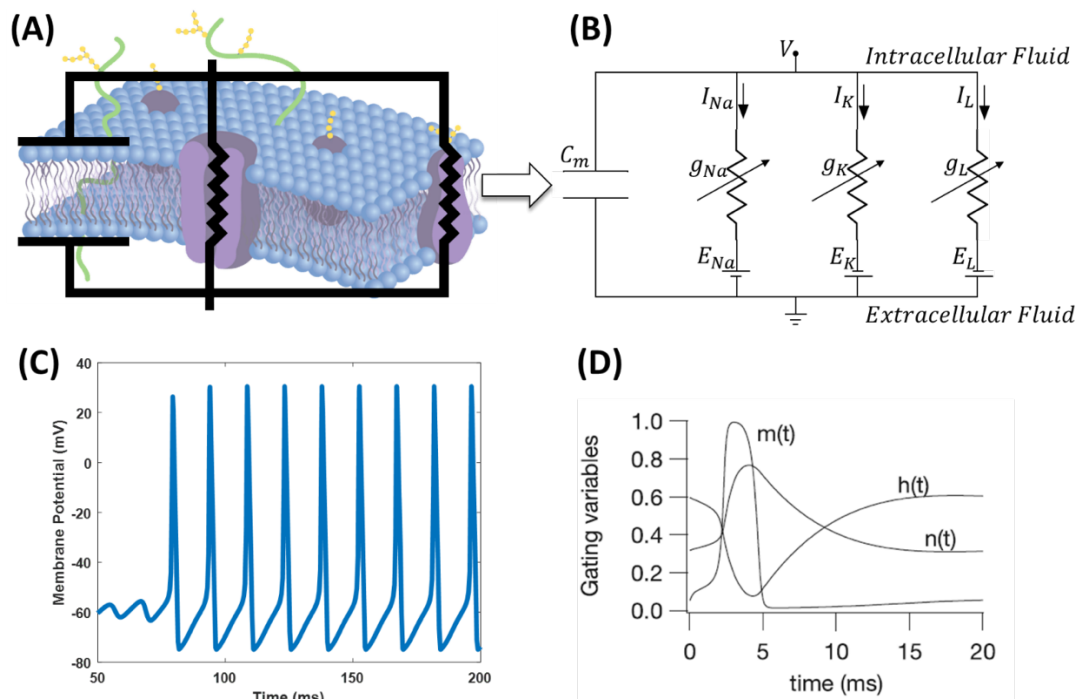


Figure 2.20: The Hodgkin-Huxley (H-H) model. (A) The cell membrane represented as a capacitor and ionic channels as conductors. (B) The electrical circuit proposed by H-H for the squid nerve axon, where the cell membrane is represented as capacitor (C_m), the voltage and time-dependent ionic channels as variable resistors with electrical conductance (g_x , $x = Na, K, leak$) and the electrochemical gradients (E_x , $x = Na, K, leak$), driving the flow of respective ions depending on the concentration of ions on either side of the membrane, and hence generating a current (I_x , $x = Na, K, leak$). (C) Changes in membrane potential with time on the application of a stimulus current of 10 mA and finally, and (D) Changes in the gating variables controlling the Na^+ current (m and h) and the K^+ current (n) during the AP [133].

2.5.1.1 Atrial cell models

In the early 1980s, the advancement of patch clamp techniques [134] and the characterisation of the biophysical properties of various ionic currents in human atrial cells led to the formulation of detailed biophysical models specifically for those cells [135,136]. Over the years, such techniques have aided in the measurement of various membrane currents, resulting in increasing complexity of I_{ion} (equation 2.4) in the atrial cell models. Some models also incorporate the influence of paracrine or autonomic effects [137] or intracellular calcium dynamics [138,139] on the cell electrophysiology, which can play significant roles in influencing atrial repolarization in both normal and pathological conditions. These models have facilitated simulation of the effect of anti-arrhythmic drugs and channel mutations on cellular and organ function, linking the molecular level effects of drugs and disease conditions with cellular and organ level function, and helped in translating molecular and preclinical physiological studies into clinical practice [140]. However, no single model incorporates all key molecular and cellular components. Therefore, limitations of a model need to be considered before applying them to clinical problems [141].

2.5.1.2 Simplified cell models

The focus of this work is primarily to study the behaviour of re-entry in 3D atrial geometries subjected to variability in structure and electrophysiology. This requires the use of large-scale tissue simulations involving millions of computational grid points to represent the geometry. In such cases both computational efficiency and tractability of the simulation results can be improved by using simplified cell models with significantly lower number of variables and equations compared to biophysically detailed models [27].

Simplified models fall under three categories: direct reductions of more detailed models, generic models and phenomenological models. Out of these, reduced models [142] and generic models [143], despite being computationally efficient, lack the ability to reproduce realistic cellular properties like APD restitution and memory which are critical for RD mechanisms.

Phenomenological models such as the Fenton-Karma (FK) model [71], on the other hand, aim to reproduce key dynamical properties of cells and tissue without including much biophysical detail. For instance, rather than including the descriptions of ten or more ion channels, pumps, and exchangers, a phenomenological model constitutes of a summary of inward and outward

currents relying on fewer variables and equations. These models allow us to substantially reduce computational costs, while providing a level of detail sufficient to preserve re-entrant behaviour seen in more complex models [27]. As the focus of this work is on the behaviour of re-entry in atrial myocardium, we used the FK model modified for atrial myocytes [144]. The following section will provide a brief overview of the FK model, which was originally proposed for a ventricular myocyte, and explain the modifications made in order to reproduce behaviour observed in atrial myocytes in normal and pathological conditions.

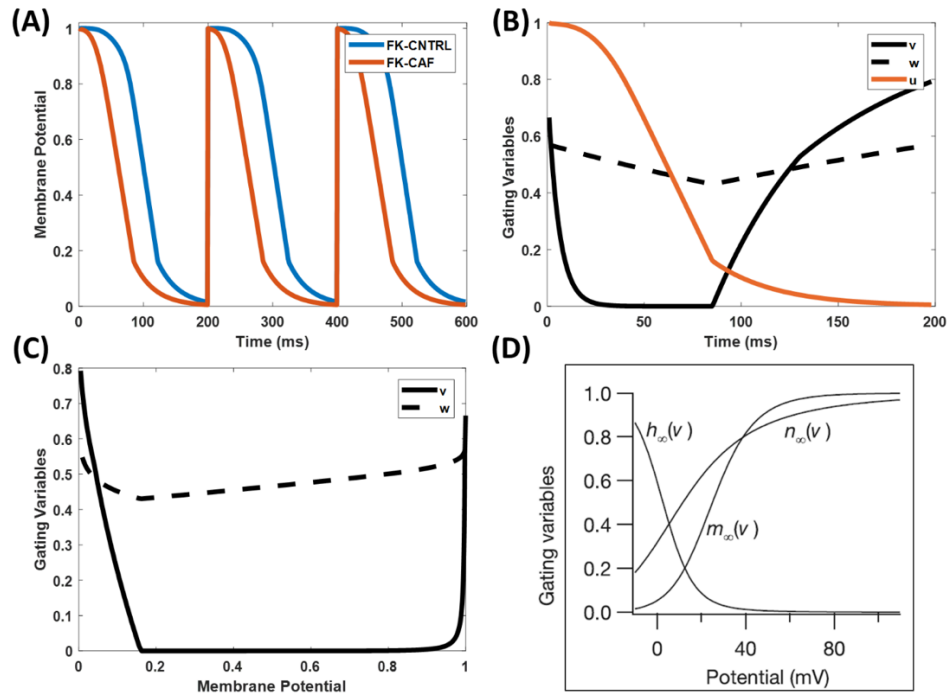


Figure 2.21: The atrial Fenton-Karma model. (A) The membrane potential during periodic pacing (BCL of 200 ms) of FK-CNTRL (blue) and FK-CAF (orange) models with parameters obtained from Goodman et al. (Table 1). The respective changes in gating variables; v and w , after application of the stimulus current is shown with respect to time (B) and the membrane potential (C). These changes can be directly compared against the 3 gating variables in H-H model [133], where the curves are smoother (D).

2.5.1.3 Ionic model: The Fenton-Karma model

In the FK ionic model [71], I_{ion} is a combination of three currents:

$$I_{ion} = I_{fi}(V; v) + I_{so}(V) + I_{si}(V; w) \quad (2.7)$$

The currents are: (i) fast-inward current (I_{fi}) analogous to Na^+ current, which is responsible for depolarization of the membrane; its kinetics is controlled by the inactivation-activation gating

variable, v , which inactivates this current after depolarization and reactivates it after repolarization, (ii) the slow outward current (I_{so}) analogous to the K^+ currents, which is responsible for the repolarization of the membrane and is the only current which is ungated and purely voltage dependent and (iii) the slow inward current (I_{si}) analogous to Ca^{2+} current that balances the I_{so} during the plateau phase and is dependent on the gating variable w .

The equations for the model are presented in a simplified form and adopted from the original paper [71] by defining the dimensionless membrane potential u (such that $u = 0$ when the voltage V is at RMP (V_o) and $u = 1$ when V is at its peak (V_{fi}), equation 2.8) and currents J_n are the scaled version of $I_{n=fi,so,si}$ (equation 2.7) with the units of inverse time (equation 2.9).

$$u = (V - V_o)/(V_{fi} - V_o) \quad (2.8)$$

$$J_n = I_n/(C_m(V_{fi} - V_o)) \quad n = fi, so, si \quad (2.9)$$

The equations for the gating variables are:

$$\frac{du}{dt} = -J_{fi}(u; v) - J_{so}(u) - J_{si}(u; w) \quad (2.10)$$

$$\frac{dv}{dt} = \Theta(u_c - u) \left(\frac{1 - v}{\tau_v^-(u)} \right) - \Theta(u - u_c) \left(\frac{v}{\tau_v^+} \right) \quad (2.11)$$

$$\text{Where } \tau_v^-(u) = \Theta(u - u_v) \tau_{v1}^- + \Theta(u_v - u) \tau_{v2}^-$$

$$\frac{dw}{dt} = \Theta(u_c - u) \left(\frac{1 - w}{\tau_w^-} \right) - \Theta(u - u_c) \left(\frac{w}{\tau_w^+} \right) \quad (2.12)$$

The equations for the currents are:

$$J_{fi}(u; v) = -\frac{v}{\tau_d} \Theta(u - u_c) (1 - u) (u - u_c) \quad (2.13)$$

$$J_{so}(u) = -\frac{u}{\tau_o} \Theta(u_c - u) + \frac{1}{\tau_r} \Theta(u - u_c) \quad (2.14)$$

$$J_{si}(u; w) = -\frac{w}{2\tau_{si}} (1 + \tanh [k(u - u_c^{si})]) \quad (2.15)$$

It is worth noting that, unlike the equations for gating variables in detailed models such as H-H model (equation 2.6), which are based on smooth functions, in the FK model the gating variables are modelled using Heaviside step function, $\Theta(x)$ defined by:

$$\Theta(x) = \begin{cases} 1 & x \geq 0 \\ 0 & x < 0 \end{cases} \quad (2.16)$$

The original study performed by Fenton and Karma presented parameter values for ventricular myocyte models. In this study, however, our goal is to study re-entry in AF, and we will be parameterising the model to match the restitution curves recorded from healthy and electrically remodelled atrial tissue. Due to lack of data from human atrial cells, we have chosen the available parameter set for sheep atria published by Goodman et al. [144], which is summarised in Table 2.1. Here, we have two sets of parameters for the atrial FK model: (i) for healthy cells (FK-CNTRL) and (ii) chronic AF (FK-CAF). The dimensionless membrane potential, u , computed with the two sets of parameters are presented in Figure 2.21A, while the three FK model variables; u , v and w computed only for FK-CAF are plotted as a function of time (following a supra-threshold stimulus) in Figure 2.21B-C.

Variable	FK-CAF	FK-CNTRL	Variable	FK-CAF	FK-CNTRL
τ_d	0.125 ms	0.125 ms	τ_{wclose}	300 ms	300 ms
τ_r	70 ms	65 ms	τ_{wopen}	400 ms	90 ms
τ_{si}	114 ms	47 ms	u_c	0.16	0.16
τ_o	32.5 ms	32.5 ms	u_v	0.04	0.04
τ_{vclose}	5.75 ms	5.75 ms	u_c^{si}	0.85	0.85
τ_{v1}	82.5 ms	160.0 ms	k	10	10
τ_{v2}	60 ms	40 ms	C_m	1 μFcm^{-2}	1 μFcm^{-2}

Table 2.1: Parameters of the FK model obtained from Goodman et al [144] who calculated them by fitting APD and CV restitution curves from sheep atria. Here time is in the units of ms and $\tau_d \equiv C_m/g_{fi}$.

2.5.1.4 The Courtemanche-Ramirez-Nattel ionic model

Another model that has been used in this dissertation is a modified version of Courtemanche-Ramirez-Nattel (CRN) model [136]. The CRN model was developed in 1998 (Figure 2.22A), and unlike FK (Figure 2.22B) captures the detailed ion channel kinetics, calcium dynamics and cellular ion homeostasis with 21 variables, providing a balance between complexity and utility. This complex model provides a high level of biophysical detail and can be used to validate

findings from the simplified FK model. In this study, we use a modified version of the CRN model by Colman et al. [145], which captures cell electrophysiology of AF patients.

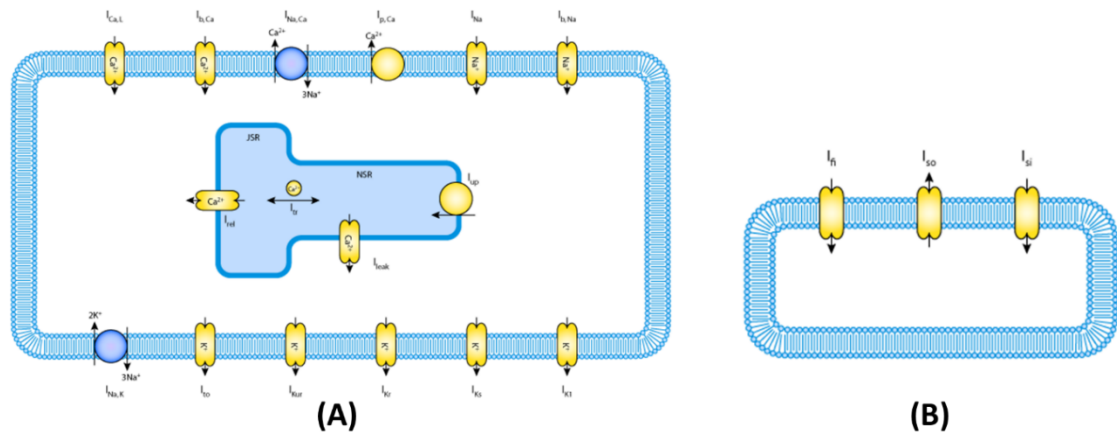


Figure 2.22: A schematic representation of (A) the CRN model and the (B) FK model. In both schematics, the bi-lipid layer of the cell membrane is represented in light blue, while the ionic pumps, exchangers and currents included in the model are represented by yellow objects. The CRN model has an additional isolated compartment for calcium exchange in the sarcoplasmic reticulum (SR) which is absent in the FK model. Figures adopted from CellML model repository [146].

2.5.2 Modelling multiscale excitation propagation in the atria

The advancement of imaging techniques, both *ex-vivo* (histology) and *in-vivo* (MRI, CT), provided an abundance of the organ level data of cardiac structure, including patient-specific 3D geometries and approximate fibre orientations[147,148]. This facilitated the simulation of the electrical behaviour at the organ level, with the cell electrophysiology models incorporated into anatomically detailed 3D models of the atria and the ventricles. This section provides a brief overview of the modelling transition from the cellular level to the tissue and organ level.

2.5.2.1 Mono-domain equations

The propagation of AP in cardiac tissue occurs through cardiac myocytes that are electrically coupled via gap junctions which allow the passage of ions between the intracellular fluids of adjacent cells as described in detail in Section 0. At the cellular level, the AP propagation is discrete, as there is a small delay between the depolarization of a myocyte and its neighbours due to limited bandwidth of the gap junctions [27]. However, at a larger spatial scale of the tissue level, the propagation can be considered continuous, as shown in experimental recordings

from cultured ventricular cells of a rat [149]. This forms the basis for the continuum assumption underlying cardiac tissue electrophysiology modelling. According to this assumption, cardiac tissue can be considered as a continuum excitable medium where “cells” have shared extracellular and intracellular spaces with finite conductivities. There are two main types of mathematical representation for the continuum model: the monodomain model and the bidomain model [27]. The bidomain model account for the distinctive extracellular and intracellular conductivities, while the monodomain is based on an assumption that these conductivities are proportional. Although the bidomain model is arguably a better representation of reality, it has been shown that differences in simulation of AP propagation on the scale of the human heart using both models is extremely small in the absence of currents applied into the extracellular space (i.e., external pacing, defibrillation shocks, etc) [150]. The full derivation of both models can be found, for example, in Keener and Sneyd [18]. The monodomain equation is given by:

$$\frac{\partial V}{\partial t} = \nabla \cdot (\mathbf{D} \nabla V) - \frac{I_{ion}}{C_m} \quad (2.17)$$

$$\bar{\mathbf{D}} = \begin{bmatrix} D_{\parallel} & 0 & 0 \\ 0 & D_{\perp 1} & 0 \\ 0 & 0 & D_{\perp 2} \end{bmatrix} \quad (2.18)$$

Here, ∇ is the gradient operator and \mathbf{D} is the diffusion coefficient tensor derived from the values of conductivities between the myocytes, the membrane capacitance and the surface to volume ratio. The diffusion coefficients are measured in units of m^2s^{-1} . In cardiac tissue, excitation propagation is faster or slower depending on the distribution and orientation of the fibres therefore, \mathbf{D} is a tensor whose components determine the rate of spread of electrical activity. The coordinate system represented by the diagonal matrix, $\bar{\mathbf{D}}$ (equation 2.18), is localised along the local fibre directions, and these directions form the eigenbasis of \mathbf{D} . Here D_{\parallel} , $D_{\perp 1}$ and $D_{\perp 2}$ are the diffusion coefficients along the axis of the fibre, transverse to it and across the myocardial sheet, respectively. Due to a lack of sheet structure in the atria, $D_{\perp 1} = D_{\perp 2} = D_{\perp}$ is considered and the ratio D_{\parallel}/D_{\perp} is called the anisotropic ratio (AR). In case of isotropic myocardium, $\text{AR} = 1$ and the monodomain equation reduces to equation 2.17B, where D is a scalar quantity.

$$\frac{\partial V}{\partial t} = D \nabla^2 V - \frac{I_{ion}}{C_m} \quad (2.17B)$$

In reaction-diffusion equation 2.17B, $\frac{I_{ion}}{C_m}$ is the reaction term corresponding to the current generated locally at the cell membrane during AP propagation, while $D \nabla^2 V$ is the diffusion term, which corresponds to the flow of currents between cells.

2.5.2.2 Boundary conditions

To implement the mono-domain model (equation 2.17) in a 2D-3D tissue geometry, the extracellular space is assumed to be bounded. This means that there is no current flowing from the extracellular space into the adjacent spaces. This can be implemented mathematically by using the Neuman (no-flux) conditions on the boundary (equation 2.19).

$$\hat{\mathbf{n}} \cdot (D \nabla V) = 0 \quad (2.19)$$

Here, $\hat{\mathbf{n}}$ is the normal unit vector to the boundary. In the 3D studies presented in this thesis, the boundary condition is applied by creating a boundary layer around the outer surfaces of the atria (both epicardial and endocardial) and applying the Neuman conditions along the normal.

2.5.3 Numerical solvers

The general solution to nonlinear partial differential equations (PDEs), such representing the monodomain equation (Section 2.5.2.1, equation 2.17), cannot be obtained analytically. Numerical methods provide a convenient way in which these continuous equations can be discretised, such that their solutions can be computed in an iterative manner using computers. It is noteworthy that the choice of numerical scheme has a significant influence on the accuracy, stability and the computational cost of the implemented method [27], all of which should be considered while designing the modelling approach. In the following sections, we discuss in detail numerical schemes used to perform the simulations presented in this thesis.

2.5.3.1 Explicit Euler method

The explicit forward Euler (FE) method is the simplest numerical integration method to solve the 1st order differential equations describing the time-dependent propagation of the AP. Let's first consider an ODE of the form of equation 2.20 (which is similar to the equations (2.6)).

$$\frac{dy}{dt} = f(y, t) \quad (2.20)$$

It can be assumed that over a small time interval, dt , there is a constant rate of change in y . Then the value of y at the new time step, $t + dt$, can be estimated by equation 2.21:

$$y_{t+dt} = f(y, t) * dt + y_t \quad (2.21)$$

If the value for y at $t = 0$ is known, then the values for y at $t = dt, 2dt, \dots, Ndt$ can be calculated from equation 2.21 over the entire time interval Ndt , provided that dt is small.

The explicit nature of this method makes it easy to implement and each time step is associated with a low computational cost. However, the time step needs to be small enough to increase the accuracy and guarantee the stability of the diffusion operator [27] (discussed below in Section 2.5.4.2). Implicit methods, such as the implicit Runge-Kutta methods [151], could allow for a larger time step without the loss of accuracy and stability, but at the expense of the computational cost of solving a set of non-linear system of equations at each time step. Therefore, its simplistic and cost-effective nature makes the explicit forward Euler a popular numerical scheme for solving the monodomain equations for cardiac tissues [27,152].

2.5.3.2 Finite difference method

In cardiac electrophysiology, the monodomain equations can be solved in a 3D geometry using the finite difference method (FDM), the finite elements method (FEM) and the finite volume method (FVM) [27]. Amongst them, FDM is relatively simple and one of the most commonly used technique of discretizing the monodomain equations [150,153] and has therefore been used throughout the studies presented in this thesis. The region over which the simulations are performed is discretised in space and time, and approximations of the continuous solutions are computed at these discrete space or time points.

The principle behind FDM is simple: approximating the partial derivatives in the PDEs by replacing them with difference quotients calculated based on the Taylor series expansion of the required function (equation 2.22, 23). The geometry is represented by a structured grid: typically, uniform squares in 2D problems and cubic voxels for 3D geometries.

In a 2D case (Figure 2.23), the partial derivatives of a differentiable function, $u(x, y)$, can be approximated (equation 2.24 and 2.25) using a central difference scheme derived from the

Taylor expansion of $u(x, y)$. Here dx and dy represents the spacing between measurements in the x and y direction respectively (Figure 2.23). The error between the approximate and the exact solution is called the discretization or truncation error, as it comes from the fact that only a finite part of the Taylor series is used in the approximation. For a sufficiently small spatial step dx , the error associated is dominated by the term $O(dx^2)$, as all the higher order terms are neglected. Therefore, the step size (dx) must be small enough to keep this approximation valid.

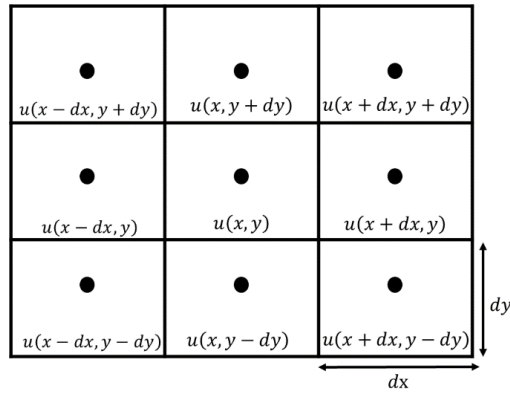


Figure 2.23: Finite difference approximation in a 2D grid.

Using the Taylor expansion for u around x :

$$u(x + dx, y) = u(x, y) + dx * \partial_x u(x, y) + \frac{dx^2}{2} * \partial_{xx} u(x, y) + \dots \quad (2.22)$$

$$u(x + dx, y) = u(x, y) + dx * \partial_x u(x, y) + O(dx^2) + \text{smaller terms} \quad (2.23)$$

We obtain the following expression for the first derivatives in a centred difference scheme:

$$\partial_x u(x, y) = \frac{u(x + dx, y) - u(x - dx, y)}{2dx} \quad (2.24)$$

Likewise, for $\partial_y u(x, y)$:

$$\partial_y u(x, y) = \frac{u(x, y + dy) - u(x, y - dy)}{2dy} \quad (2.25)$$

This approximation can be extended for the computation of second order partial derivatives such as those in the mono-domain equations:

$$\partial_{xx} u(x, y) = \frac{u(x + dx, y) + u(x - dx, y) - 2u(x, y)}{dx^2} \quad (2.26)$$

$$\partial_{yy}u(x,y) = \frac{u(x,y+dy) + u(x,y-dy) - 2u(x,y)}{dy^2} \quad (2.27)$$

Using the formalism presented above, the transmembrane potential for a 1D cable of coupled cells can be calculated using continuous monodomain equation (equation 2.17) written as:

$$\frac{\partial V}{\partial t} = D \partial_{xx}V(x,t) - \frac{I_{ion}}{C_m} \quad (2.28)$$

The voltage of every cell at any time point ($t + dt$) can be calculated on application of the numerical solvers, FE and FDM discussed earlier in the discretized form given by

$$V_x^{t+dt} = dt \left(\frac{D(V_{x+dx}^t + V_{x-dx}^t - 2V_x^t)}{dx^2} - \frac{I_{ionx}}{C_m} \right) + V_x^t \quad (2.29)$$

Note that even though FDM is straightforward and easy to implement, representing smooth surfaces found in cardiac geometries with steps poses a challenge in implementing boundary conditions. This puts a further constrain on the space step needed to adequately represent curved surfaces with a computational grid used in the FDM. Besides, the time and space step are chosen to satisfy the stability criterion [27] given below (N is the dimension of the system):

$$dt \leq \frac{dx^2}{2ND} \quad (2.30)$$

FEM is an alternative approach very widely used in cardiac modelling and simulation [14,154,155]. In this method the complex geometries are divided into small sub-domains that can be of non-uniform size and shape. The solution within each domain is approximated via interpolation functions. An advantage of FEM over FD is that complex, curved geometries can be modelled accurately [156]. However, FEM comes with higher computational and development effort compared to FD [27].

Software implementation

The monodomain simulations of 3D atria models were performed using a parallelized FD solver originally implemented and validated by Clayton et al. [157]. The solver was coded in C and adapted under MPI to run on a local HPC server. Furthermore, the C code was also time optimised by converting to Cuda and adapting it to run on a GPU cluster. On top of the existing code, additional modules for (i) modelling fibrotic tissue and (ii) calculating the running position of the RD tip were implemented in 3D. The mathematical formulation for the latter is

described in Appendix 8.1.3. Finally, for post processing, Matlab toolkits were developed for construction of RD probability maps and target areas from 3D atrial simulation data.

2.5.4 Role of modelling and simulations in understanding AF mechanisms

The last two decades witnessed a rapid growth in the complexity in 3D biophysical atrial models to improve their physiological accuracy and predictive power, and as a result, in their ability to provide valuable insights into the complex mechanisms underlying AF. This section presents a brief overview of the models integrating atrial structure, electrical heterogeneity, anisotropy and AF remodelling.

The role of atrial shape and structure in wave propagation during AF has been studied using models with variable degrees of anatomical detail. Earlier studies [158–160] used caricature atrial geometries, whereas recent models [147,148,154] have integrated detailed structural data obtained from ex-vivo or in-vivo atrial imaging (MRI, computed tomography). These studies highlighted the importance of specialised atrial structures in AF mechanisms. Thus, the crista terminalis and pectinate muscles were found to play an important role in the formation and maintenance of RDs during AF [148].

Electrical heterogeneity within the atria is another factor that can affect AF dynamics. Experimental data from animal [161,162] and humans [163] have indicated the existence of intrinsic regional variations in AP morphology and APD within the atria. These regional differences in AP can be incorporated into 3D atrial models by altering the underlying cellular ion channel properties, to match the respective experimental data obtained from myocytes from different atrial regions. Such region-specific electrophysiology has been considered in 3D atrial models under healthy and remodelled conditions [145,164]. Computational studies have shown that APD gradients in the atria can lead to the generation of RDs [145,165] and increase the complexity of arrhythmia [166] during AF. Moreover, modelling and simulation studies have reported that the regional differences in APD could play a more important role than the presence of AF-induced electrical remodelling [164].

In addition to APD heterogeneity, the atria are also characterised by high levels of conduction anisotropy due to the underlying complex arrangement of myocardial fibres. The fibre orientation in the atrium can be obtained from ex-vivo images [44,148] and mapped onto the 3D atria using rule-based methods [164,167]. Simulation studies in animals and humans have

suggested the combined effect of anisotropy and electrical heterogeneity increases both the vulnerability window for initiation of RDs and the duration of AF episodes, especially at the PV sleeves [145,165,168,169].

As mentioned above, AF progression is strongly linked to both electrical and structural remodelling (see Section 2.4.1.3 for more details). The former reduces APD and the latter slows down AP conduction, and hence, jointly they reduce the atrial wavelength (proportional to a product of APD and CV), which facilitates the initiation and maintenance of RDs. Krogh-Madsen et al. [170], modelled structural remodelling in chronic AF by decreasing diffusive coupling uniformly across the atria in the presence and absence of electrical remodelling (the latter was modelled as reduced APD). They found that: (i) RD duration and maximum number of RDs was inversely proportional to the wavelength and (ii) in the absence of either structural or electrical remodelling, flutter like re-entry circuits were found at anatomical obstacles (e.g., the PVs and MV). However, the combination of both types of remodelling facilitated sustained RDs in atrial free walls. The study highlighted the importance of including both electrical and structural remodelling in the 3D atrial models to study AF dynamics. However, the studies cited above lack considered patient-specific atrial structural features.

More recent whole atrial models have started to incorporate patient-specific 3D atrial structure and fibrosis distribution obtained from medical imaging data [15,171–173]. Fibrosis has typically been reconstructed from LGE-MRI and modelled as regions of altered electrical properties in atrial tissue (described in Section 2.5.5 below). Modelling studies have found that patient-specific fibrotic distribution in the atria plays a critical role in determining the locations of RDs [14,15,174]. Zahid et al. reported that RDs localise at specific fibrotic tissue regions with high density and entropy. These findings were confirmed by identification of such RDs using non-invasive mapping data in humans [13,56]. The correlation between RD locations and fibrosis was higher in the LA compared to the RA [13,56]. Note, however, that there also exists evidence against the correlation of RDs locations and fibrotic regions [175,176]. Such variable results indicate that the specific locations of RDs within the atria may not only be determined by fibrosis alone but by a complex combination of atrial structural factors (geometry, thickness and fibres) [173]. Therefore, the systematic evaluation of all atrial structural factors is important for understanding the mechanisms of AF.

2.5.5 3D atrial models with patient-specific fibrosis

Atrial fibrosis is multifactorial (see section 0), and hence, several modelling approaches have been developed to model different aspects of atrial structural changes associated with fibrosis.

Fibrotic regions are commonly modelled as regions with reduced electrical conductivity and altered anisotropy, to reflect the decreases in inter-cellular coupling due to gap junction remodelling and interstitial collagen deposition [14,15,171,174]. However, the transition between healthy and fibrotic regions have been modelled using two different approaches. Some studies [14,15] have used binary intensity LGE-MRI thresholding to distinguish between healthy and fibrotic tissue, whereas others [171] gradually reduced the diffusive coupling and increased the anisotropy ratio depending on the LGE-MRI intensity. The later approaches enabled reproducing local activations in the patient-specific LA models, which were in agreement with clinical data. Moreover, this approach was consistent with in-vivo measurements of conduction velocity (CV), which showed lower CV values in areas with high LGE-MRI intensity associated with fibrosis [177]. Similar approach was adopted by Morgan et al. [174] to represent patchy fibrosis in the patient-specific 3D atrial model and show that RDs can anchor primarily to the border zone between healthy and fibrotic tissue.

Modelling and simulation studies have also investigated the arrhythmogenic potential of fibrotic regions (discussed in Section 2.4.2.1) using models with variable structural complexity, for example, to study the effect of fibrosis micro-structure. Spach et al. [178] have mimicked the effect of diffuse fibrosis by removing lateral gap junction coupling between myocytes. They showed that introducing such anisotropy in the models increased the likelihood of partial conduction block and formation of RDs. Subsequent studies have modelled collagen deposition by representing them as insulating barriers or obstacles in atrial tissue [179–181]. Jacquemet et al. [179] represented intestinal fibrosis by introducing random collagenous septa disconnecting cardiac fibres in the transverse direction and showed that reduction in transverse CV was proportional to the length of the collagenous septa. Costa et al. [180], Vigmond et al. [181] and Tanaka et al. [182] have introduced nonconductive regions with various sizes throughout tissue based on patient-specific fibrosis imaging data. These studies provided insights into the effect of fibrosis at the microstructure level and allowed mimicking fractionation of atrial electrograms observed at arrhythmogenic sites using EAM. Although the effects of fibrosis at

this micro-scale are an important contributor to AF arrhythmogenesis, the inherent limitations of LGE-MRI prevent it from identifying such fine details [183]. Therefore, in patient-specific LA models reconstructed from LGE-MRI typically include large, continuous fibrotic patches.

Fibroblast proliferation and coupling with myocytes [184] have also been incorporated into atrial models by Morgen et al. [174], Maleckar et al. [185], McDowell et al. [172] and Ashihara et al. [186]. They have shown that an increase in myocyte-fibroblast coupling and fibroblast density reduces excitability and promotes APD reduction, facilitating slower conduction and wave breakup. Furthermore, McDowell et al. [172] reported that myocyte-fibroblast coupling is a necessary condition for the generation of RDs during ectopic pacing at PVs. However, a more recent study performed by Morgen et al. [174] using atrial fibroblast model has shown that the effects of decreased inter-myocyte coupling and increased anisotropy in fibrotic regions on conduction are greater than those of myocyte-fibroblast coupling.

Thus, 3D atrial models have progressively incorporated several levels of electrophysiological and structural details, down to image-derived features such as patient-specific fibrosis distributions. However, a recent study by Roney et al. [187] has demonstrated that although models with different level of detail enable reproducing different features of AF dynamics, none of them has so far produced an exact representation of clinical data. Therefore, individual studies should focus on electrophysiological and structural details that are relevant to the aspects of AF dynamics under consideration. In future, even closer integration between cell-to-organ 3D atrial models, experimental and clinical data will be required to establish a truly global mechanistic picture of AF.

Chapter 3

A Mechanistic Study:

Drift of RDs induced by AWT gradients

3.1 Section Outline

This chapter aims to investigate the effect of atrial wall thickness (AWT) on the dynamics of re-entrant drivers (RDs) associated with atrial fibrillation (AF) and to compare it to other known effects such as those of atrial fibrosis. In this proof-of-concept study, all the simulations were performed using a simple 3D slab representation of the LA wall. The motivation behind investigating effects of AWT on re-entry is summarised in Section 3.2, and the steps involved in the model construction and simulations are discussed in Section 3.3. The simulation study is divided into two parts: (i) Study 1a (Section 3.4.1) investigates the effect of AWT on the RD dynamics and (ii) Study 1b (Section 3.4.2) investigates the comparative effects of AWT and fibrosis on RDs. Section 3.5 analyses the simulation results, dissecting the AWT effects on RDs and comparing them with competing influence of fibrosis. Finally, the limitations (Section 3.5.3) and the main findings of the chapter are summarised (Section 3.6).

3.2 Introduction and Motivation

The three-dimensional structure of atrial tissue is an important determinant of electrical behaviour [148,188]. In particular, experimental studies in isolated sheep hearts [189] and theoretical studies [190] have indicated AWT to be a potential factor that influences the dynamics of RDs underlying arrhythmias in the heart. Junctions between thick and thin tissue regions could create a source-to-sink mismatch which may affect the RD propagation and even anchor RDs [190]. However, even recent theoretical studies using established concepts such as filament tension have not fully explained AWT effects of RDs [190]. Therefore, there is a need to elucidate the mechanisms by which RDs can be affected by non-uniform atrial structure.

Moreover, it is also important to evaluate the effect of AWT in comparison to/combination with other well-established factors such as atrial fibrosis (discussed in Chapter 2, Section 0), which affects the atrial electrophysiology by altering conduction velocity and anisotropy of the atrial

tissue. Computational and clinical studies have reported an association between fibrotic regions and RDs, indicating it as a potential target for CA [174,177,191]. However, the understanding of how RDs are influenced by a combination of structural factors, such as fibrosis and AWT, is limited. Evaluating the combined effects of these factors can be important in the identification of locations of RDs that could ultimately be used to guide CA procedures.

The complexity of atrial structure (including 3D geometry, size, heterogeneous wall thickness and curvature, fibre arrangement, development of fibrosis) and function (heterogeneity in electrical properties, innervation, etc.) makes it extremely challenging to quantify the effect of individual factors on AF arrhythmogenesis from experimental recordings. In this situation, biophysical modelling and simulations provides a platform for integrating all these underlying factors and evaluating the contributions of specific factors affecting AF independently.

The aim of this chapter is to use a simple atrial model to systematically analyse the mechanistic influence of AWT features and fibrotic tissue on the dynamics of RDs sustaining AF. The atrial wall geometry is represented by a 3D slab, abrupt changes in AWT are modelled using a step, and fibrotic tissue is modelled using a cylindrical region of altered tissue properties. Further in the thesis (Chapter 4) we will extend this mechanistic study to patient-specific atrial geometries that capture both realistic AWT variations and fibrotic tissue distributions.

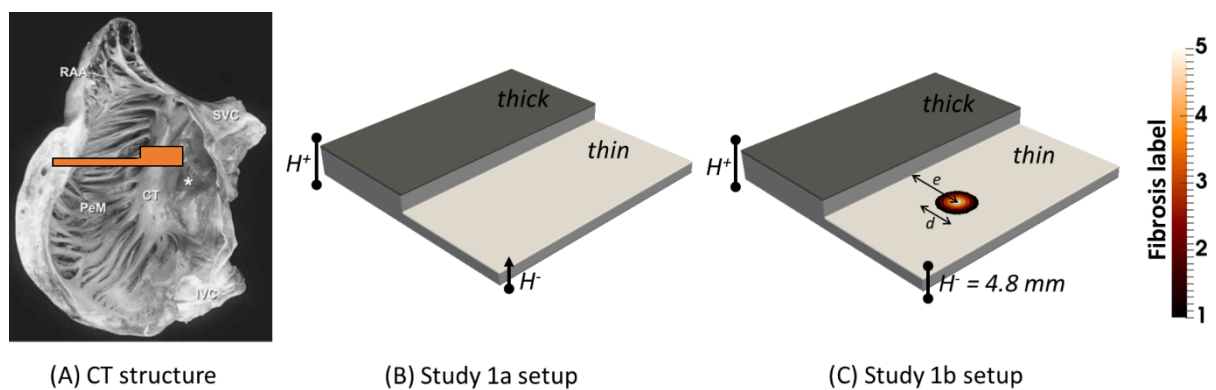


Figure 3.1: Diagram of the 3D atrial tissue setup. (A) The internal structure of the crista-terminalis (CT) with the orange bar indicating the change in thickness profile in the surrounding area. The setups used in Study 1a and 1b are shown in part (B) and (C), respectively. In the diagrams, the thick region is indicated with dark grey and has a constant height of $H^+ = 7.5$ mm in both setups, whereas the thin side shown in light grey: (i) in study 1a has a varying height, H^- between 5.7 mm to 3 mm and (ii) in study 1b has a constant H^- of 4.8 mm. In addition to change in thickness, setup 1b (C) also has a cylindrical fibrotic patch of diameter, $d = 9$ mm, positioned on the thinner side at distance, $e = 10.5$ mm from the step.

3.3 Methods

The study in this chapter is presented in two parts: (i) in Study 1a, we perform simulations in an idealized 3D atrial slab with a varying thickness step (Figure 3.1, B) to evaluate the mechanistic influence of AWT on the RDs dynamics; (ii) in Study 1b, we use a single cylindrical fibrotic patch added to the slab near the step (Figure 3.1, C) to investigate the competing effects of fibrosis and AWT on RDs.

3.3.1 Simulating cardiac electrophysiology

The electrical activation in the 3D atrial model was simulated based on the monodomain equations with no-flux boundary conditions imposed at the slab boundaries (described in Chapter 2, Section 2.5.2). The equations were solved using forward Euler and centred finite differences schemes with temporal and spatial steps of 0.005 ms and 0.3 mm. Our model was isotropic and the diffusion tensor was replaced by a scalar diffusion coefficient $D = 0.1 \text{ mm}^2 \text{ ms}^{-1}$, carefully chosen to produce an atrial conduction velocity of 0.60 m s^{-1} within a typical range of AF [192]. These parameters were found to generate stable numerical solutions for the explored conditions (Appendix, Section 8.1.2). For membrane kinetics the ionic current, I_{ion} , in equation 2.17 (Chapter 2, Section 2.5.2.1) we used the Fenton-Karma model [71] modified to accurately describe the restitution properties of remodelled atrial cells [144]. This atrial Fenton-Karma (aFK) cell electrophysiology model accurately captures the main characteristics of atrial action potential and its restitution, while keeping the computational time relatively short. More details of the model are presented in Chapter 2, Section 2.5.1.3.

In order to check the independence of the simulation results on the choice of model, a subset of the simulations in Study 1a was repeated using the Courtemanche-Ramirez-Nattel (CRN) model [136], which describes atrial electrophysiology in more detail (Chapter 2, Section 2.5.1.4). The latter has also been modified to match the restitution properties of remodelled atrial cells [145]. The APD₉₀ restitution curves were found to closely match between aFK and remodelled CRN (Appendix, Figure A. 1). The diffusion coefficient for the CRN model was also chosen as $0.16 \text{ mm}^2 \text{ ms}^{-1}$ to produce an atrial CV of 0.60 m s^{-1} , same as in the aFK model.

3.3.2 Study 1a: Influence of AWT step on the RD dynamics

Model Geometries: The simulations were performed on a 3D atrial tissue slab of $200 \times 200 \times 25$ voxels corresponding to a tissue size of $60 \times 60 \times 7.5 \text{ mm}^3$ with a surface area of 3600 mm^2 , similar to that of the LA [193]. A diagram of this setup is presented in Figure 3.1B. Here, an AWT step was introduced at the middle of the slab, with thickness of the right-hand side (H^+) fixed at 7.5 mm and that of the left-hand side (H^-) was varied between 5.7 mm and 3 mm. Four atrial geometries were defined, H1 to H4 with $H^- \in \{5.7, 4.8, 3.9, 3.0\}$. Detailed description of each geometry is provided in Table 3.1.

Geometry	Thick, H^+ (mm)	Thin, H^- (mm)	Step height, $H^+ - H^-$ (mm)
H0		0.0	0
H1		5.7	1.8
H2	7.5	4.8	2.7
H3		3.9	3.6
H4		3.0	4.5

Table 3. 1: The properties of the 3D atrial slabs (H1-H4).

Simulation Protocol: RDs were initiated using the cross-field protocol shown in Figure 3.2. An S1 stimulus was applied by introducing a voltage step (voltage: 1 (aFK) and 20 mV (CRN); duration: 1 ms) to part of the tissue slab $0.15 \times 60 \times 7.5 \text{ mm}^3$, initiating a plane wave with the wavefront parallel to the AWT step (Figure 3.2, A). After 70ms, an S2 stimulus was applied in the direction perpendicular to the wavefront, by resetting the voltage (voltage: 0 (aFK) and 20 mV (CRN); duration: 2ms) in part of the tissue $60 \times (30 + X) \times 7.5 \text{ mm}^3$ (Figure 3.2, B). The S1-S2 interval and the location X was varied to initiate RDs at multiple locations. In Study 1a, the location X was varied from 7.5 mm to 0 mm in steps of 1.5 mm on both sides of the step (Figure 3.2E). This was also repeated using the CRN model to check the independence of results on the model choice. The RDs tip trajectory was tracked for 10s in each simulation.

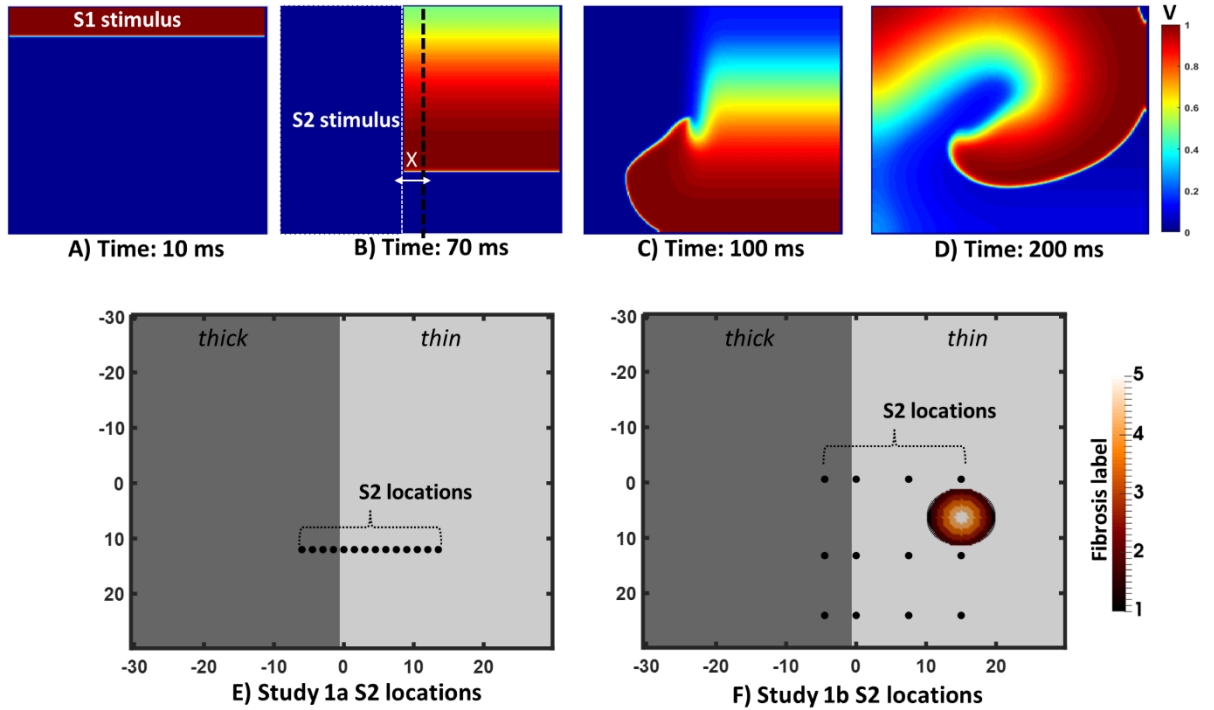


Figure 3.2: The RD initiation protocol in the slab with an AWT step and varying stimulus locations. The change in voltage (V) over time on the flat top surface of the slab is presented above (A-D), where (A) show the S1 stimulus applied at 0 ms, (B) the S2 stimulus applied at 70 ms and X indicates its position with respect to the AWT step. Panels (C-D) show the evolution of a RD over time. The diagrams in the panels below show all the different locations of the S2 stimulus (marked by a black circle) used for Study 1a (E) and Study 1b (F).

Identifying and tracking the RD tip: The algorithm for tracking the RD tip was adapted from the method described previously [71] and developed here for a 3D atrial tissue slab. The curvature of the wavefront is highest at the tip of the RD, and hence, it can be assumed [68] that the velocity at the tip (which is inversely proportional to the curvature) is approximately zero and the voltage does not change over small-time intervals. Therefore, in a given 2D plane (Figure 3.3), if the voltage, V , varies over time, t , at locations indicated by grid point (x_i, y_j) , then the tip is located at point \mathbf{p} which satisfies the following interlinked equations:

$$\frac{\partial V(\mathbf{p}, t)}{\partial t} = 0 \quad (3.1)$$

$$V(\mathbf{p}, t) = V(\mathbf{p}, t + dt) = V_{iso} \quad (3.2)$$

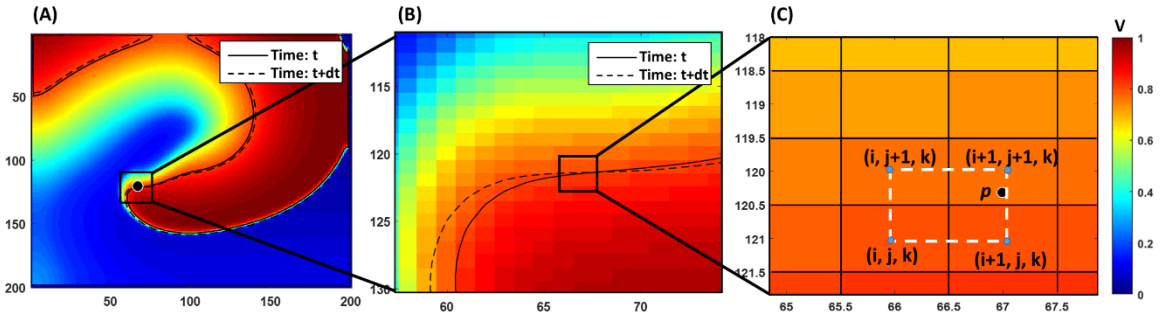


Figure 3.3: The steps involved in identifying the tip of the RD. (A) The spiral wave in a 2D cross-section of the plane-slab (Figure 1, H0). (B) Zooming in on the tip site and (C) tip location identified by bilinear interpolation at individual pixel level at a point in time.

Following this assumption [68], the tip of a RD is identified by calculating the intersection point between two successive (i.e., separated by a time interval dt) iso-potential lines of constant membrane potential (V_{iso}) representing a boundary between the depolarized and repolarized regions of the tissue (Figure 3.3A). In our model, the tip tracking was performed with V_{iso} and dt values set to 0.8 and 0.005 ms, respectively. However, the desired intersection point might not lie at the sampled grid points (Figure 3.3B) and could therefore result in a resolution-dependent tip trajectory. In order to overcome this issue, Fenton et al. [71], proposed using bilinear interpolation to approximate $V(\mathbf{p}, t)$ and $V(\mathbf{p}, t + dt)$, which allows for more precise calculation for the RD tip position (Figure 3.3C). The steps involved in this interpolation and calculation of the RD tip are presented in detail in Appendix 8.1.3. In addition to tracking the RD tip, we also computed the velocity of the tip over the entire duration of the simulation at a time resolution of 1 ms. These calculations were performed on a 2D slice taken from the middle of the 3D slab. An example of the tracking of the RD tip and calculation of the tip velocity is presented in Figure 3.4 for a period of 1s.

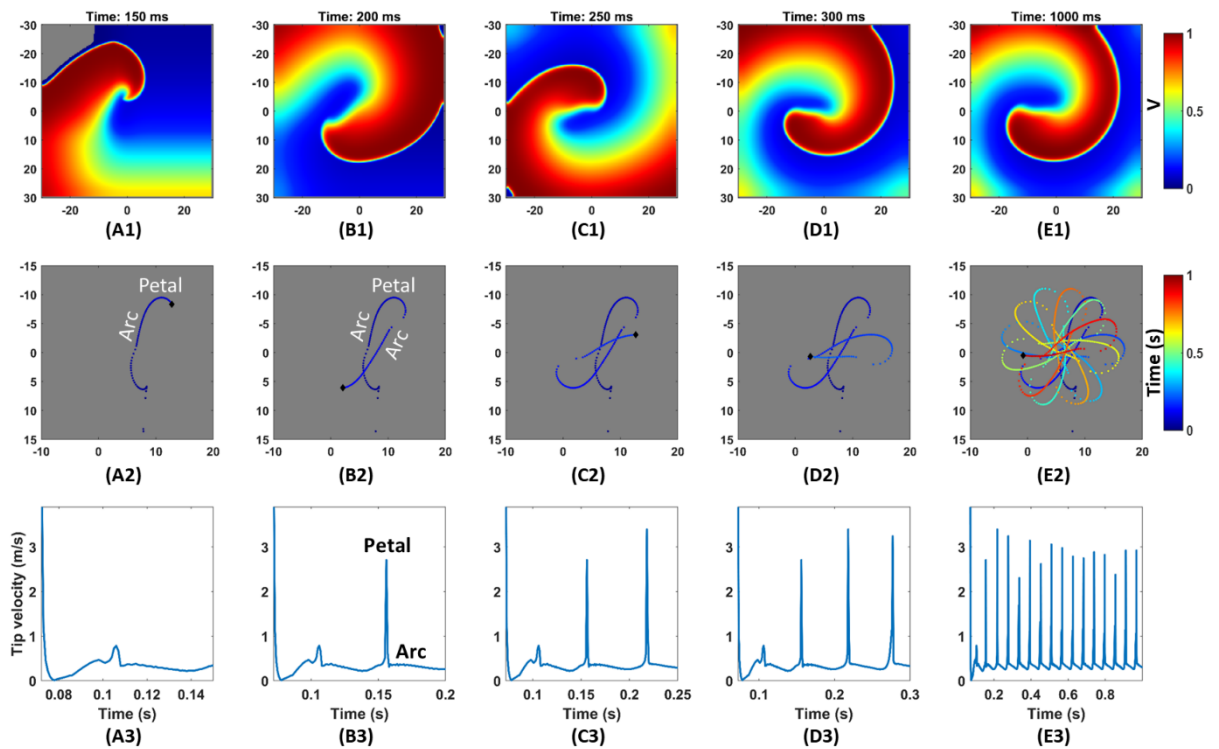


Figure 3.4: The hypotrochoidal (“flower-like”) pattern traced by the RD tip over time. Row 1: the snapshot of the voltage map of the RD at different instances of time (150 ms to 1000 ms). Row 2: the corresponding RD tip trajectory colour coded in time and Row 3: the corresponding tip velocity while the trajectory is being tracked. In rows 1 and 2, the axes labels are in units of mm.

Tracking RD core and measuring drift velocity: The RD was undergoing two simultaneous motions: (i) meandering of the RD tip around a central core to form a flower-like pattern and (ii) a vertical drift due to the presence of the thickness gradient. In this study, we were particularly interested in the vertical drift motion induced by the presence of the AWT step. Therefore, the drift velocity of the RD for all the models was computed by tracking the central core of the flower-like pattern formed by the RD tip every second (Figure 3.5). As this pattern was symmetrical, the core was identified by surrounding the pattern with a square bounding box and computing its centre as shown in Figure 3.5A. The core was identified every 1s in order to track the movement (two examples, Figure 3.5 B & C) of the RD over 10s of simulation, and its drift velocity (Figure 3.5C) was computed by measuring the vertical displacement of the RD core over time (Figure 3.5D).

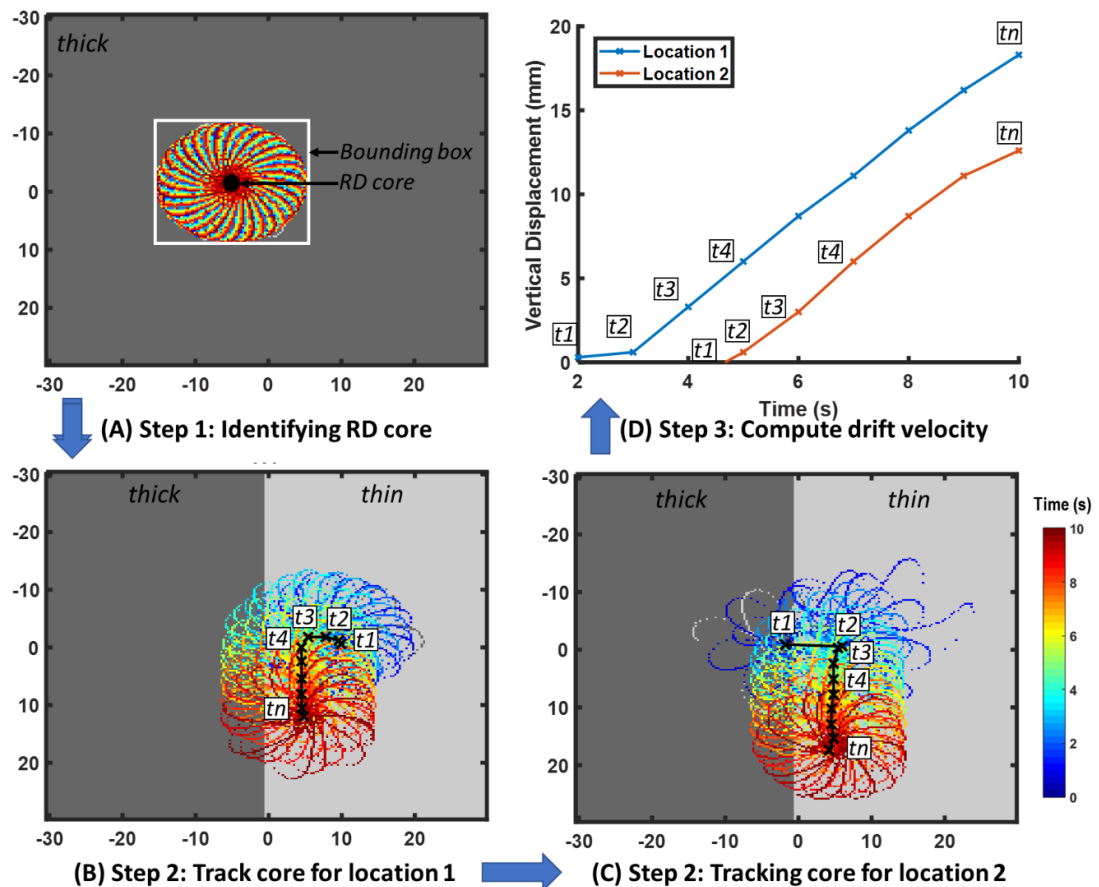


Figure 3.5: Steps to track the RD core and calculate its drift velocity. Step 1, (A) identifying the core (black star) of the meandering trajectory of the RD tip (rainbow colour) using the centre of the bounding box (white). Step 2, tracking the RD core (X) every 1s; here we show two examples of RDs initiated at: (B) location 1 on the thinner side and (C) location 2 on the thicker side of the model H1. Here, t_1 to t_n indicate different locations of the core over 10s of simulation, which are connected using a black line to mark the path of the RD's drift. Finally, in Step 3 (D), the distance time plot for every location is generated and the slope is used as an estimate for the drift velocity.

Computing Electrophysiology Metrics: In order to evaluate the effect of AWT step on wave propagation, electrophysiology metrics, APD_{90} and CV, were computed for all the slab models of varying step height (H1-4) using the S1 stimulus applied after pre-pacing at a BCL of 400 ms for 10 beats to achieve steady-state (Figure 3.6). The metrics were then quantified on the 11th beat. Two separate wavefront propagation directions were considered: forward (initiated on the thicker side) and backward (initiated on the thinner side). The APD_{90} was defined as the time interval between the moments of AP initiation and 90% repolarization.

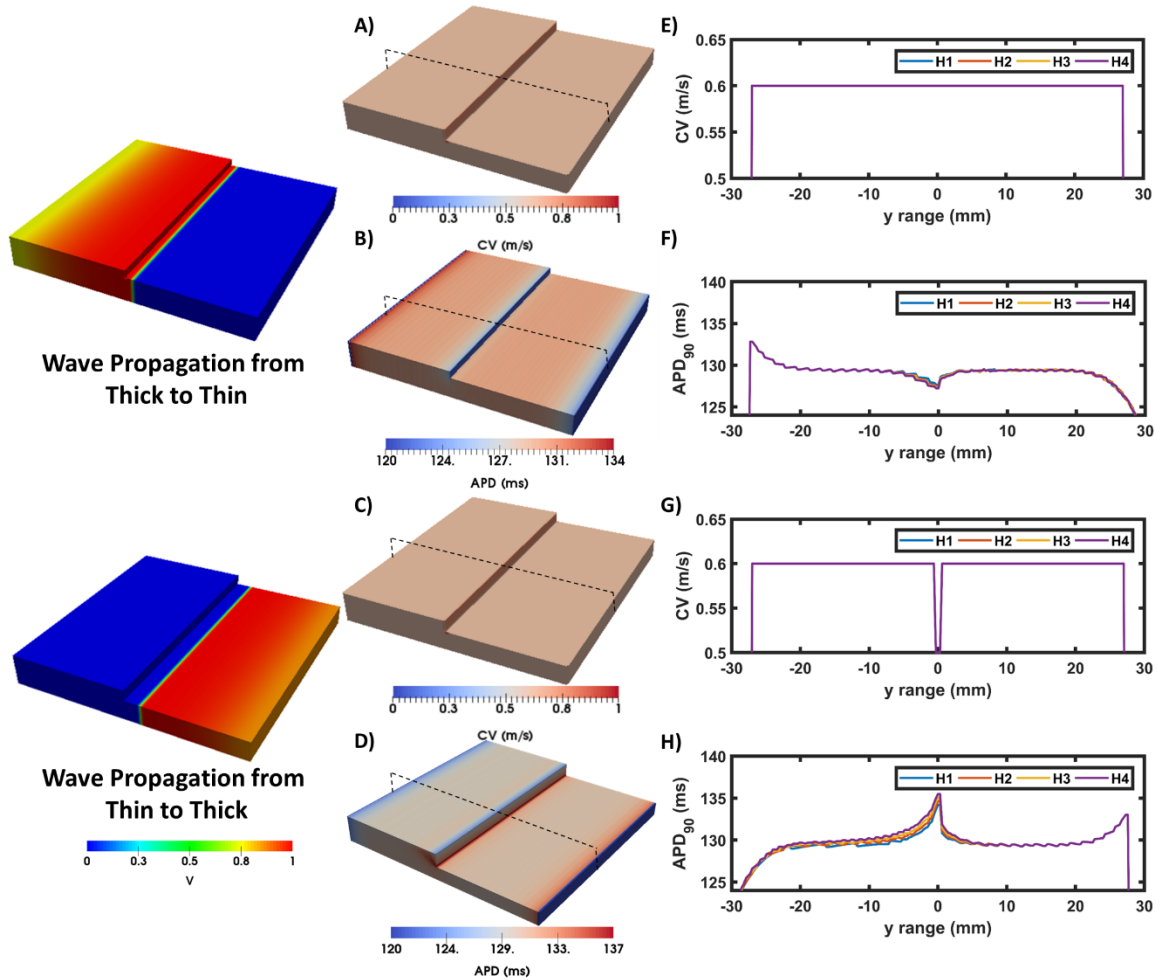


Figure 3.6: CV and APD measured for forward and backward wave propagation directions. The left panels show the APD and CV profiles along a vertical line crossing the middle of the slab (black dotted line in A-B) in the plane just below the step.

3.3.3 Study 1b: Comparative influence of fibrosis and AWT step on the RD dynamics

Model Geometries: In Study 1b, the comparative effect of AWT and fibrosis on the RD dynamics was investigated by incorporating a cylindrical fibrotic patch of 9-mm diameter positioned 10.5 mm away from the AWT step on the thinner side (Figure 3.1, C). This was done for slab H2 with the step height of 2.7 mm. The rationale of placing the fibrotic region on the thinner side of the step was to mimic conditions when fibrotic tissue could be present in regions surrounding thick structures such as the crista terminalis (CT) in the RA.

Model Parameters: To model patchy fibrosis, we adopted the methodology from the study of Morgan et al. [174]. Each fibrotic patch was divided into 5 distinct levels representing increasingly severe fibrosis. The diffusion coefficient D was progressively decreased by

16.67% to model the effect of fibrosis on slowing atrial conduction in fibrotic regions: level 0 corresponded to healthy tissue with $D = 0.1 \text{ mm}^2 \text{ ms}^{-1}$; inside the fibrosis patch, the value of D for levels 1 to 5 was $0.083 \text{ mm}^2 \text{ ms}^{-1}$, $0.067 \text{ mm}^2 \text{ ms}^{-1}$, $0.050 \text{ mm}^2 \text{ ms}^{-1}$, $0.033 \text{ mm}^2 \text{ ms}^{-1}$ and $0.017 \text{ mm}^2 \text{ ms}^{-1}$, respectively. We did not use the value $D = 0$ for level 5, because there is no experimental evidence suggesting that dense fibrotic regions are completely non-conductive.

Stimulation Protocol and Analysis: RDs were initiated at multiple sites using the same cross-field protocol as in Study 1a. However, in this case, the location of the S2 stimulus, X was varied relative to the step and the fibrotic patch (Figure 3.2F): (i) 4.5 mm away from the step on the thick side (column P), (ii) on the step (column Q), (iii) 7.5 mm (column R) and (iv) 15mm (column S) away from the step on the thin side. The RD tip trajectories were analysed to explore their dynamics in each case. The choice of 4.5 mm as the extreme limit of the RD initiation distance to the left of the patch was to ensure that the RDs was sensitive only to the AWT gradient and not the fibrotic patch. Likewise, the choice of 15 mm as the extreme limit on the right side was to ensure the sensitivity of RDs only to the fibrotic patch. The tip of the RDs for all the simulations were tracked using the method described in Study 1a.

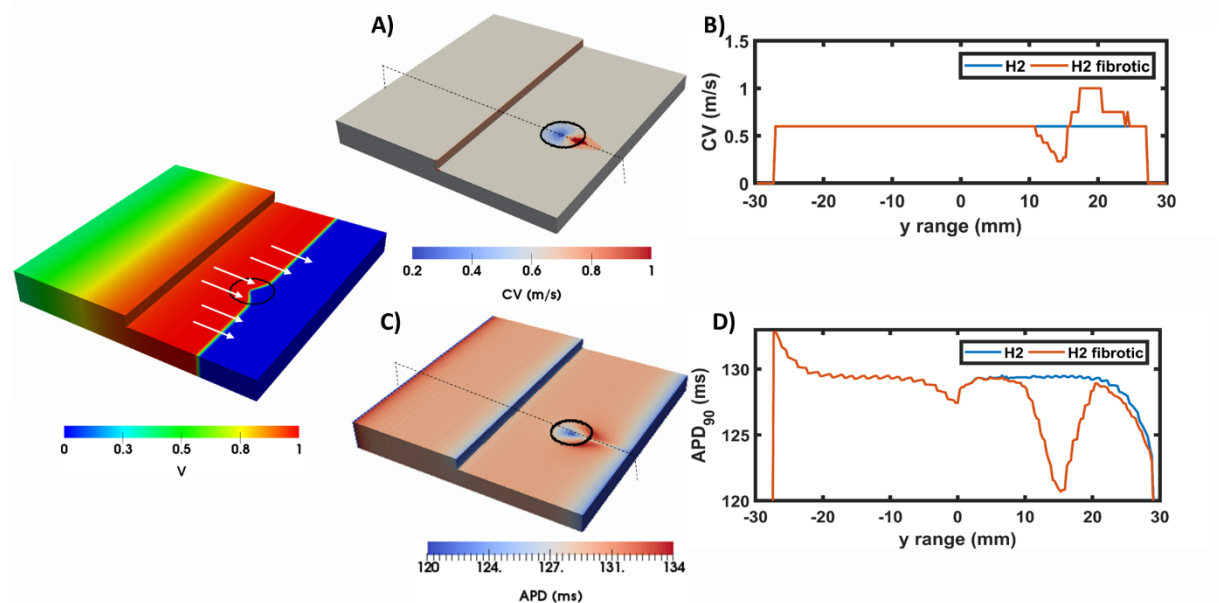


Figure 3.7: CV and APD measured on the slab with a step and fibrotic patch. The left panel shows the APD and CV profile along a vertical line crossing the middle of the slab (black dotted line in A-B).

3.4 Results

3.4.1 Study 1a: 3D Atrial Slab with AWT step

The RDs initiated in the 3D atrial tissue slab meandered to form a characteristic hypotrochoidal (“flower-like”) pattern, with the RD tip moving along the “petals” in the outward clockwise direction around a central core (Figure 3.4). The velocity of the RD tip was recorded as it was following the flower-like trajectory and presented in Figure 3.4, A3-E3. During the petal formation by the RD tip, the wavefront at the tip propagates through a region which is completely recovered, thereby giving the maximum curvature of the trajectory, with the tip propagating at 2.76 ± 0.37 m/s (Figure 3.4, A). However, when the tip is tracing an arc, the wavefront at the tip propagates through a region that is not completely recovered (Figure 3.4, B). This causes the front to propagate in another direction, where the tissue is more excitable. This deviation generates the low curvature part of the trajectory or the arc with tip propagating at a much lower velocity of 0.38 ± 0.19 m/s. This process occurs periodically, and the trajectory shown in Figure 3.4C is generated, which is being referred to as “the flower-like pattern”. This pattern was stable over the duration of 10s, its radius was 10.4 mm, and the RD tip motion to complete one rotation around the pattern took 500 ms (Figure 3.5, A).

With the introduction of a step change in AWT in the slab (Figure 3.5, B and C), in addition to meandering around the core, the RD also drifted in a direction perpendicular to the direction of AWT change. Moreover, in these cases, the direction and nature in which the RD drifted was dependent on its initiation location with respect to the step and the step height.

3.4.1.1 Effect of varying S2 stimulus location from the AWT step on RDs

A map of trajectories for RD initiated from different locations (shown in Figure 3.2, E) using all the 4 models (H1-4, Table 3. 1) with varying step height is shown in the Appendix, Figure A. 5. In the main text, Figure 3.8 and Figure 3.9 present a simplified version of the former figure, summarising the key behaviours and drift directions observed from these representative simulations.

The core of RDs initiated on the thicker side (L1, Figure 3.8D) first drifted towards the AWT step, eventually crossing it and drifting along it on the thinner side. The core of RDs initiated on the thinner side (L2-3, Figure 3.8D), on the other hand, drifted towards the step and along it, but didn't cross over to the thicker side. Besides, RDs that were initiated far away from the step (Appendix, Figure A. 5) were not influenced by the AWT gradient and remained stationary.

This behaviour can be more noticeably observed in Figure 3.9A, where the trajectory of the RD is shown for each slab of increasing step height (H1-H4). Here, it can be clearly seen that after the RD anchored to the step, its core moved vertically along the step at a specific distance from it. The core always drifted on the thinner side, and its distance from the step decreased with increasing the step height (Figure 3.9 (i-iv)). For the chosen aFK model parameters with a diffusion coefficient of $0.1 \text{ mm}^2/\text{ms}$, the RDs anchored to the AWT gradient if they were in the range between 1.8 and 4.5 mm (H1-4) from the step, when they were initiated on the thick side, or less than 12 mm (H1-3) / 15 mm (H4) on the thin side.

3.4.1.2 Effect of varying AWT step height on RD velocity

The RD drift along the AWT step became faster as the height of the step (H1- 4) was increased. The drift velocity was computed by measuring the vertical displacement of the RD core over time, which was done for each model (H1-4) as shown in Figure 3.9B. The drift velocity was 2.3 mm/s for the smallest step H1 and 4.8 mm/s for the largest step H4, both measured for the initial location L1 on the thick side (Figure 3.8D) Similarly, for the initial location L3 on the thin side, drift velocity was 2 mm/s for H1 and 4 mm/s for H4. Therefore, drift velocity of the RD core increased with increasing the AWT gradient. Note that the direction in which the RD meanders to form the petals (clockwise in these simulations), and hence the direction of drift along the step (downwards here) is determined by the cross-field initiation protocol. However, the anchoring of the RD to the thickness step does not depend on the wave's chirality.

Additionally, with the introduction of the AWT step and its increasing height, the velocity of the RD tip was recorded, while the tip zigzagged between the thick and thin side of the step, and showed a large variation in peak velocity (Figure 3.10, B1-B3) compared to the control case of a uniform slab (Figure 3.10, B0). The RD tip moved from the thick to thin region of the slab (red dots, $2.13 \pm 0.18 \text{ m/s}$) with an average higher velocity compared to the velocity with which it moved in the opposite direction (black dots, $0.4 \pm 0.11 \text{ m/s}$). Moreover, the maximum velocity recorded for tips moving from thick to thin side of the step increased from the maximum velocity of 3.4 m/s in control to 4.43 m/s, 5.38 m/s, 6.56 m/s for slabs H2-H4. Therefore, as the height of the step was increased, the tip velocity when it moved from the thick to thin region also increased.

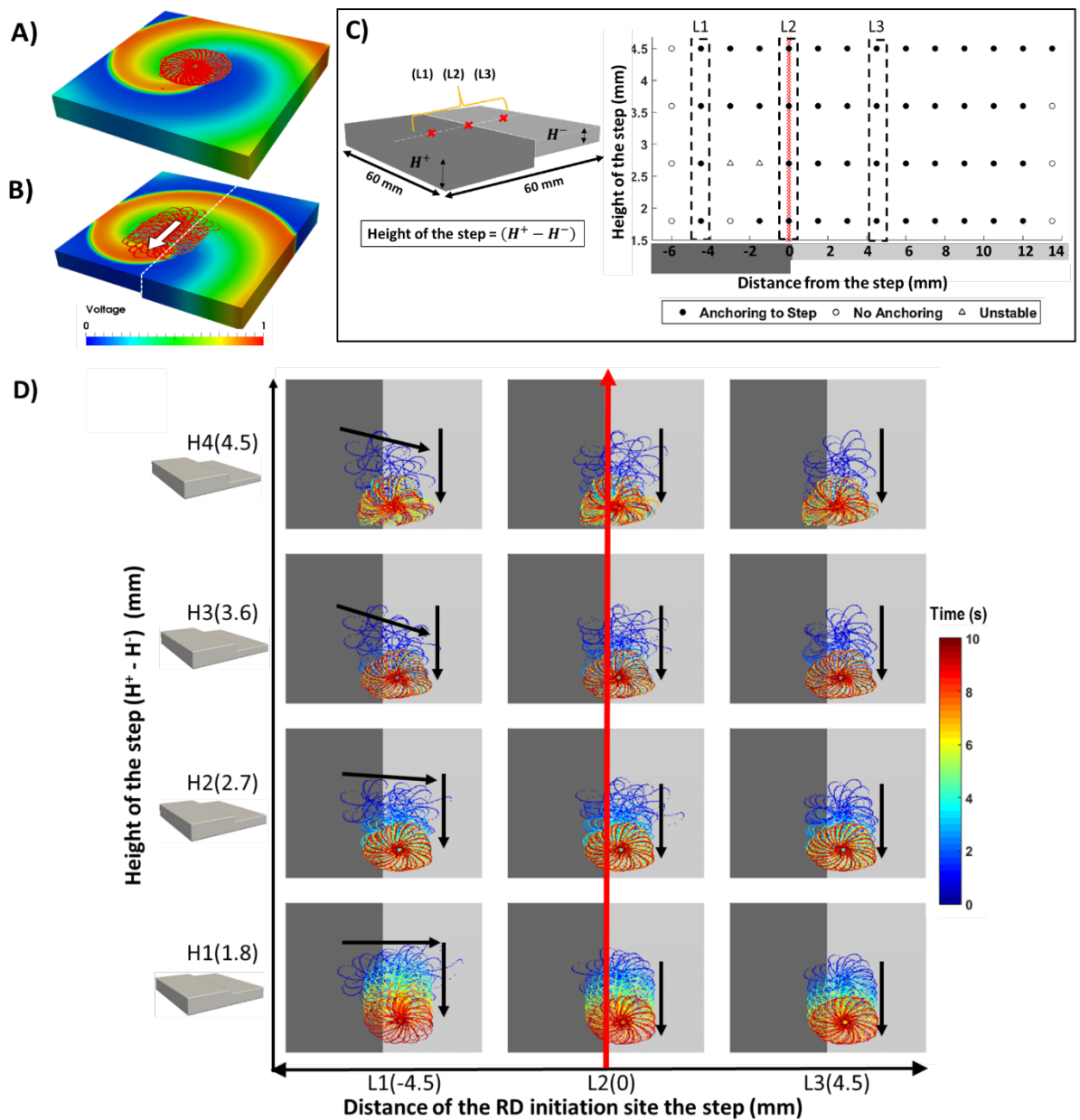


Figure 3.8: Effects of AWT step on the RD dynamics in atrial slab (Study 1a) with the aFK model. Tip trajectories obtained by simulation of RDs at multiple locations on a 3D atrial slab with varying step height (H1-4): (A) RDs meander to form a flower-like pattern that was stationary in a slab with uniform thickness, but (B) in the slab with an AWT step, drifted towards and then along the step. (C) Outcome of the simulations for different RD initiation sites and step heights. (D) The RD tip trajectories for three initiation locations (L1-3): L1) on the thicker side closer to the step – RD drifted towards the thinner side and then downwards along the step, L2) on the step – RD drifted down along the step and L3) on the thinner side – RD drifted towards the step and then down along the step. A detailed version of Panel (D) can be found in Appendix, Figure A. 5.

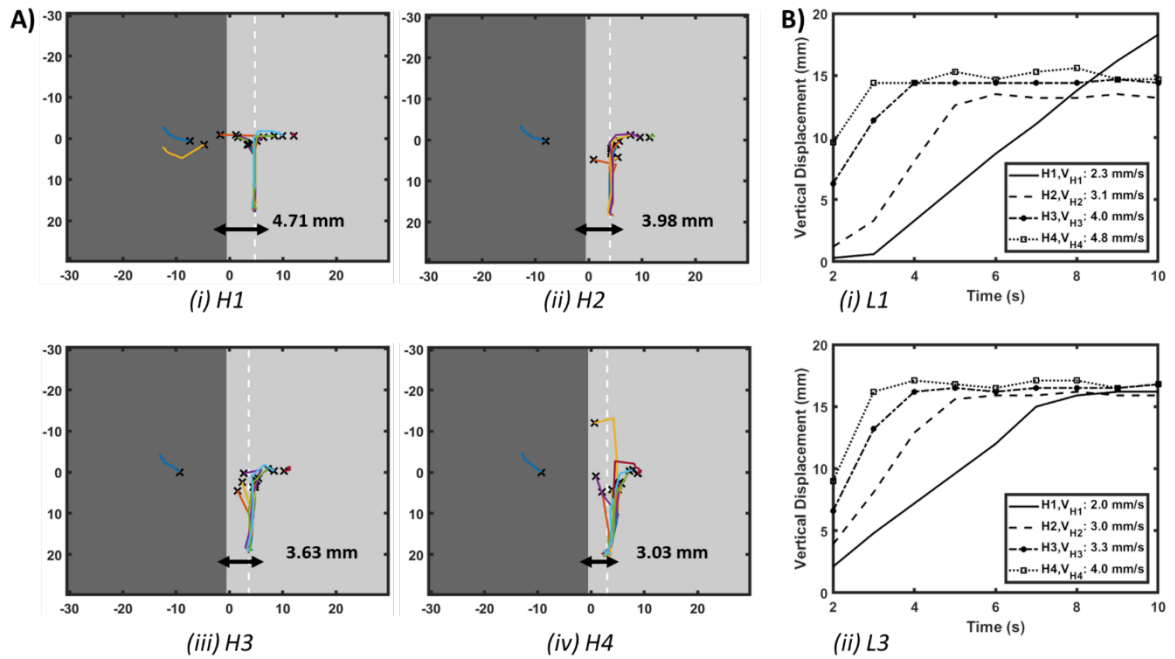


Figure 3.9: Effect of AWT gradients on the drift velocity of RDs in a slab (Study 1a) with aFK model. (A) Trajectories of the core of RDs initiated at multiple locations on the slabs with varying step height (H1-4, see Figure 3.8D) is shown with lines of different colours. Here the X marks the site of the initial RD core for every location and the white dashed line in each slab indicates the location where the core of all the RDs stabilised after anchoring to the AWT step. (B) Vertical displacements of the RD core for locations L1 on the thick side and L3 on the thin side of the step (shown in Figure 3.8D) over 10s are shown in panel (B(i)) and (B(ii)), respectively, for each of the slabs with height H1-H4. As the height of the step was increased, the velocity of the vertical drift of the RDs also increased.

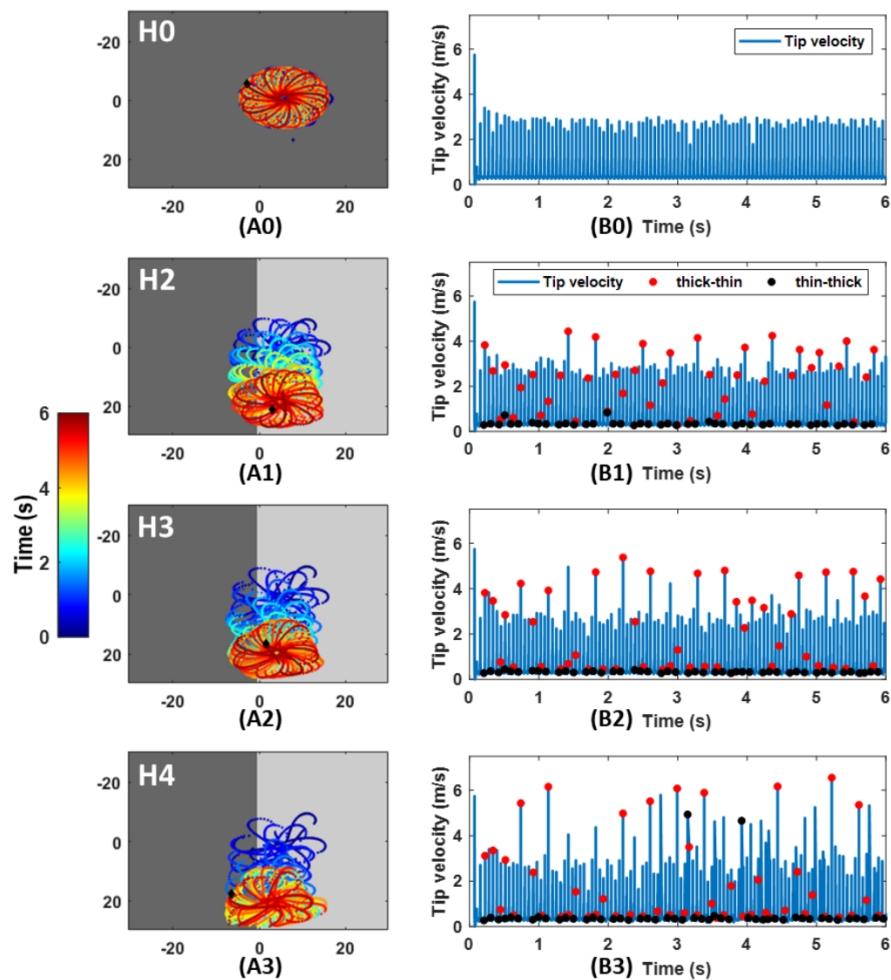


Figure 3.10: Effect of AWT gradients on the tip velocity of RD as it zig-zagged between the thick and thin region of the atrial slab. The RD tip trajectory over 6s in the control uniform slab and the slabs with increasing AWT step height (H2-H4) is shown in A0 and A1-A3. The corresponding tip velocity for each case is presented on the left in B0 and B1-B3. In red, are all the points at which the tip transitioned from the thick to the thin side while in black are all the points at which the tip moved in the opposite direction. The velocity at the tip recorded in the former cases (red) is generally much greater than the latter (black) in cases H2-H4, approximately by $\sim 81\%$. Moreover, the maximum tip velocity recorded increased from 3.4 m/s in control to 4.43 m/s, 5.38 m/s, 6.56 m/s for slabs H2-H4, indicating a relation between increase in the step height and tip velocity at the junction.

3.4.1.3 Effect of change in atrial electrophysiology model on RDs

Simulations of the 3D slab with the CRN atrial cell model demonstrated similar behaviour of the RDs (Figure 3.11). The RD tip in the CRN-based model also meandered to form a flower-like pattern with radius of 12 mm and one complete rotation around the pattern taking about 700 ms. Similar to the aFK-based model, anchoring of the RDs to the AWT step was observed, indicating that the anchoring phenomena is model-independent.

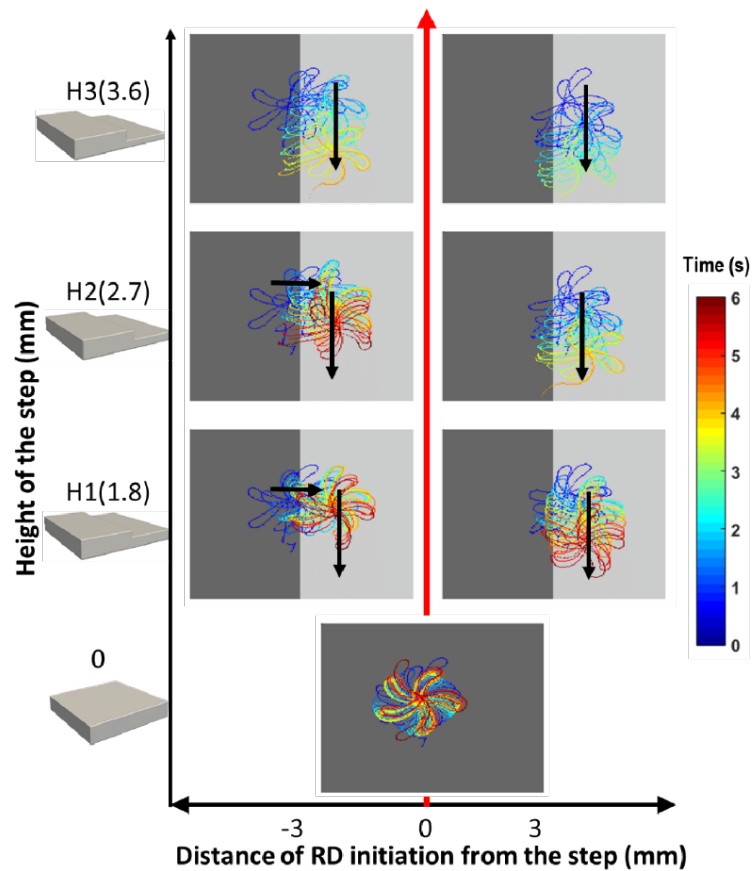


Figure 3.11: Effects of AWT step on the RD dynamics in 3D slab with the CRN atrial cell model (Study 1a). The characteristic flower-like pattern formed by the RD tip was stationary on a uniform thickness slab (bottom panel) and drifted towards and then along the step for the slab with AWT gradient (other panels). The core of RDs initiated on the thicker side of the 3D slab crossed over to the thinner region before drifting along the step. Black arrows indicate the direction of the drift.

3.4.2 Study 1b: Comparative effect of AWT and fibrosis on RDs

Results of the simulations comparing the effects of AWT and fibrosis in the 3D slabs are shown in Figure 3.12 for all 12 different locations (Figure 3.2, F) of the RD initiation, with both the AWT step height (H2, 2.7 mm) and location of the synthetic fibrotic patch kept constant.

In control cases of the AWT step only and the fibrotic patch only (Figure 3.12, A and B, respectively), the RDs either drifted towards and anchored to the step (9 out of 12 locations) or anchored to the fibrotic patch and drifted in a clockwise direction around it (4 out of 12 locations). Note that the RDs did not anchor when initiated at a distance of 12 mm (Figure 3.12, A) and 10.5 mm (Figure 3.12, B) from the AWT step on the thinner side and fibrotic patch, respectively.

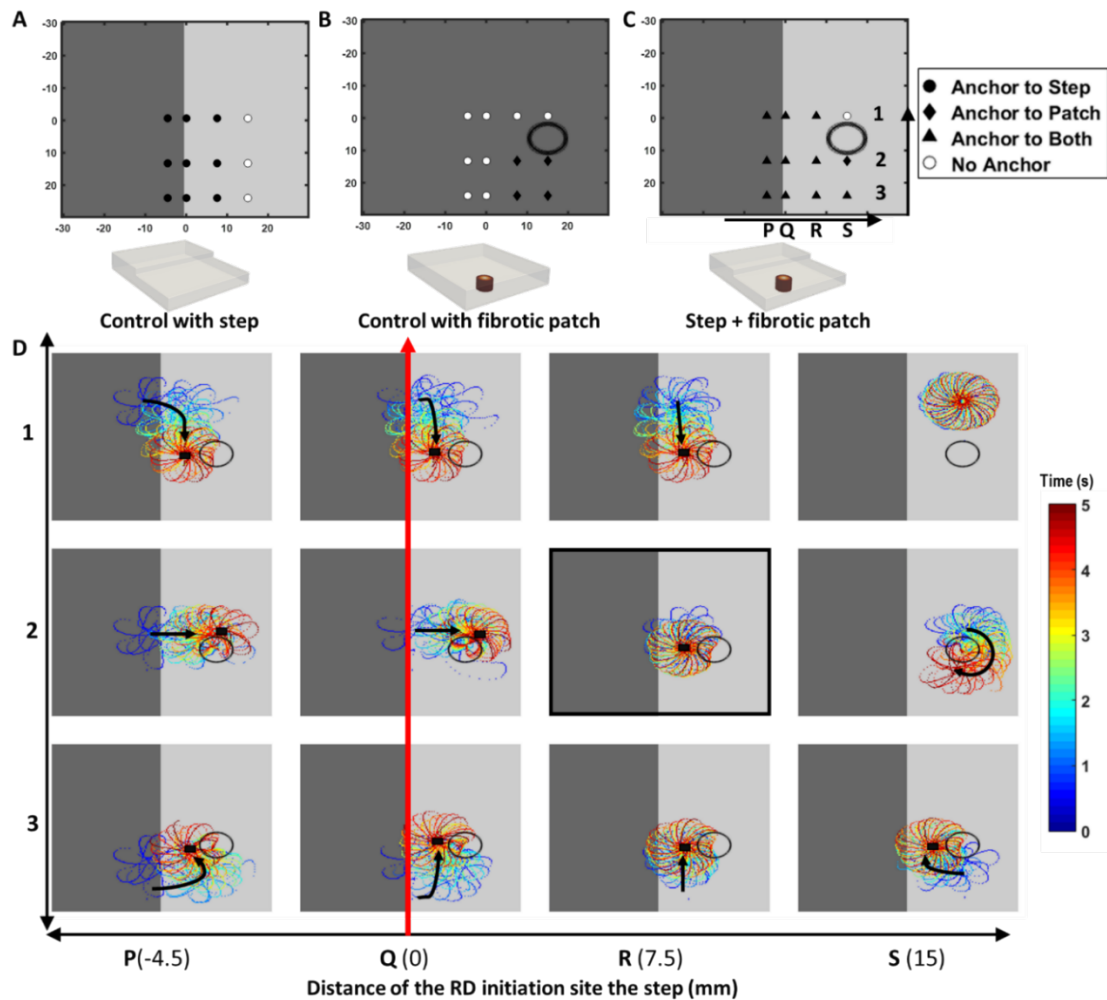


Figure 3.12: Competing effects of AWT and fibrosis in the 3D atrial slab (Study 1b). Outcomes of the RD simulations performed for 12 initiation locations (P1 to S3) with: (A) a step change in AWT, (B) a cylindrical fibrotic patch (shown with a black circle), (C) both AWT step and fibrosis. In cases (A) and (B), RDs anchored to the step (for locations marked with a filled black circle) and fibrotic patch (for locations marked with black diamond), respectively. White circles mark locations where the RDs did not anchor to either. In case (C), the majority of the RDs anchored between the AWT step and fibrotic patch (for locations marked with a black triangle). These RD tip trajectories on the top surface of the 3D slab are shown for the 12 locations (P1 to S3) in the panel (D). Black arrows indicate the direction of RD core drift, and black squares mark locations where they became stationary and anchored.

In the presence of both the AWT step and the patch together (Figure 3.12C), the majority of the RDs stabilised and anchored between the patch and the step (8 out of 12 locations). Analysing the RD trajectories in the latter case (Figure 3.12D), we found that RDs initiated on the thicker side, which were insensitive to the fibrotic patch alone, now drifted towards the patch located in the thinner region due to the influence of the AWT gradient. Once the RDs reached the region

between the AWT step and the fibrotic patch, they could either drift downwards along the step or drift rightward and rotate clockwise around the patch. Opposing influences from the AWT step and the fibrotic patch in this case can cancel each other out, with the RD becoming stationary and anchoring between the two structures.

Furthermore, in case of location R2 (highlighted in Figure 3.12D), increasing the step height from H2 to H4 caused the RDs to anchor to the step (Appendix, Figure A. 6). However, increasing the distance between the step and the RD initiation site (from 7.5 mm to 15 mm), while preserving the distance between the initiation site and the patch, resulted in the RD anchoring to the patch (Appendix, Figure A. 6).

3.5 Discussion

The computational study performed on the 3D atrial tissue slabs enabled us to successfully evaluate the mechanistic influence of AWT step and fibrotic tissue on the drift and anchoring of the RDs sustaining AF. The key findings of the presented work are: (1) the sharp gradients of AWT act as anchoring locations for RDs; (2) in the presence of fibrosis, the AWT step acts as a competing attractor for the RDs. Such AWT gradients are commonly present between the RA wall and the CT and pectinate muscles [194] and could help explain the presence of RDs at these sites recorded in animal experimental models [173,189].

The drifting behaviour of RDs caused by variation in myocardial thickness has previously been studied by Biktasheva et al. [190]. However, their numerical study was limited to simple 2 variable ionic cell models (FitzHugh-Nagumo and self-oscillatory Oregonator model) and has not explained the mechanism underlying the anchoring of RDs to the AWT step. The study presented in this chapter reproduced their findings using the FK ionic model for remodelled atrial cells [71] and CRN model [136] that provides a detailed description of ionic currents and AP.

The atrial FK and CRN models have slightly different shaped hypotrochoidal (“flower-like”) patterns. The latter (Figure 3.11) is more asymmetric with longer period of rotation compared to the former (Figure 3.8), which effects the drift velocity. Since both models have similar APD restitution curves (Figure A.1), the differences in meandering patterns could be explained by the differences in excitability of the underlying medium determined by the model parameters. However, despite these differences the anchoring of the RD to the AWT step was consistent between the models and the relationship between increase in height and increase in the drift

velocity was preserved. This suggests that the anchoring of RDs to regions with large AWT gradients is a model-independent phenomenon and is a purely structural effect inherent from the geometry.

Furthermore, our study explored the underlying mechanisms. Our simulation results identified two factors that affected RD anchoring to the AWT step: (i) the position (thick or thin side) and distance from the step at which the RDs are located and (ii) the height of the step itself.

3.5.1 Influence of the AWT step parameters on the RD dynamics

The patterns of RD drifting and anchoring were investigated by initiating the RDs at multiple locations around the thick and thin areas of the slab (Figure 3.2E). Our results showed that only RDs initiated within a short distance from the AWT step ultimately anchored to it (Figure 3.8C). For our choice of model parameters, this distance range was 4.5 mm on the thicker side and 12 mm (H1-3) to 15 mm (H4) on the thinner side from the step. RDs located within this range, however, showed two distinct patterns of anchoring, which depended on their position with respect to the step (Figure 3.8D). If initiated on the thicker side, RDs first drifted across the AWT step into the thin region and then drifted along the step. If initiated on the thinner side, RDs drifted towards the AWT step and remained on the same side, while drifting along the step. Moreover, the velocity with which the RD tip crossed over from the thick to the thin region (Figure 3.10, $2.13 \pm 0.18\text{m/s}$) was substantially higher than the tip velocity in the opposite direction (Figure 3.10, $0.4 \pm 0.11\text{m/s}$). These results suggest that the presence of a thickness step facilitates the anchoring of RDs exclusively on the thinner side of the step.

The effect of the AWT step height on the anchoring of RD was investigated by using 4 atrial slab models of the increasing height (Table 3.1). AWT of the thicker side of the slabs (7.5 mm) was comparable to the range of 4.2 ± 1.2 mm to 6.3 ± 1.5 mm observed for CT in the RA [194], while the AWT of the thinner side (3 mm – 5.7 mm) was representative of AWT for the RA wall [195]. Our simulation results showed that an increase in the height of the AWT step leads to an increase in velocity with which the RDs drift along the step (Figure 3.9). This result is consistent with theoretical predictions by Biktasheva et al. [190], where the drift velocity of the RD was reported to be proportional to the height of the step. Note that the RD drift was absent for AWT step height of 0.3 mm, which is the resolution of the mesh used for the simulations. Moreover, for a thickness gradient below 1 mm, the drift velocity was negligible (< 1 mm/s). Therefore, critical thickness for observing RD drift is approximately 1 mm. However, it should

be noted that this value may be affected by model parameters (diffusion coefficient, excitability, etc.) and the location of the RD with respect to the step. The mechanism underlying the increase in drift velocity with increase of AWT step height could be linked with increasing source-sink mismatch, which facilitates faster condition in the direction along the gradients.

3.5.2 Mechanisms of the AWT step effects on the RD dynamics

We hypothesize that the drift of RDs towards regions of high AWT gradients and their subsequent anchoring is likely to be based on a large source-to-sink mismatch at the step between thin and thick tissue. Previous theoretical work by Wang et al. [196] and computational studies by Cherry et al. [197] and Connolly et al. [198], have explored the effects of tissue geometry on electronic modulation of repolarization. We believe that anchoring of RDs to the step between thick and thin tissue is a similar case, where repolarization and CV at the AWT gradient are altered due to source-to-sink mismatch, which facilitates the anchoring.

3.5.1.1 RD drift from thin to thick side of AWT step

The case of the RD tip propagating from the thin to thick side of an AWT step is shown in Figure 3.13, A-B. We hypothesise that an electrotonic current resulting from the source-to-sink mismatch at the step changes CV in the surrounding tissue, and the reduced CV helps stabilise the RDs in these locations. The simulation results confirmed our hypothesis by showing a decrease in CV from 0.6 m/s to 0.54 m/s (Figure 3.6, C and G) when a plane wave propagated from thin to thick side of the step. Moreover, the wavefront at the RD tip (Figure 3.13A) encounters a region of prolonged APD (+5 ms, Figure 3.6, D and H) due to the electrotonic effects at the AWT step. The latter are due to uneven electrotonic loading of the cells at the step by their neighbours from the thin and thick sides, which generates an inward current to the earlier repolarized cells and prolongs their APD [197,199]. As a wave propagating from the thin to thick side at the AWT step encounters larger number of cells upstream vs. downstream, APD is increased on the thin side (Figure 3.6D). Previous computer models and experimental studies have shown that in the presence of APD or CV gradients, RDs drift towards regions of longer APD [74,200,201] and slower propagation. For waves propagating from the thin to thick side, the AWT step meets both these conditions, and hence the RDs remain localised to the thin side of the step.

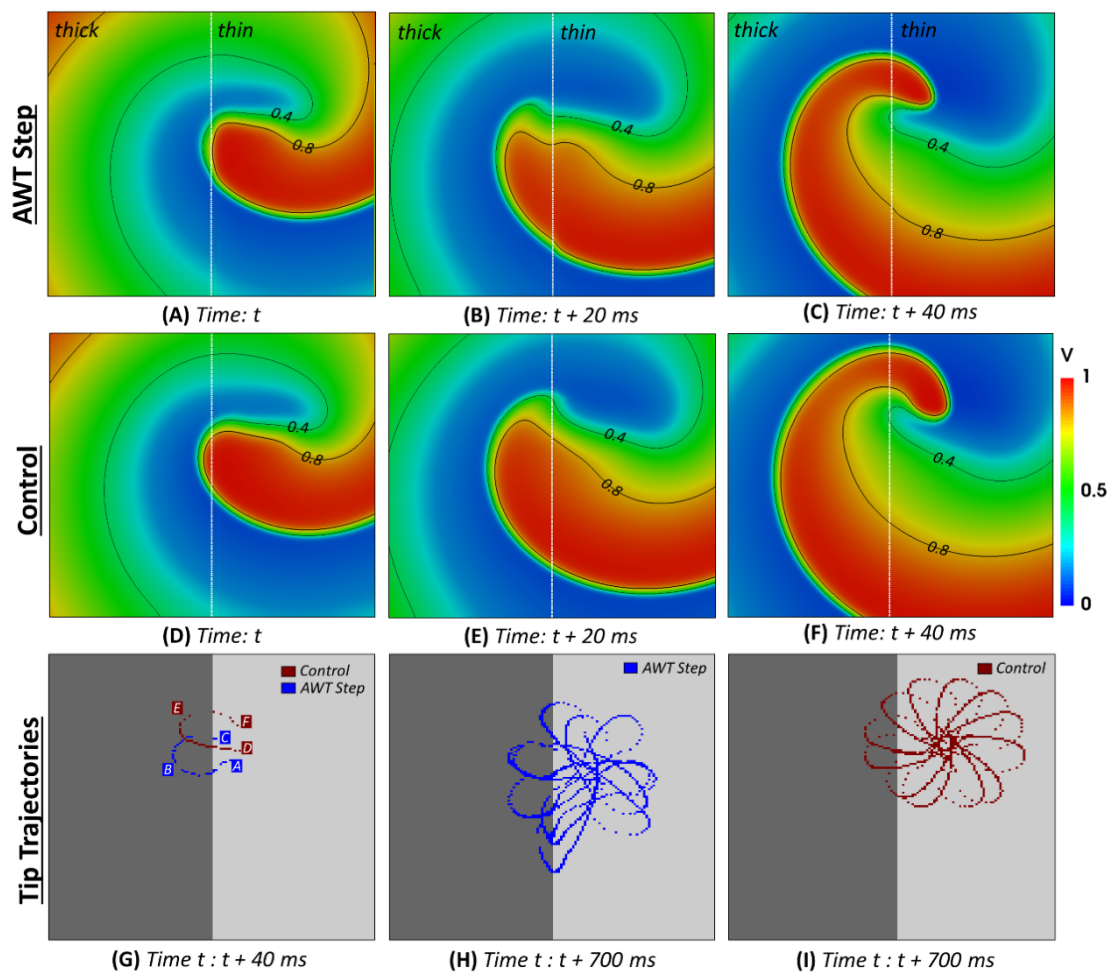


Figure 3.13: Changes in the RD wavefront during propagation at the AWT step. Colour coded voltage maps showing the behaviour of the RDs in a slab with the AWT step (A-C, H4) and in a control uniform slab (D-F, H0) at different moments of time. In Panel G, the corresponding RD tip trajectories over the 40 ms are overlaid to show the trajectory changes between the step (blue, A-C) and control case (red, D-F). In the presence of the step, the tip moves vertically down before entering the thick part of the slab (G, A-B). This additional vertical drift accumulates over 700 ms and results in drift of the RD along the AWT step (H). In the absence of the step, the RD traces a perfect arc (G, D-E) and the flower-like pattern remains localised at the same position of the slab (I).

Moreover, the prolonged APD at the step acts like a barrier preventing the spread of current produced by the wavefront: the effect of this can be seen as a characteristic notch on the RD wavefront (Figure 3.13B), which is absent in control (Figure 3.13E). This is equivalent to a local decrease in excitability of the tissue close to the step, and therefore an increase in the curvature of the trajectory [71], which results in the drift of the RD tip along the step (Figure 3.13, G-H). An example trajectory of the RD tip travelling from the thin to thick side and back is shown in Figure 3.13G, where the trajectories in the presence and absence of AWT step in

the slab are overlaid in blue and red, respectively. In the former case, the tip encounters refractory tissue towards the thick side of the step. This causes the wavefront to propagate downwards along the step before entering the thick region, where the tissue is more excitable. This deviation increases the curvature of the trajectory, and the petal is formed at a lower position compared to control (Figure 3.13G). Furthermore, across a period of 700 ms, periodic interactions of the RD tip with the AWT step results in drift of the RD tip along the step (Figure 3.13H) compared to control (Figure 3.13I). Similar mechanism has been proposed for RD drift and anchoring to non-excitable or partially excitable obstacles, such as fibrotic regions and ablation scar [202]. In our case, it explains the drift of the RD tip along the AWT step observed in our simulations and a lower RD tip velocity recorded during propagation from the thin to thick region compared to the opposite direction.

3.5.1.2 RD drift from thick to thin side of AWT step

Thus, wave propagation from the thin to thick side slows down due to source-sink mismatch at the step. Conversely, wave propagation in the opposite direction should speed up. Our CV measurements during plane-wave propagation were unable to capture this effect (Figure 3.6A). However, the velocity of the RD tip travelling from the thick to thin side was greater than that in the opposite direction (Figure 3.10). Moreover, in this case, the electrotonic loading effects at junction results in a decrease of APD (-3 ms, Figure 3.6, B and F). Therefore, during wave propagation from the thick to thin side, the reduced APD coupled with increased CV does not facilitate the RD drift of towards the junction. This could explain why the RDs initiated on the thick side were not influenced by the present of the AWT step, unless the radius of the flower-like pattern directly overlapped with the step location. Only in the latter cases, once the RD tip drifted to the thin side, the effects of source-sink mismatch described above prevented its return to the thick side and facilitated the RD anchoring to the AWT step on the thin side.

3.5.1 Competing influence of fibrosis and AWT on RDs

Fibrotic tissue in the atrial myocardium is widely believed to be one of the most important substrates that promotes abnormalities in local AP conduction and facilitates AF perpetuation [174,177,191]. However, the role of fibrosis in anchoring RDs has never been compared with other atrial structural features that can also affect the RD dynamics, such as sharp gradients in AWT observed within the atrial geometries.

For the first time, we showed the RD anchoring between regions with a sharp AWT gradient (such as the CT region) and local fibrosis patches. Hence, locations of the RD stabilisation in the atria can be strongly influenced by both the presence of fibrosis, as predicted in previous studies [15,174], and the AWT gradients. These results can be explained by relative effects of (i) fibrotic patches providing slow conduction zones anchoring RDs (Figure 3.7), and (ii) large AWT gradients creating substantial source-to-sink mismatches. Therefore, atrial tissue regions between a fibrotic patch and a large AWT gradient experience both competing influences and are most likely to anchor RDs. In addition, our simulations showed that RDs anchored to the fibrotic patch only when they were initiated further away from the AWT step. Hence, anchoring of the RDs to either the AWT gradients or fibrotic patches may depend on 1) their comparative ability to provide suitable substrate and 2) their relative distance from the RD initiation site. The specific detail in which the RDs anchor to fibrotic regions and their implications in patient-specific AF models will be investigated in further detail in Chapter 4 and 5.

3.6 Limitations

Previous simulation studies have reported complex fibre orientation to have significant effects on atrial conduction [148,165]. In this study, however, we did not consider fibre orientations in the modelling approach specifically because we wanted to evaluate the effect of thickness independently in the absence of other factors which could influence the behaviour of the RDs. This is the main limitation of our work as abrupt changes in fibre orientations have been previously reported to affect the RD dynamics. Understanding the combined effect of AWT gradient and anisotropy warrants future investigation. Note also that the aFK model developed by Goodman et al. [144] was based on data from tachypaced sheep atrial cells, due to a lack of equivalent human data. However, comparison of APD between the aFK model and in the CRN model for a remodelled human atrial myocyte showed a good agreement between the two models: less than 5% difference in APD in the considered range of frequencies between 6-10 Hz. Moreover, the main result of the study – that RDs anchor to regions with large AWT gradients – was qualitatively similar between the aFK and CRN models.

Another limitation of this study is a simple representation of the atrial structure with a 3D slab geometry with a sharp transition in the AWT at the step. Such sharp transition in tissue properties is a simplification of the variety of thickness gradients observed in atrial anatomical structures, such as the crista terminalis, pectinate muscles, etc. However, as our primary

objective was to elucidate the mechanisms underlying the anchoring effect of a single AWT gradient, using the simple model was warranted. In the next Chapter, we will consider the dynamics and anchoring of RDs in realistic 3D atrial geometries with patient-specific AWT and fibrosis distributions.

3.7 Conclusions

This chapter elucidated the role of AWT in the dynamics of RDs and compared the AWT effects with the respective effects of fibrosis. The main finding is that sharp gradients of AWT provide anchoring locations for RDs. In this sense, AWT gradients have a comparable effect on RDs as fibrotic tissue, and hence both factors can equally influence RD activity during AF. Furthermore, we have elucidated the mechanism underlying the anchoring of RD to regions of sharp AWT gradients and concluded that drift and anchoring of RDs is dependent on the amplitude of the AWT gradient, as well as distance of the RD initiation site from the gradient. Therefore, it is important to consider the role of structural features with large AWT gradients, such as the CT in the RA, when identifying the RDs locations during AF treatment planning.

Chapter 4

Image-Based Computational study: Role of Patient-Specific AWT and Fibrosis

4.1 Section Outline

This chapter aims to investigate the influence of AWT gradients on the RD dynamics in realistic 3D atrial geometries and evaluate the comparative effects of patient-specific AWT gradients and fibrosis distribution. In the previous chapter, the effect of AWT on RDs was evaluated using a simple 3D slab model (Study 1 above). In this chapter, this study is extended to realistic RA and LA geometries. The motivation for investigating AWT and fibrosis is first described (Section 4.2), and the protocols used for constructing patient-specific RA and LA models and performing simulations are then detailed (Section 4.3). For both atria (RA: Study 2 and LA: Study 3), the study has two parts (Section 4.4). In part (a), the RD dynamics is evaluated only in the presence of AWT. In part (b), the RDs are explored in the presence of both AWT and fibrosis. Section 4.5 analyses the simulation results, compares the RD dynamics in LA and RA, with and without fibrosis, and discusses clinical implications. Finally, the limitations (Section 4.6) and the main findings of the chapter are summarised (Section 4.7).

4.2 Introduction and Aims

AWT has emerged as a potential arrhythmogenic factor in AF patients and has been linked with both atrial remodelling [203,204] and post-ablation AF recurrence [205]. Optical recordings in sheep RA have provided experimental evidence for RDs stabilizing at interfaces between thick and thin atrial muscle [189]. Moreover, the association of complex fractionated electrograms (CFAE) with LA AWT has also been reported [206], pointing to the presence of AF substrate in these regions. These findings show a potential of AWT gradients as a marker for identifying RD locations in the atria. However, the influence of AWT gradients on the RD dynamics in realistic atrial geometries is unknown and warrants further investigation.

There are certainly other factors that influence the locations of the RDs in AF patients. One of the major candidates is atrial fibrosis, which is a product of AF-induced structural remodelling and is the most studied example of an arrhythmogenic substrate in AF patients. It has been reported to correlate with both AF incidence and post-ablation recurrence [120]. Moreover, recent clinical [13,56] and computational [15,174] have provided evidence that fibrotic tissue can stabilise RDs in AF patients. However, other studies have reported controversial results [175]. Such differences in RD behaviour among different studies / AF patient groups could be related to the effects of factors other than fibrosis, such as patient-specific atrial architecture and AWT. Previous simulation studies based on patient-specific atrial models have only accounted for atrial fibrosis and have not included details of AWT. Hence, this chapter aims to investigate the influence of AWT gradients on the RD dynamics in realistic atrial geometries and evaluate the comparative effects of patient-specific fibrosis distribution and AWT gradients.

Until recently, the lack of imaging tools to generate whole organ AWT maps prevented modelling studies from reconstructing patient-specific atrial geometries. However, novel MRI [195] and computer-tomography [207] protocols now allow for generation of such patient-specific AWT maps. These data provide the basis for exploring the RD dynamics in patient-specific atrial models, to understand the role of AWT gradients in influencing RD locations. Moreover, MRI enables the reconstruction of fibrosis distributions in AF patient [81]. Elucidating the relationships between AWT gradients, fibrosis and RD locations can lead to an improved understanding of AF mechanisms, and ultimately help identify patient-specific ablation targets, improving the efficacy of treatment.

In summary, this study aims to investigate the mechanistic influence of two structural factors: (i) AWT and (ii) fibrosis on the dynamics of RDs sustaining AF. To this end, computational simulations of atrial electrophysiology were performed on realistic RA and LA geometries obtained from MRI of 6 patients. Our working hypothesis is that competing influences of AWT gradients and fibrotic patches on conductive properties of atrial tissue determine anchoring locations of RDs in 3D atrial models.

4.3 Methods

In the study presented in this chapter, we extend the study from the idealised 3D atrial slab with AWT step to simulations on realistic models of atrial geometries derived from MRI data. The general workflow used for construction of the realistic models is shown in Figure 4.1. Here we first investigate the role of AWT and morphology of the RA (Study 2a) and LA (Study 3a) on the RD dynamics (Figure 4.1, top row). Then in the second part, we evaluate the combined effect of patient-specific AWT and fibrosis on the RD dynamics (Figure 4.1, bottom row). In the RA (Study 2b), the effect of fibrosis is modelled using a cylindrical fibrotic patch, while in the LA (Study 3b), fibrosis is incorporated from patient-specific late gadolinium enhanced (LGE) MRI. LGE-MRI data was not acquired in the right atrium in these patients.

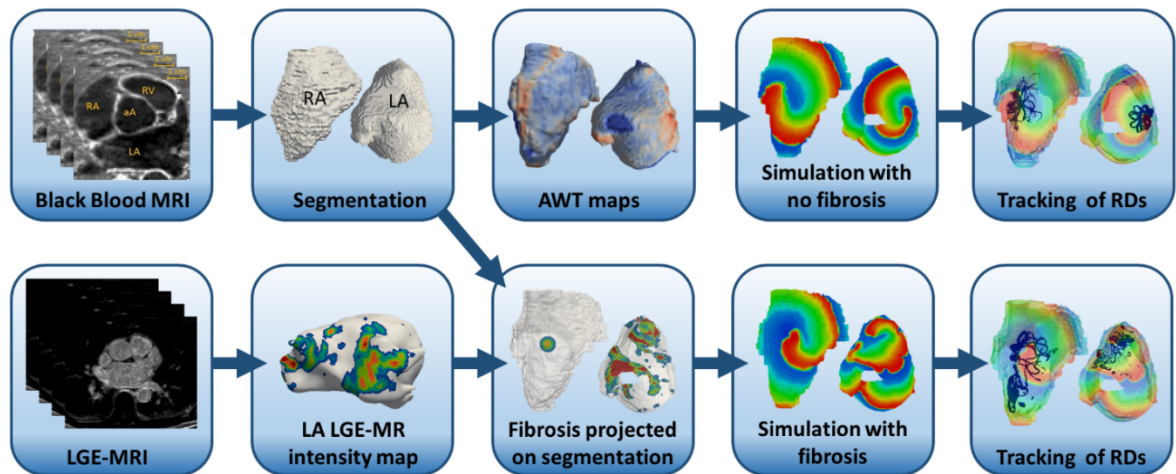


Figure 4.1: Workflow for the image-based atrial modelling (Studies 2 & 3). Top row: Segmentation and registration of LA and RA geometries from black-blood MRI used in simulations to investigate the role of AWT in the RD dynamics in the RA (Study 2a) and LA (Study 3a). Bottom row: Patient-specific fibrosis distributions segmented from LGE-MRI (bottom row) in the LA (Study 3b) and a synthetic fibrotic patch in the RA (Study 3a) used to evaluate the relative effects of fibrosis and AWT gradients on the RD dynamics in the realistic atrial geometries.

4.3.1 Simulating cardiac electrophysiology

The 3D atrial simulations were performed using the same framework, as described in Chapter 2. Briefly, the standard mono-domain equation was solved with no-flux boundary conditions using forward Euler and centred finite differences schemes with temporal and spatial steps of 0.005 ms and 0.3 mm. As in Chapter 3, our model was isotropic, and the diffusion tensor was replaced by a scalar diffusion coefficient $D = 0.1 \text{ mm}^2 \text{ ms}^{-1}$, carefully chosen to match an atrial

conduction velocity of 0.60 m s^{-1} typical of AF [192]. For I_{ion} , we used the Fenton-Karma electrophysiology model [71] modified to accurately describe the restitution properties of remodelled atrial cells [144]. This atrial Fenton-Karma (aFK) cell model accurately captures the main characteristics of atrial action potentials and its restitution properties, while keeping the computational time relatively short.

4.3.2 Study A: Influence of patient-specific AWT on the RD dynamics

Reconstruction of atrial geometries and AWT: Four healthy volunteers and two paroxysmal AF patients were imaged using a black-blood MRI protocol (1.5T, cardiac and respiratory gating, acquisition resolution: $1.4 \times 1.4 \times 1.4 \text{ mm}^3$). Further details on the image acquisition and analysis can be found in the original publication [195]. Briefly, the RA and LA geometries of healthy volunteers and patients, respectively, were obtained by manual segmentation using ITK - SNAP (Kitware). The segmented geometries were interpolated to an isotropic resolution of 0.3 mm using a custom build program in Matlab and smoothed using 3D Slicer [208], to produce geometries with resolutions suitable for simulations. Also, note that the RA geometries weren't acquired in patients because of long scan times which were beyond the time restrictions placed on patient MRI scans.

AWT measurements: The AWT was computed using the average of nearest neighbour method, adopted from Varela et al. [195]. This specific method was chosen because of its simple implementation, low computational cost and its success in measurements of cortical thickness in the brain [209,210]. Triangular meshes were computed for the epicardial and endocardial surfaces of the original geometries before interpolation using a marching cubes algorithm and resampled to increase mesh quality with Matlab, resulting in an average edge length of $0.96 \pm 0.03 \text{ mm}$. Following this, AWT maps were computed by: 1) measuring the distance between each node in the epicardial surface and its nearest node in the endocardial surface; 2) reversing this computation from the endocardial surface; 3) averaging the outcomes of 1) and 2). In the RA, the region with the highest AWT ($5.10 \pm 1.00 \text{ mm}$ against $1.8 \pm 0.4 \text{ mm}$ in the surrounding RA wall) can be identified as the crista terminalis, CT [194]. We refer to this region as the CT in the following text. In 2 out of 4 patients, this region was characterised by a large AWT gradient ($4.75 \pm 0.95 \text{ mm}$ in the CT region against $2.91 \pm 0.60 \text{ mm}$ in the RA wall), whereas in other patients the region was less prominent ($2.90 \pm 1.04 \text{ mm}$ against $2.45 \pm 0.54 \text{ mm}$ in the RA).

4.3.3 Study B: Competing effect of AWT and fibrosis on the RD dynamics

4.3.3.1 Study 2b (Model construction in the RA)

In the RA, due to lack of patient-specific fibrosis data, we added a synthetic 3D spherical fibrotic patch of diameter 9 mm, with similar labels 1 to 5 of decreasing diffusion coefficient as done before for the 3D slab (described in Chapter 3, Section 3.3.3), in a region near the thick RA muscle bundle of the CT. This enabled a direct comparison of the effect of AWT and fibrosis on the RD dynamics in the RA. The choice of 9 mm diameter was based on calculating an average fibrotic patch size in the LA (Study 3b).

4.3.3.2 Study 3b (Patient-specific fibrosis in the LA)

The two paroxysmal AF patients also underwent LGE-MRI in the same scanning session and in the same phase of the cardiac cycle as the black-blood MRI acquisition, to detect fibrosis in the LA (1.5T, cardiac and respiratory gating, acquisition resolution: $1.3 \times 1.3 \times 2 \text{ mm}^3$).

For Study 3b, the segmentation of fibrotic LA tissue was performed by analysing the image intensity ratio (IIR), computed by dividing individual voxel intensities by the mean blood pool intensity. IIR values >1.08 were classified as the border zone (BZ) and >1.24 as dense fibrosis. The lower IIR threshold of 1.08 was obtained as an average of the previously proposed values of 1.2 [88] and 0.97 [87]. The upper IIR threshold of 1.24 was chosen as all the LGE MR images were acquired post-ablation, and therefore, the IIR threshold had to be lower than that reported for dense scar representing the ablation lesions, 1.32 [88]. Transition from the BZ to dense fibrosis was represented by labelling segmented fibrotic tissue from 1 to 5 according to LGE-MRI intensity, where level 5 corresponded to dense fibrosis (regions with $\text{IIR} > 1.24$) and level 1-4 corresponded to variable degree of diffuse fibrosis (regions with $1.08 < \text{IIR} < 1.24$ split into four equal intervals). Next, the LA geometry with realistic AWT and the fibrosis distribution had to be nonlinearly registered using MIRTk [211], as they were obtained from different MRI sequences as discussed above. Following this, fibrotic regions were projected onto the LA geometries with transmural uniformity for the same patients using Paraview (Kitware) and Matlab (Mathworks, Inc).

The fibrotic regions with labels 1-5 were incorporated in the atrial model using the same diffusion coefficient values as Chapter 3 (Section 3.3.3), for computational tractability.

4.3.4 Simulation protocol for RD initiation

A single RD was initiated using a cross-field protocol at different locations within the atrial geometries. In the RA (Study 2), RDs were initiated in the vicinity of the CT region at 6 to 9 different locations, where a large AWT gradient was typically observed. The S1 stimulus (non-dimensional voltage: 1; duration: 1ms) was applied along a plane parallel to the superior vena cava, and after 50 ms S2 stimulus (non-dimensional voltage: 0; duration: 2 ms) was applied in a plane perpendicular to that of S1. For each of the 4 RAs, the locations of S1 and S2 were varied such that the intersection between the two planes was located near the CT region. An example for Person 1 in Study 2(a) is shown in Figure 4.2, where 9 such locations have been marked with yellow crosses. Likewise, in Study 2(b), initiation locations were chosen such that in some cases the distance from the AWT gradient is fixed, but the distance from the fibrotic patch is varied and in others vice versa. Here again, an example of Person 1 is shown in Figure 4.3. In the LA (Study 3), 4 initiation locations were selected across the atrial wall. Simulations were performed in both geometries with and without fibrosis for a duration of at least 3s: an example is shown in Figure 4.7 for Person 5.

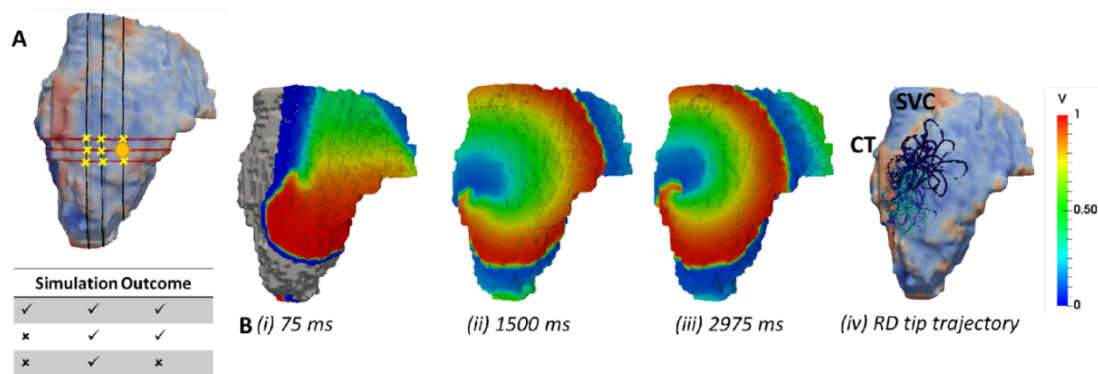


Figure 4.2: Anchoring of RD to AWT gradient at the CT region in the RA of Person 1. (A) All RD initiation locations are marked by yellow crosses, and in the table below, ✓ corresponds to anchoring to the CT region and ✗ to no anchoring. The voltage maps for RD initiated at the location marked by a yellow circle (in A) is shown in panel B (i-iii) for different moments of time, and the complete tip trajectory with the RD anchored to the CT region is shown in panel B (iv).

For each simulation, the movement of the RD was tracked by recording its tip location (see details above) for each time step over the duration of the entire simulation [71]. The protocol for calculating the RD tip, presented in Chapter 3, was extended to 3D to perform tip tracking

on the surface of the atrial walls. The resultant RD trajectories were then overlaid separately on the AWT and fibrosis maps for each patient-specific atrial geometry.

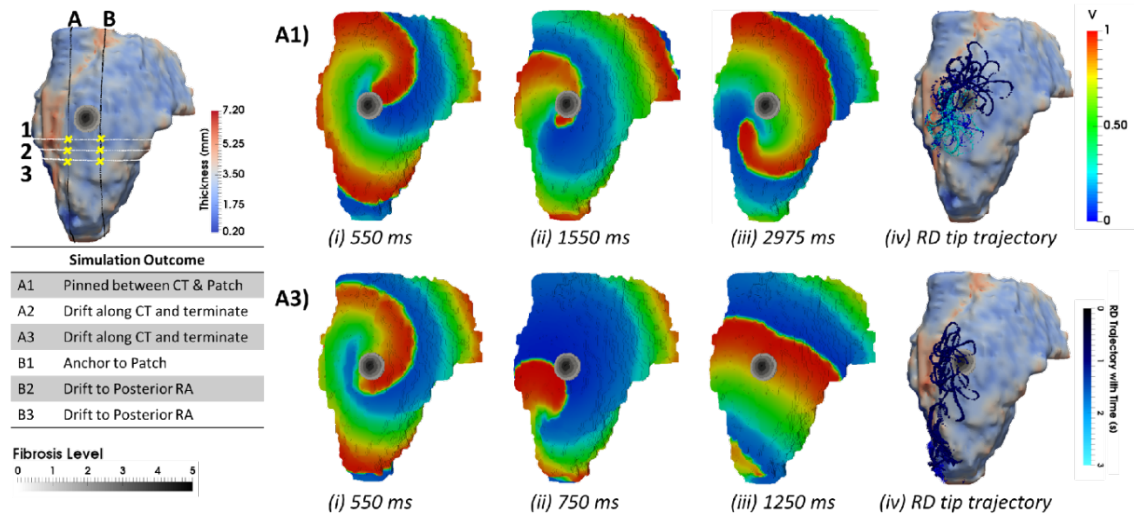


Figure 4.3: Anchoring of RD to AWT gradient at the CT region and the fibrotic patch in the RA of Person 1. Line A marks an approximate horizontal distance of 3mm from the AWT gradient (CT region) and edge of the fibrotic patch, while Line B marks a horizontal distance of 13 mm from the CT region and 1 mm from the edge of the patch. The vertical distance of locations 1-3 from the centre of the fibrotic patch was gradually increased (A1, 6.6mm; A2, 10.2 mm; A3, 13.8 mm), while the distance from the CT region was approximately constant. The voltage maps for RD initiated at location A1 and A3 are shown in Panel (A1) and (A3), respectively, at different moments of time (i-iii), and the RD tip trajectories are shown in (iv). For the initiation location A1 close to the fibrotic patch, the RDs anchored between the CT region and the fibrotic patch (A1). For the location A3 further away from the patch, the RDs drifted along the AWT gradient at the CT region towards the mitral valve (A3). The outcomes of simulations for the RDs initiated at different locations are provided in the table.

4.4 Results

In the patient-specific atrial models, RDs was successfully initiated in 4 RAs and 2 LAs using the cross-field protocol with or without fibrosis. This resulted in the formation of either 1-2 RDs in the first 1s of simulation. In the following 3-5s, these RDs meandered and eventually either stabilised at distinctive locations in the atrial wall or broke down into multiple RDs, which were dependent on the patient-specific AWT gradients and fibrosis distribution.

4.4.1 Study 2: Right Atrial Geometry

The average AWT values computed in the CT region and the surrounding RA wall of Person 1 (Figure 4.4A; CT: 3.45 ± 0.86 mm; RA: 2.09 ± 0.38 mm) and Person 2 (Figure 4.4B; CT: 4.75 ± 0.95 mm; RA: 2.91 ± 0.60 mm) showed a higher gradient in AWT compared to Person 3

(Figure 4.4C; CT: 3.04 ± 0.65 mm; RA: 3.00 ± 0.54 mm) and 4 (Figure 4.4D; CT: 2.90 ± 1.04 mm; RA: 2.45 ± 0.54 mm). Hence, Person 1 and 2 had a more prominent CT region compared to Person 3 and 4 as shown in Figure 4.4 (A, B vs C, D).

In the Person 1 and 2 with more prominent CT region, 55% of the RDs initiated at different locations drifted towards the CT region, either anchoring to it (Figure 4.4A (i), B (i)) or crossing over it to the posterior side of the RA (Figure 4.4A (ii), 4B (ii)). As an example, the 3D atrial voltage map in Person 1 is shown in Figure 4.2. However, in the RA of Person 3 and 4 (Figure 5C, 5D), the CT regions had thickness comparable to the remaining RA wall. Hence, the RDs neither drifted towards the CT nor anchored at any location (Figure 4.4C (i), D (i)). Instead, they either drifted towards the superior vena cava or the tricuspid valve or terminated.

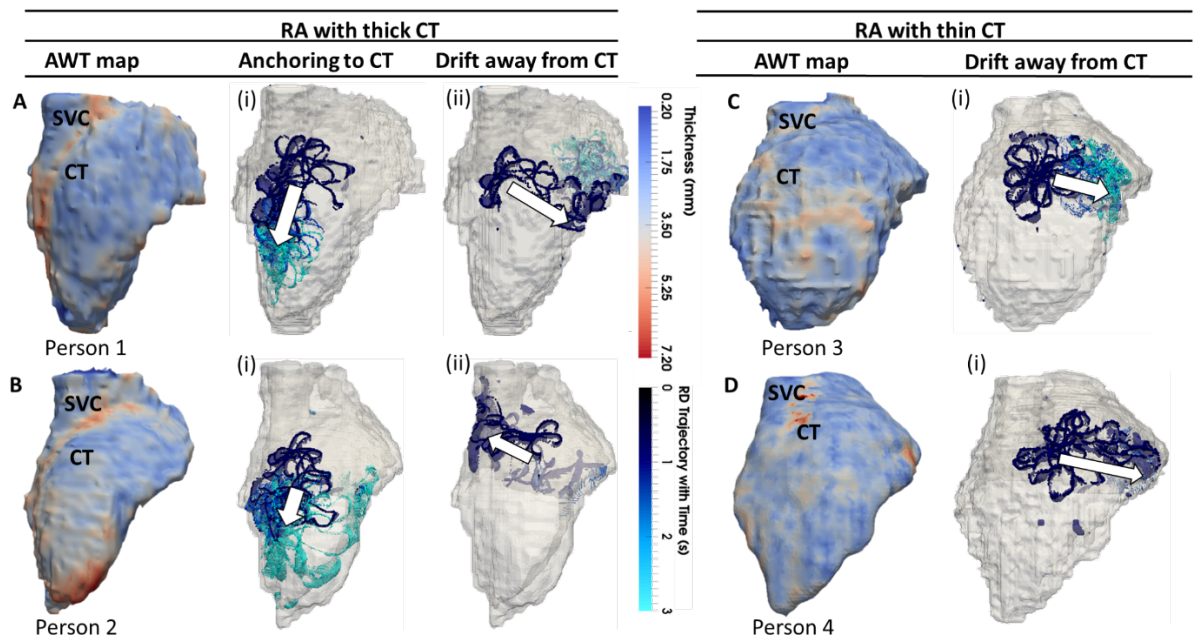


Figure 4.4: Effects of AWT on the RD dynamics on the RA. Trajectories of RDs (blue), initiated at 4 to 9 locations in the RA, are overlaid on the AWT map for 4 different subjects. In Person 1 (Panel A) and 2 (Panel B), the CT region had a higher AWT compared to rest of the RA wall, while in Person 3 (Panel C) and 4 (Panel D) the CT region was not distinguishable by thickness. The majority of RDs initiated in Person 1 (6 out of 9 sites), and Person 2 (4 out of 9 sites) drifted towards the thick CT region and anchored to it (A (i) & B (i)), but some also drifted towards the opposite side of the RA geometry (A (ii) & B (ii)). However, none of four RDs initiated in Person 3 and Person 4 anchored to the CT region, drifting away towards the SVC or TCV instead (C (i) & D (i)). Here and below, white arrows indicate the direction of RD drift after initiation.

When the RA simulations were repeated in the presence of a synthetic fibrotic patch, the RD trajectories were affected in all patients. The voltage maps for 2 different simulations in Person

1 are shown in Figure 4.3, and as an example, the summary of the RD trajectories in Person 1 and 4 are presented in Figure 4.5. For the RA of Person 1 with a prominent CT region (Figure 4.5A), RDs initiated closer to the fibrotic patch either stabilised between the CT region and the patch (Figure 4.5B (ii)), or anchored to the latter (Figure 4.5C (ii)), depending on the distance from their initiation site to either structure. However, in the RAs with no distinguishable thickness gradient at the CT region (Figure 4.5D), all RDs anchored to the fibrotic patch (Figure 4.5E (ii) and F (ii)).

For the RDs to anchor, the critical proximity to the CT region and the patch is challenging to determine in realistic RA geometry because, unlike AWT in a rectangular slab, the CT region is not a simple straight line. However, in an example provided for Person 1 (Figure 4.3), RDs initiated at the middle between edges of the CT region and the fibrotic patch (~ 3 mm from either structure horizontally and 6.6 mm vertically) (Figure 4.3, location A1), stabilised and anchored between them. Increasing the horizontal distance between the RD and the CT to 13 mm (Figure 4.3, location B1) led to the RD anchoring to the fibrotic patch.

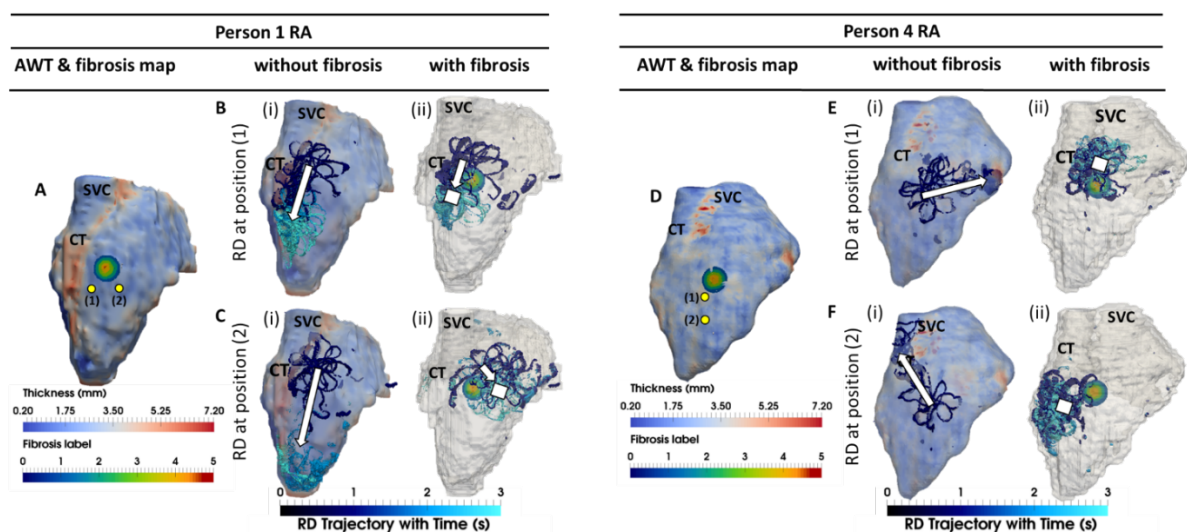


Figure 4.5: Competing effects of AWT and fibrosis in the RA. The RD trajectories (blue) in the RA, obtained by initiating RDs at two locations (yellow dots) without and with the presence of fibrosis are overlaid on the maps of AWT and fibrosis distribution, respectively, for Person 1 (A) and 4 (D). In Person 1 in the absence of fibrosis, RDs initiated at both locations (B (i), C (i)) drifted towards the CT region with a large AWT gradient. However, in the presence of fibrosis, RD initiated at position 1 anchored between the CT and fibrotic patch (B (ii)), and while RD initiated at position 2 anchored to the patch (C (ii)) which was located further away from the CT region. In Person 4 in the absence of fibrosis, RDs initiated at both positions (E (i), F(i)) neither drifted towards the thin CT nor showed any anchoring. In the presence of fibrosis, RDs initiated at both positions (E (ii), F (ii)) anchored to the fibrotic patch. SVC: Superior vena cava. White squares mark locations where the RDs anchored.

4.4.2 Study 3: Left Atrial Geometry

The AWT maps computed for LA geometry of Person 5 (Figure 4.6A) showed higher AWT in the LA roof (4.77 ± 0.60 mm) compared to the rest of the atrial wall (2.96 ± 0.31 mm). Therefore, in the respective simulations, RDs drifted towards and along the LA roof (Figure 4.6C (i)) when initiated in its proximity but drifted towards the PVs (Figure 4.6B (i)) if initiated further away. The LA of Person 6 (Figure 4.6D) was characterised by roughly uniform AWT (2.53 ± 1.20 mm), and RDs initiated in this geometry drifted either towards the PVs (Figure 4.6E (i)) or the mitral valve (Figure 4.6F (i)).

In the LA, LGE-MRI intensity-based segmentations yielded different fibrosis distributions in the two AF patients, as shown in Figure 4.6A, D. Both Person 5 and 6 had fibrotic tissue in the LA regions surrounding the PVs, with a higher degree of fibrosis in one patient (14% of the atrial volume, Figure 4.6A) compared to the other (10%, Figure 4.6D). In Person 5, LA simulations repeated with the presence of fibrosis showed either stable RD anchoring to the BZs of fibrotic tissue (Figure 4.6C (ii)) or transient anchoring where RDs stabilised at a fibrotic patch in the first 1 s of simulation and then drifted to a new location in another fibrotic region and stabilised there (Figure 4.6B (ii)). 3D atrial voltage maps for the cases presented in Figure 4.6C (i) and (ii) are illustrated in Figure 4.7A1 and A2, respectively. Furthermore, in one particular case, we also observed the breakdown of the primary RD into multiple wavelets meandering between fibrotic patches (Figure 4.7, B1) which was previously stable without the presence of fibrosis (Figure 4.7, B2). In Person 6 however, simulations repeated with the presence of fibrosis in the LA showed either stable RDs forming macroscopic re-entry around the PVs (Figure 4.6E (ii)) or RDs anchored to a fibrotic region (Figure 4.6F (ii)) near the PV.

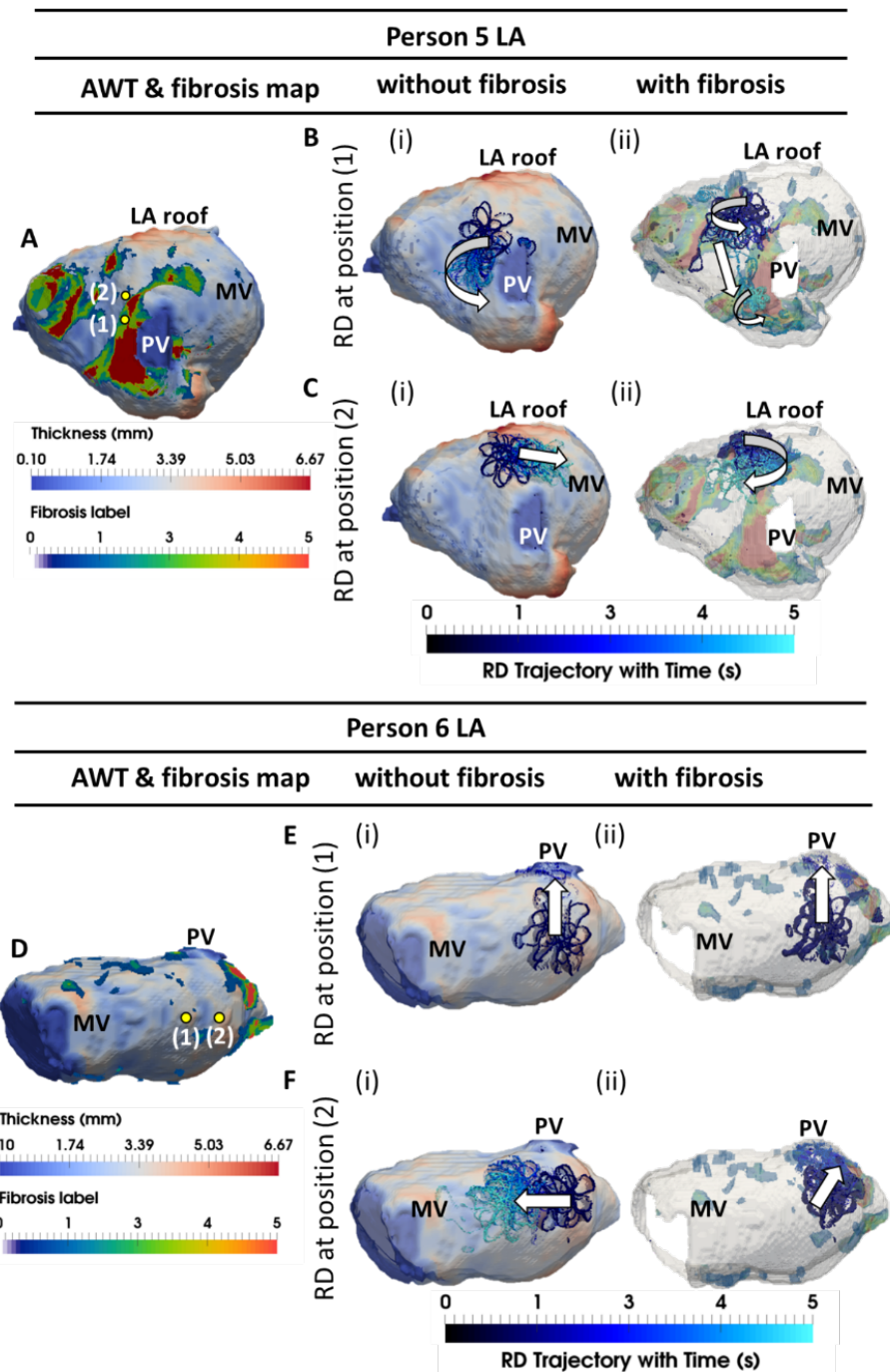


Figure 4.6: Competing effects of AWT and fibrosis in the LA. The RDs trajectories (blue) in the LA, obtained by initiating RDs at two locations (yellow dots), without and with the presence of fibrosis, are overlaid on the AWT map and fibrosis distribution (A & D), respectively, for Person 5 (top) and 6 (bottom). In Person 5 in the absence of fibrosis, RDs initiated at position 1 and 2 drifted towards the PVs (B (i)) and LA roof (C (i)), respectively. With additional fibrosis, RDs drifted from its initial location to a new location (B (ii)) for position 1 and anchored to the fibrotic patch (C (ii)) for position 2. In Person 6 without fibrosis, RDs initiated at positions 1 and 2 drifted towards the PVs (E (i)) and MV (F (i)), respectively. With fibrosis, RDs continued to drift towards the PVs (E (ii)) for position 1 but anchored to the fibrotic patch (F (ii)) for position 2. PV: Pulmonary vein, MV: Mitral valve.

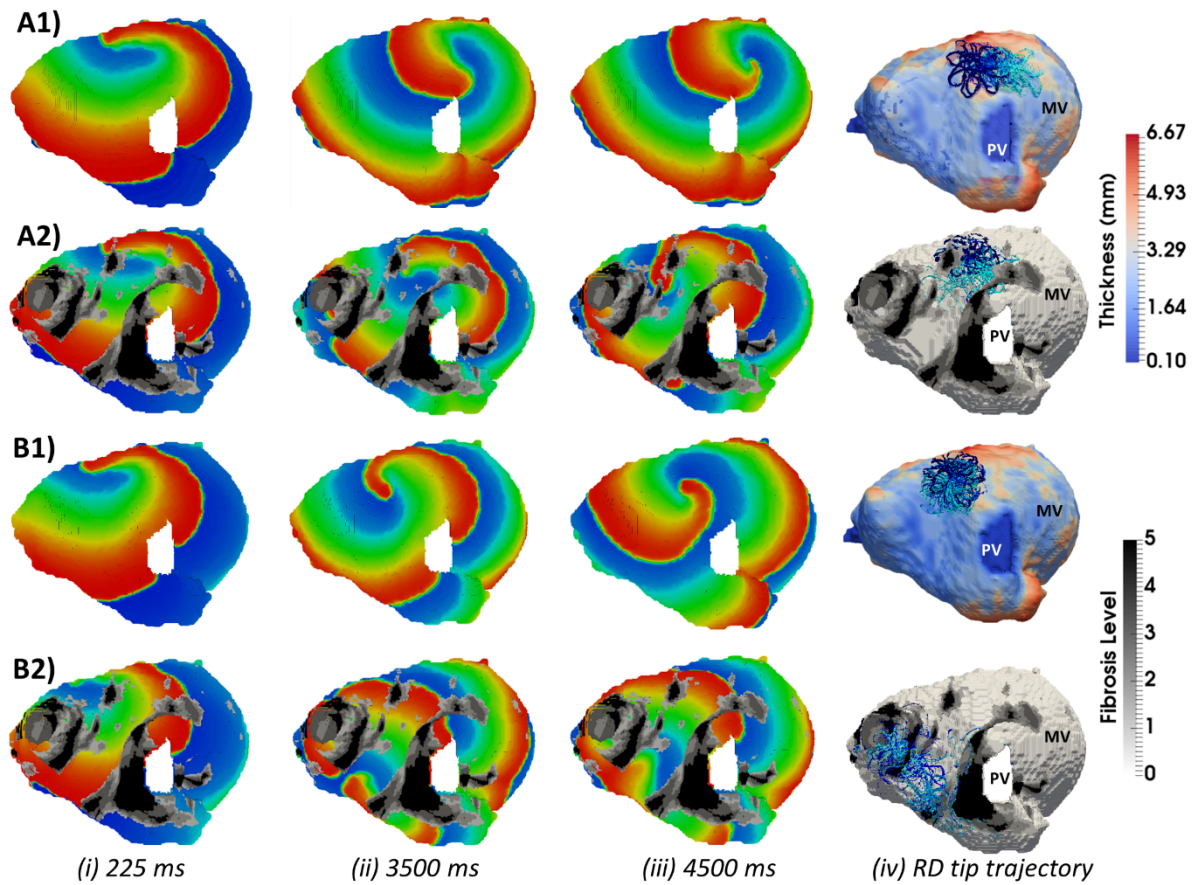


Figure 4.7: Competing effects of AWT and fibrosis in the LA. The voltage map for RD initiated at Position 2 and Position 3 are shown at different moments of time (i–iii) where red corresponds to excitation and blue to membrane potential closer to rest. Row 1 and 2 correspond to simulations without and with fibrosis, respectively. For each simulation, the RD tip trajectories (blue) are overlaid on their corresponding AWT and fibrosis map (iv). In simulations without fibrosis (at A1) RD drifts along the large AWT gradient at the LA roof and (at B2) RD stabilise near the PV. While in the presence of fibrosis (at A2), the same RD anchors to the fibrotic patch and (at B2), and the RD breakdown into multiple wavelets meandering between fibrotic patches.

4.5 Discussion

In this study, we used modelling and simulation to investigate the effect of AWT gradients on drift and anchoring of the RDs in both fibrotic and non-fibrotic atria for different patient-specific fibrosis distribution using MRI-based realistic 3D atrial geometries. To the best of our knowledge, this is the first study that compares the direct influence of AWT and fibrosis on the dynamics of RDs in realistic atrial geometries. We further elucidated how AWT gradients interact with fibrosis to determine locations of RDs. The results obtained from the RA and LA model simulations confirmed that drift direction and anchoring points of RDs are determined by the interplay of competing influences of the patient-specific AWT gradients and fibrosis.

4.5.1 Variation of AWT in subject-specific atrial geometries

In this study, image-based RA and LA geometries from 4 healthy volunteers and 2 paroxysmal AF patients were used to assess the link between RD activity and regions of large AWT gradients. The subject-specific AWT maps were computed in accordance with the average of nearest neighbour method, proposed by Varela et al. [195]. This specific method was chosen because of its simple implementation, low computational cost and its success to measure cortical thickness in the brain [209,210]. It is worth noting that there are other methods for calculating the thickness, for example, those based on the Laplace's equation [207], which may produce disparate thickness estimates, particularly in high-curvature regions.

In the RA, the AWT measurements showed a large inter- and intra-subject variability. In 2 of the RAs, the CT was comparatively thicker (4.75 ± 0.95 mm in the CT region against 2.91 ± 0.60 mm in the RA wall) than the surrounding atrial wall while in the others, such a distinction was absent (2.90 ± 1.04 mm against 2.45 ± 0.54 mm in the RA wall). The thickness values associated with the CT may be a result of its underlying morphology which is reported to vary among subjects depending on their gender, age, disease condition, etc. [194]. However, in the LA of two paroxysmal AF patients, the thickness of the atrial walls was roughly uniform, with an average of 2.96 ± 0.31 mm and 2.53 ± 1.20 mm, respectively. The atrial roof in one of the patients was thicker (4.77 ± 0.60 mm) compared to the rest of the atrial wall (2.96 ± 0.31 mm). This agrees with the LA roof measurements in AF patients [203]. The lack of AWT variability among our LA models could be due to our limited dataset of only 2 PAF patients. Further imaging studies are required to explore the AWT variability with AF disease type.

Furthermore, in the RA, the largest AWT is at the CT (6-8 mm). Given that the MRI resolution was 1.4 mm isotropic, this structure can be captured well. In the LA, the AWT gradient is largest at the LA-PV junction. However, these small gradients could lie below this MRI resolution. Hence, to avoid artefacts in this study the PV sleeves were removed.

4.5.2 Effect of subject-specific AWT on the RD dynamics

In Chapter 3, we used a simple 3D atrial slab model to conclude that regions with sharp AWT steps alter the excitability of the surrounding tissue and help in stabilizing RDs. In this study, we extended the same hypothesis to realistic atrial geometries. Our results in patient-specific atrial geometries are in agreement with our previous reported results in the 3D atrial slab.

In the RA without fibrosis, our results showed that RDs anchored to the CT region in subjects with a large AWT relative to the surrounding RA wall (Person 1 and 2 in Figure 4.4). This finding is in agreement with previous clinical [212] and modelling [213,214] studies, which have reported RD activity at the CT region. It is currently accepted that CT acts as a line of conduction block due to its high anisotropy owing to abrupt changes in fibre orientation which facilitate faster conduction from the sinus node to the inferior RA but blocks conduction in the posterior wall [215], making it a common site for initiation and anchoring of RDs during atrial arrhythmias. However, in addition to the transverse conduction block, the thickness of the CT has also been attributed to clinical incidences of RA flutter. Morita et al. [216] reported that the thickness, width and area measured using intracardiac echocardiography was significantly higher in patients with typical atrial flutter ($n = 12$) than with non-atrial flutter ($n = 13$). Moreover, Ohkubo et al. [217] reported a thicker and more continuous CT region in chronic atrial flutter patients compared to PAF patients. Despite evidence that AWT could play an important role in RA arrhythmias, the underlying mechanism by which AWT gradients could play a role in stabilising RDs at the CT hasn't been elucidated before. In our study, by directly using patient-specific RA models, we demonstrated that the source-sink effects associated with thickening (shown in Chapter 3) of the atrial myocardium at the CT, could facilitate anchoring of the RDs to this region. Sharp AWT gradients and abrupt changes in fibre orientation can act together to make CT a typical location and source of RA arrhythmias.

In the two RA with more homogeneous AWT (Person 3 and 4 in Figure 4.4), there was no clear link between the RD dynamics and specific AWT features. Instead, the direction of RD drift was always towards the tricuspid valve in the RA. Of note, in this study, we only evaluated the

CT thickness of volunteers, and further studies are needed to understand how electrical and structural remodelling alters the thickness of the CT region in AF patients and how that would alter the locations of re-entrant activity.

In the LA model without fibrosis, RDs were mostly localised in regions surrounding the PVs and MV openings (Figure 4.6 (i)). In the absence of structural features with large AWT gradient, the RD drift could be explained by the underlying curvature of the 3D atrial geometry [67,218]. The only exception was Person 5, where the RD anchored to a large AWT gradient at the LA roof. In fact, a recent clinical study by Kun et al. [203] reported a progressive increase of LA roof thickness with atrial remodelling and LA roof thickness > 3.10 mm to be a predictor of poor response to CA.

Our findings suggest that information from AWT may aid in designing personalised ablation strategies in patients whose atria are characterised by large variations in thickness. Patient MRI can be used to reconstruct 3D atrial structure and identify patient-specific areas of large AWT gradients and fibrosis prior to CA procedures. Models built based on such data can then predict the RD locations, and therefore aid in selecting the optimal CA strategy for a given patient.

4.5.3 Competing influence of subject-specific AWT and fibrosis on the RDs

Incorporating atrial fibrosis in the models changed the anchoring locations of the RDs in the patient-specific RA and LA geometries (Figure 4.5 and Figure 4.6, (ii)). In the RA with thick CT, the RDs anchored at regions between areas with a large AWT gradient (such as the CT region) and the local fibrotic patch. In RAs with less prominent CT, the RDs were instead permanently localised in regions surrounding the fibrotic patch (Figure 4.5, E(ii) & F(ii)). Hence, in atrial geometries with large gradients of AWT, the locations of the RDs stabilisation can be strongly influenced by both the presence of fibrosis, as predicted by previous studies [15,174] and also the AWT gradients. These results are in close agreement with our study performed in a 3D slab, where RDs were anchored between the AWT step and fibrotic patch.

The anchoring of the RD to these regions could be linked to two competing attractive influences from the slow conducting region of the fibrotic patch and source-sink mismatch from the large AWT gradient at the CT, which do not compensate each other exactly in these particular cases. However, if this balance is disturbed by either an increased thickness of the CT or a fibrotic patch located further away, the RD would have anchored instead to the other one. Therefore,

while evaluating the RD locations in atrial geometries with features of large AWT gradient, such as CT in the RA, patient-specific fibrosis distribution and AWT should be evaluated. Our results could explain why the correlation between LGE-derived fibrosis and RDs locations reported by Cochet et al. [13] was weaker in the RA than the LA. This may be explained by the higher variability in AWT in the RA compared to the LA, with the AWT gradients in the RA providing alternative anchoring locations for the RDs.

In the LA, simulations repeated with LGE-MRI-derived fibrotic patches clearly showed stabilisation of RDs near the patches in all patients. In the exceptional case of Person 5 (Figure 4.7, B2), with a high fibrosis burden, RDs were unstable and formed multiple wavelets meandering between fibrotic patches. These results may contribute to the understanding of why PVI is effective for paroxysmal AF patients with low fibrosis burden [219]. In paroxysmal AF, the number of RDs near the PVs is higher than the number of focal triggers [220] – the presence of RDs near the PVs, and therefore the success of PVI, in those patients may be explained by the lack of other anchoring locations, such as large AWT gradients or fibrotic patches. However, for AF patients with high fibrosis burden, the altered atrial substrates can result in the drift and multiplication of RDs in regions of slow conduction, such as the BZs of fibrotic tissue [174]. Therefore, assessment of patient-specific fibrosis distribution in the LA of persistent AF patients, facilitated by LGE-MRI, may assist in the prediction of RD locations. In the following part of this thesis, we will focus on the effects of patient-specific fibrosis distribution on the anchoring of RDs in the LA and the implication for AF therapy.

4.6 Limitations

In this study, we used a synthetic cylindrical fibrotic patch in the RA, which was a simplified representation of fibrotic patches of irregular geometry obtained from patient LGE-MRI. The lack of patient-specific RA fibrosis data in our study was due to routine pre-ablation LGE-MRI scans being restricted to the LA. Previous computational study by Zahid et al. [15] performed with patient-specific fibrosis distribution has linked RD behaviour to the heterogeneity fibrotic density. While a simple cylindrical patch in the RA was not patient-specific, using it enabled us to focus on the relative mechanistic influences of slow-conducting fibrotic tissue and AWT gradients, without considering additional complex effects of the fibrosis shape.

Another important limitation of this study is related to the reconstruction of fibrosis from LGE-MRI which has been discussed in Chapter 2, Section 2.4.2.2. Although these limitations need

to be carefully considered when designing a personalized MRI-based CA therapy, we believe they do not impact the main mechanistic finding of our study – that RDs anchor to regions with large AWT gradients and fibrotic structures.

In our study, fibrosis was modelled as regions of progressively slow conduction linked with LGE-MRI intensity. The LGE-MRI threshold of 1.08 IIR (level 1) and 1.24 IIR (level 5) was obtained from previous studies validated by electro-anatomical mapping data [87,88], but the IIR threshold values for splitting the border zone into levels 1 to 4 was not validated due to lack of experimental data. However, the correlation between decrease in conduction velocity and increase in IIR has been reported [177]. Therefore, our approach of gradually decreasing CV across fibrosis levels 0 to 5 is in agreement with patient studies. Recent studies have also shown that additional small effects of fibroblast-myocyte coupling [174] and paracrine effects [187] could also influence the RD stabilisation. However, data on such effects in human are unavailable, and modification of the model parameters based on ex-vivo animal data can produce results that are inconsistent with clinical data [187], and such effects were not considered in this study. Moreover, in this study we have only considered fully transmural fibrosis. Ex-vivo imaging studies show intramural fibrosis could affect the RD dynamics and facilitate epicardial-endocardial dissociation [221]. In future studies, intramural fibrosis should be incorporated to analyse its effects on epicardial-endocardial dissociation in AF [58,59,222]. However, atrial walls are very thin (< 3mm), which makes non-invasive imaging of transmural fibrosis challenging due to partial volume effects.

Finally, this study was conducted with a small dataset of 6 atrial models. In future, the image-based simulation pipeline developed in this chapter could be extended to include large number of patients and healthy volunteers of both genders. The other limitations consistent with work presented in other Chapters, and possible ways to address them in the future are summarised in Chapter 7.

4.7 Conclusions

This study (i) elucidated the role of AWT as a factor strongly influencing the RD dynamics and a marker for RD locations in the patient's atria and (ii) compared the AWT effects with the respective effects of fibrosis. In the RA, RDs stabilised around structural features with large AWT gradients, while the addition of fibrotic patches provided an alternative attractor for the RDs. In the LA, which had more uniform AWT distributions, RD locations were determined

by the distribution of fibrotic patches or by anatomical features such as the PVs. These findings corroborate our hypothesis that anchoring locations of RDs are dependent on the relative influence of gradients in AWT and fibrosis, and suggests the non-invasive assessment of AWT and fibrosis using MRI may inform clinical interventions in AF patients.

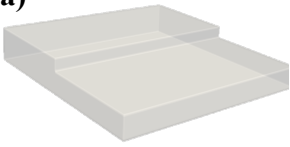
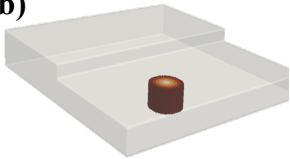
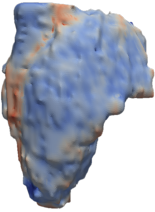
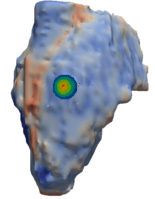
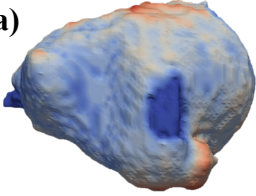
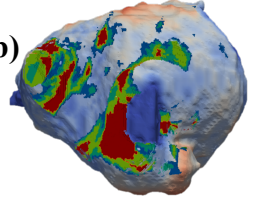
	Geometry	Thickness	Fibrosis	RD Outcome
Study 1: 3D Atrial Slab	a) 	✓ Height of the step	✗ None	<ul style="list-style-type: none"> • RDs drift and anchor to the step. • The sensitivity of the RD to the step increased with increase in the step height.
	b) 	✓ Height of the step	✓ Cylindrical fibrotic patch	<ul style="list-style-type: none"> • RDs anchor between the step and fibrotic patch. • The relative locations of the step and the fibrotic patch together influences the dynamics of the RDs.
Study 2: Right Atrium (RA)	a) 	✓ AWT for the RA geometry	✗ None	<ul style="list-style-type: none"> • RDs anchor to the CT region only in RA with large thickness gradient at the CT.
	b) 	✓ AWT for the RA geometry	✓ Spherical fibrotic patch	<ul style="list-style-type: none"> • RDs stabilise either at the CT region or the fibrotic patch, or the region between them, depending on their initial distance from these features.
Study 3: Left Atrium (LA)	a) 	✓ AWT for the LA geometry	✗ None	<ul style="list-style-type: none"> • RDs stabilise either near the PVs or the mitral valve. No effect of thickness noticed, since AWT is near-uniform.
	b) 	✓ AWT for the LA geometry	✓ Fibrosis from LGE-MRI	<ul style="list-style-type: none"> • RDs either anchor to or multiply into multiple RDs at the fibrotic patches.

Table 4.1: Effects of AWT and fibrosis of the RD dynamics. The table summarises the key results obtained from the study presented in Chapter 3 and 4 which were aimed at investigating the competing influence of AWT gradients and fibrosis on RDs sustaining AF.

Chapter 5

Predicting Locations of RDs from Patient-Specific Distribution of Fibrosis in the LA

5.1 Section Outline

This chapter aims to use image-derived patient-specific LA models to explore RD stabilisation in fibrotic regions and generate maps of RD locations that can be targeted by therapy (Figure 5.1). The motivation behind investigating the RD locations based on patient-specific fibrosis distribution is summarised in Section 5.2, and the steps involved in the model construction and simulations are discussed in Section 5.3. The results for the simulation study are presented in Section 5.4 and analysed in Section 5.5, dissecting the effects of patient-specific fibrosis distribution and burden on RDs and comparing them with competing prior studies. Finally, the clinical impact and the main findings of the chapter are summarised in Section 5.6.

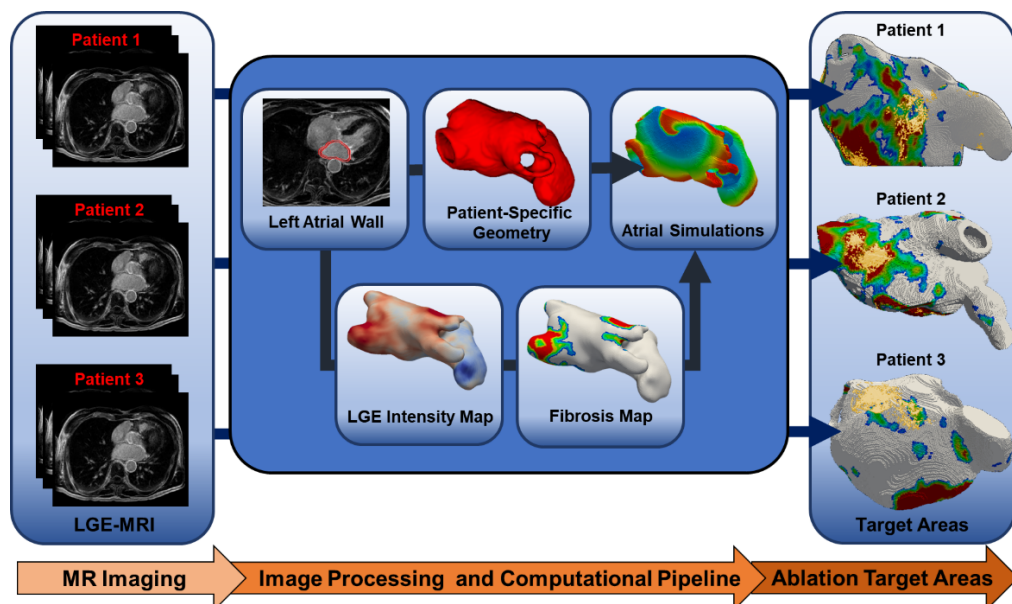


Figure 5.1: A schematic image of the chapter outline

5.2 Introduction and Motivation

Catheter Ablation (CA) is a well-established strategy for the restoration of sinus rhythm in AF patients who do not respond well to anti-arrhythmic drugs, with success rates of up to 70% in patients with episodes of AF lasting less than 1 week (paroxysmal AF or PAF). The widely accepted CA strategy to restore sinus rhythm is the electrical isolation of pulmonary vein (PV) sleeves in the left atrium (LA), which are believed to be the primary substrate for the generation of the ectopic beats and/or anchoring of re-entrant drivers (RDs) responsible for triggering and sustaining AF in the LA [6–8]. However, about 30% of AF patients are asymptomatic, which leads to delayed diagnosis and the development of persistent AF (PsAF). In these patients, the success rate with CA drops to 42% [11], often requiring additional ablation procedures.

A potential factor for the failure of CA, specifically in PsAF patients, could be the presence of high degrees of electrophysiological and structural remodelling, notably the development of fibrosis throughout the LA during the progression from PAF to PsAF [77,81,85,223]. As discussed in Chapter 2 (Section 0), fibrotic regions in the atria slow down or completely block propagation of electrical excitation waves, thus providing a substrate for RDs sustaining AF [75,221,224] beyond the PVs. This can explain the existence of multiple RDs far from the PV region in PsAF patients [55,114]. In these patients, despite advances in CA strategies – that either target the AF substrate by applying additional linear CA lesions in the LA roof and MV, or try to eliminate RDs by utilizing complex fractionated atrial electrograms (CFAE), focal and impulse rotor modulation (FIRM) or electrocardiographic imaging (ECGI) – the long-term therapy success is limited [106,117] (see also in Chapter 2, Section 2.4.3.3). This can be explained by the highly empirical nature of CA therapy, which targets atrial regions without knowledge of the underlying arrhythmogenic mechanisms and patient-specific nature of AF substrate.

The extent of fibrosis quantified from LGE-MR images is known to be an important predictor of post-ablation recurrence [81]. Recent clinical studies have reported that low-voltage areas, identified from atrial tissue mapping and also associated with the presence of fibrosis, can be directly targeted by CA to improve patient outcomes [100,102,123,126]. However, in cases where fibrosis is extensive, particularly in patients with a high fibrotic burden (FB), creating ablation lesions around/over the entire fibrotic region can result in substantial damage to the atria. Therefore, despite the ability of imaging methods to identify and quantify the extent and

location of fibrosis in the atria, there exists a knowledge gap regarding optimal ways to target fibrotic regions during CA in a patient-specific manner.

Recent computational studies of patient-specific atrial models, which have been based on the reconstruction of fibrosis from LGE-MRI, have provided the first insights into the role of fibrosis in the dynamics of electrical RDs sustaining AF [14,15,225]. In particular, patient-specific models have suggested that regions with a high heterogeneity in fibrotic density (the fibrosis border zone or BZ) are common anchoring sites for the RDs sustaining AF [15,174]. Targeting these fibrotic regions by CA procedures may, therefore, improve their outcomes. These computational model predictions have been validated in a recent clinical study that linked the patient-specific LGE areas with locations of RDs recorded using ECGI [13]. Moreover, very recent modelling studies performed in parallel by Boyle et al. [226,227] have indicated an 83% overlap between RDs predicted by patient-specific biophysical models of the atria and the respective locations found with FIRM and a moderate agreement with ECGI. In addition to shedding light into the role of fibrosis in the RD dynamics, these studies pave the way for identification of patient-specific RDs locations from image-based 3D atrial models.

Furthermore, Costa et al. [180], Vigmond et al. [181] and Tanaka et al. [182] have also introduced micro-structural nonconductive regions (percolation or edge-splitting) with various sizes throughout atrial tissue. These studies provided insights into the effect of fibrosis at the microstructure level and allowed mimicking fractionation of atrial electrograms observed at arrhythmogenic sites using EAM. Although the effects of fibrosis at this micro-scale are an important contributor to AF arrhythmogenesis, the inherent limitations of LGE-MRI prevent it from identifying such fine details [183]. The precision in imaging of atrial fibrosis with currently available LGE-MRI technologies remains limited. The imaging resolution only allows for capturing large (or clusters of small) fibrotic patches, but not for distinguishing between different types of fibrosis. Histological evidence points to the presence of such types as diffuse and interstitial fibrosis regions in the atrial myocardium, which cannot be captured reliably using MRI. Therefore, in patient-specific atrial models reconstructed from LGE-MRI typically include large, continuous fibrotic patches.

In this chapter, we used patient-specific atrial models to identify optimal target areas for CA by exploring the links between MRI-derived fibrosis distributions and RD locations. Specifically, 3D left atrial (LA) models based on patient LGE-MRI were used to achieve the following aims:

1) explore the dynamics of RD stabilisation in patient-specific fibrotic areas and 2) generate personalised RD location maps – potential ablation target areas – that identify the regions with the highest probability of RDs. The findings were correlated with the MRI-based Utah fibrosis score [228]. The first aim can help clarify how different characteristics of fibrotic distributions can affect the RD dynamics, while the second may in the longer-term help predict patient-specific CA targets. This will eliminate the need of extensive atrial voltage mapping and ablation in a patient, thus facilitating faster, safer and more efficient therapy.

5.3 Methods

5.3.1 Atrial electrophysiology model

The atrial simulations were performed using the same framework as described in Chapter 4.

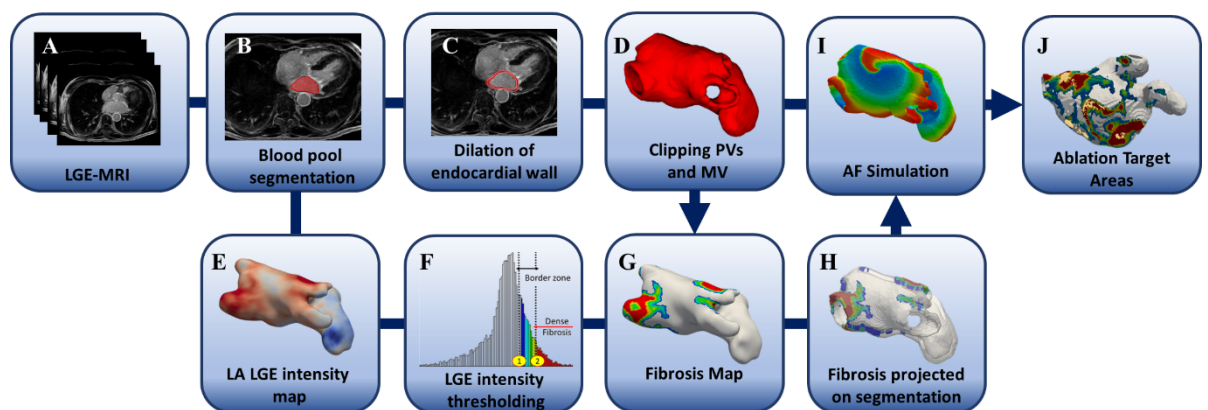


Figure 5.2: Workflow for identifying patient-specific target areas with the highest probability of harbouring RDs. The personalised left atrial models are generated by segmentation of patient-specific LA geometry and fibrotic regions from LGE-MRI scans.

5.3.2 3D patient-specific LA models

The patient-specific LA geometries and fibrosis distribution were reconstructed from LGE-MRI to generate patient-specific LA models. RDs were initiated at multiple (8-12) locations in each LA model using a cross field protocol and their tip was tracked for 6s. The locations where each RD stabilised after 6s was identified and labelled as being part of: (i) healthy tissue, (ii) PV region or (iii) fibrotic patches. Each tissue voxel was additionally assigned a probability value, by investigating how many times it was visited by an RD tip over the course of the simulation. The most likely locations of RDs are expected to be prime targets for CA and were thus defined as the target areas (see workflow in Figure 5.2). Note that the RDs which anchored

to the PV openings, which resulted from clipping of the PVs near their ostia and were non-physiological, were excluded from the definition of the target areas.

5.3.2.1 Reconstruction of patient-specific LA geometry and fibrosis distribution from LGE MRI

Two PsAF and four PAF patients (see Table 5.1) were imaged under ethical approval and following written informed consent as a part of the study by Chubb et al. [229]. All imaging was performed on a 1.5T Phillips MRI scanner and included a LGE-MRI sequence: a 3D inversion recovery spoiled gradient echo, acquired 20-30 min after the administration of the extracellular gadolinium-based contrast agent Gadovist (Bayer Healthcare Pharmaceuticals). Images were acquired using cardiac and respiratory gating, with a spatial resolution of $1.3 \times 1.3 \times 4 \text{ mm}^3$. Further information about the used LGE sequence can be found in [229]. Moreover, the 3D LGE-MRI signal intensity was assessed following the approach of Chubb et al. [229], where a single signal intensity value was assigned to each point on the endocardial surface by using a mean intensity projection (MIP) technique.

Patient	AF	Age	Gender	% Fibrosis	Utah Score
P1	PsAF	71	Male	39	4
P2	PsAF	65	Male	29	3
P3	PAF	72	Male	25	3
P4	PAF	57	Male	22	3
P5	PAF	58	Male	16	2
P6	PAF	53	Male	11	2

Table 5.1: Characteristics of the 6 AF patients whose LA models were used in the study. PsAF: persistent AF, PAR: paroxysmal AF. The patients have been labelled 1 to 6 (column 1), in the decreasing order of their fibrosis burden (column 5) and assigned a Utah score (column 6) in accordance with [81].

The LA geometries were obtained by manual segmentation of the LGE MR images (Figure 5.2, A) MITK [230], where the endocardial wall was identified by segmenting the LA blood pool (Figure 5.2, B). The epicardial wall was generated by dilating the endocardial wall by 3 mm (Figure 5.2, C), which is reported as the average LA wall thickness in AF patients [195]. The PV sleeves and MV were removed and the segmented image was resampled to a resolution of 0.3 mm to generate patient-specific LA geometries, to be used in the finite difference electrophysiology simulations (Figure 5.2, D).

The patient-specific fibrosis distribution in the LA of the AF patient was generated based on the image intensity of the LGE-MRI data (Figure 5.2, E-G) similar to the method presented in Chapter 4, Section 4.3.3.2. Briefly, a voxel was considered to be part of a fibrotic patch when the ratio of the voxel intensity to the mean blood pool intensity, the image intensity ratio (IIR), exceeded an empirical threshold set by [87,88], as described previously in Chapter 4, Section 4.3.3.2. An example of fibrosis quantification is shown in Figure 5.3A, B for Patient 2 (high fibrosis) and Patient 6 (low fibrosis), respectively. Voxels were labelled as being healthy tissue ($IIR < 1.08$, white region of the histogram in Table 5.2), dense fibrosis ($IIR > 1.24$, red region of the histogram) and the region around the dense fibrotic patch corresponds to the BZ ($1.08 < IIR < 1.24$, histogram with colours blue to yellow). The fibrosis maps obtained by intensity thresholding of LGE-MRI data for all the 6 AF patients are shown in Figure 5.4. These fibrotic regions were registered (Paraview, Kitware, Clifton Park, NY, USA) and subsequently projected onto the LA geometry (Matlab, Mathworks, Natick MA, USA), such that the fibrosis patches were fully transmural (Figure 5.2H).

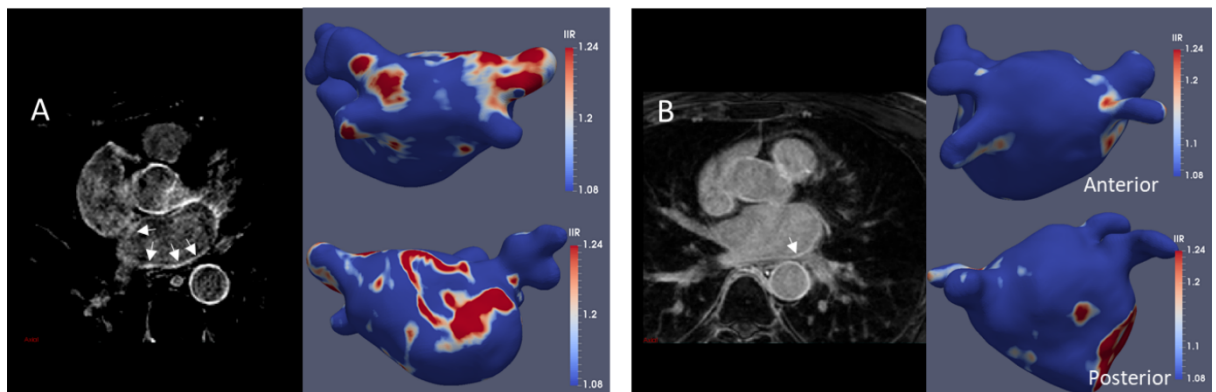


Figure 5.3: Left atrial fibrosis quantification from LGE-MRI. (A) Highly fibrotic LA of Patient 2 and (B) low fibrotic LA of Patient 6, with atrial shell threshold set at an IIR of 1.08 and 1.24. In the LGE images on the left of panel A and B, the white arrows point to regions of enhanced signal intensity.

The 6 patients was classified into one of the following four Utah categories [81,228] described previously in Chapter 2, Section 2.4.3.3, depending on their relative fibrosis burden (FB): Utah 1 ($FB \leq 5\%$), Utah 2 ($5\% < FB \leq 20\%$), Utah 3 ($20\% < FB \leq 35\%$) or Utah 4 ($FB > 35\%$). As summarised in Table 5.2, the patients were labelled 1 to 6 in decreasing order of their FB.

5.3.2.2 Fibrosis implementation in the computational LA models

To study how the RDs interact with fibrotic regions and to design a novel tool for identifying patient-specific regions where they stabilise, we used 3D atrial models with patchy fibrosis represented as regions of slow conduction [174]. Fukomuto et al. [177], performed LGE imaging and LA activation mapping during sinus rhythm in 22 patients before PVI and reported an association between CV and IIR (0.20 m/s decrease in CV per unit increase in IIR, $P < 0.001$). In the fibrotic tissue therefore, the decrease in CV was set proportional to the recorded LGE-MRI intensity. This was achieved by altering the diffusion coefficient, D , in these regions using the same method as that in Chapter 4. Briefly, healthy tissue with an IIR < 1.08 corresponded to $D = 0.1 \text{ mm}^2/\text{ms}$, dense fibrotic tissue with IIR > 1.24 to $D = 0.017 \text{ mm}^2/\text{ms}$ and the fibrotic BZ with $1.08 < \text{IIR} < 1.24$ to intermediate values of D calculated via linear interpolation between 0.1 and $0.017 \text{ mm}^2/\text{ms}$ (Table 5.2). In control models without fibrosis, the patient-specific LA geometry was preserved, but D was set to $0.1 \text{ mm}^2/\text{ms}$ for all patients.

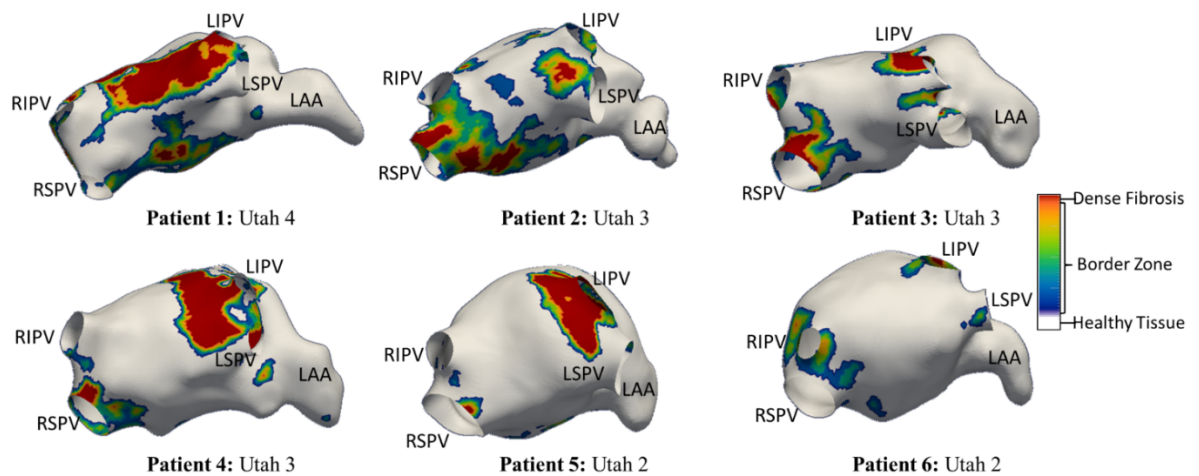


Figure 5.4: Patient-specific fibrosis distribution in 6 AF patients with Utah scores from 2 to 4. The fibrotic regions are colour-coded to show dense fibrotic tissue (red) surrounded by a BZ of intermediate properties. The healthy atrium is shown in white. LIPV: left Inferior PV, RIPV: Right Inferior PV, LSPV: left Superior PV, RSPV: Right Superior PV and LAA: Left Atrial Appendage.

5.3.3 AF simulation protocol and data analysis

Each patient-specific LA model was paced 7 times at a basic cycle length (BCL) of 130 ms at locations near the PVs (Figure 5.5, P1). A plane wave was initiated in 20 ms after the last ectopic beat (Figure 5.5, P2). The interaction between the plane wave and the ectopic beats allowed for the generation of RDs. By varying the pacing site, the direction of the plane wave

and the time interval between them, RDs were initiated in 8-12 different locations in each LA model. In each simulation, we: (i) tracked the RD tips for a duration of 6 s (using method described in Chapter 3), (ii) identified the regions where they were localised in the last 1 s of the simulation, and (iii) constructed a RD tip frequency map by recording the number of times each tissue voxel was visited by the RD tips over the entire course of the simulation. In all the cases, the RDs stabilised within 6s of the start of the simulations as illustrated in Figure 5.8 (A-B) and Figure 5.9. Therefore, 6s was chosen as the upper limit for identifying the RD locations.

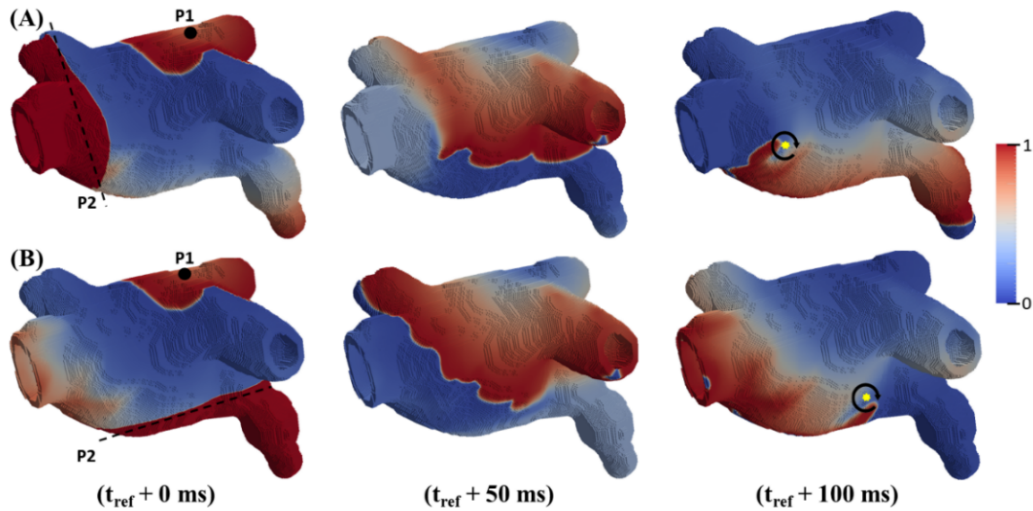


Figure 5.5: AF initiation protocol. Two examples of RDs initiated using the cross-filed protocol is presented in rows, (A) and (B), respectively. Here in every simulation, P1 is the location of the ectopic beat near the PVs and P2 is the location of the plane wave. It is the interaction between P1 and P2 that results in the formation of RDs.

For each patient, all the RD tip frequency maps obtained in the AF simulations were combined to construct patient-specific RD probability maps, showing the relative frequency with which, each voxel was visited by the RDs (see Figure 5.6). The normalised tip probability maps were thresholded to mark locations with the normalised probability over 0.2 as target areas. The simulations and the analysis process were performed in all the 6 LA models with and without the presence of fibrotic tissue. The target areas identified from both the cases were compared using the Dice score [231], a standard metric for measuring the degree of spatial overlap between two datasets, A and B using the following equation 5.2.

$$dice(A, B) = \frac{2 * |A \cap B|}{|A| + |B|} \quad (5.2)$$

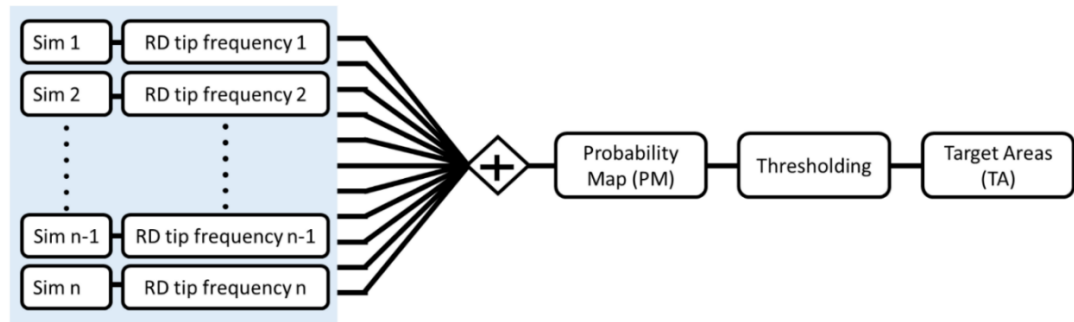


Figure 5.6: The pipeline for identifying target areas from the RD probability map. Sim: simulation

FIBROSIS MODELLING

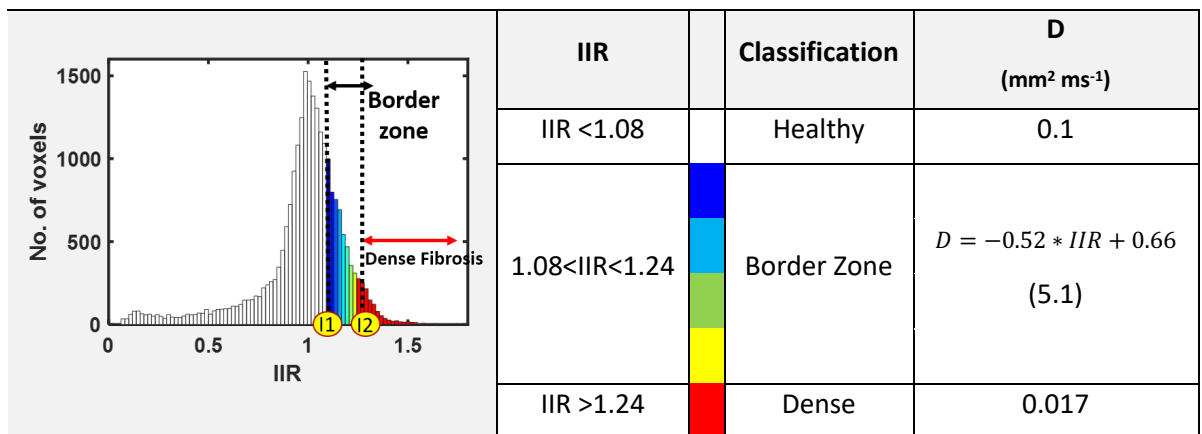


Table 5.2: Segmentation and modelling of fibrosis. Labelling of voxels in the LA patient geometries according to their LGE-MRI intensity ratio (IIR) relative to the blood pool. Voxels with $IIR > 1.24$ are part of a fibrotic core. $IIR < 1.08$ corresponds to healthy tissue and the intermediate values of IIR form a fibrotic border zone with intermediate properties [87,88].

5.4 Results

5.4.1 Patient-specific fibrosis distribution in 3D atrial models

The LGE-MR image intensity-based reconstruction yielded different fibrosis distributions in all 6 AF patients, as shown in Figure 5.4. Large variations in the extent and severity of fibrosis were observed across the LA models (Table 5.3). Amongst the PsAF patients, P1 had the highest FB of 39% and was classified into Utah 4 category, and P2 with 29% FB was in Utah 3 category. In the PAF patients, P3 and P4 with a moderate FB of 25% and 22%, respectively, were in Utah 3 category; P5 and P6 with mild FB were in Utah 2 category.

Patient	% FB	% Volume of largest patch	% FB of PVs	% FB of LA wall	% Volume* of dense tissue
P1	39	37.95	28.84	71.16	12.98
P2	29	18.27	42.86	57.14	6.38
P3	25	16.63	35.31	64.69	6.37
P4	22	8.54	63.28	36.82	8.18
P5	16	6.42	42.10	52.10	6.48
P6	11	4.08	64.53	35.47	0.24

Table 5.3: Properties of patient-specific fibrosis distributions. The size of the primary fibrotic patch decreases with the fibrotic burden (FB).

In addition to differences in severity, a large variation in the size distribution of the fibrotic patches was also observed across all patient-specific LA models, as summarised in Table 5.3. These estimates suggested the size of the largest fibrotic patch recorded per patient increased with increasing the overall FB. Moreover, each individual patient LA was characterised by the presence of a primary fibrotic patch with a volume significantly greater than the secondary surrounding patches. The distribution of fibrotic regions between the PV regions and remaining LA wall was recorded across the patient-specific LA models. In P1 (Utah 4), P2 and P3 (both Utah 3) with the highest FB, the majority of the fibrotic regions were at the LA wall and as the FB decreased the fibrotic regions were mostly located in the PV region in P4 – 6 (Table 5.3).

5.4.2 Atrial fibrosis influences the distribution of RDs across patient-specific LA models

In the patient-specific LA models, AF was successfully initiated in all 6 patients using the cross-field protocol. The RD initiation protocol was applied to each patient-specific LA model, either

with or without fibrosis, and resulted in the formation of either 1-2 RDs in the first 1s of simulation. In the following 5s, these RDs meandered and eventually stabilised at distinctive locations in the atrial wall, which were dependent on the patient-specific fibrosis distribution and geometry. The choice of a total of 6s for the simulation was used to allow sufficient time for the transition to occur from the transient drifting of the RDs to their stable localization. To get a better understanding of how the distribution of RDs across the patient-specific geometries were affected by the overall FB, we classified the RDs in every model into 3 groups according to the region where they stabilised in the last 1s of the 6s-long simulations. The outcomes of this classification are summarised in Figure 5.7 with a bar plot showing the % of the total RDs anchored to: (i) fibrotic patch in blue, (ii) PVs in orange and (iii) healthy non-PV tissue in grey for all 6 patient-specific LA models with (A) and without fibrosis (B).

Persistent AF Patients (Utah 4 & 3: $FB > 25\%$): In these patients (Figure 5.7A, Patient 1 and 2), the RDs stabilised primarily at fibrotic regions (P1: 56%, P2: 79%), compared to lower probabilities of stabilisation in the PVs region (P1: 17%, P2: 21%). However, when the same LA simulations were repeated for these patients without fibrosis, the RDs stabilised primarily at the PVs (Figure 5.7B, P1: 65%, P2: 79%). This suggests that in these PsAF patients with very high FB, the presence of large quantities of slow conducting fibrotic tissue influenced the RD locations, facilitating their anchoring to the fibrotic patches instead of the PVs.

Paroxysmal AF Patients (Utah 3: $20\% < FB < 25\%$): In this category of AF patients with intermediate levels of fibrosis (Patients 3 and 4), the RDs stabilised with similar probability in all three regions (Figure 5.7A, P3: 38%, P4: 48% at the PVs). Comparing the distribution of RDs across different regions in simulation with (Figure 5.7A) and without fibrosis (Figure 5.7B) suggests that fibrosis around the PVs in these patients facilitated anchoring of RDs to the PVs. Moreover, despite having similar FB, the variation in distribution of the RDs across the patient-specific LA models (Figure 5.7 A, P3 & P4) can be explained by the difference in spatial distribution and sizes of fibrotic patches in the respective LA models.

Paroxysmal AF Patients (Utah 2: $FB < 20\%$): In this category of AF patients with the lowest FB (Figure 5.7A, Patients 5 and 6), the number of RDs anchoring to PVs (P5: 57%, P6: 35%) was higher than that in the fibrotic regions (P5: 25%, P6: 6%). This agrees with clinical observations that in PAF patients with lower FB, RDs are likely to be located at the PVs. In the

absence of strong fibrosis effects, the distributions of RDs across different region in simulation with (Figure 5.7A) and without fibrosis (Figure 5.7B) showed similar trends.

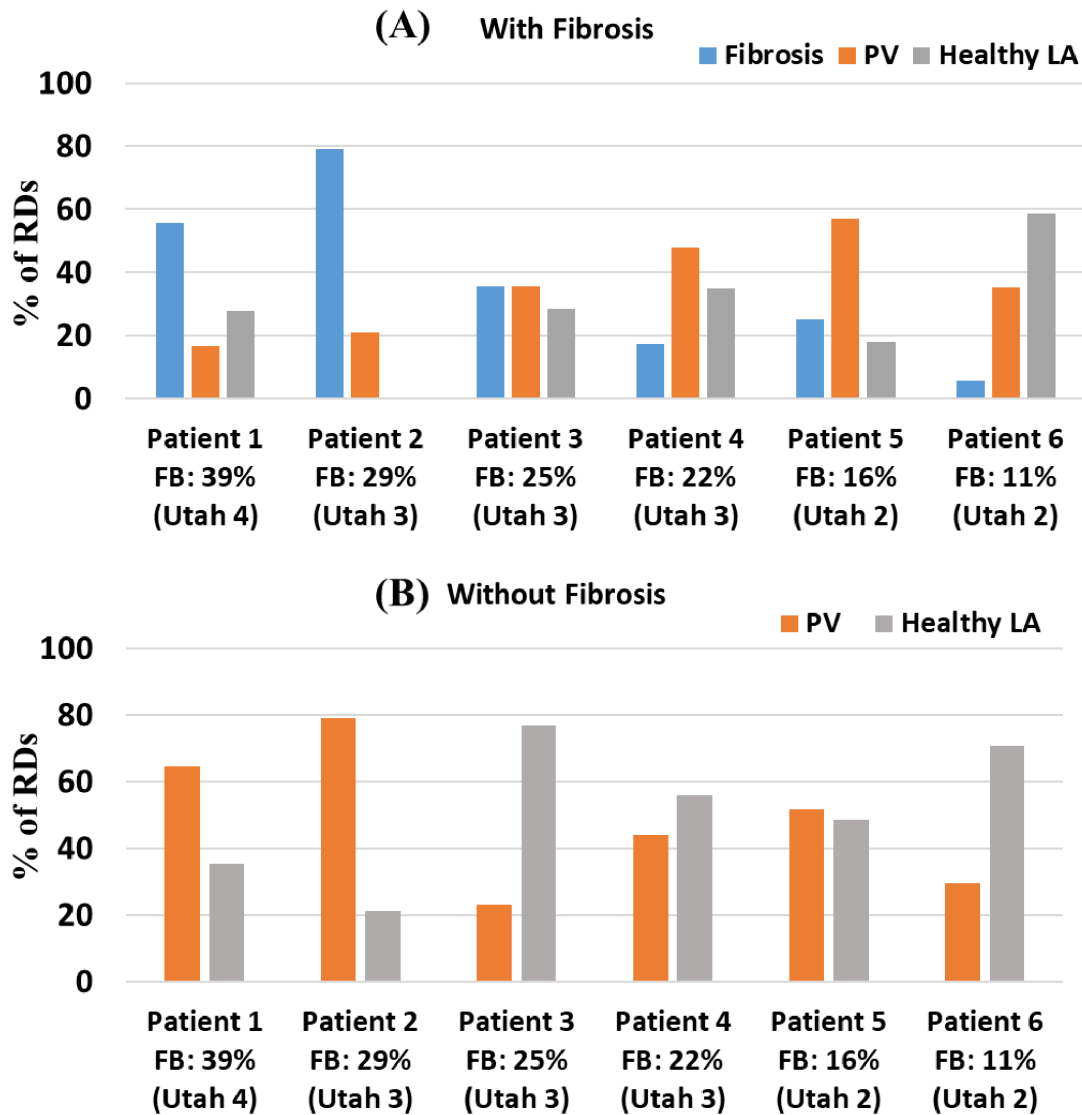


Figure 5.7: Regions of RD stabilisation in patient-specific LA models. The image shows bar chart with percentage of RDs found in different LA regions (blue: fibrosis, orange: PVs and grey: healthy LA tissue) after 6s of the simulation in the 6 patient-specific LA models with (A) and without fibrosis (B). A) In Utah 2 patients, the primary location for the RDs is the PVs. In Utah 3 patients, RDs are distributed between fibrotic regions and the PVs. In Utah 4 patients with severe fibrosis, the primary location of RDs are the fibrotic regions. FB: fibrotic burden.

5.4.3 Patient-specific fibrosis determines the RD anchoring locations

In the previous section, we reported the overall distribution of RDs across different regions of the atrial wall in the patient-specific LA models and found that RDs were most likely to anchor at fibrotic regions in patients with FB from Utah category 3 or 4. However, the basic knowledge

that RDs are present at fibrotic regions is insufficient to guide CA – we need to pinpoint the exact locations within the fibrotic patches where the RDs are localised. This warrants a detailed analysis of the mechanisms that affect RDs anchoring to specific fibrotic patches.

To illustrate the concept, Figure 5.8A, B shows voltage maps and RD tip locations in a simulation of AF maintained by a single RD anchored to a fibrotic patch in the anterior LA wall. After the initial meandering, the RD tip (shown by a yellow dot) remained at a specific location inside the fibrotic patch for the entire duration of the simulation. Similar RD behaviour has been observed in other patients. However, the specific location where the RDs anchored to fibrotic regions was dependent on the size and distribution of fibrotic patches. Moreover, the same protocol when repeated in the absence of fibrosis resulted in formations of RDs that either remained stabilised at the region where they were initiated (as in Figure 5.8C, D) or they drifted towards the PVs and MV, under the influence of the underlying atrial curvature.

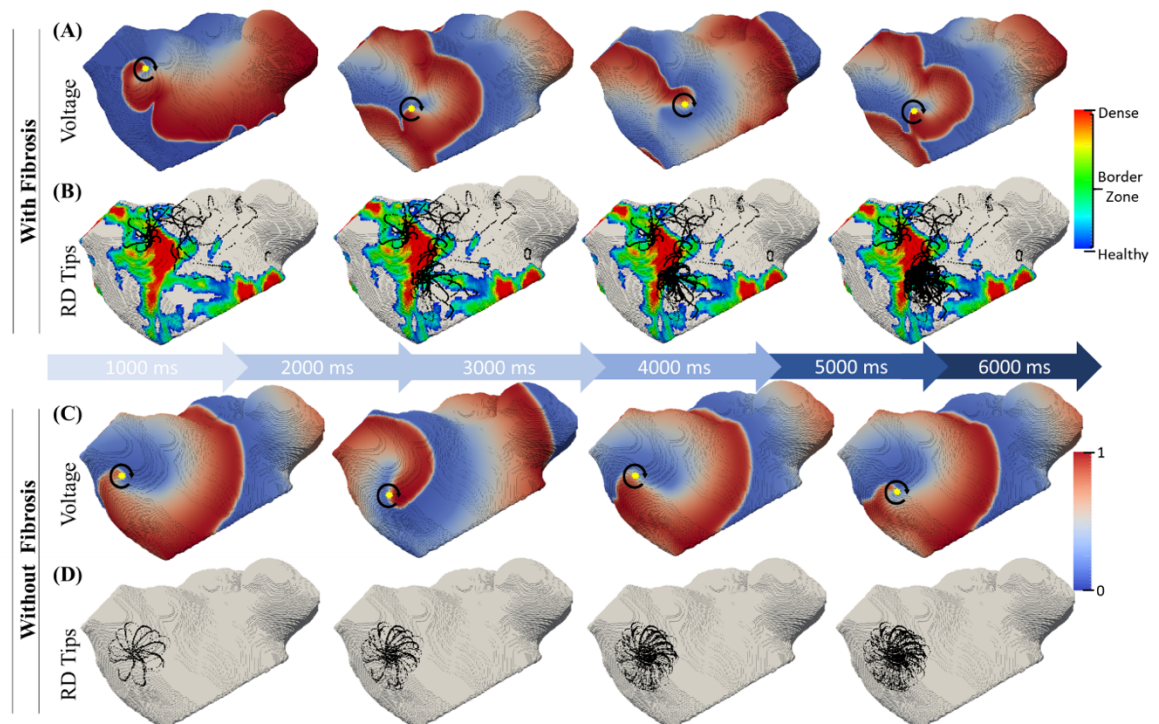


Figure 5.8: The effect of fibrosis on the RD dynamics in a patient-specific LA model. A & C: the colour-coded voltage maps (normalised, so that 0 is rest state and 1 is maximal activation) in the LA of Patient 3 over 6s of simulation with the yellow dot indicating the RD tip and the arrow pointing to the direction of rotation. B & D: the corresponding RD trajectories (grey-black) superimposed on the fibrosis distribution. In simulations with fibrosis (A-B), the primary RD drifts around and across the fibrotic patch within the first 1s and thereafter stabilises at a distinctive location within the fibrotic BZ. However, in the same simulation without fibrosis (C-D), the primary RD remains at the location of its initiation.

Further examples of RD trajectories under the influence of fibrotic patches for each of 6 patients are presented in Figure 5.9. In Patient 1 from Utah 4 category, more complex activation patterns in the voltage map were observed in addition to anchoring of RDs to fibrotic patches (Figure 5.9, A1). This was due to breakdown of the initial RD into three new ones, which all stabilised at various locations around the largest fibrotic patch and surrounding BZ. In Patients 2, 3 and 4 from Utah 3, the RDs stabilised at distinctive regions of fibrotic patches (Figure 5.9, A2-A4 and B2-B4). In Patients 5 and 6 from Utah 2, fibrotic patches were much smaller compared to those in patients from Utah 3 and 4. Hence, the RDs often stabilised between two small fibrotic patches (Figure 5.9, A5 and B6), and if fibrotic patches were in regions around the PVs (Figure 5.9, A6 and B5), fibrotic tissue aided the RDs moving towards and anchoring to the PV opening. All these examples highlight that patient-specific characteristics of fibrotic patches play a crucial role in detaining the dynamics and ultimate anchoring locations of RDs.

The dynamic nature of the RD tip trajectory makes it harder to analyse the exact anchoring location. However, the tip probability map, unique to a patient-specific set of simulations, gives an in-depth view of the specific anchoring locations in each case. Sample RD tip probability maps for some of the simulations from Figure 5.9 can be found in Appendix (Figure A. 7).

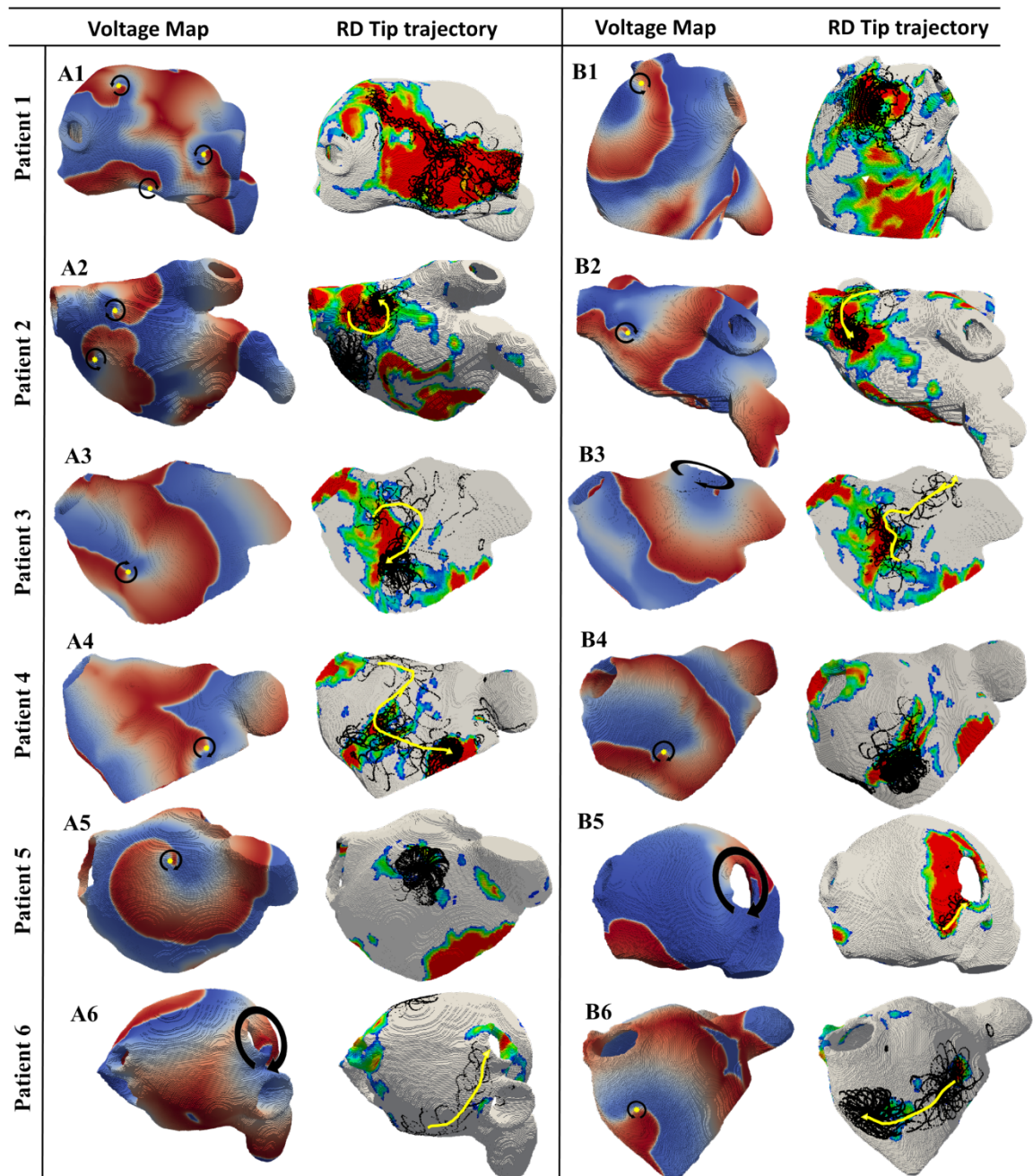


Figure 5.9: The anchoring of RDs to fibrotic patches in patient-specific LA models. For all the 6 AF patients (rows), sections A and B show the AF simulation outcomes for 2 different RD initiation sites. In each section, on the left are the colour-coded voltage maps and on the right, the respective RD trajectories (black) superimposed on the fibrosis distributions. The yellow arrows indicate the direction in which the RD drifted over 6s of the simulation. The colour map used in the figure is the same as Figure 5.8.

5.4.4 Targets for ablation identified from patient-specific LA models

In the patient-specific LA models, as presented in the previous section, the RD anchoring locations were strongly dependent on the highly heterogeneous patterns of fibrosis distributions across the patient-specific LA models. Moreover, the anchoring locations were specific to individual patches. Therefore, by analysing all the RD tip trajectories obtained from numerous locations each of the 6 patient-specific LA models (using the protocol illustrated in Figure 5.6), we identified specific locations near fibrotic regions where the RDs were most likely to be found – the areas of high probability of the tip localisation – the target areas.

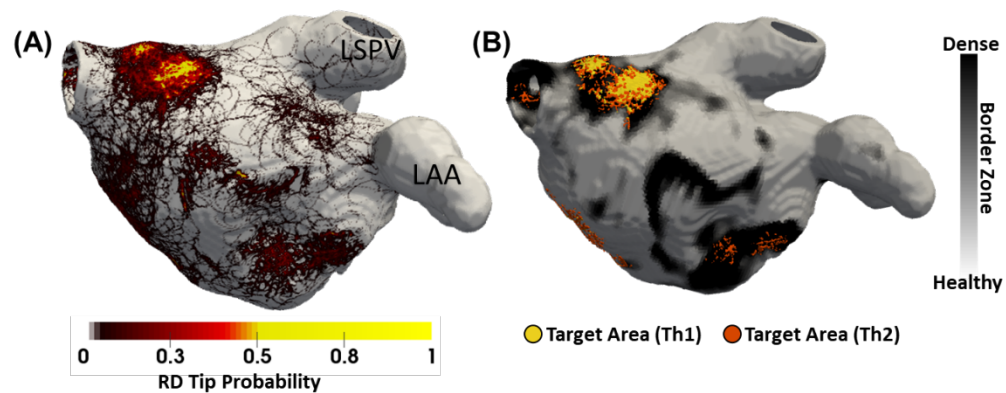


Figure 5.10: Identifying RD location maps from patient-specific tip probability maps. (A) Shows the tip probability map across the entire LA model of patient, P1 and (B) shows the locations of target areas identified by thresholding the normalised probability map (A) at two levels (yellow, Th1: 0.2) and (orange, Th2: 0.15) and overlaid on the fibrosis map (greyscale).

Figure 5.10, shows the normalised RD tip probability maps and target areas computed for the LA model of Patient 2. The tip probability map (Figure 5.10, A) captures all possible locations where the tip of the RDs have visited. The target areas (Figure 5.10, B) are computed by thresholding the probability maps such that only the locations which are most likely to be visited by the RDs are captured. In Patient 2, a higher threshold (Figure 5.10B, yellow), captures the fibrotic area which has the highest chances of anchoring RDs, while a lower threshold (Figure 5.10B, orange) captures all possible fibrotic patches where RDs were stabilised. To terminate AF, all possible patches which anchor RDs need to be targeted. The choice of threshold could influence the order in which fibrotic regions are targeted by CA, helping to guide the CA procedures.

The target areas calculated across all 6 patient-specific models with a threshold of 0.2 are shown in Figure 5.11. Here, on average 5.33 ± 2.94 target areas were identified per patient-specific

LA model. Moreover, by further analysing the distribution of the target areas (Figure 5.12A), we found that a higher percentage of target area were located within the fibrotic tissue region in patients in Utah 3 and 4 categories compared to patients in Utah 2 category. However, all target areas were relatively small, and the total volume of target areas was much lower than that of fibrosis in all patients (Figure 5.12B). The difference in the volume of fibrotic tissue and target areas was highest in Utah 4 patients, and lowest in Utah 2 patients, where RDs often stabilised around the PVs rather than fibrosis.

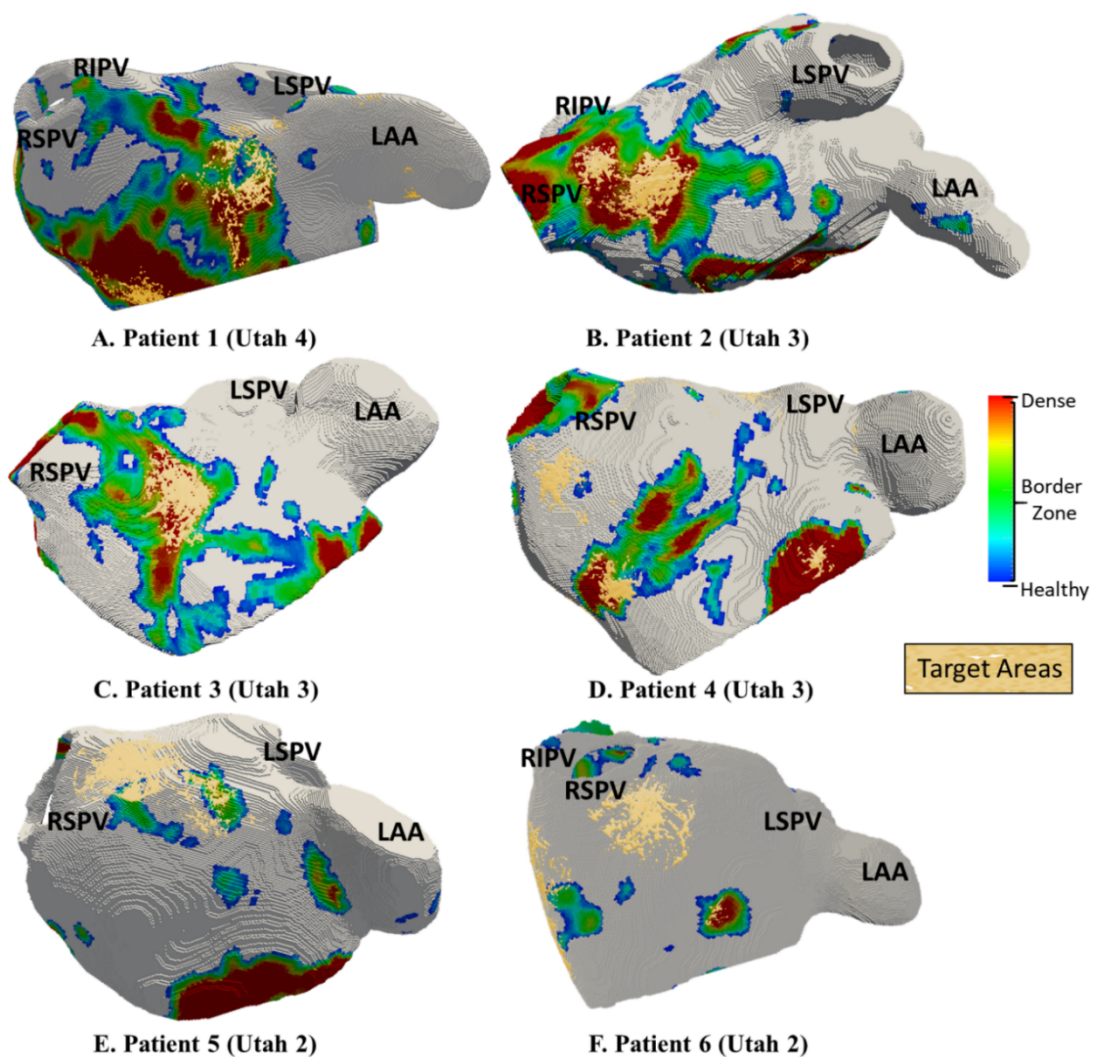


Figure 5.11: Patient-specific RD location maps – potential target areas for CA. The images show colour-coded fibrosis distributions in the 6 patient-specific LA models (A-F), with the target areas superimposed. In Utah 3 and 4 categories (Patients 1, 2 and 3), target areas are seen at specific locations within fibrotic patches and their BZs. In Utah 2 category (Patients 5 and 6), target areas are seen on the LA wall near small patches. Additionally, the target areas identified from simulations performed without fibrosis in the same LA model are presented in the Figure 5.13.

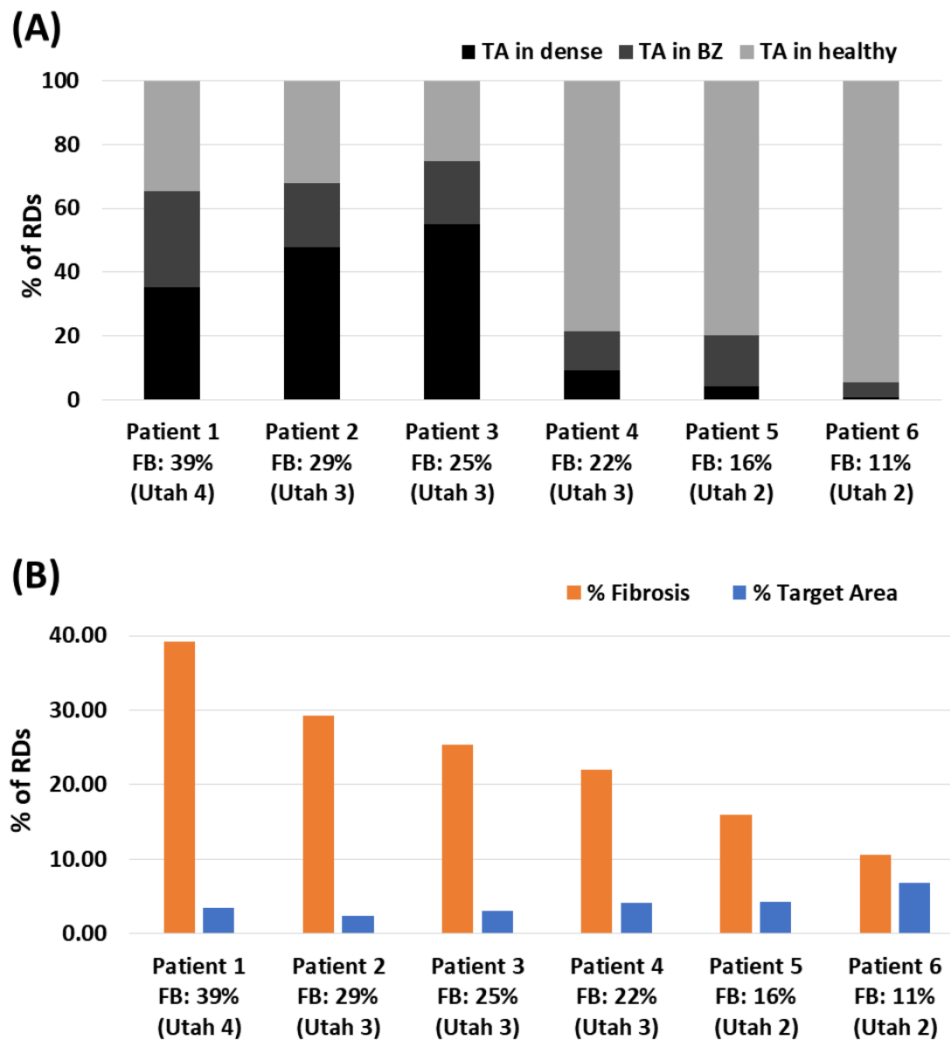


Figure 5.12: Comparison of the fibrosis burden to target area volume of in each patient-specific LA models. A: distribution of target areas across different regions of the atrial wall; dense fibrotic region (black), border zone (BZ - dark grey) and healthy tissue (light grey). The majority of target areas lie in the fibrotic region in Patients 1, 2 and 3 (FB > 25%, Utah 4 and 3), compared to much lower numbers in Patients from 4, 5 and 6 (FB < 25%, Utah 3 and 4). B: bar chart with FB (blue) and volume of all identified target areas (orange) in each model. The difference between FB and target area volume decreases with the decrease in Utah score, showing that the predicted target areas can be most efficient in improving CA in Utah 3 and 4 patients.

Additionally, we repeated all patient-specific LA simulations without fibrosis (Figure 5.13) and compared the target area locations to those in the respective LA models with fibrosis using the Dice score, a standard metric for the degree of spatial overlap. The Dice score was low for all patients, decreasing with the increase of FB. Thus, Patient 6 (FB: 11%) had Dice score of 0.52 compared to Patient 1 (FB: 39%), who had an extremely low Dice score of 0.06. This means that, in the presence of large fibrotic areas, the RDs rarely were found in the same locations

where they would be found in the absence of fibrosis. These results provide further evidence for the role of fibrosis in determining the RD locations.

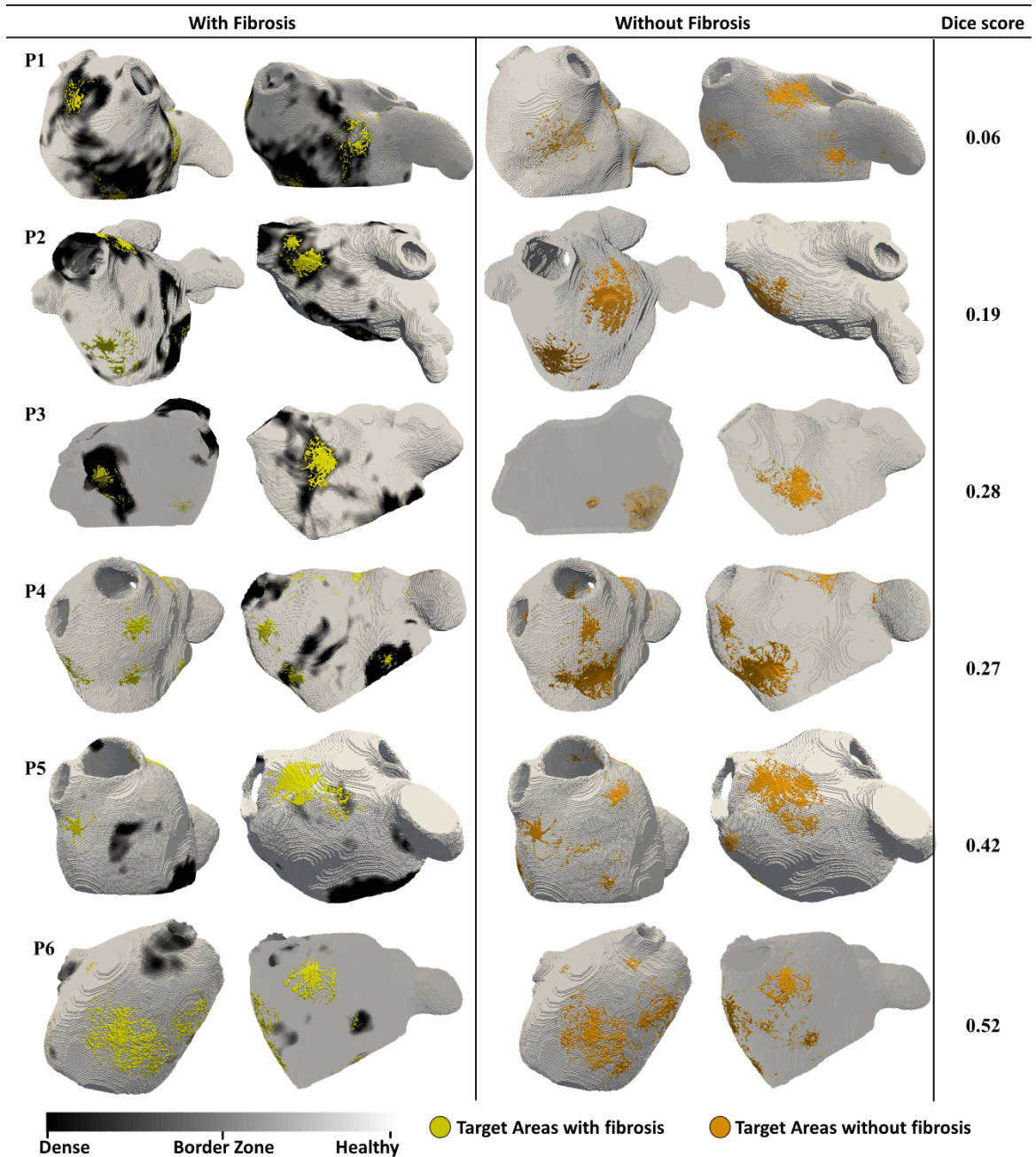


Figure 5.13: Patient-specific RD location maps – catheter ablation targets. The images show colour-coded fibrosis distributions (greyscale) in the 6 patient-specific LA models, with the target areas (with fibrosis: yellow and without fibrosis: orange) superimposed. In Utah 4 patient (P1), target areas are seen at specific locations within fibrotic patches. In Utah 3 patients (P2, P3 and P4), target areas are distributed at the BZ between fibrotic patches and healthy tissue. In Utah 2 patients (P5 and P6), target areas are seen mostly on the LA wall with some near small patches.

5.5 Discussion

The association between atrial fibrosis and AF recurrence after CA is well established [81,232]. However, the role of fibrosis in AF arrhythmogenesis has not been well understood, and the application of fibrosis imaging in guiding CA procedures has been limited. Thus, despite recent achieving of LGE MR imaging in identifying and quantifying the extent and location of fibrosis across the atria, the knowledge about fibrotic regions has not been applied during CA. Image-based computational modelling and simulation approaches help to understand the mechanistic influence of fibrosis in AF and to identify potential targets for CA. Specifically, they can predict the optimum locations of ablation lesions from patient-specific 3D atrial models, potentially helping to increase the efficiency of CA treatment in AF patients with high recurrence rates.

This chapter is dedicated to the development of the novel image-based computational approach to exploring the dynamics of RDs in the presence of patient-specific fibrosis distribution and to identifying the locations which stabilise RDs sustaining AF. Specifically, we: 1) developed 3D LA models with patient-specific geometry and distribution of fibrosis obtained from LGE-MRI of 6 AF patients, 2) applied the models to explore the dynamics of RD stabilisation in the presence of slow-conducting fibrotic patches and 3) generated patient-specific target areas for the RD locations, relative to the distribution of fibrosis to identify potential target areas for CA.

The main outcomes of this study were: (i) in AF patients from Utah 4 and 3 with high FB (>25%) RDs were more likely to be found at fibrotic regions compared to PVs (Figure 5.7A), (ii) RDs anchor to specific regions within the atrial walls, labelled as target areas identified from RD tip probability maps (Figure 5.11) and (iii) a higher percentage of target areas are located within the fibrotic tissue region in patients in Utah 3 and 4 categories compared to patients in Utah 2 category (Figure 5.12A). These results are consistent with observations in recent clinical and computational studies showing a strong spatial correlation between fibrotic regions identified from LGE-MR images and the locations of RDs sustaining AF [13,15,174].

5.5.1 Influence of atrial fibrosis on the distribution of RDs

Our main finding is that fibrotic regions were the primary anchoring locations of RDs in AF patients from Utah 3 and 4 (with FB > 25%) compared to PVs in Utah 2 (with low FB < 20%). These results are in agreement with clinical studies that have shown low success rates of PV isolation in patients with high FB [232], as well as computational studies that showed the

persistence of AF primarily in patients in Utah 4 category [14]. Hence, the higher FB translates into a higher probability of RD localisation in fibrotic regions, and patients specifically from Utah 3 and 4 categories can benefit from fibrosis-based CA in addition to the standard PVI.

It is worth noting that the RDs locations across patients with similar FB can be critically influenced by the specific fibrosis distributions. Thus, for Patients 3 and 4 (both from Utah 3 category) with a similar FB (22 - 25%), there was a sizeable difference in the locations of RD stabilisation (Figure 5.7, A). The former had the same number of RDs anchoring at fibrotic regions and PVs, whereas in the latter majority of RDs were localised at the PV region. This could be explained by the differences in the spatial distribution of fibrosis in the two patients (Figure 5.4), with Patient 3 having a larger proportion of fibrotic patches in LA wall compared to the PV region. This result suggested that, in addition to stratifying patients for CA based on FB, as previously suggested [81,120,232], the influence of the spatial distribution of fibrosis should be taken into account. The stratification should be validated in future clinical studies.

5.5.2 Comparison with previous studies of RDs and ablation

In patients with high FB (Patients 1-3), the majority of the target areas in our patient-specific models were located at distinctive regions within fibrotic patches. Otherwise, in the models with low FB (Patients 4-6), the target areas are more evenly distributed across the LA wall. In average, 5.33 ± 2.94 number of target areas were identified per patient-specific model for a chosen threshold of 0.2 on the RD probability map. These findings are consistent with recent clinical studies that reported the persistence of RDs in a small number of distinctive locations [55,114]. For example, Haissaguerre et al. [114] used ECGI and reported 2-6 RD locations and Narayan et al. [55] used invasive basket mapping and also reported distinctive RD anchoring site which can be targeted by CA. In cases where RDs anchored to fibrotic patches, our simulation results consistently showed that only some regions of fibrotic tissue harbour RDs (i.e., the volume of target areas was lower than that of fibrotic regions, Figure 5.12B). Hence, only those relatively small regions should be targeted by CA.

Furthermore, our findings agree with previous biophysical simulation studies that have also found an association between spatial distribution of fibrosis and anchoring locations of RDs [15,174,213]. In particular, Zahid et al. [15] and Boyle et al. [225–227] used similar patient-specific LA models with fibrosis to demonstrate that AF was perpetuated by RDs that persist in spatially confined regions, such as BZs between fibrotic and non-fibrotic tissue. However,

in our simulations across all the models showed that some RD locations (target areas) were outside of the fibrotic BZ (Figure 5.12, A), particularly in the dense fibrotic area and healthy tissue regions near PVs. These differences could be attributed to the choice of methodology and specific electrophysiology parameters used for modelling of fibrotic regions [187,233,234].

Our method to model fibrosis accounted for modification of electrical conductivity in fibrotic tissue, reflecting: (i) gap junction remodelling due to downregulation of Connexin 43 and (ii) reduced inter-myocyte coupling due to collagen deposition (discussed in Chapter 2, section 2.5.5). Moreover, one important advantage of our method is that we incorporated a decreasing gradient in conductivity to represent electrical changes from non-fibrotic to fibrotic regions, rather than an abrupt change in conductivity as applied in previous studies by Zahid et al. [15] and Boyle et al. [226,227]. Our approach is more physiological compared to the binary model, since abrupt changes in tissue properties are not found in atrial experiments. A similar approach has also been adopted in some previous studies by Morgan et al. [174] and Krueger et al. [171]. Having multiple levels of fibrosis within the same model allows us to overcome certain errors associated with thresholding and modelling of fibrosis. By incorporating multiple levels of fibrosis in the model, we captured the known dependence of conductive tissue properties on the level of fibrosis, as reported by Fukumoto et al [177], which can't be done with a binary approach. Other studies have also incorporated the electrotonic effects of fibroblast-myocyte coupling [174], ionic changes due to paracrine effects [15] and represented deposition of collagen using percolation method [181] or discontinuous finite elements [180]. Computational studies that compared different fibrosis modelling methodologies have reported that these additional factors further facilitated the anchoring of RDs to the fibrotic areas and their BZ due to increased APD and lower CV [187,233]. This may explain why those simulations found a large number of RDs located at the fibrotic BZ, while ours show a wider distribution. We believe that, although our representation of fibrotic tissue is simple, it is adequate for patient-specific models derived from clinical imaging data with limited resolution.

Previous computational approaches to identify RD locations in patient-specific atrial models [14,15,226,227,235] have focused on the ability of fibrotic regions to generate RDs and subsequently anchor them. However, the RD formation is not exclusively mediated by fibrotic regions. Moreover, RDs are known to drift and meander within atrial tissue, and the initial RD location is not necessarily its anchoring location. Hence, in this study, we presented a unique

approach where the initiation of the RDs was independent of fibrotic regions, which allowed us to evaluate the ultimate anchoring locations of RDs in an unbiased manner. Moreover, in all our simulations, the tip of the RDs was calculated every 1ms, while in other studies this was limited to every second [15]. The advantage of such a high frequency of RD tip calculations is a deeper insight into the RD trajectory during the anchoring process. Although this comes at a higher computational cost, one of the aims of our study was to evaluate the dynamics of RD with respect to fibrotic regions. Moreover, in order to generate the probability maps for RD tip locations, higher resolution was necessary, which justifies our computational choice.

5.5.3 Limitations

The choice of atrial electrophysiology model is known to influence the RD tip locations [236,237], but sensitivity to such a choice was not investigated in this study. Besides, the presented model does not account for heterogeneous distributions of APD and CV in the atria [15,53,169,233]. Instead, we modelled a simpler condition where APD was homogeneous and both fibrotic and non-fibrotic regions have isotropic conduction properties and CV. Ideally, patient-specific models should be parameterised using CV and APD measurements from the same patients. However, data needed to create such complex models are unavailable due to the limitations in invasive mapping technology to sample the entire atria. Previous studies [15,233] have used values either limited data sampled from discrete locations in the atria of small patient groups [238], or ex-vivo ionic data derived from canine experimental models [148].

Another limiting factor of the study is that all the subjects considered for the study were male. Gender related differences in LA electrophysiology [239], anatomy, structure and function [240,241] have been reported in animal studies [242]. These differences have been attributed to disparities identified in calcium and sodium channel regulation and the effects of sex hormones [241,243]. However, the question of atrial differences between the human genders remains controversial due to limited data. In this study, we considered only male subjects due to the availability of data. Further experimental and modelling studies are required to understand gender related differences in AF mechanisms. This will allow for further personalisation of AF therapy.

Atrial fibre orientation is known to be complex [244] and can also have significant effects on atrial conduction [148,165]. Specifically, change in fibre orientation has been reported at the PV sleeves, which can lead to significant repolarization heterogeneities and unstable RD

behaviour [245,246]. Moreover, significant inter-patient variability in the PV fibre directions has been reported to affect inducibility and stabilisation of RDs at LA-PV junction [155]. Therefore, incorporating fibre information will increase the predictive strengths of the model. However, in this study fibre orientation was not incorporated due to the absence of relevant patient-specific data. An adequate reconstruction of the complex atrial fibre architecture from patient data is hindered by limitations of existing imaging techniques. The modelling approach presented in the current study is entirely based on patient imaging-derived data available in the clinic. Future studies aiming to incorporate information about fibre orientation into patient-specific atrial models are discussed in Chapter 7, Section 7.3.

Limitations of EAM in identified locations of RDs in the atria (discussed in Chapter 2, Section 2.4.3.2) also led to a lack of validation for the predicted RD locations. Recent advances in identifying RDs using non-invasive ECGI [12,13,247] could be used for validation of the models by measuring the correlation between the model predictions and the actual recordings.

Another simplification made in the study was that all the pacing locations (AF triggers) were kept in the regions surrounding the PVs. However, such triggers can sometimes arise from regions outside the PVs [248]. In future, the pacing location evenly cover the entire atrial wall rather than a few specific locations. Initiating RDs from every node within the geometry (> 60000 points) for each patient data comes at a high computational cost (~3 hours per simulation), and an efficient approach should keep a balance between the two.

In the image-processing pipeline, the empirical IIR threshold to differentiate between fibrotic and non-fibrotic regions from LGE-MR images will affect the shape and size of the fibrotic areas and the BZ and hence the dynamics of the RDs. However, the optimum value is unknown. Therefore, the work presented in Chapter 6 aims to investigate the sensitivity of the anchoring locations of the RDs – target areas to the change in shape and size of the fibrotic areas as a result of uncertainties in LGE thresholding. The other limitations consistent with work presented in other Chapters, and possible ways to address them in the future are summarised in Chapter 7.

5.6 Conclusions

In conclusion, this chapter presented an image-based computational workflow to identify patient-specific locations of RDs from LGE-MRI data. The simulations showed that RD sustaining AF typically anchored to specific regions of fibrotic patches. Therefore, the RD

locations were determined by unique patient-specific distributions of fibrotic tissue, identifying areas that may potentially be targeted by therapy. These results may be particularly relevant to AF patients with high fibrosis burden in the LA, where the model-predicted target areas could inform CA. The next chapter will use a subset of the predicted patient-specific target areas to test the efficacy of respective patient-specific CA strategies in-silico.

Chapter 6

Virtual Catheter Ablation of Atrial Fibrillation: Target Areas Identified from Image-Based Models

6.1 Section Outline

The study presented in this chapter aims to: (1) test new CA strategies by simulating ablation of target areas predicted from image-based LA models (detailed in Chapter 5) and (2) explore the sensitivity of the predicted target areas locations on the choice of LGE-MR image intensity thresholding parameters. In this proof-of-concept study, all the simulations were performed using 2 of the 6 patient-specific LA models. The motivation behind investigating CA strategies is summarised in Section 6.2, and the methodology of the virtual ablation using the LA models and the sensitivity study are discussed in Section 6.3. Finally, the limitations (Section 6.5.3) and the main findings (Section 6.6) of the chapter are summarised.

6.2 Introduction and Motivation

Despite advances in CA therapy over recent decades, the success is limited particularly in PsAF patients with high post-ablation AF recurrence rates [249]. The extent of fibrosis characterised from LGE-MR images is known to be an important predictor of post-ablation recurrence [81]. Ablation strategies that target low-voltage areas (believed to be a surrogate of fibrosis) in addition to pulmonary vein isolation (PVI) have shown to improve the success rate [100,123], although the superiority of this substrate-based ablation strategy compared to the PVI-only ablation has not yet been confirmed by large clinical trials. Moreover, CA strategies targeting fibrotic regions greatly vary between clinical centres. For instance, some studies target the entire fibrotic region [102], while others either isolate the fibrotic regions [100] or specifically target fibrotic areas with distinctive activation patterns [123]. This ambiguity can be explained by the lack of mechanistic knowledge of the links between fibrosis and AF. Moreover, empirical ablation of extensive fibrosis areas in patients with a high fibrotic burden (FB) can create proportionally extensive CA lesions and result in substantial damage to the atria. This warrants the development of mechanism-based strategies that can aid in the identification of optimal patient-specific ablation lesions and the standardisation of CA therapy across multiple centres.

6.2.1 Model-based ablation strategies

Personalised computational models provide a promising tool for improving CA [225,250–253], as also shown in the Chapter 5. For example, they can link the structural information obtained from atrial imaging data and electrophysiological information from ECGs and non-invasive mapping to elucidate the dynamics of AF drivers in a patient-specific manner [254]. Such studies have suggested that specific fibrotic architecture may be needed to harbour RDs, which could aid in the non-invasive identification of targets for CA [15]. Prakosa et al. [255] has proven that predictions based on personalised models can help in termination of infract-related ventricular tachycardia in both animals and patients without the need of prior electro-anatomic mapping. Similar approaches are also being developed for AF [225,252], but the progress is hindered by the complexity of its mechanisms and the underlying fibrosis architecture.

Chapter 5 presented our own image-based computational workflow for the identification of the most likely anchoring location of RDs – potential target areas for CA. Specifically, the LA models with patient-specific fibrosis distribution were applied to simulate multiple AF scenario and to identify regions where the RDs are most likely to anchor in a given patient across all scenarios. The next logical step of this study is to test whether CA on these regions, would indeed be beneficial in terms of terminating RDs and preventing their recurrence. However, before such an approach could be tested in AF patients, using our computational workflow to perform virtual ablation of the target areas presents a safe exploratory option. Moreover, knowledge of the mechanistic links between RD locations and success of clinical CA strategies is limited. Therefore, the first aim of the study is to perform CA of the predicted target areas in the patient-specific models and then compare its success with the existing CA strategies, thus identifying the optimal strategy given the knowledge of RD locations.

6.2.2 Challenges of fibrosis imaging in the atria

Despite advances in personalised computational models in understanding and improving CA, their success ultimately comes down to the quality of imaging data the models are based on. Limitations of the image-based models that utilise patient-specific LA geometry and fibrosis distribution were discussed in the relevant section of Chapter 5. Here, we focus on the limitations of LGE-MRI data used to personalise the models. Throughout the study, we used the image intensity ratio (IIR) between atrial myocardium and the blood pool to identify and segment fibrosis from LGE-MR images [83]. However, the optimal cut-off value to

differentiate between fibrotic and non-fibrotic tissue is still being debated (also discussed further in Chapter 2, Section 2.4.2.2).

Therefore, the second aim of the study was to perform a simple sensitivity analysis to determine how dynamics of RDs, and hence the target area locations, would be affected by alterations in intensity thresholding of the LGE-MRI. In order to achieve this, we first evaluated the RD dynamics in relation to a single fibrotic patch with varying size and shape in a 3D slab of atrial tissue. The results were then extended to a 3D patient-specific atrial model with multiple fibrotic regions.

6.3 Methods

6.3.1 Virtual ablation of the predicted target areas

Figure 6.1 summarises the complete workflow for predicting optimal CA strategies from patient-specific biophysical models of the LA. The blue panels correspond to the construction of patient-specific models from LGE-MR images and generation of target areas (Figure 6.1, A-D), which has been described in Chapter 5; the grey panels correspond to virtual ablation of the predicted target areas and beyond. In the first part of the study, we performed virtual ablation of the target areas (Figure 6.1, E) in 2 AF patients with fibrosis classification of Utah 3 (Patient 2 & 3 from Chapter 5). In the following text, they will be referred to as P2 and P3.

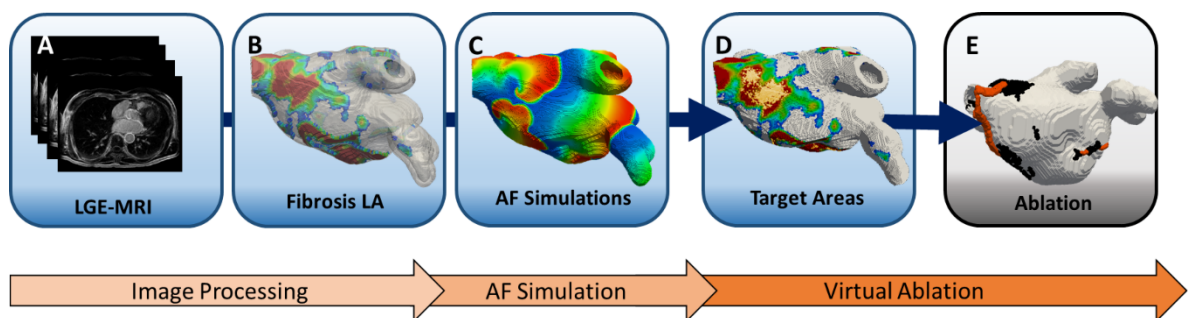


Figure 6.1: The workflow for reconstruction of the image-based LA model (A-B), perform patient-specific AF simulations (C), predict the RD locations (D) and then perform virtual ablations (E) of the predicted target areas.

6.3.1.1 AF Ablation Strategies

The CA lesions were modelled as cylindrical transmural regions of unexcitable tissue with a diameter of 3 mm [256] to account for the catheter tip shape. The continuous CA lesions were implemented using five strategies; Strategy 1 and 2 are used clinically [9], Strategy 3 is based

on our model's predictions from Chapter 5 and Strategies 4 and 5 are combinations of the model predictions with clinical strategies. Further details of each strategy are provided below:

1. *Strategy 1: PV isolation (Figure 6.2, A)*

The 2 right and 2 left PVs were electrically isolated by a continuous set of ablation lesions encircling the PVs and isolating them from the remaining LA body.

2. *Strategy 2: PV isolation with linear lesions (Figure 6.2, B)*

If the RDs still persisted after the application of Strategy 1, additional linear lesions were applied: one on the LA roof to connect the left and right circular PVI lesions and another to connect the roof lines with the mitral valve (MV) opening.

3. *Strategy 3: target area guided ablation (Figure 6.2, C)*

Ablation lesions were applied to the voxels within the target areas identified from the patient-specific AF simulations. This approach has similarities to DECAAF II, an ongoing prospective multicentre randomised trial in which all fibrotic regions identified from LGE-MRI are targeted by CA. However, our approach only targets areas that typically are located near fibrotic regions but are much smaller than the entire fibrosis.

4. *Strategy 4: target area guided ablation with linear lesions (Figure 6.2, D)*

If RDs still persisted after the application of Strategy 3, additional linear lesions were applied to join the target areas to the nearest anatomical boundary – the PVs or the MV.

5. *Strategy 5: target area guided ablation with linear lesions and PVI (Figure 6.2, E)*

If the RDs still persisted after the application of Strategy 4, Strategy 1: PVI was applied.

All CA lesions were applied after 6s of the AF simulation to analyse if these lesions terminated the existing RDs within 2 s. The CA strategy was considered successful if either AF converted to atrial tachycardia (AT) or the RDs were completely terminated. In this study, we refer to macroreentrant AT when re-entrant waves rotate around scar tissue formed after ablation (discussed in further detail in the Chapter 2, Section 2.4.3.2). The mean frequency (MF) of activations in the LA model before and after CA was recorded for all the strategies and conversion of AF to AT was evaluated by reduction in the MF [257]. The MF was computed by averaging over the dominant frequency calculated for every location of the LA geometry for the last 1s of the simulation. Moreover, for target area guided CA strategies 3 and 4, we also tested if these lesions prevented AF inducibility in the models. To achieve this, the protocol used for AF initiation was repeated after the application of the ablation lesions.

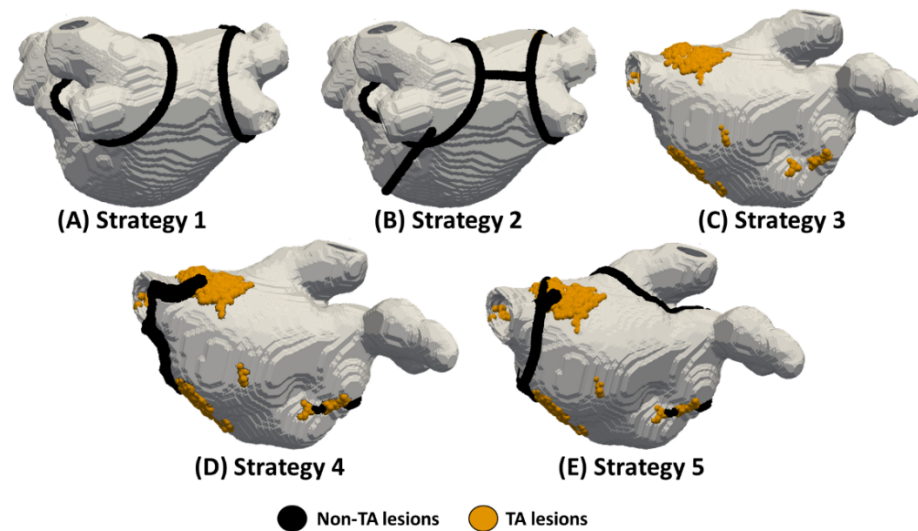


Figure 6.2: CA strategies tested using virtual ablation platform. (A) Strategy 1: Circumferential PVI, (B) Strategy 2: PVI plus additional linear lesions at the LA roof and a line joining the PV to the MV, (C) Strategy 3: ablation on the target areas, (D) Strategy 4: target area guided ablation with additional linear lesions leading to unexcitable boundaries (PV and MV) and (E) Strategy 5: target area guided ablation with linear lesions plus PVI.

6.3.1.2 Virtual Ablation Simulation Protocol

All the simulations were performed using the image-based 3D atrial models of Patients 2 and 3 described in Chapter 5. The choice of these patient models was motivated by the highest correlation found between the RD location and fibrotic region in Figure 5.7. However, Patient 1 was not ablated due to extensive fibrosis (Utah 4) and clinically they would not be considered for CA procedure. While, Utah 2 patients can probably be successfully ablated using PVI.

6.3.2 LGE-MR intensity thresholding and RD locations

In the second part of the study, the goal was to analyse the effect of IIR threshold on RD localisation and the corresponding target areas. Therefore, we systematically altered the chosen IIR threshold values in the original pipeline (Chapter 5, Section 5.3.2.1), which resulted in altering the size of the BZ surrounding the fibrotic patch. Previously, two IIR thresholds were used (Figure 6.3, B): (i) voxels below an IIR of 1.08 (referred to as I1) were healthy tissue, (ii) voxels above an IIR of 1.24 (referred to as I2) were dense fibrotic regions and the voxels with intermediate values between I1 and I2 correspond to the BZ. This gave us the control case, while fibrotic patches with varying BZ size were created by altering the IIR threshold, I1, which differentiates between healthy and fibrotic tissue while keeping I2 constant. The rationale behind altering only one of the two thresholds was to maintain computational tractability.

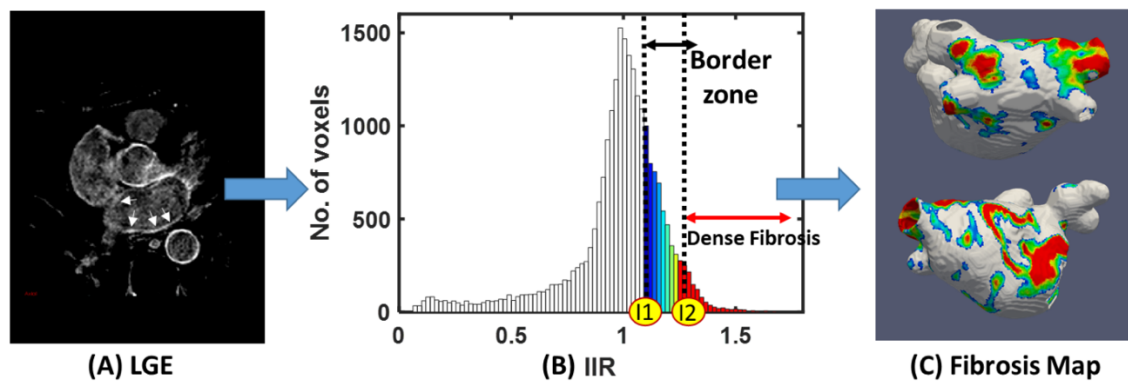


Figure 6.3: LGE-MRI intensity thresholding for fibrosis assessment. (A) LGE MR image slice with arrows indicating fibrotic regions, (B) the intensity thresholding parameters and (C) the extracted fibrosis map.

The study consists of two parts where we investigate the effects of BZ size in: (1) a 3D atrial slab with a single fibrotic patch and (2) the LA model with patient-specific fibrosis distribution. The second part in realistic atrial models will provide further insight on how the LGE-MRI thresholding affects the localisation of RDs in the presence of multiple fibrotic patches.

6.3.2.1 Study 1: The 3D atrial slab study

Model Geometries: The simulations were performed on a 3D atrial tissue slab of $200 \times 200 \times 25$ voxels corresponding to a tissue size of $60 \times 60 \times 7.5 \text{ mm}^3$ with a surface area of 3600 mm^2 , similar to that described in Chapter 3. A diagram of this setup is presented in Figure 6.4. Here the effect of fibrotic patches with different BZ sizes on the RD dynamics was investigated by incorporating a realistic patch from the fibrosis distribution of Patient 2 (Figure 6.4, A).

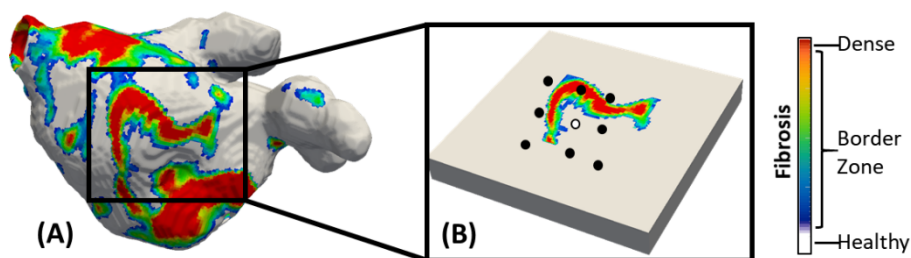


Figure 6.4: 3D atrial slab with realistic fibrotic patch. (A) LA model with patient-specific distribution of fibrosis and (B) Projection of the fibrotic patch on a 3D atrial slab with black dots indicating the RD initiation locations.

Model Parameters: In the fibrotic patch, increasing and decreasing the control value for I1 by 5% resulted in a relatively small and large BZ, respectively. Setting I1 equal to I2 generated conditions for no BZ. The different values for I1 used in the generation of fibrotic patches with no, small, and large BZs compared to the control are summarised in Table 6.1.

Model	% Change	I1	I2
No BZ ($I1_{\text{noBZ}}$)	-100.0	1.240	
Small BZ ($I1_{+5\%}$)	-36.90	1.134	1.24
Control ($I1_{\text{control}}$)	-	1.080	
Large BZ ($I1_{-5\%}$)	+45.34	1.026	

Table 6.1: The chosen IIR cut-off values used in Study 1. Column 2 shows the % change in size of the BZ with respect to the control, while columns 3 and 4 present the IIR threshold values used.

Stimulation Protocol and Analysis: RDs were initiated at multiple sites surrounding the fibrotic patch (Figure 6.4, B), using the same cross-field protocol as in Study 1 from Chapter 3. The tips of the RDs for all the simulations were tracked using the method described in Chapter 3 and the target areas were computed using the method described in Chapter 5 (Figure 5.6).

6.3.2.2 Study 2: The patient-specific LA study

Model Geometries: All simulations were performed with the LA model of Patient 2 and 3.

Model Parameters: The previously stated IIR thresholds (in Chapter 5) were altered by increasing the I1 by 1% and 3%. These values were selected such that the BZ decreased while the overall volume of fibrosis (i.e., FB) did not change by more than 10% (see Discussion).

Model	I1	I2	FB
$I1_{\text{control}}$	1.080		29 %
$I1_{+1\%}$	1.091	1.24	27 %
$I1_{+3\%}$	1.112		22 %

Table 6.2: The chosen IIR values and resultant FB in Study 2.

Stimulation Protocol and Analysis: RDs were initiated at multiple sites using the same protocol as in Chapter 5. The tip of the RDs for all the simulations were tracked and the target areas were computed using the method described in Chapter 5, Figure 5.6.

Data Analysis: The degree of overlap between target areas in models based on $I1_{\text{control}}$ with those based on $I1_{+1\%}$ and $I1_{+3\%}$, was evaluated by measuring the Dice score [231] of the CA lesions applied on top of the target areas and formed continuous fully transmural regions.

6.4 Results

6.4.1 Effect of different ablation strategies on the termination of RDs

6.4.1.1 PV Isolation with and without linear lesions

Ablation of the PVs (in Strategy 1) failed to terminate RDs in the majority of cases (P2: 6/10, P3: 4/8). As shown in Figure 6.5 (A1 and B1), RDs located far from the PVs were unaffected. These RDs persisted even after additional linear lesions were applied at the roof and the MV (Figure 6.5, C1 and D1, in Strategy 2). In the few cases where AF did terminate, the RDs were present inside or near the isolated PV regions. After CA, these RDs either anchored to the lesions encircling the PVs (P2: 1/10, P3: 2/8) resulting in AT or terminated (P2: 3/10, P3: 2/8).

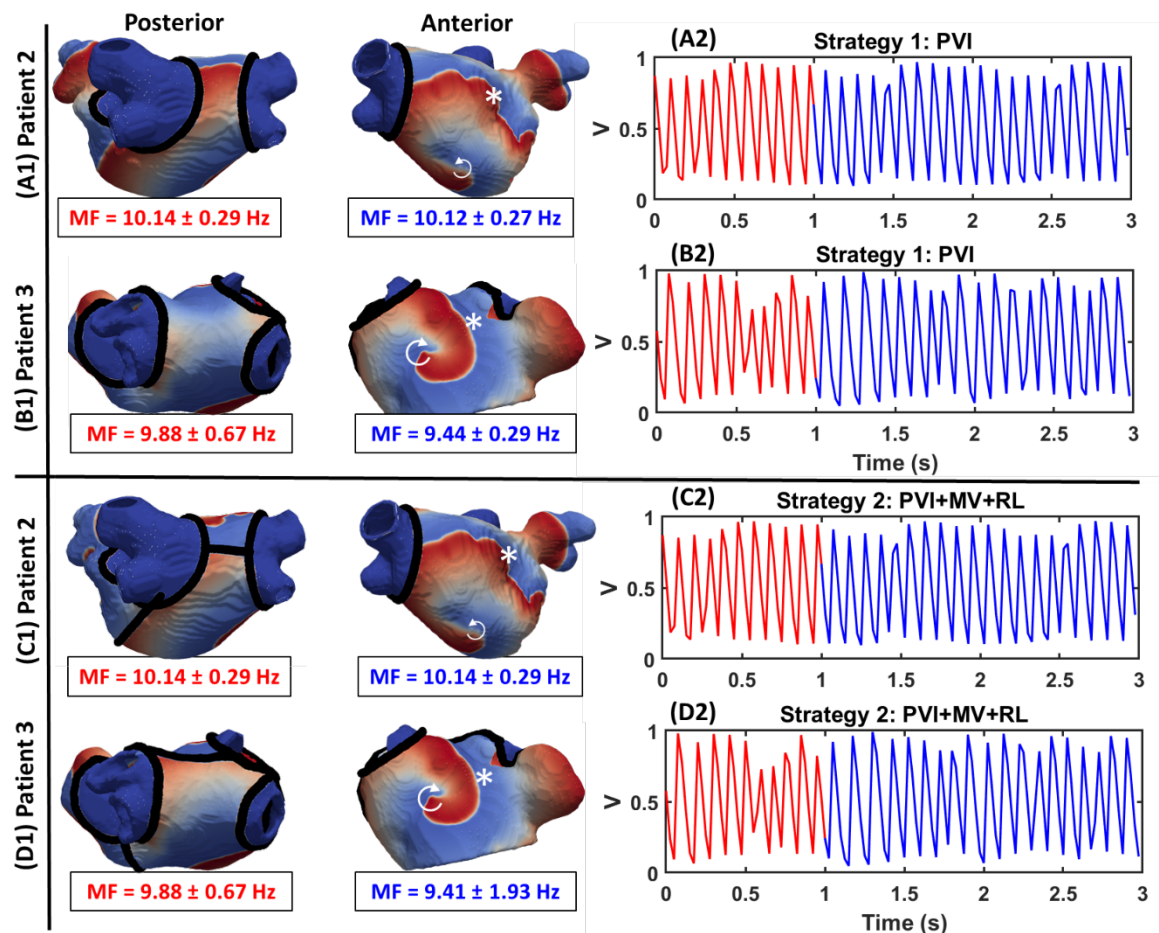


Figure 6.5: CA with the clinical used ablation Strategies 1 and 2 failed to terminate AF in the majority of cases. Left: Voltage maps showing the behaviour of RDs after: (A1-B1) Strategy 2 and (C1-D1) Strategy 2 in Patient 2 and 3, respectively. Right: Transmembrane voltage at the point indicated by * in the respective LA models, plotted before (red) and after (blue) CA. Both strategies failed to terminate RDs in all cases and the mean frequency (MF) remained unaffected. Here and in the next figure, the white arrow indicates the directions of RD movement.

6.4.1.2 target area guided ablation with and without PVI

CA on the target areas were performed using Strategies 3, 4 and 5. First, with Strategy 3, the application of CA lesions on top of the target areas either resulted in the RDs anchoring around the newly formed ablation scar (Figure 6.6, A1 and B1) and AF converting to AT (P2: 4/10, P3: 4/8) or had no effect (P2: 5/10, P3: 4/8). Examples of the conversion from AF to AT in Patient 2 and 3 are shown in Figure 6.6, A2 and B2. Here, MF dropped by 26% and 41%, respectively.

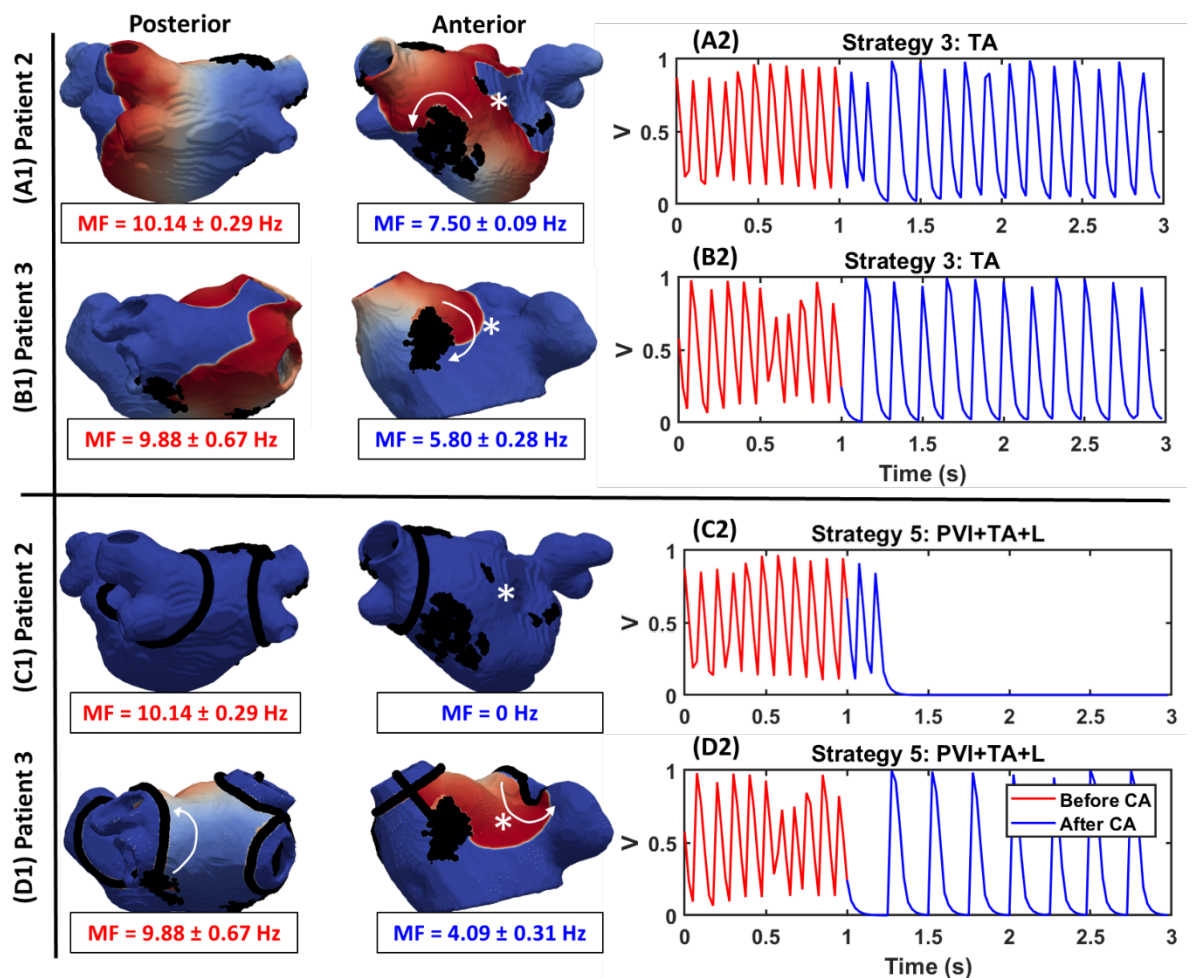


Figure 6.6: Target area guided ablation with Strategy 5 successfully terminated AF. Voltage maps showing the behaviour of RDs after CA of: (A1-B1) target areas and (C1-D1) target areas plus linear lesions joining them to the PVI lesions and the mitral valve (MV) in Patient 2 and 3, respectively. Panels on the right (A2-D2) show the voltage at the point indicated by * in the respective LA models, before (red) and after (blue) CA. Out of the two strategies, PVI plus target area guided ablation successfully terminated AF in both patients.

However, Strategy 4 connecting the target areas with linear ablation lesions to the nearest boundary (the PVs or MV) terminated AF in the majority of the cases (P2: 6/10, P3:4/8). In case of Patient 2, all RDs were terminated (Figure 6.6, C1), while in Patient 3 AF was converted to AT (Figure 6.6, D1) with a reduction in MF by 59%. In Strategy 5, application of PVI in addition to Strategy 4 resulted in a further increase of AF termination rate in both patients (P2: 9/10, P3: 8/8). The outcomes for all virtual CA strategies in both patients are summarised in Figure 6.7.

Patient 2: AF Cases	Ablation strategy					Patient 3: AF Cases	Ablation strategy				
	PVI	PVI + L	TA	TA+L	PVI + TA+L		PVI	PVI + L	TA	TA+L	PVI + TA+L
1	✓	✓	✗	✗	✓	1	✓	✓	✓	✓	✓
2	✓	✓	✓	✓	✓	2	✓	✓	✗	✗	✓
3	✗	✗	✗	✗	✓	3	✓	✓	✗	✗	✓
4	✗	✗	✓	✓	✓	4	✗	✗	✓	✓	✓
5	✗	✗	✓	✓	✓	5	✗	✗	✗	✗	✓
6	✓	✓	✗	✗	✓	6	✗	✗	✓	✓	✓
7	✗	✗	✗	✓	✓	7	✗	✗	✓	✓	✓
8	✓	✓	✓	✓	✓	8	✓	✓	✗	✗	✓
9	✗	✗	✗	✗	✗						
10	✗	✗	✗	✓	✓						

✗ AF persisted ✓ AF terminated ✓ Converted to AT

Figure 6.7: The outcome of CA using different strategies in Patient 2 (A) and Patient 3 (B). The summary of the mean frequencies (MF) recorded for these cases are presented in Appendix, Table A. 2.

6.4.1.3 AF inducibility after ablation

AF recurrence after CA is a huge clinical problem. In order to check for AF recurrence, we tested for AF inducibility (Figure 6.8) after CA with Strategies 3 and 4. CA performed using Strategy 3 did not prevent the RDs from being initiated in either patient. However, it resulted in AT rather than AF in the majority of cases (P2: 8/10, P3: 8/8), with MF of ~ 6 Hz (Figure 6.8, A). In the remaining cases, RDs were located either outside the target areas or between the CA ablation lesion (Figure 6.8, C), and hence were induced in the same way as before CA.

However, using Strategy 4 completely prevented the initiation of RDs: neither AF nor AT was initiated (Figure 6.8, B), even in 8 cases where AT was initiated after Strategy 3 in Patient 2. Moreover, joining the CA lesions converted AF to AT in one additional case (Figure 6.8, D). In Patient 3, all RDs corresponded to AT with a lower MF (~ 5 Hz) compared to Strategy 3.

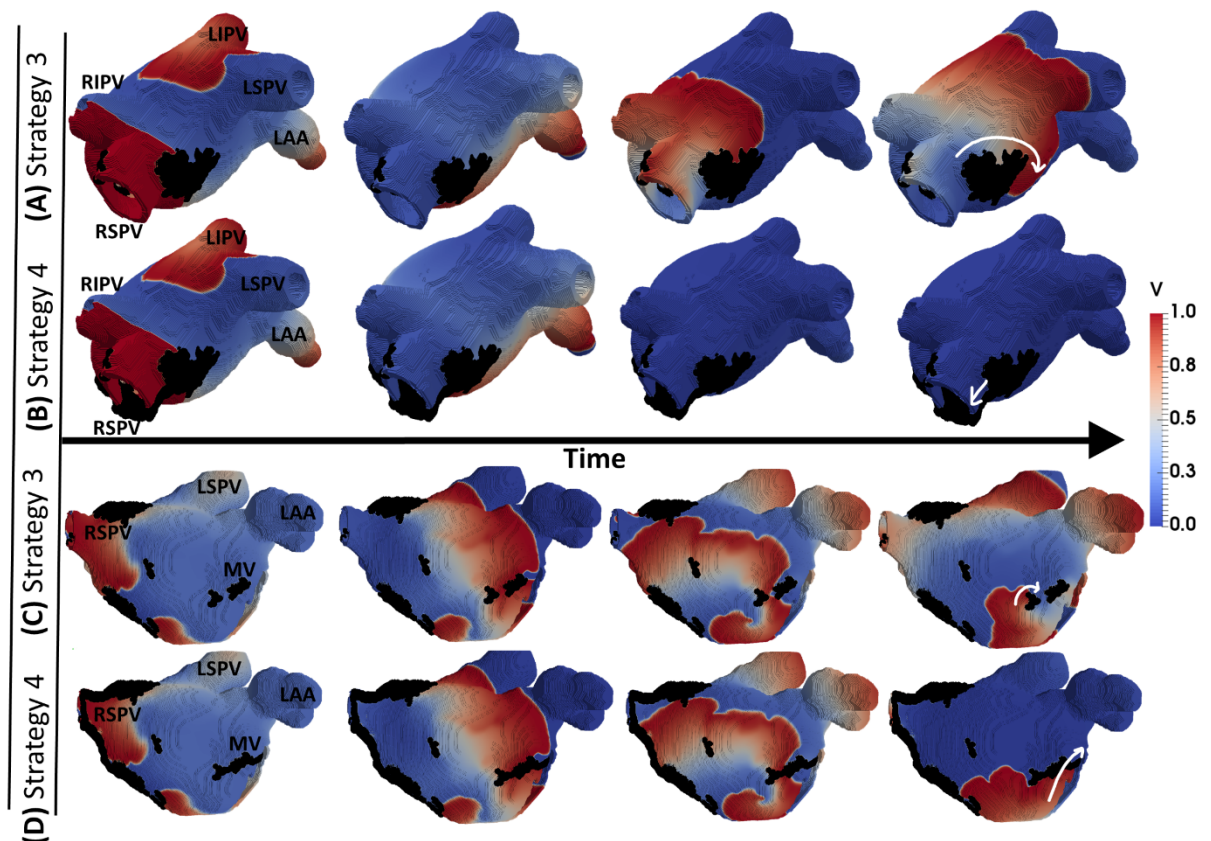


Figure 6.8: AF inducibility following CA Strategies 3 and 4. (A and C) The RDs were initiated following ablation Strategy 3: (A) the RD anchored to the newly formed scar generating AT, or (C) the RD found a new pathway between two target areas and stabilised. However, following ablation Strategy 4 (B and D), where the target areas were connected to the PV or MV, the RD either terminated (B) or anchored around the MV and generated AT (D).

6.4.2 Effect of IIR threshold on target areas

6.4.2.1 The 3D atrial slab study

In the 3D atrial slab with a single fibrotic patch, varying BZ size (Figure 6.9, A-D) influenced the specific meandering trajectories of the RDs around the patch. In the absence of BZ (Figure 6.9, A), the RD did not meander and its trajectory encircled a portion of the dense fibrotic region (Figure 6.9, A (i)). Hence, the majority of the RDs (7/9) remained anchored to the fibrotic patch, whereas RDs initiated far from it meandered away (2/9). The target area, in this case, was located precisely at the border between fibrotic and non-fibrotic tissue (Figure 6.9, A (iv)).

In the presence of a slow conducting BZ around the dense fibrotic region, the RD meandered zig-zagging between the dense fibrotic region and the surrounding BZ (Figure 6.9, B-D (ii)). The extent of meandering increased with the increased size of the BZ, and hence the target area

regions in such cases (Figure 6.9, B-D, (iv)) were further spread across the patch compared to the patch with no BZ. Moreover, as the BZ size was increased, the RDs – that had been anchored to the fibrotic patch in case with no BZ (7/9) – were no longer anchored and meandered away from the patch. In case of the smallest BZ, 4/9 RDs remained anchored at the patch, while for the largest BZ only 2/9 were anchored; other RDs meandered away. The degree of overlap between the identified target areas measured using the Dice score was 0.99 across all cases.

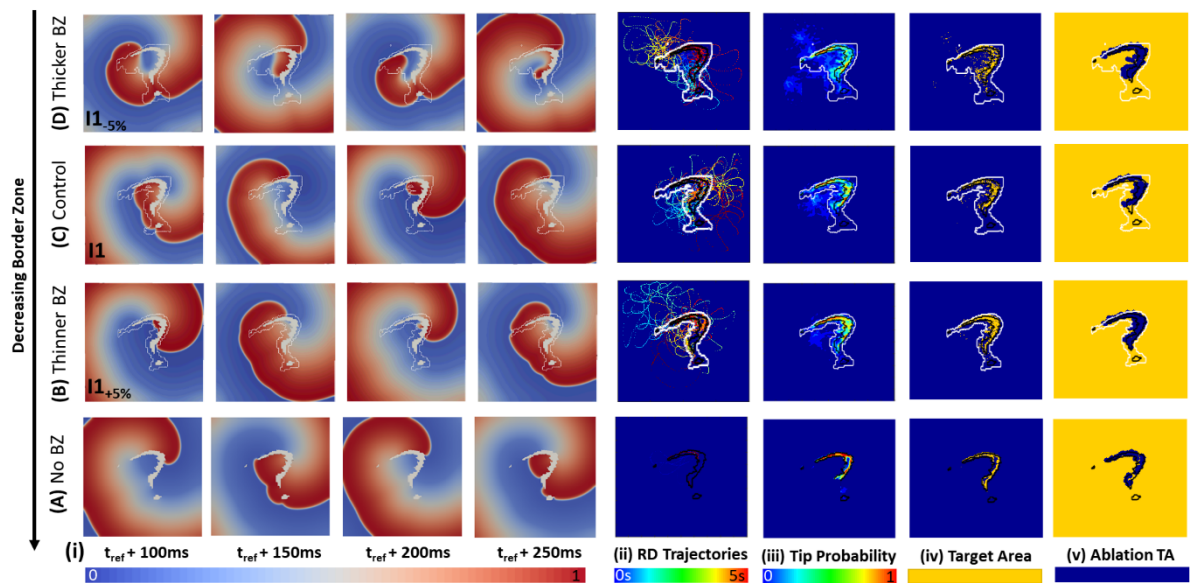


Figure 6.9: Effect of the BZ size on the dynamics of RDs in a 3D tissue slab. The voltage maps showing the behaviour of RDs over a period of 150 ms, for a RD initiated at one of the 9 locations, are shown in panel (A-D, (i)). The further column (A-D, ii) shows the corresponding tip trajectories. Here each row (A-D) represent a fibrotic patch with (A) no BZ to a fibrotic patch with the (D) largest BZ, respectively. The RD tip probability maps and the corresponding target areas obtained for each case is shown in columns (iii) and (iv), respectively. Finally, the ablation lesions following the virtual CA of the identified target areas are shown in column (v).

6.4.2.2 The patient-specific LA study

In the patient-specific LA model, the sensitivity of the target areas to the IIR threshold (I_1) was tested by increasing the control value ($I_{1\text{control}}$) by 1% ($I_{1+1\%}$) and 3% ($I_{1+3\%}$), which decreased the FB by 2% and 5% (Table 6.2), respectively, and also decreased the size of the BZ surrounding the dense fibrotic region (Figure 6.10, A1-C1). On repeating the simulations from Chapter 5 (Section 5.3.3), we found that out of 5 target areas identified using $I_{1\text{control}}$ (Figure 6.10, D, black), changing the intensity threshold to $I_{1+1\%}$ resulted in 4 of the target areas (Figure 6.10, D, blue) still present in the same fibrotic patch and 1 target area disappearing. Further increasing the threshold to $I_{1+3\%}$ resulted in 3 of the target areas (Figure 6.10, D, orange) present

in the same position and 2 of the control target areas disappearing. The overlap between CA lesions targeting the target areas in the models with $I1_{\text{control}}$ and $I1_{+1\%}$ and $I1_{+3\%}$, evaluated by computing the Dice score was 0.59 and 0.61, respectively.

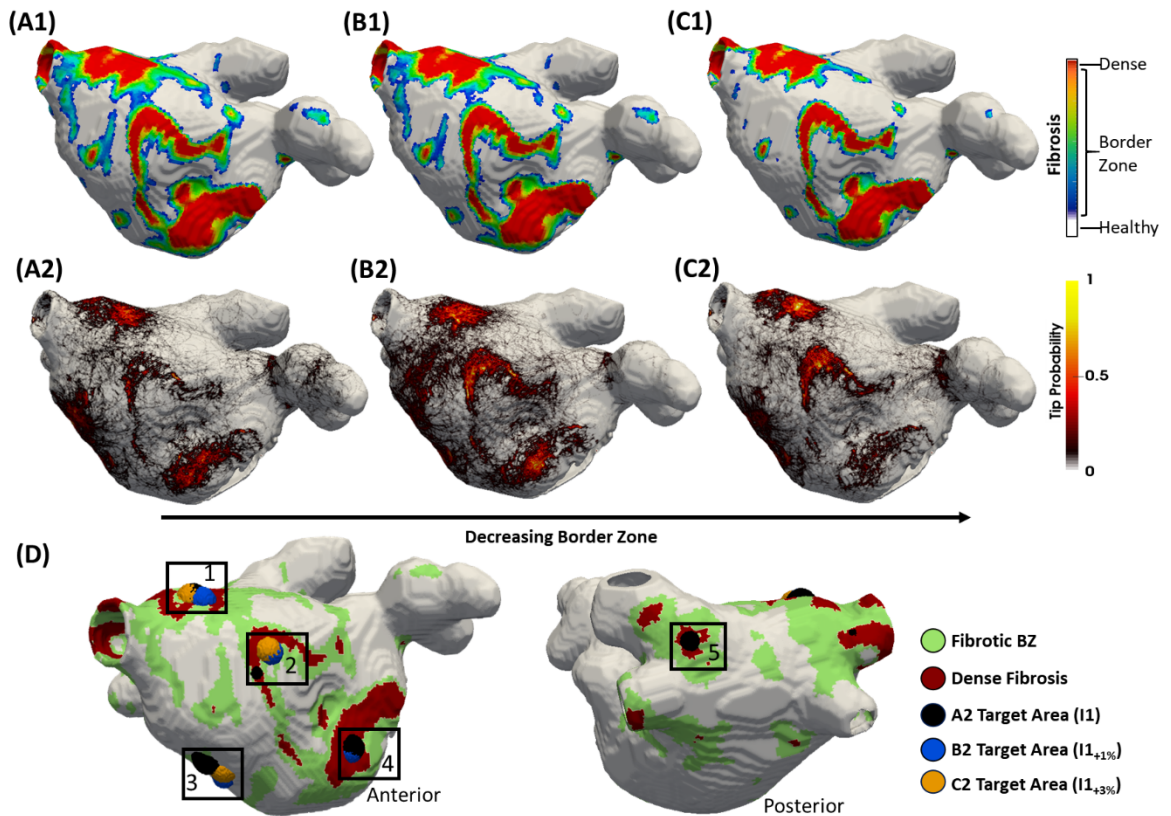


Figure 6.10: Effect of the BZ size on the dynamics of RDs in the patient-specific LA model. The fibrosis maps and the corresponding tip probability maps, for different sizes of BZ are shown in panels (A1–C1) and (A2–C2), respectively. Here, cases A–C were obtained by using the threshold $I1$, $I1_{+1\%}$ and $I1_{+3\%}$, respectively. Panel D shows the overlap between the target areas for each BZ case ($I1$: black, $I1_{+1\%}$: blue and $I1_{+3\%}$: orange) with a sphere, whose centre is the centroid of the patch and the radius represent the size of the target areas. The control ($I1$) case had 5 distinct target areas regions, out of which 3 (label 1–3) consistently overlapped with target areas identified across the other cases and the other 2 (label 4–5) gradually disappeared as the threshold was increased.

6.5 Discussion

In Chapter 5, we presented an image-based computational workflow for the prediction of potential target areas for CA in AF patients with an existing LGE-MRI scans of the LA. In this chapter, we first used the previously constructed patient-specific LA models to perform virtual CA of our predicted target areas and compare its success in-silico with existing clinical CA strategies. Second, we investigated the sensitivity of the RD dynamics and the corresponding target area locations to the LGE intensity thresholding. Our simulation results showed that target area-guided CA combined with existing clinical strategies (Strategies 4-5) has a higher success rate compared to PVI with and without additional linear lesions (Strategies 1-2). Therefore, this study predicts that targeting atrial regions with high probability of RDs anchoring, as identified from patient-specific simulations, can improve the clinical CA efficacy in AF patients. However, our results also highlight the potential sensitivity of the identified patient-specific target areas to specific image processing methods used for the quantification of atrial fibrosis from LGE-MR images.

6.5.1 Virtual Ablation on the predicted target areas

To meet the first aim of the study, we used LA models of two AF patients from Utah 3 category (Chapter 5): one with persistent AF (Patient 2) and another with paroxysmal AF (Patient 3). We tested two clinical strategies: (1) PVI and (2) PVI with additional linear lesions at the LA roof and MV. The former is considered a cornerstone of CA in PAF patients [99], while the latter has been used in combination with PVI in patients with chronic forms of AF [258]. We then compared the outcomes of these two CA strategies with three target area guided ablation strategies: (3) ablation of the target areas only, (4) ablation of the target areas with additional application of linear lesions joining the target areas to the nearest boundary (the PVs or MV), and (5) the ultimate strategy that combined target area guided ablation with PVI and a connecting set of linear lesions.

Our simulation results demonstrated that in cases where clinical CA strategies (Strategies 1-2) were unable to terminate AF, Strategy 4 successfully terminated AF in majority of these cases for both patient-specific LA models either by eliminating the RDs and AF or by converting AF to AT (Figure 6.7). Strategy 5, combining Strategies 1 with Strategy 4, resulted in an increase in AF termination rate (P2: 90%, P3: 100%) compared to Strategies 1 only (P2: 40%, P3:50%).

Our study shows that if RDs are present in regions far away from the PVs, clinical strategies based on PVI (Strategy 1) would not be efficient in terminating AF. Although the additional linear lesions joining the PVI at the roof and to the MV (Strategy 2) are known to modify the atrial substrate and compartmentalize the atria into smaller regions, we found it does not always facilitate the termination of RDs that are located within these compartments. This is most often the case in PsAF patients with fibrotic remodelling in the atria, which favours maintenance of AF drivers in regions outside the PVs, as evidenced by clinical findings [55,114]. The non-PV drivers can explain why large-scale randomised clinical trials have found a lack of reduction in the AF recurrence rates after PVI even with additional linear ablation lesions [106]. Moreover, AF-induced remodelling develops in a patient-specific manner [182], and hence the RD locations are also expected to be patient-specific and the standardised CA strategies may not work for everyone. This suggests that our image-based, mechanistic approach to CA, based on the knowledge of RD locations underlying AF, can help improve the existing CA strategies.

Virtual ablation of target areas alone (Strategy 3) resulted in the stabilisation of meandering RDs in the vicinity of ablated regions, and the conversion of AF to AT with a lower MF (Figure 6.6, A-B). Similar findings have been reported in a study by Bayer et al. [235], where CA directly targeted the RD tip. Although this strategy reduced MF to about 6 Hz in some simulations, in most cases the patients remained in rapid AT with MF of up to 8 Hz. However, connecting the target areas to the nearest boundary (PVs or MV) using additional linear lesions (Strategy 4) either terminated all RDs (Figure 6.6, C1) or generated a single re-entrant circuit (Figure 6.6, C2) with lower MF (5-6 Hz) than with Strategy 3. Moreover, Strategy 4 was also superior to Strategy 3 in preventing AF inducibility. Connecting all target area ablation lesions with linear lesions leading to unexcitable boundaries resulted in either termination of all RDs (Figure A. 8, A to B), or conversion of AF to AT due to an RD anchoring around the MV (Figure A. 8, C to D). Here the linear lesions connecting the target areas to the boundaries prevent the RD formation.

Furthermore, when we combined target area guided ablation with PVI by joining the respective CA lesions with additional linear lesions (Strategy 5), the previously sustained RDs located far away from the PVI lesions were either completely terminated or AF converted to AT with a lower MF (< 5 Hz). These results are consistent with previous clinical studies that have shown that CA of regions with high-frequency activity (associated with RDs) identified with spectral

analysis resulted in AF termination by direct transition to either sinus rhythm or AT [111,257,259]. Moreover, CA at such high-frequency sites typically prolongs AF cycle length [257,260], which is consistent with the decrease in MF following target area ablation reported in this study. Overall, our novel Strategy 5 proved to be the most efficient (P2: 90%, P3: 100%).

Note that a recent clinical study by Calvo et al. [259] have used a similar approach, where ablation on RD domains identified using EAM was performed with limited linear lesions joining the identified RD domains with the unexcitable boundaries (PVI lesion in the LA). Their results showed a reduction in dominant frequency and acute termination to sinus rhythm in 15% of persistent AF patients, and 1 year follow up showed 70% of the patients to be free from AF. Our simulation results are consistent with these findings and can explain the mechanism underlying its success. Note also that Calvo et al. relied on EAM to identify the RD domains, which can be unreliable due to limitations of EAM technology (e.g., poor atrial coverage and mapping resolution). Our personalised image-based computational models can enable the identification of these regions with greater accuracy, which further highlights the potential of such models for improving the efficiency of CA in chronic AF patients. However, it is important to note that the acute termination does not predict long term success. Future clinical trials are required to predict the long-term success of this strategy.

6.5.2 LGE-MR intensity thresholding and RD locations

Patient-specific fibrosis distribution is an important component of personalised computational models [14,225,235,250]. Moreover, computational studies have shown that the spatial architecture of fibrosis influences the induction and anchoring locations of RDs associated with AF [15,182]. Therefore, a standardised method of extracting fibrosis distribution from patient LGE-MRI data is of great importance for the success of such approaches. However, there is no consensus on the LGE-MRI intensity threshold settings for clinical assessment of fibrosis.

In this study, we varied the IIR threshold used for differentiating between fibrotic BZ and healthy tissue by $\pm 5\%$ in the 3D slab model, while in the patient-specific models we varied it by $+1\%$ and $+3\%$ and evaluated its effects on the RD anchoring locations. A larger variation was used in case of the slab model, as we were interested in evaluating the effect of large changes in the BZ size on the RD dynamics. Our simulation results showed that, although anchoring of RDs to the fibrotic patch was affected by the BZ size, locations of the target areas remained unaltered within this patch. However, in the patient-specific models, we focused on

the identification of such target area locations with smaller variations that maintained realistic BZ size.

Our simulation results in the patient-specific model show that altering the intensity threshold by up to +3%, 3 out of 5 target areas identified from the control are located within the same fibrotic patches with an average displacement of 3.21 ± 2.62 mm, while the remaining 2 disappeared. This could be explained by a decrease in the BZ size due to increased intensity threshold, which influences the anchoring of the RDs to fibrotic patches as seen in our 3D slab simulations. These results demonstrate that the choice of the LGE-MRI intensity threshold for assessment of fibrosis can influence the locations of RDs.

Although our results suggest that AF simulations performed with models based on I_{control} identified a subset of target areas that were consistent with models based on both $I_{+1\%}$ and $I_{+3\%}$, a single threshold may not help identify all the target areas. Therefore, the clinical deployment of personalised computational models should take into careful consideration the fact that these models inherit the limitations of the current fibrosis imaging and mapping techniques. One of the major limitations is the dependence of both LGE-MR imaging and voltage mapping methods on a set of empirical intensity thresholds for the identification of fibrosis [87].

6.5.3 Limitations

In the study, all the CA lesions were applied simultaneously. However, in the clinic, they are applied in a sequential manner. This could potentially influence the outcome of virtual ablation. Furthermore, the virtual lesions were ‘perfect lesions’ that were fully transmural and maintain a complete conduction block. This is hard to achieve clinically and depends on the operator and the location of ablation. Previous studies have shown that incomplete lesions can prevent termination of AF and increase its recurrence [261,262]. Another limitation of this study is that our AF simulation workflow used the cross-filed protocol rather than fast pacing (e.g., by McDowell et al. [14]) to initiate AF. Although the workflow is designed to predict the ultimate RD anchoring sites rather than the initiation sites, the latter may also be important for AF termination and its recurrence prevention. However, our workflow could be easily adjusted to include fast pacing for the evaluation of both RD anchoring and initiation mechanisms.

For the LGE-MRI segmentation sensitivity test, we only considered the effects of change in one of the IIR thresholding parameters, which differentiates between fibrotic BZ and healthy tissue. A more thorough evaluation of the fibrosis segmentation is warranted in future studies. Besides, we have not assessed the sensitivity to varying electrophysiological properties of atrial tissue (e.g., conduction velocity and APD), which should also be addressed in the future.

6.6 Conclusions

This chapter demonstrates how patient-specific computational models could be used for successfully guiding CA treatment for AF termination. Simulations of the patient-specific LA models showed that RDs sustaining AF were localised at specific regions of fibrotic tissue (target areas), which potentially could be targeted to optimize CA. Performing virtual ablations on the target areas and connecting them to the nearest PVs or MV has superior anti-fibrillatory effect compared to ablating the target areas alone, as well as compared to clinically accepted strategies such as PVI. Success of the image-based computational identification of RDs and guidance of CA can also depend on the accuracy of fibrosis segmentation from patient LGE-MRI data.

Chapter 7

Conclusions

7.1 Summary

AF is the most common cardiac arrhythmia and a huge healthcare problem, but its mechanisms are incompletely understood, and clinical therapies such as CA have poor long-term outcomes. The work presented in this dissertation was set out to evaluate the influence of patient-specific atrial structure on electrophysiological mechanisms, specifically the dynamics of re-entrant drivers (RDs) of AF. The study focused on atrial wall thickness (AWT) and atrial fibrosis, both of which can be reconstructed from medical imaging data and have been linked to atrial structural remodelling underlying the progression of AF. The specific aims of this study were to: 1) develop image-based 3D atrial models using patient MRI data, 2) apply the models to dissect the mechanistic links between atrial structure and RD dynamics, 3) use the simulation outcomes to quantify the ultimate patient-specific RD locations, and then 4) evaluate CA strategies that can efficiently terminate the RDs and may improve AF therapy in the clinic.

7.2 Main Findings

The main outcomes of the work are summarised below reflecting the structure of its chapters

1. Sharp gradients in AWT determine the drift direction and anchoring locations of RDs.

Basic effects of AWT gradients on the dynamics of RDs were investigated in Chapter 3. In this study, we used a 3D atrial tissue slab with an AWT step to explore how sharp AWT gradients can stabilise RDs. Moreover, we combined the AWT step with the presence of fibrotic tissue to explore how additional structural effects can influence the RDs. The key findings of this work were: (i) the sharp gradients of AWT act as anchoring locations for RDs; (ii) in the presence of fibrosis, the AWT step acts as a competing attractor for the RDs. The underlying mechanism that enabled anchoring of RDs to these locations was based on slow conduction, which was due to a large source-to-sink mismatch in regions of high AWT gradient and reduced cell-to-cell coupling in fibrotic regions. Our simulations showed that several factors influenced

the dynamics of RDs: the height of the step, the distance of the RD initiation site from the AWT step, as well as the relative distance of the RD initiation site from the step and the fibrotic patch.

2. Patient-specific AWT gradients and fibrotic patches are important attractors of RDs.

In Chapter 4, we investigated the influence of AWT gradients on the RD dynamics in realistic, image-based atrial geometries and evaluated the comparative effects of patient-specific AWT gradients and fibrosis distribution. To the best of our knowledge, this is the first study that compares such effects in realistic atrial geometries. In this study, we used MRI-based RA and LA geometries from 4 healthy volunteers and 2 paroxysmal AF patients. The key findings of this work were as follows: (i) in the RA, RDs stabilised around structural features with large AWT gradients, while the addition of fibrotic patches provided an alternative attractor for the RDs and (ii) in the LA, which had more uniform AWT distribution, the RD locations were determined by the distribution of fibrotic patches or by anatomical features such as the PVs. These findings may explain why CA in the RA often targets the crista terminalis, a thick ridge forming a prominent AWT gradient, while CA procedures in the LA focus on the PVs.

3. RD locations in the LA can be identified from patient-specific fibrosis distribution.

In Chapter 5, we focused on the effects of fibrosis on RD dynamics in the LA. Specifically, we: (i) developed 3D LA models with patient-specific geometry and distribution of fibrosis obtained from LGE-MRI of 6 AF patients, (ii) applied the models to explore the dynamics of RD stabilisation in the presence of slow-conducting fibrotic patches and (iii) generated patient-specific maps of the RD locations, relative to the distribution of fibrosis, to identify potential targets for CA. The key finding of this work was that RDs were typically found at fibrotic regions in AF patients from Utah 3 and 4 categories with high FB (>25%), but more often near the PVs in patients from Utah 2 category. The RDs anchored to specific, relatively small regions, labelled as target areas, with a high percentage of target areas located within the fibrotic tissue region in patients from Utah 3 and 4 categories. Thus, the RD locations in patients with high FB were determined by unique patient-specific fibrosis distribution. Such locations were much smaller than the entire fibrotic area and may potentially be targeted by CA therapy.

4. Image-based models enable evaluation of efficient virtual ablation strategies for AF.

Chapter 6 used predictions of the image-based LA models to simulate and evaluate several CA strategies for terminating AF. Specifically, we (i) simulated virtual ablation of target areas

predicted from the models and compared its success with existing clinical CA strategies and (2) explored sensitivity of the predicted target area locations on the choice of LGE-MRI thresholding parameters. The main finding of this work was that performing virtual ablations of the target areas and connecting them with linear lesions to the nearest PVs or MV had superior anti-fibrillatory effect compared to ablating the target areas alone, as well as compared to clinically accepted strategies such as PVI. However, the success of the image-based computational identification of RDs and guidance of CA can also depend on the accuracy of fibrosis segmentation from patient LGE-MRI data. These findings provide an initial evaluation of the image-based computational tools that, after careful clinical validation, can potentially be used for the guidance of CA in AF patients.

7.3 Future work

The image-based computational workflow presented in this dissertation is a promising tool which can build up on mechanistic knowledge and help improve CA therapy in the future. To facilitate future clinical application, it needs to be further developed and clinically validated.

First, the workflow can be extended to incorporate further patient-specific details, such as atrial fibre orientation and electrophysiological heterogeneity. Such details have been shown to play important roles in the genesis of AF [145,147,148], and their integration may substantially increase the predictive power of the models. However, limitations of existing imaging techniques hinder an adequate reconstruction of the complex atrial fibre architecture from patient data. High resolution ex-vivo imaging protocols [263] cannot be applied to AF patients in a clinical setting, while alternative strategies based on invasive electro-anatomical mapping suffer from poor atrial coverage and resolution [264]. Hence, future patient-specific modelling will be reliant on the improvement of imaging technology to reconstruct fibre orientations in-vivo.

Second, one of the strengths of the workflow is in the simple and efficient representation of the atrial electrophysiology using the Fenton-Karma model. This was chosen due to its ability to reproduce APD restitution properties of remodelled atrial cells at a low computational cost. This allowed us to perform a large number of 3D image-based simulations within a clinically-compatible timescale. Moreover, simple, standardised electrophysiology across patient-specific models enabled an unbiased evaluation of the atrial structure effects on AF dynamics. Future studies could extend the existing workflow to incorporate more detailed models that capture

multiple ionic currents in an atrial cell, as well as regional differences in atrial cellular electrophysiology, such as the CRN model and its modifications [145,153]. Although such models are more computationally expensive, they may help provide more in-depth insights into the interplay between atrial electrophysiology and structure during AF. This will facilitate future population studies into the role of inter-patient variability in AF dynamics [265]. Moreover, future studies will also need to investigate the influence of electro-mechanical coupling in the atria on AF [266]. This would lead to the improved understanding of the impact of RDs on atrial contraction, as well as the effects of contraction of the underlying electrophysiology via the stretch-activate channels.

Third, translating the workflow to the clinic will require a further reduction of the related computational costs. Possible solutions include the application of graphics processing unit (GPU) technologies, enabling fast simulation on desktop computers, and well as the development of deep learning inspired tools that could be used to increase the predictive capabilities of the computational framework. Recent work from our group demonstrated that deep neural networks could be used to reduce the use of computational atrial models and to predict optimal CA strategies directly from patient-specific imaging data [267]. Hence, future image-based computational workflows could integrate deep learning algorithms as a low-cost step that complements or replaces the 3D models.

Finally, the workflow for identification of CA targets needs to be validated against patient-specific electrophysiology datasets and tested prospectively in a large cohort of AF patients.

Chapter 8

Appendix

8.1 Numerical Implementation

8.1.1 A single cell model

The atrial cell models used in work presented in this thesis were: (i) atrial Fenton Karma cell model (aFK) and the modified Courtemanche-Ramirez-Nattel (CRN) model. Figure A. 1 below shows the comparison of APD_{90} restitution curves.

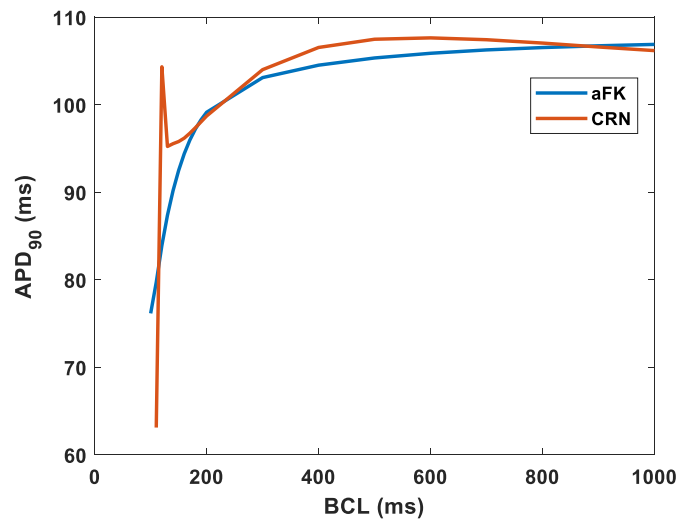


Figure A. 1: APD_{90} restitution plot for aFK and modified CRN models.

8.1.2 3D action potential propagation

3D geometries used for performing simulations in this thesis were: (A) a rectangular 3D slab (Chapter 3) and (B) patient-specific 3D geometries derived from MRI data (Chapter 4-6). In these geometries, the isotropic mono-domain equation (Chapter 2, Section 2.5.2.1, eq 2.17) was solved with no-flux boundary condition. The space (dx) and time step (dt) were set to of 0.3 mm and 0.005 ms, respectively. The isotropic diffusion coefficient (D) in the model used was 0.1 mm²/s for healthy tissue. While, the lowest D used for the model was 0.016 mm²/ms for dense fibrotic regions. Von Neumann stability analysis (described in Chapter 2, section 2.5.3.2) for the chosen parameters were satisfied as follows:

$$\frac{D\Delta t}{\Delta x^2} \leq \frac{1}{2N}$$

$$LHS: \frac{D\Delta t}{\Delta x^2} = \frac{(0.1)(0.005)}{0.3^2} = 0.0056$$

$$RHS: \frac{1}{2N} = \frac{1}{2(3)} = 0.1667$$

$$0.0056 \leq 0.1667$$

Numerical integration steps satisfy Von Neumann stability criterion

To test the convergence of the numerical solution in space, a benchmark problem was designed based on Niederer et al. [268]. Briefly, the tissue geometry used was a 3D rectangular slab of dimension $3 \times 7 \times 21$ mm (Figure A. 2). The mono-domain equation was solved for four spatial resolutions ($dx = 0.1, 0.2, 0.3$ and 0.5 mm), each with a time step of 0.005 ms and no-flux boundary conditions. The AP propagation was simulated with an initial stimulus delivered to a region of volume $1.5 \times 1.5 \times 1.5$ mm, located at the corner of the cuboid (Figure A. 2, (A), red box) at BCL of 400ms. The activation time (AT), defined as the time at which the membrane potential reaches its peak value ($V=1$), was recorded for each spatial step at the 10th beat. The results were compared by analysing the AT values along a diagonal line across the geometry (Figure A. 2, P1-P3). The ATs measured at the far edge P3 obtained with different spatial steps are summarised in Table A. 1. These calculations show that for the spatial step of 0.3 mm, the error with respect to solution for the smallest spatial step of 0.1 mm is within 10% [27]. Therefore, 0.3 mm is a viable choice for the numerical implementation.

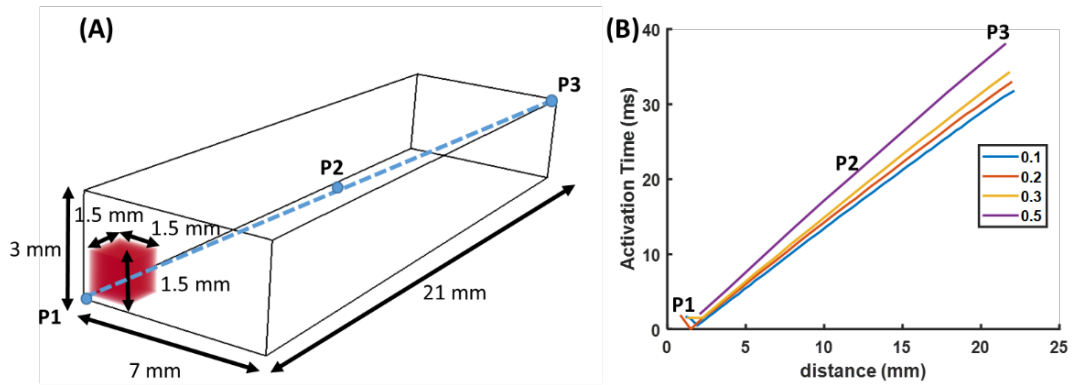


Figure A. 2: The numerical convergence test. (A) A schematic image of the geometry used for the simulations. The initial stimulus was applied on the region in red and the activation time (AT) was measured along a line from P1 to P3 and the plot of the AT is shown in panel (B).

Step size (dx)	AT (ms)	$\frac{AT_{0.1} - T}{AT_{0.1}}$
0.1	31.80	-
0.2	33.00	3.88 %
0.3	34.30	7.86 %
0.5	38.10	19.81 %

Table A. 1: The activation time (AT) values for different spatial resolutions.

8.1.3 Implementation for RD Tip Tracking Algorithm

In the main text, we defined the tip of the RD as the intersection between two successive iso-potential surfaces, $v^t(\mathbf{r}) = V_{iso}$, where V_{iso} is a convenient choice of iso-value to differentiate between wavefront and wave-back, $\mathbf{r} = (x, y, z)$ is the position vector and, $dv(\mathbf{r})/dt = 0$. The simulations are performed in discrete space (dx, dy and $dz = \Delta$) and time (dt) steps, and therefore, the problem of finding the intersection points can be represented with

$$v^t(\mathbf{r}) = v^{t+dt}(\mathbf{r}) = V_{iso} \quad \text{A.1}$$

In 3D geometry, the intersection between two successive iso-potential surfaces is a line (also known as filament) defined by a series of points inside the geometry. In our discrete 3D geometry with equal spacing (dx, dy and $dz = \Delta$), a location (x, y, z) corresponds to a cubic voxel (Figure A. 3, A) of side Δ , centred at a point given by $x = i\Delta, y = j\Delta$ and $z = k\Delta$. Each point on the filament can be identified by calculating the intersection points between the two iso-potential lines on the all the faces of a cube with sides ($x = i\Delta, y = j\Delta$ and $z = k\Delta$) centred at $(i + 0.5, j + 0.5, k + 0.5)$. Each face is defined by a set of 4 grid points and the voltage (V) within each face of the cube can be estimated using bilinear interpolation.

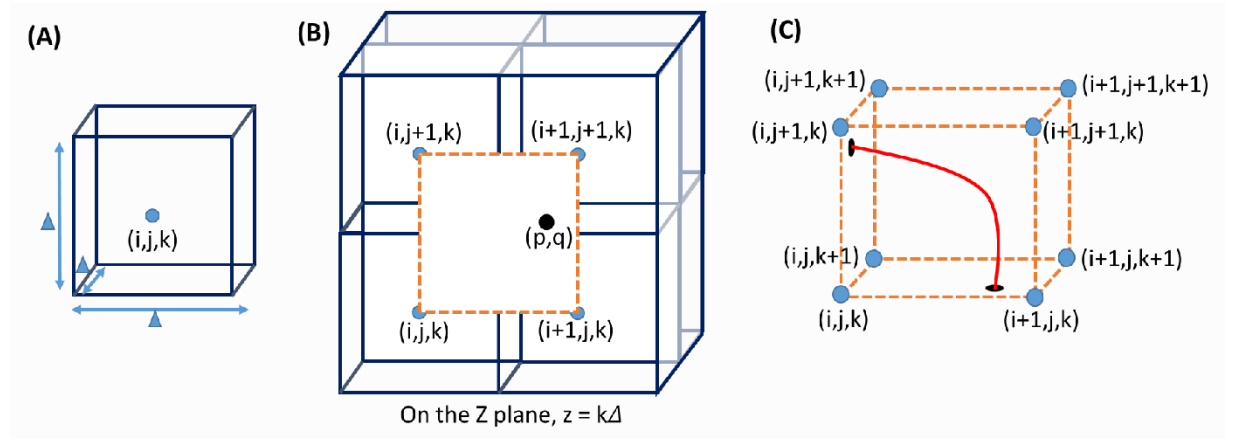


Figure A. 3: Bilinear interpolation to calculate the location of the RD tip. (A) A voxel with centre defined at the grid point (i,j,k) and edges of length Δ , which group together in 8 to form a cube centred at $(i + 0.5, j + 0.5, k + 0.5)$ and (B) the tip of the RD calculated on the z plane of this cube, where points (p,q) are defined in the local coordinates. (C) the filament of the RD (in red) identified by calculating the tip of the RD (marked by a black circle) on all faces of a cube defined by 8 grid points in the geometry.

For simplicity, we first calculate the position of the RD tip on the face of the cube where $z = k\Delta$ (Figure A. 3, B). Here, we begin by converting the global coordinate system into a local system by defining local coordinates for each dimension, such that they vary between 0 and 1:

$$p = \frac{x - i\Delta}{\Delta} \quad \text{A.2}$$

$$q = \frac{y - j\Delta}{\Delta} \quad \text{A.3}$$

Then the voltage at a location (p, q) , at time t and $t + 1$, using bilinear interpolation estimate for a point inside this rectangle is given by a weighted sum of the measured voltage values at the four corners (equation A.4 and A.5). The weighted can be written in terms of the local coordinates of the target point, (p, q) as follows;

$$V_{p,q}^t = V_{i,j,k}^t(1-p)(1-q) + V_{i+1,j,k}^t(p)(1-q) + V_{i+1,j+1,k}^t(pq) + V_{i,j+1,k}^t(1-p)(q) \quad \text{A.4}$$

$$V_{p,q}^{t+1} = V_{i,j,k}^{t+1}(1-p)(1-q) + V_{i+1,j,k}^{t+1}(p)(1-q) + V_{i+1,j+1,k}^{t+1}(pq) + V_{i,j+1,k}^{t+1}(1-p)(q) \quad \text{A.5}$$

The location for the tip of the RD can be found at the point where $v(p, q) = v^{t+dt}(p, q) = V_{iso}$. Therefore, both equations A.4 and A.5 must be equated to V_{iso} . After re-arranging, this leads us to the following equations A.6 and A.7.

$$pq[V_{i,j,k}^t - V_{i+1,j,k}^t + V_{i+1,j+1,k}^t - V_{i,j+1,k}^t] + q[V_{i,j+1,k}^t - V_{i,j,k}^t] + p[V_{i+1,j,k}^t - V_{i,j,k}^t] + [V_{i,j,k}^t - V_{iso}] = 0 \quad \text{A.6}$$

$$pq[V_{i,j,k}^{t+1} - V_{i+1,j,k}^{t+1} + V_{i+1,j+1,k}^{t+1} - V_{i,j+1,k}^{t+1}] + q[V_{i,j+1,k}^{t+1} - V_{i,j,k}^{t+1}] + p[V_{i+1,j,k}^{t+1} - V_{i,j,k}^{t+1}] + [V_{i,j,k}^{t+1} - V_{iso}] = 0 \quad \text{A.7}$$

The main idea is that we solve for p and q , which satisfy both equations A.6 and A.7.

Here, a detailed derivation of the steps involved is provided:

First, for the simplification purpose, we replace the constants in equations A.6 and A.7 with notations summarised below in A.9, to get to equation A.10 and A.11.

$AC = V_{i,j,k}^{t+1} - V_{i+1,j,k}^{t+1} + V_{i+1,j+1,k}^{t+1} - V_{i,j+1,k}^{t+1}$	$AD = V_{i,j,k}^{t+1} - V_{i+1,j,k}^{t+1} + V_{i+1,j+1,k}^{t+1} - V_{i,j+1,k}^{t+1}$	A.9
$GC = V_{i,j+1,k}^t - V_{i,j,k}^t$	$GD = V_{i+1,k}^{t+1} - V_{i,j,k}^{t+1}$	
$BC = V_{i+1,j,k}^t - V_{i,j,k}^t$	$BDC = V_{i+1,j,k}^{t+1} - V_{i,j,k}^{t+1}$	
$DC = V_{i,j,k}^t - V_{iso}$	$DD = V_{i,j,k}^{t+1} - V_{iso}$	

This leads us to:

$$0 = (p * q * AC) + (q * GC) + (p * BC) + DC \quad \text{A.10}$$

$$0 = (p * q * AD) + (q * GD) + (p * BD) + DD \quad \text{A.11}$$

Second, subtraction of equation A.10 from A.11 after the multiplication with the terms represented by AD and AC, respectively, gives us equation A.12.

$$q * [GC * AD - GD * AC] + p * [BC * AD - BD * AC] + [DC * AD - DD * AC] = 0 \quad \text{A.12}$$

Third, simplification of equation A.12 by replacing some of the constant terms using notations summarised in A.13 leads to equation 14.

$$\begin{array}{l} R = GC * AD - GD * AC \\ S = DC * AD - DD * AC \end{array} \quad \text{A.13}$$

$$Q = BC * AD - BD * AC$$

$$(q * R) + (p * Q) + S = 0 \quad \text{A.14}$$

Equation A.14 can be rearranged to the value of q ,

$$q = -(p * QR) - SR \quad \text{A.15}$$

Here, $QR = Q/R$ and $SR = S/R$

The next step is replacing q in equation A.10 with equation A.15 and forming the final quadratic equation A.16 with only one variable p .

$$p^2 * (AC * QR) + p * (AC * SR + GC * QR - BC) + (GC * SR - DC) = 0 \quad \text{A.16}$$

In order to solve equation A.16, we replace the constants with notations summarised below in A.17, and get the final simplified equation A.18.

$$\begin{array}{l} T = AC * QR \\ U = AC * SR + GC * QR - BC \end{array} \quad \text{A.17}$$

$$Vv = GC * SR - DC$$

$$p^2 * T + p * U + Vv = 0 \quad \text{A.18}$$

The final step is finding the solution to this quadratic equation A.18. Here, we evaluate the discriminant (D , equation A.19). The value of D provides critical information about the number and nature of the solutions to the quadratic equation.

$$D = \sqrt{U^2 - 4 * T * Vv} \quad \text{A.19}$$

$$p = \frac{-U \pm \sqrt{D}}{2 * T} \quad \text{A.20}$$

In this context, if the value of D^2 is negative, this would mean that the solutions of equation A.18 are imaginary. Therefore, the tip of the RD does not lie within these set of selected pixels. However, if the value of D^2 is positive, this would mean the solutions are real and the RD tip could be located here. The value of p can be found using equation A.20, and subsequently, the value of q can be computed from equation A.15. However, the final test before we can compute the tip location is testing whether the value of p and q lie between 0 and 1, i.e. the bounds of the selected voxels. If they are within these limits, then the location of the tip in terms of its Cartesian coordinates can be calculated using the following equations A.21-23.

$$x = (i + p)\Delta \quad \text{A.21}$$

$$y = (j + q)\Delta \quad \text{A.22}$$

$$z = k\Delta \quad \text{A.23}$$

Next, we repeat the same steps to determine the intersection of the filament with the other faces of the cube, $x = i\Delta$ and $y = j\Delta$, in a similar way. After identification of tips across all faces of the cube, we get the entire filament of the RD in 3D (Figure A. 3, C) and track its location over time. An example of the tip tracking on voltage data on a slab is shown in Figure A. 4

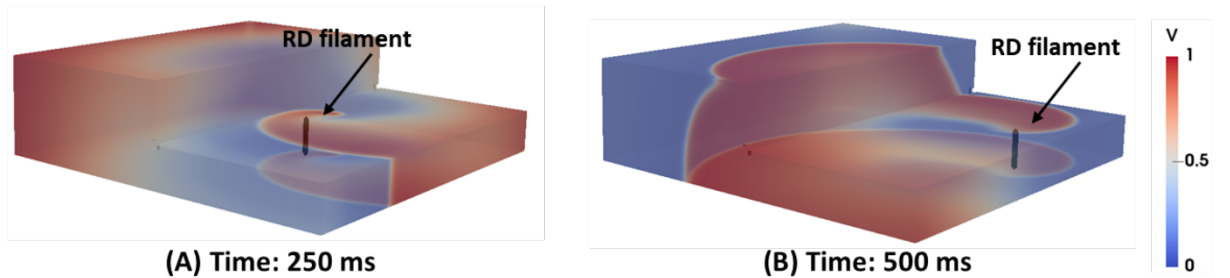


Figure A. 4: Tracking the RD filament over time. The tracking algorithm was implemented with a V_{iso} of 0.8 and time step of 0.05 ms across all the planes to generate the filament (black) shown at 250 ms (A) and 500 ms (B).

8.2 Appendix to Chapter 3

8.2.1 RD tip trajectories in 3D slab with varying AWT step

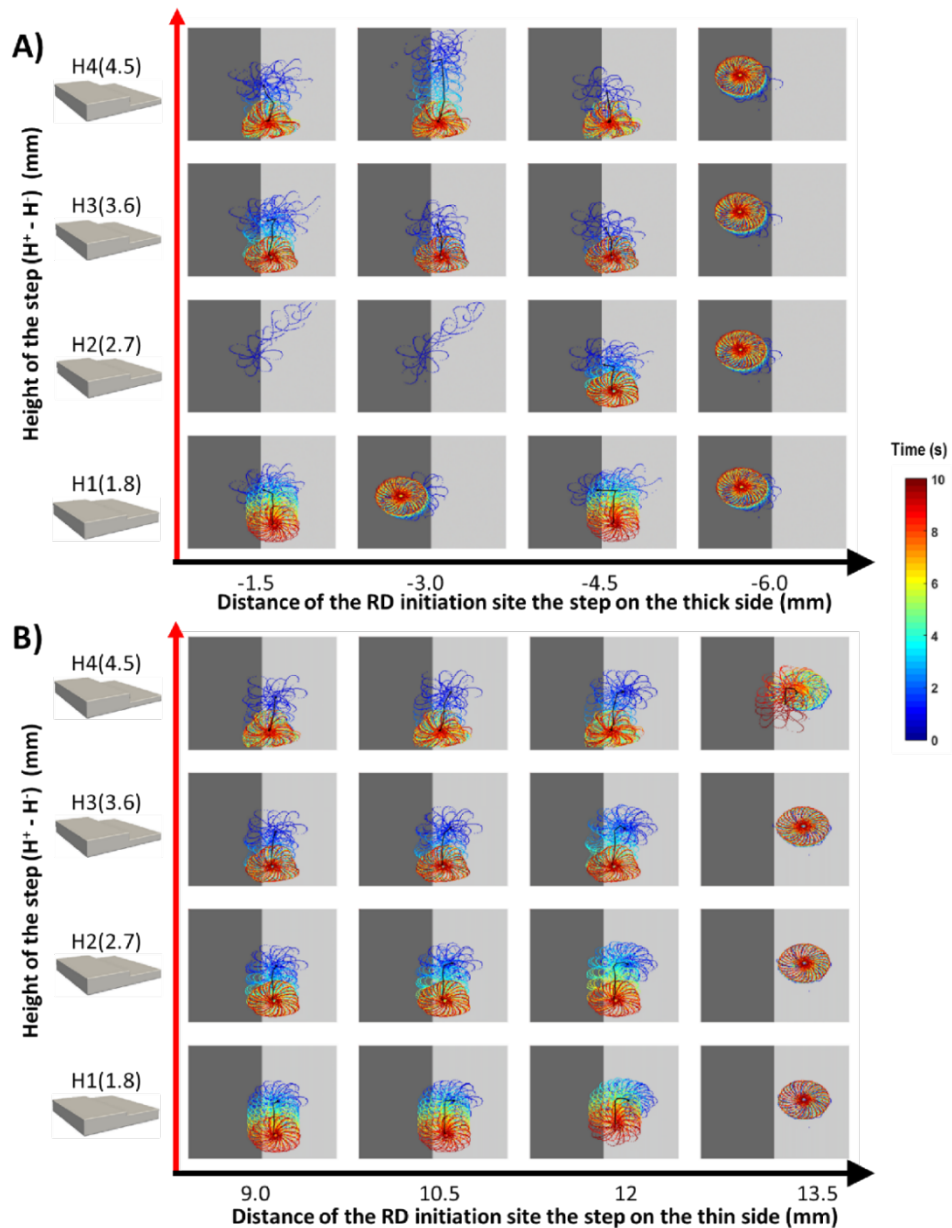


Figure A. 5: Effects of changes in AWT step height and RD initiation location on the anchoring of RDs in 3D atrial slab (Study 1a) with aFK model. Tip trajectories obtained by initiating RDs at multiple locations on the thick (A) and thin (B) side of the 3D slab, while varying the height of the step (H1-4). (A) RDs initiated on the thick side of the slab first drift towards the AWT step, eventually crossing it and drifting along it on the thinner side with exception to H2, where the RDs terminated. (B) RDs initiated on the thin side drifted towards the step and along it, but didn't cross over to the thicker side. Note that the core of the RDs initiated beyond 4.5 mm on the thick side and 12 mm (H1-3) / 15 mm (H4) on the thin side were not sensitive to the step (panels on the right).

8.2.2 Anchoring of RDs in 3D slab with ATW step and fibrotic patch

C

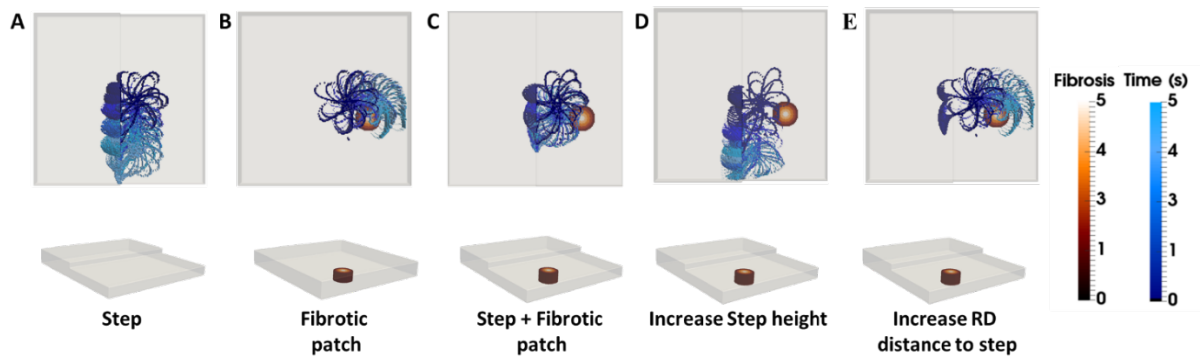


Figure A. 6: RD tip trajectories with the AWT step and fibrosis in a 3D atrial slab. The trajectories are shown for the initiation location H2 (Figure 4D of the main thesis) in the slab with AWT step only (A), fibrotic patch only (B), and both (C). In the first two cases, the RD anchored to the step and the fibrotic patch, respectively. However, in the latter case the RD stopped drifting and stabilised between the step and the fibrotic patch. Increasing the step height from H2 to H4 resulted in the RD drifting to the step (D), while increasing the distance from the step to the RD initiation site (from 7.5 mm to 15 mm) resulted in the RD drifting to the fibrotic patch (E).

8.3 Appendix to Chapter 5

8.3.1 Anchoring of RDs at specific locations inside fibrotic patches

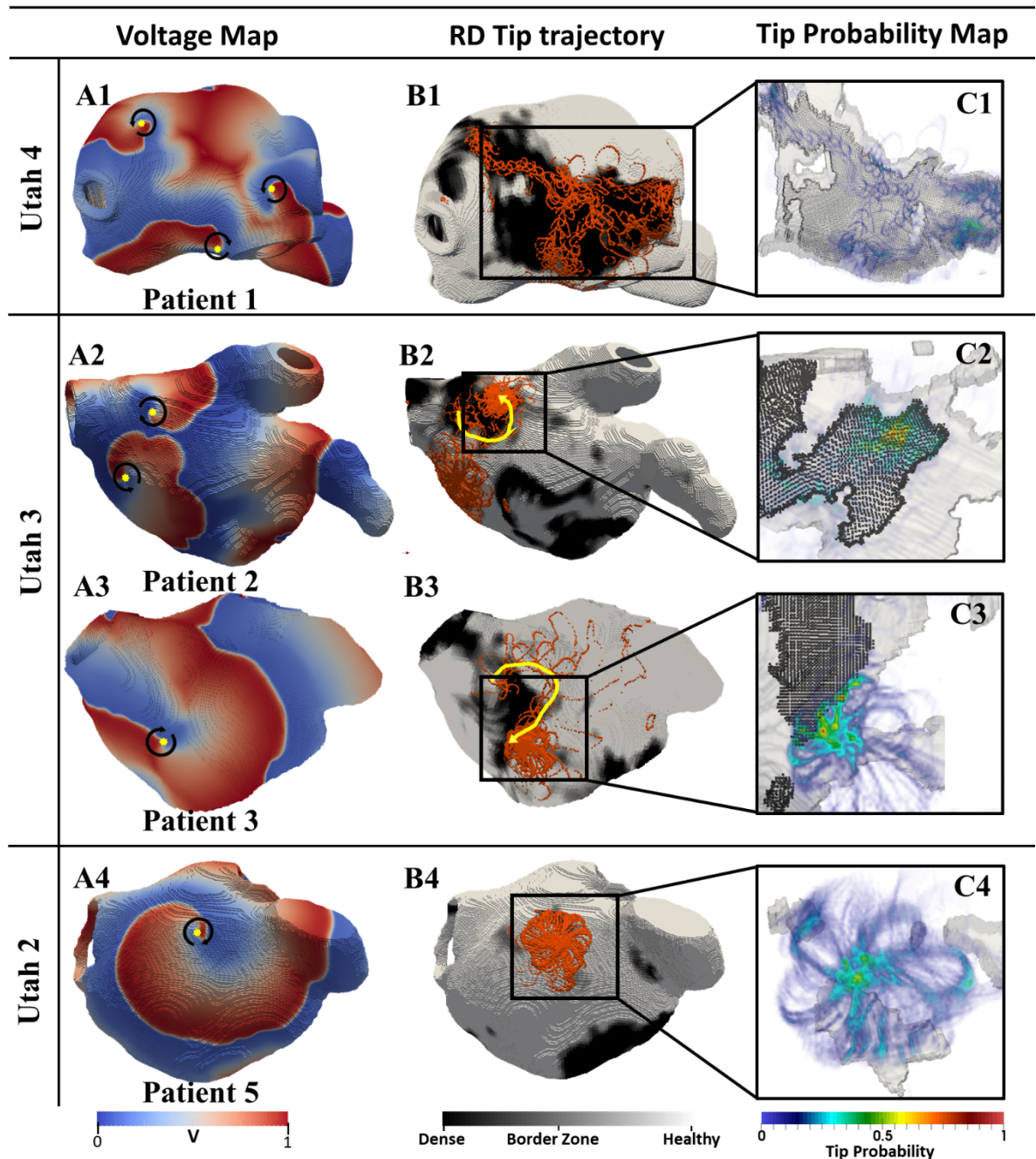


Figure A. 7: The anchoring of RDs to specific locations inside fibrotic patches across patient-specific LA models. Simulation results are shown for 4 AF patients (rows) from different Utah categories. On the left (A1 - 4) are the colour-coded voltage maps and in the middle (B1 - 4) are the respective RD trajectories (orange) superimposed on the fibrosis distributions. On the right (C1 - 4) are the corresponding RD tip probabilities, indicating the exact regions of the patch where the RDs anchored. The yellow arrows indicate the direction in which the RD drifted.

8.4 Appendix to Chapter 6

The MF of atrial activations in Patients 2 and 3 before/after the application of CA strategies.

AF Cases	1	10.06 ± 0.19	6.25 ± 0.02	5.62 ± 0.01	4.14 ± 0.30
	2	7.90 ± 0.30	8.11 ± 0.09	8.11 ± 0.09	0
	3	10.06 ± 0.20	9.37 ± 0.03	9.37 ± 0.03	0
	4	9.87 ± 0.68	5.84 ± 0.30	5.62 ± 0.00	4.09 ± 0.31
	5	10.23 ± 0.32	9.37 ± 0.03	9.37 ± 0.03	4.12 ± 0.31
	6	10.21 ± 0.34	5.94 ± 0.31	4.36 ± 0.11	4.03 ± 0.31
	7	10.19 ± 0.32	5.87 ± 0.31	4.35 ± 0.13	4.04 ± 0.31
	8	10.10 ± 0.28	10.09 ± 0.25	10.08 ± 0.25	4.03 ± 0.31
		Control	TA	TA+L	PVI+TA+L
Patient 3					
AF Cases	1	10.03 ± 0.26	10.03 ± 0.26	10.03 ± 0.27	0
	2	10.07 ± 0.26	7.50 ± 0.11	0	0
	3	10.10 ± 0.28	10.10 ± 0.28	10.10 ± 0.28	4.64 ± 1.45
	4	10.12 ± 0.27	7.50 ± 0.09	0	0
	5	10.41 ± 0.31	6.22 ± 0.15	0	0
	6	10.10 ± 0.29	10.10 ± 0.29	10.10 ± 0.29	4.38 ± 0.00
	7	10.40 ± 0.34	10.14 ± 0.34	0	0
	8	10.43 ± 0.29	6.25 ± 0.07	0	0
	9	10.02 ± 0.21	10.02 ± 0.21	10.02 ± 0.21	10.02 ± 0.21
	10	9.62 ± 0.62	8.12 ± 0.10	0	0
		Control	TA	TA+L	PVI+TA+L
Patient 2					

Table A. 2: The mean frequencies (MF) calculated before and after virtual CA in Patient 2 (bottom) and 3 (top).

TA: target areas

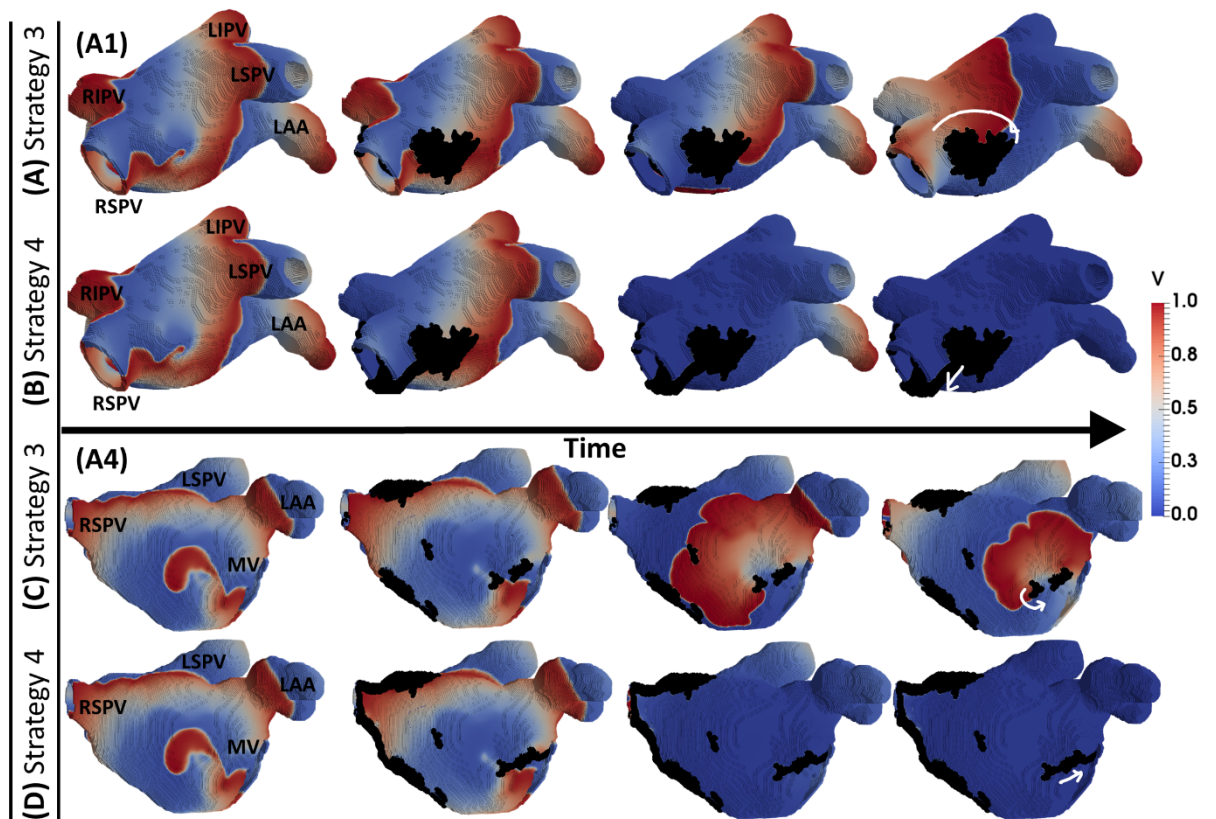


Figure A. 8: The termination of AF using ablation Strategies 3 and 4 in Patient 2. The RDs did not terminate following ablation strategy 3 in either case (A and C). However, the RD terminated following ablation Strategy 2 in both cases, where the target areas were connected to the PV (B) and the MV (D).

References

1. Andrade J, Khairy P, Dobrev D, Nattel S. The clinical profile and pathophysiology of atrial fibrillation: Relationships among clinical features, epidemiology, and mechanisms. *Circ Res*. 2014 Apr 25;114(9):1453–68.
2. Nattel S, Burstein B, Dobrev D. Atrial remodeling and atrial fibrillation: mechanisms and implications. *Circ Arrhythm Electrophysiol*. 2008 Apr;1(1):62–73.
3. Kannel WB, Wolf PA, Benjamin EJ, Levy D. Prevalence, Incidence, Prognosis, and Predisposing Conditions for Atrial Fibrillation: Population-Based Estimates. *Am J Cardiol*. 1998 Oct 16;82(7 A):2N-9N.
4. Kirchhof P, Benussi S, Kotecha D, Ahlsson A, Atar D, Casadei B, et al. 2016 ESC Guidelines for the management of atrial fibrillation developed in collaboration with EACTS. *Eur Heart J*. 2016 Jan 1;37(38):2893–2962.
5. Chugh SS, Havmoeller R, Narayanan K, Singh D, Rienstra M, Benjamin EJ, et al. Worldwide Epidemiology of Atrial Fibrillation. *Circulation*. 2014 Feb 25;129(8):837–47.
6. Gray RA, Pertsov AM, Jalife J. Spatial and temporal organization during cardiac fibrillation. *Nature*. 1998 Mar 5;392(6671):75–8.
7. Sahadevan J, Ryu K, Peltz L, Khrestian CM, Stewart RW, Markowitz AH, et al. Epicardial mapping of chronic atrial fibrillation in patients: preliminary observations. *Circulation*. 2004 Nov 23;110(21):3293–9.
8. Oral H, Knight BP, Tada H, Özaydin M, Chugh A, Hassan S, et al. Pulmonary vein isolation for paroxysmal and persistent atrial fibrillation. *Circulation*. 2002 Mar 5;105(9):1077–81.
9. Calkins H, Hindricks G, Cappato R, Kim Y-H, Saad EB, Aguinaga L, et al. 2017 Expert Consensus Statement on Catheter and Surgical Ablation of Af. *Hear Rhythm*. 2017 Oct 1;20(10):e275–444.
10. Haïssaguerre M, Jaïs P, Shah DC, Takahashi A, Hocini M, Quiniou G, et al. Spontaneous Initiation of Atrial Fibrillation by Ectopic Beats Originating in the Pulmonary Veins. *N Engl J Med*. 1998 Sep 3;339(10):659–66.
11. Ganesan AN, Shipp NJ, Brooks AG, Kuklik P, Lau DH, Lim HS, et al. Long-term outcomes of catheter ablation of atrial fibrillation: a systematic review and meta-analysis. *J Am Heart Assoc*. 2013 Apr;2(2):e004549.
12. Haïssaguerre M, Hocini M, Shah AJ, Derval N, Sacher F, Jais P, et al. Noninvasive panoramic mapping of human atrial fibrillation mechanisms: A feasibility report. *J Cardiovasc Electrophysiol*. 2013 Jun 1;24(6):711–7.
13. Cochet H, Dubois R, Yamashita S, Al Jefairi N, Berte B, Sellal JM, et al. Relationship Between Fibrosis Detected on Late Gadolinium-Enhanced Cardiac Magnetic Resonance and Re-Entrant Activity Assessed With Electrocardiographic Imaging in Human Persistent Atrial Fibrillation. *JACC Clin Electrophysiol*. 2018;4(1):17–29.

14. McDowell KS, Zahid S, Vadakkumpadan F, Blauer J, MacLeod RS, Trayanova N. Virtual electrophysiological study of atrial fibrillation in fibrotic remodeling. *PLoS One*. 2015 Feb 18;10(2):e0117110.
15. Zahid S, Cochet H, Boyle PM, Schwarz EL, Whyte KN, Vigmond EJ, et al. Patient-derived models link re-entrant driver localization in atrial fibrillation to fibrosis spatial pattern. *Cardiovasc Res*. 2016 Jun 1;110(3):443–54.
16. Roney CH, Williams SE, Cochet H, Mukherjee RK, O'Neill L, Sim I, et al. Patient-specific simulations predict efficacy of ablation of interatrial connections for treatment of persistent atrial fibrillation. *Europace*. 2018 Nov 1;20(suppl_3):iii55–68.
17. Iaizzo PA. Handbook of cardiac anatomy, physiology, and devices, third edition. Iaizzo PA, editor. *Handbook of Cardiac Anatomy, Physiology, and Devices, Third Edition*. Totowa, NJ: Humana Press; 2015. 1–817 p.
18. Keener JP. *Mathematical physiology 2009 : systems physiology ii*. Springer; 2008.
19. Wapcaplet. Diagram of the human heart [Internet]. 2006. Available from: [https://commons.wikimedia.org/wiki/File:Diagram_of_the_human_heart_\(cropped\).svg](https://commons.wikimedia.org/wiki/File:Diagram_of_the_human_heart_(cropped).svg)
20. Mammalian Heart and Blood Vessels [Internet]. Available from: <https://opened.cuny.edu/courseware/module/815/student/>
21. Hoda SA. Rubin's Pathology: Clinicopathologic Foundations of Medicine. *JAMA J Am Med Assoc*. 2004;292(11):1376–7.
22. Beigel R, Wunderlich NC, Ho SY, Arsanjani R, Siegel RJ. The Left Atrial Appendage: Anatomy, Function, and Noninvasive Evaluation. *JACC Cardiovasc Imaging*. 2014 Dec 1;7(12):1251–65.
23. Jiang Z, Pajic M, Moarref S, Alur R, Mangharam R. Modeling and verification of a dual chamber implantable pacemaker. In: *Lecture Notes in Computer Science (including subseries Lecture Notes in Artificial Intelligence and Lecture Notes in Bioinformatics)*. 2012. p. 188–203.
24. Kashou AH, Kashou HE. Physiology, Sinoatrial Node (SA Node). *StatPearls*. 2018.
25. Levy MN. Sympathetic-Parasympathetic Interactions in the Normal Heart. In 1989. p. 137–48.
26. Kerin NZ, Louridas G, Edelstein J, Levy MN. Interactions among the critical factors affecting sinus node function: The quantitative effects of the duration and frequency of atrial pacing and of vagal and sympathetic stimulation upon overdrive suppression of the sinus node. *Am Heart J*. 1983;105(2):215–23.
27. Clayton RH, Bernus O, Cherry EM, Dierckx H, Fenton FH, Mirabella L, et al. Models of cardiac tissue electrophysiology: Progress, challenges and open questions. *Prog Biophys Mol Biol*. 2011;104(1–3):22–48.
28. Walker CA, Spinale FG. The structure and function of the cardiac myocyte: A review of fundamental concepts. *J Thorac Cardiovasc Surg*. 1999 Aug 1;118(2):375–82.
29. Matias VRF, Al-Amoudi A, Dubochet J, Beveridge TJ. Cryo-transmission electron

- microscopy of frozen-hydrated sections of *Escherichia coli* and *Pseudomonas aeruginosa*. *J Bacteriol.* 2003 Oct;185(20):6112–8.
30. CK-12. Phospholipid Bilayer (Read) | Biology | CK-12 Foundation [Internet]. 2018 [cited 2019 Nov 23]. Available from: <https://www.ck12.org/biology/phospholipid-bilayer/lesson/Phospholipid-Bilayers-BIO/>
 31. Lodish H, Berk A, Zipursky SL, Matsudaira P, Baltimore D, Darnell J. Membrane Proteins. In: *Molecular Cell Biology*. W. H. Freeman; 2000.
 32. Grant AO. Cardiac ion channels: Basic science for the clinical electrophysiologist. *Circ Arrhythmia Electrophysiol.* 2009 Apr 1;2(2):185–94.
 33. Pandit S V. Ionic Mechanisms of Atrial Action Potentials. In: *Cardiac Electrophysiology: From Cell to Bedside: Seventh Edition*. 2017.
 34. Nerbonne JM, Guo W. Heterogeneous expression of voltage-gated potassium channels in the heart: Roles in normal excitation and arrhythmias. *J Cardiovasc Electrophysiol.* 2002;13(4):406–9.
 35. Nerbonne JM, Kass RS. Molecular physiology of cardiac repolarization. *Physiol Rev.* 2005 Oct;85(4):1205–53.
 36. Kuo SR, Trayanova NA. Action potential morphology heterogeneity in the atrium and its effect on atrial reentry: a two-dimensional and quasi-three-dimensional study. *Philos Trans A Math Phys Eng Sci.* 2006 Jun 15;364(1843):1349–66.
 37. Colman MA. Mechanisms of atrial arrhythmias: insights from the development of a biophysically detailed model of the human atria. University of Manchester; 2013.
 38. Nolasco JB, Dahlen RW. A graphic method for the study of alternation in cardiac action potentials. *J Appl Physiol.* 1968 Aug;25(2):191–6.
 39. Weiss JN, Qu Z, Chen P-S, Lin S-F, Karagueuzian HS, Hayashi H, et al. The Dynamics of Cardiac Fibrillation. *Circulation.* 2005 Aug 23;112(8):1232–40.
 40. Davis LM, Kanter HL, Beyer EC, Saffitz JE. Distinct gap junction protein phenotypes in cardiac tissues with disparate conduction properties. *J Am Coll Cardiol.* 1994 Oct;24(4):1124–32.
 41. Davis LM, Rodefeld ME, Green K, Beyer EC, Saffitz JE. Gap junction protein phenotypes of the human heart and conduction system. *J Cardiovasc Electrophysiol.* 1995 Oct;6(10 Pt 1):813–22.
 42. Dössel O, Krueger MW, Weber FM, Wilhelms M, Seemann G. Computational modeling of the human atrial anatomy and electrophysiology. *Med Biol Eng Comput.* 2012;50(8):773–99.
 43. Feld GK, Mollerus M, Birgersdotter-Green U, Fujimura O, Bahnson TD, Boyce K, et al. Conduction velocity in the tricuspid valve-inferior vena cava isthmus is slower in patients with type I atrial flutter compared to those without a history of atrial flutter. *J Cardiovasc Electrophysiol.* 1997 Dec;8(12):1338–48.
 44. Ho SY, Anderson RH, Sánchez-Quintana D. Atrial structure and fibres: Morphologic bases of atrial conduction. *Cardiovascular Research* May, 2002 p. 325–36.

45. Bers DM. Excitation-Contraction Coupling. In: *Cardiac Electrophysiology: From Cell to Bedside: Seventh Edition*. 2017.
46. Bers DM. Cardiac excitation–contraction coupling. *Nature*. 2002 Jan;415(6868):198–205.
47. Wolf PA, Abbott RD, Kannel WB. Original Contributions Atrial Fibrillation as an Independent Risk Factor for Stroke : The Framingham Study. 1948;983–9.
48. Benjamin EJ, Levy D, Vaziri SM, D’agostino RB, Belanger AJ, Wolf PA. Independent Risk Factors for Atrial Fibrillation in a Population-Based Cohort: The Framingham Heart Study. *JAMA J Am Med Assoc*. 1994 Mar 16;271(11):840–4.
49. Lau DH, Nattel S, Kalman JM, Sanders P. Modifiable Risk Factors and Atrial Fibrillation. *Circulation*. 2017 Aug 8;136(6):583–96.
50. Heijman J, Voigt N, Nattel S, Dobrev D. Cellular and molecular electrophysiology of atrial fibrillation initiation, maintenance, and progression. *Circ Res*. 2014 Apr 25;114(9):1483–99.
51. Iwasaki YK, Nishida K, Kato T, Nattel S. Atrial fibrillation pathophysiology: Implications for management. *Circulation*. 2011;124(20):2264–74.
52. Nattel S, Dobrev D. Controversies about Atrial Fibrillation Mechanisms: Aiming for Order in Chaos and Whether it Matters. *Circ Res*. 2017 Apr 28;120(9):1396–8.
53. Nattel S, Harada M. Atrial remodeling and atrial fibrillation: Recent advances and translational perspectives. *J Am Coll Cardiol*. 2014;63(22):2335–45.
54. Nattel S. New ideas about atrial fibrillation 50 years on. *Nature*. 2002;415(6868):219–26.
55. Narayan SM, Krummen DE, Shivkumar K, Clopton P, Rappel W-J, Miller JM. Treatment of atrial fibrillation by the ablation of localized sources: CONFIRM (Conventional Ablation for Atrial Fibrillation With or Without Focal Impulse and Rotor Modulation) trial. *J Am Coll Cardiol*. 2012 Aug 14;60(7):628–36.
56. Haissaguerre M, Shah AJ, Cochet H, Hocini M, Dubois R, Efimov I, et al. Intermittent drivers anchoring to structural heterogeneities as a major pathophysiological mechanism of human persistent atrial fibrillation. *J Physiol*. 2016 May 1;594(9):2387–98.
57. van der Does LJME, Kik C, Bogers AJJC, Allessie MA, de Groot NMS. Dynamics of Endo- and Epicardial Focal Fibrillation Waves at the Right Atrium in a Patient With Advanced Atrial Remodelling. *Can J Cardiol*. 2016 Oct 1;32(10):1260.e19-1260.e21.
58. De Groot N, Van Der Does L, Yaksh A, Lanfers E, Teuwen C, Knops P, et al. Direct Proof of Endo-Epicardial Asynchrony of the Atrial Wall During Atrial Fibrillation in Humans. *Circ Arrhythmia Electrophysiol*. 2016 May 1;9(5).
59. Gutbrod SR, Walton R, Gilbert S, Meillet V, Jaïs P, Hocini M, et al. Quantification of the transmural dynamics of atrial fibrillation by simultaneous endocardial and epicardial optical mapping in an acute sheep model. *Circ Arrhythmia Electrophysiol*. 2015 Apr 20;8(2):456–65.
60. Atenza F, Martins RP, Jalife J. Translational research in atrial fibrillation: A quest for

- mechanistically based diagnosis and therapy. *Circ Arrhythmia Electrophysiol.* 2012 Dec;5(6):1207–15.
61. Oral H, Crawford T, Frederick M, Gadeela N, Wimmer A, Dey S, et al. Inducibility of paroxysmal atrial fibrillation by isoproterenol and its relation to the mode of onset of atrial fibrillation. *J Cardiovasc Electrophysiol.* 2008 Jul 8;19(5):466–70.
 62. Nattel S, Xiong F, Aguilar M. Demystifying rotors and their place in clinical translation of atrial fibrillation mechanisms. *Nat Rev Cardiol.* 2017;14(9):509–20.
 63. Jalife J, Berenfeld O, Mansour M. Mother rotors and fibrillatory conduction: a mechanism of atrial fibrillation. *Cardiovasc Res.* 2002 May 1;54(2):204–16.
 64. Atienza F, Martins RP, Jalife J. Translational research in atrial fibrillation: a quest for mechanistically based diagnosis and therapy. *Circ Arrhythm Electrophysiol.* 2012 Dec;5(6):1207–15.
 65. Allesie MA, Bonke FIM, Schopman FJG. Circus Movement in Rabbit Atrial Muscle as a Mechanism of Tachycardia II . The Role of Nonuniform Recovery of Excitability in the Occurrence of Unidirectional Block , as Studied with. *Circ Res.* 1976;39(2):168–77.
 66. WIENER N, ROSENBLUETH A. The mathematical formulation of the problem of conduction of impulses in a network of connected excitable elements, specifically in cardiac muscle. *Arch Inst Cardiol Mex.* 1946 Jul;16(3):205–65.
 67. Fast VG, Kléber AG. Role of wavefront curvature in propagation of cardiac impulse. Vol. 33, *Cardiovascular Research*. Narnia; 1997. p. 258–71.
 68. Pandit S V, Jalife J. Rotors and the dynamics of cardiac fibrillation. *Circ Res.* 2013;112(5):849–62.
 69. Comtois P, Kneller J, Nattel S. Of circles and spirals: Bridging the gap between the leading circle and spiral wave concepts of cardiac reentry. *Europace.* 2005;7:10–20.
 70. Gray RA, Jalife J, Panfilov A V, Baxter WT, Cabo C, Davidenko JM, et al. Mechanisms of cardiac fibrillation. *Science.* 1995 Nov 17;270(5239):1222–6.
 71. Fenton FH, Karma A. Vortex dynamics in three-dimensional continuous myocardium with fiber rotation : Filament instability and fibrillation. *Chaos An Interdiscip J Nonlinear Sci.* 1998 Mar;8(1):20–47.
 72. Efimov IR, Krinsky VI, Jalife J. Dynamics of rotating vortices in the Beeler-Reuter model of cardiac tissue. *Chaos, Solitons and Fractals.* 1995 Mar 1;5(3–4):513–26.
 73. Krinsky VI, Efimov IR, Jalife J. Vortices with linear cores in excitable media. *Proc R Soc London Ser A Math Phys Sci.* 1992 Jun 8;437(1901):645–55.
 74. Davidenko JM, Pertsov A V., Salomonsz R, Baxter W, Jalife J. Stationary and drifting spiral waves of excitation in isolated cardiac muscle. *Nature.* 1992 Jan;355(6358):349–51.
 75. Nguyen TP, Qu Z, Weiss JN. Cardiac fibrosis and arrhythmogenesis: The road to repair is paved with perils. *J Mol Cell Cardiol.* 2014;70:83–91.
 76. Avitall B, Bi J, Mykitysey A, Chicos A. Atrial and ventricular fibrosis induced by atrial fibrillation: Evidence to support early rhythm control. *Hear Rhythm.* 2008 Jun;5(6):839–

- 45.
77. Platonov PG, Mitrofanova LB, Orshanskaya V, Ho SY. Structural Abnormalities in Atrial Walls Are Associated With Presence and Persistency of Atrial Fibrillation But Not With Age. *J Am Coll Cardiol*. 2011 Nov 15;58(21):2225–32.
78. Miragoli M, Salvarani N, Rohr S. Myofibroblasts induce ectopic activity in cardiac tissue. *Circ Res*. 2007 Oct;101(8):755–8.
79. De Jong S, Van Veen TAB, Van Rijen HVM, De Bakker JMT. Fibrosis and cardiac arrhythmias. *J Cardiovasc Pharmacol*. 2011;57(6):630–8.
80. Hansen B, Zhao J, Fedorov V V. Fibrosis and Atrial Fibrillation: Computerized and Optical Mapping: A View Into the Human Atria at Submillimeter Resolution. *JACC Clin Electrophysiol*. 2017 Jun 1;3(6):531–46.
81. Marrouche NNF, Wilber D, Hindricks G, Jais P, Akoum N, Marchlinski FF, et al. Association of atrial tissue fibrosis identified by delayed enhancement MRI and atrial fibrillation catheter ablation: The DECAAF study. *JAMA - J Am Med Assoc*. 2014 Feb 5;311(5):498–506.
82. Kim RJ, Chen EL, Lima JA, Judd RM. Myocardial Gd-DTPA kinetics determine MRI contrast enhancement and reflect the extent and severity of myocardial injury after acute reperfused infarction. *Circulation*. 1996 Dec 15;94(12):3318–26.
83. Pontecorboli G, Ventura RMFI, Carlosena A, Benito E, Prat-Gonzales S, Padeletti L, et al. Use of delayed-enhancement magnetic resonance imaging for fibrosis detection in the atria: A review. *Europace*. 2017 Feb 1;19(2):180–9.
84. McGann CJ, Kholmovski EG, Oakes RS, Blauer JJE, Daccarett M, Segerson N, et al. New Magnetic Resonance Imaging-Based Method for Defining the Extent of Left Atrial Wall Injury After the Ablation of Atrial Fibrillation. *J Am Coll Cardiol*. 2008 Oct 7;52(15):1263–71.
85. Oakes RS, Badger TJ, Kholmovski EG, Akoum N, Burgon NS, Fish EN, et al. Detection and Quantification of Left Atrial Structural Remodeling With Delayed-Enhancement Magnetic Resonance Imaging in Patients With Atrial Fibrillation. *Circulation*. 2009 Apr 7;119(13):1758–67.
86. Chubb H, Karim R, Roujol S, Nuñez-Garcia M, Williams SE, Whitaker J, et al. The reproducibility of late gadolinium enhancement cardiovascular magnetic resonance imaging of post-ablation atrial scar: A cross-over study. *J Cardiovasc Magn Reson*. 2018 Dec 19;20(1):21.
87. Khurram IM, Beinart R, Zipunnikov V, Dewire J, Yarmohammadi H, Sasaki T, et al. Magnetic resonance image intensity ratio, a normalized measure to enable interpatient comparability of left atrial fibrosis. *Hear Rhythm*. 2014 Jan;11(1):85–92.
88. Benito EM, Carlosena-Remirez A, Guasch E, Prat-González S, Perea RJ, Figueras R, et al. Left atrial fibrosis quantification by late gadolinium-enhanced magnetic resonance: A new method to standardize the thresholds for reproducibility. *Europace*. 2017 Aug 1;19(8):1272–9.
89. Kehr E, Sono M, Chugh SS, Jerosch-Herold M. Gadolinium-enhanced magnetic resonance imaging for detection and quantification of fibrosis in human myocardium in

- vitro. *Int J Cardiovasc Imaging*. 2007 Dec 6;24(1):61–8.
90. Beinart R, Khurram IM, Liu S, Yarmohammadi H, Halperin HR, Bluemke DA, et al. Cardiac magnetic resonance T1 mapping of left atrial myocardium. *Heart Rhythm*. 2013 Sep;10(9):1325–31.
 91. Ling LH, McLellan AJA, Taylor AJ, Iles LM, Ellims AH, Kumar S, et al. Magnetic resonance post-contrast T1 mapping in the human atrium: Validation and impact on clinical outcome after catheter ablation for atrial fibrillation. *Heart Rhythm*. 2014;11(9):1551–9.
 92. Nattel S. Experimental evidence for proarrhythmic mechanisms of antiarrhythmic drugs. *Cardiovasc Res*. 1998 Mar 1;37(3):567–77.
 93. Nattel S, Quantz MA. Pharmacological response of quinidine induced early afterdepolarisations in canine cardiac purkinje fibres: Insights into underlying ionic mechanisms. *Cardiovasc Res*. 1988 Nov 1;22(11):808–17.
 94. McMillan B, Gavaghan DJ, Mirams GR. Early afterdepolarisation tendency as a simulated pro-arrhythmic risk indicator. *Toxicol Res (Camb)*. 2017 Nov 1;6(6):912.
 95. Brennan T, Fink M, Rodriguez B. Multiscale modelling of drug-induced effects on cardiac electrophysiological activity. *Eur J Pharm Sci*. 2009 Jan 31;36(1):62–77.
 96. Marrouche NF, Brachmann J, Andresen D, Siebels J, Boersma L, Jordaens L, et al. Catheter Ablation for Atrial Fibrillation with Heart Failure. *N Engl J Med*. 2018 Feb;378(5):417–27.
 97. Blomström-Lundqvist C, Gizurarson S, Schwieler J, Jensen SM, Bergfeldt L, Kennebäck G, et al. Effect of Catheter Ablation vs Antiarrhythmic Medication on Quality of Life in Patients With Atrial Fibrillation. *JAMA*. 2019 Mar 19;321(11):1059.
 98. Packer DL, Mark DB, Robb RA, Monahan KH, Bahnson TD, Poole JE, et al. Effect of Catheter Ablation vs Antiarrhythmic Drug Therapy on Mortality, Stroke, Bleeding, and Cardiac Arrest Among Patients With Atrial Fibrillation. *JAMA*. 2019 Apr 2;321(13):1261.
 99. Calkins H, Kuck KH, Cappato R, Brugada J, Camm AJ, Chen S-A, et al. 2012 HRS/EHRA/ECAS expert consensus statement on catheter and surgical ablation of atrial fibrillation: recommendations for patient selection, procedural techniques, patient management and follow-up, definitions, endpoints, and research trial design. *J Interv Card Electrophysiol*. 2012 Mar 1;33(2):171–257.
 100. Kottkamp H, Berg J, Bender R, Rieger A, Schreiber D. Box isolation of fibrotic areas (BIFA): A patient-tailored substrate modification approach for ablation of atrial fibrillation. *J Cardiovasc Electrophysiol*. 2016;27(1):22–30.
 101. Yu HT, Shim J, Park J, Kim IS, Kim TH, Uhm JS, et al. Pulmonary Vein Isolation Alone Versus Additional Linear Ablation in Patients with Persistent Atrial Fibrillation Converted to Paroxysmal Type with Antiarrhythmic Drug Therapy: A Multicenter, Prospective, Randomized Study. *Circ Arrhythmia Electrophysiol*. 2017 Jun;10(6).
 102. Yamaguchi T, Tsuchiya T, Nakahara S, Fukui A, Nagamoto Y, Murotani K, et al. Efficacy of Left Atrial Voltage-Based Catheter Ablation of Persistent Atrial Fibrillation. *J Cardiovasc Electrophysiol*. 2016 Sep 1;27(9):1055–63.

103. Patel AM, D'Avila A, Neuzil P, Kim SJ, Mela T, Singh JP, et al. Atrial tachycardia after ablation of persistent atrial fibrillation: identification of the critical isthmus with a combination of multielectrode activation mapping and targeted entrainment mapping. *Circ Arrhythm Electrophysiol*. 2008;1(1):14–22.
104. Haïssaguerre M, Sanders P, Hocini M, Takahashi Y, Rotter M, Sacher F, et al. Catheter ablation of long-lasting persistent atrial fibrillation: Critical structures for termination. *J Cardiovasc Electrophysiol*. 2005;16(11):1125–37.
105. García-Cosío F, Pastor Fuentes A, Nú A. Arrhythmias (IV). Clinical approach to atrial tachycardia and atrial flutter from an understanding of the mechanisms. Electrophysiology based on anatomy. *Rev española Cardiol*. 2012;65(4):363–75.
106. Verma A, Jiang CY, Betts TR, Chen J, Deisenhofer I, Mantovan R, et al. Approaches to catheter ablation for persistent atrial fibrillation. *N Engl J Med*. 2015 May 7;372(19):1812–22.
107. Willems S, Klemm H, Rostock T, Brandstrup B, Ventura R, Steven D, et al. Substrate modification combined with pulmonary vein isolation improves outcome of catheter ablation in patients with persistent atrial fibrillation: a prospective randomized comparison. *Eur Heart J*. 2006 Nov 13;27(23):2871–8.
108. Stavrakis S, Po S. Ganglionated Plexi Ablation: Physiology and Clinical Applications. *Arrhythmia Electrophysiol Rev*. 2017 Dec;6(4):186–90.
109. Kashimura S, Nishiyama T, Kimura T, Nishiyama N, Aizawa Y, Takatsuki S. Vein of Marshall partially isolated with radiofrequency ablation from the endocardium. *Hear case reports*. 2017 Feb;3(2):120–3.
110. Nademanee K, McKenzie J, Kosar E, Schwab M, Sunsaneewitayakul B, Vasavakul T, et al. A new approach for catheter ablation of atrial fibrillation: mapping of the electrophysiologic substrate. *J Am Coll Cardiol*. 2004 Jun 2;43(11):2044–53.
111. Sanders P, Berenfeld O, Hocini M, Jaïs P, Vaidyanathan R, Hsu L-FF, et al. Spectral analysis identifies sites of high-frequency activity maintaining atrial fibrillation in humans. *Circulation*. 2005 Aug 9;112(6):789–97.
112. Ganesan AN, Kuklik P, Lau DH, Brooks AG, Baumert M, Lim WW, et al. Bipolar electrogram Shannon entropy at sites of rotational activation implications for ablation of atrial fibrillation. *Circ Arrhythmia Electrophysiol*. 2013 Feb;6(1):48–57.
113. Narayan SM, Baykaner T, Clopton P, Schricker A, Lalani GG, Krummen DE, et al. Ablation of rotor and focal sources reduces late recurrence of atrial fibrillation compared with trigger ablation alone: Extended follow-up of the CONFIRM trial (conventional ablation for atrial fibrillation with or without focal impulse and rotor modulat. *J Am Coll Cardiol*. 2014;63(17):1761–8.
114. Haïssaguerre M, Hocini M, Denis A, Shah AJ, Komatsu Y, Yamashita S, et al. Driver domains in persistent atrial fibrillation. *Circulation*. 2014 Aug 12;130(7):530–8.
115. Roney CH, Cantwell CD, Bayer JD, Qureshi NA, Lim PB, Tweedy JH, et al. Spatial Resolution Requirements for Accurate Identification of Drivers of Atrial Fibrillation. *Circ Arrhythmia Electrophysiol*. 2017 May 1;10(5).
116. Miller JM, Kalra V, Das MK, Jain R, Garlie JB, Brewster JA, et al. Clinical Benefit of

- Ablating Localized Sources for Human Atrial Fibrillation: The Indiana University FIRM Registry. *J Am Coll Cardiol*. 2017 Mar 14;69(10):1247–56.
117. Mohanty P, Trivedi C, Gianni C, Della Rocca DG, Di Biase L, Natale A. Long-Term Outcome of Pulmonary Vein Isolation With and Without Focal Impulse and Rotor Modulation Mapping: Insights From a Meta-Analysis. *Circ Arrhythm Electrophysiol*. 2018 Mar 1;11(3):e005789.
 118. Wijffels MCEF, Kirchhof CJHJ, Dorland R, Allessie MA. Atrial fibrillation begets atrial fibrillation: A study in awake chronically instrumented goats. *Circulation*. 1995 Oct 1;92(7):1954–68.
 119. Guettler N, Nicol E, Schmitt J, Rajappan K. Mechanisms of Atrial Fibrillation and Their Impact on Strategies for Catheter Ablation. *Eur J Arrhythmia Electrophysiol*. 2018;4(2):56–64.
 120. McGann C, Akoum N, Patel A, Kholmovski E, Revelo P, Damal K, et al. Atrial fibrillation ablation outcome is predicted by left atrial remodeling on MRI. *Circ Arrhythmia Electrophysiol*. 2014;7(1):23–30.
 121. Khurram IM, Habibi M, Gucuk Ipek E, Chrispin J, Yang E, Fukumoto K, et al. Left Atrial LGE and Arrhythmia Recurrence Following Pulmonary Vein Isolation for Paroxysmal and Persistent AF. *JACC Cardiovasc Imaging*. 2016 Feb;9(2):142–8.
 122. Rolf S, Kircher S, Arya A, Eitel C, Sommer P, Sergio R, et al. Tailored atrial substrate modification based on low-voltage areas in catheter ablation of atrial fibrillation. *Circ Arrhythmia Electrophysiol*. 2014;7(5):825–33.
 123. Jadidi AS, Lehrmann H, Keyl C, Sorrel J, Markstein V, Minners J, et al. Ablation of Persistent Atrial Fibrillation Targeting Low-Voltage Areas with Selective Activation Characteristics. *Circ Arrhythmia Electrophysiol*. 2016 Mar 10;9(3):e002962.
 124. Wang X, Li Z, Mao J, He B. A novel individualized substrate modification approach for the treatment of long-standing persistent atrial fibrillation: Preliminary results. *Int J Cardiol*. 2014 Jul 15;175(1):162–8.
 125. Yang G, Yang B, Wei Y, Zhang F, Ju W, Chen H, et al. Catheter Ablation of Nonparoxysmal Atrial Fibrillation Using Electrophysiologically Guided Substrate Modification During Sinus Rhythm After Pulmonary Vein Isolation. *Circ Arrhythmia Electrophysiol*. 2016 Feb;9(2):e003382.
 126. Blandino A, Bianchi F, Grossi S, Biondi-Zoccai G, Conte MR, Gaido L, et al. Left Atrial Substrate Modification Targeting Low-Voltage Areas for Catheter Ablation of Atrial Fibrillation: A Systematic Review and Meta-Analysis. *PACE - Pacing Clin Electrophysiol*. 2017 Feb;40(2):199–212.
 127. Mohanty S, Mohanty P, Di Biase L, Trivedi C, Morris EH, Gianni C, et al. Long-term follow-up of patients with paroxysmal atrial fibrillation and severe left atrial scarring: comparison between pulmonary vein antrum isolation only or pulmonary vein isolation combined with either scar homogenization or trigger ablation. *EP Eur*. 2017 Nov 1;19(11):1790–7.
 128. Robinson PA, Rennie CJ, Rowe DL, O'Connor SC, Wright JJ, Gordon E, et al. Neurophysical Modeling of Brain Dynamics. *Neuropsychopharmacology*. 2003 Jul

- 24;28(S1):S74–9.
129. Jain RK. Determinants of Tumor Blood Flow: A Review. *Cancer Res.* 1988;48(10):2641–58.
 130. Hodgkin A, Huxley A. A quantitative description of membrane current and its application to conduction and excitation in nerve. *Bull Math Biol.* 1990;52(1–2):25–71.
 131. Plonsey R, Barr RC. Bioelectricity: A quantitative approach. *Bioelectricity: A Quantitative Approach.* 2007. 1–528 p.
 132. Keener J. J. S. *Mathematical Physiology.* Vol. 8, Interdisciplinary Applied Mathematics. 1998. 766 p.
 133. Keener J, Sneyd J. Excitability. In 2009. p. 195–228.
 134. Hamill OP, Marty A, Neher E, Sakmann B, Sigworth FJ. Improved patch-clamp techniques for high-resolution current recording from cells and cell-free membrane patches. *Pflügers Arch Eur J Physiol.* 1981 Aug;391(2):85–100.
 135. Nygren A, Fiset C, Firek L, Clark JW, Lindblad DS, Clark RB, et al. Mathematical Model of an Adult Human Atrial Cell. *Circ Res.* 1998 Jan 23;82(1):63–81.
 136. Courtemanche M, Ramirez RJ, Nattel S. Ionic mechanisms underlying human atrial action potential properties: insights from a mathematical model. *Am J Physiol.* 1998 Jul;275(1 Pt 2):H301–21.
 137. Maleckar MM, Greenstein JL, Trayanova N, Giles WR. Mathematical simulations of ligand-gated and cell-type specific effects on the action potential of human atrium. *Prog Biophys Mol Biol.* 2008 Oct;98(2–3):161–70.
 138. Grandi E, Pandit S V., Voigt N, Workman AJ, Dobrev D, Jalife J, et al. Human Atrial Action Potential and Ca²⁺ Model. *Circ Res.* 2011 Oct 14;109(9):1055–66.
 139. Koivumäki JT, Korhonen T, Tavi P. Impact of Sarcoplasmic Reticulum Calcium Release on Calcium Dynamics and Action Potential Morphology in Human Atrial Myocytes: A Computational Study. McCulloch AD, editor. *PLoS Comput Biol.* 2011 Jan 27;7(1):e1001067.
 140. Niederer SA, Lumens J, Trayanova N. Computational models in cardiology. *Nat Rev Cardiol.* 2019 Feb 25;16(2):100–11.
 141. Grandi E, Dobrev D, Heijman J. Computational modeling: What does it tell us about atrial fibrillation therapy? *Int J Cardiol.* 2019 Jul 15;287:155–61.
 142. Bernus O, Wilders R, Zemlin CW, Verschelde H, Panfilov A V. A computationally efficient electrophysiological model of human ventricular cells. *Am J Physiol - Hear Circ Physiol.* 2002 Jun;282(6):H2296–308.
 143. FitzHugh R. Impulses and Physiological States in Theoretical Models of Nerve Membrane. *Biophys J.* 1961 Jul 1;1(6):445–66.
 144. Goodman AM, Oliver RA, Henriquez CS, Wolf PAD. A membrane model of electrically remodelled atrial myocardium derived from in vivo measurements. *Europace.* 2005 Sep;7(SUPPL. 2):135–45.

145. Colman MA, Aslanidi O, Kharche S, Boyett MR, Garratt C, Hancox JC, et al. Pro-arrhythmogenic effects of atrial fibrillation-induced electrical remodelling: Insights from the three-dimensional virtual human atria. *J Physiol*. 2013 Sep 1;591(17):4249–72.
146. Project IP. Physiome Model Repository [Internet]. 2001 [cited 2019 Nov 27]. Available from: <https://models.physiomeproject.org/welcome>
147. Zhao J, Butters TD, Zhang H, Pullan AJ, LeGrice IJ, Sands GB, et al. An image-based model of atrial muscular architecture effects of structural anisotropy on electrical activation. *Circ Arrhythmia Electrophysiol*. 2012 Apr;5(2):361–70.
148. Aslanidi O, Colman MA, Stott J, Dobrzynski H, Boyett MR, Holden A V., et al. 3D virtual human atria: A computational platform for studying clinical atrial fibrillation. *Prog Biophys Mol Biol*. 2011 Oct;107(1):156–68.
149. Fast VG, Kléber AG. Microscopic conduction in cultured strands of neonatal rat heart cells measured with voltage-sensitive dyes. *Circ Res*. 1993 Nov;73(5):914–25.
150. Potse M, Dubé B, Richer J, Vinet A, Gulrajani RM. A comparison of monodomain and bidomain reaction-diffusion models for action potential propagation in the human heart. *IEEE Trans Biomed Eng*. 2006 Dec;53(12):2425–35.
151. Sundnes J, Lines GT, Tveito A. Efficient solution of ordinary differential equations modeling electrical activity in cardiac cells. *Math Biosci*. 2001;172(2):55–72.
152. Vigmond EJ, Weber dos Santos R, Prassl AJ, Deo M, Plank G. Solvers for the cardiac bidomain equations. *Prog Biophys Mol Biol*. 2008 Jan 1;96(1–3):3–18.
153. Seemann G, Sachse FB, Karl M, Weiss DL, Heuveline V, Dössel O. Framework for Modular, Flexible and Efficient Solving the Cardiac Bidomain Equations Using PETSc. In 2010. p. 363–9.
154. Seemann G, Höper C, Sachse FB, Dössel O, Holden A V., Zhang H, et al. Heterogeneous three-dimensional anatomical and electrophysiological model of human atria. *Philos Trans A Math Phys Eng Sci*. 2006 Jun 15;364(1843):1465–81.
155. Roney CH, Bayer JD, Cochet H, Meo M, Dubois R, Jaïs P, et al. Variability in pulmonary vein electrophysiology and fibrosis determines arrhythmia susceptibility and dynamics. Marsden AL, editor. *PLOS Comput Biol*. 2018 May 24;14(5):e1006166.
156. Vigmond EJ, Aguel F, Trayanova NA. Computational techniques for solving the bidomain equations in three dimensions. *IEEE Trans Biomed Eng*. 2002 Nov 1;49(11):1260–9.
157. Clayton RH, Holden A V. Propagation of normal beats and re-entry in a computational model of ventricular cardiac tissue with regional differences in action potential shape and duration. *Prog Biophys Mol Biol*. 2004 Jun 1;85(2–3):473–99.
158. Blanc O, Virag N, Vesin J-M, Kappenberger L. A computer model of human atria with reasonable computation load and realistic anatomical properties. *IEEE Trans Biomed Eng*. 2001;48(11):1229–37.
159. Harrild D, Henriquez C. A computer model of normal conduction in the human atria. *Circ Res*. 2000;87(7):E25–36.

160. Vigmond EJ, Ruckdeschel R, Trayanova N. Reentry in a morphologically realistic atrial model. *J Cardiovasc Electrophysiol*. 2001;12(9):1046–54.
161. Feng J, Yue L, Wang Z, Nattel S. Ionic mechanisms of regional action potential heterogeneity in the canine right atrium. *Circ Res*. 1998;83(5):541–51.
162. Li D, Zhang L, Kneller J, Nattel S. Potential ionic mechanism for repolarization differences between canine right and left atrium. *Circ Res*. 2001 Jun 8;88(11):1168–75.
163. Chen SA, Hsieh MH, Tai CT, Tsai CF, Prakash VS, Yu WC, et al. Initiation of atrial fibrillation by ectopic beats originating from the pulmonary veins: Electrophysiological characteristics, pharmacological responses, and effects of radiofrequency ablation. *Circulation*. 1999 Nov 2;100(18):1879–86.
164. Krueger MW, Dorn A, Keller DUJ, Holmqvist F, Carlson J, Platonov PG, et al. In-silico modeling of atrial repolarization in normal and atrial fibrillation remodeled state. *Med Biol Eng Comput*. 2013 Oct;51(10):1105–19.
165. Varela M, Colman MA, Hancox JC, Aslanidi O. Atrial Heterogeneity Generates Re-entrant Substrate during Atrial Fibrillation and Anti-arrhythmic Drug Action: Mechanistic Insights from Canine Atrial Models. Doessel O, editor. *PLoS Comput Biol*. 2016 Dec 16;12(12):e1005245.
166. Ridler ME, Lee M, McQueen D, Peskin C, Vigmond E. Arrhythmogenic consequences of action potential duration gradients in the atria. *Can J Cardiol*. 2011;27(1):112–9.
167. Fastl TE, Tobon-Gomez C, Crozier A, Whitaker J, Rajani R, McCarthy KP, et al. Personalized computational modeling of left atrial geometry and transmural myofiber architecture. *Med Image Anal*. 2018 Jul 1;47:180–90.
168. Aslanidi O V., Colman MA, Varela M, Zhao J, Smaill BH, Hancox JC, et al. Heterogeneous and anisotropic integrative model of pulmonary veins: Computational study of arrhythmogenic substrate for atrial fibrillation. *Interface Focus*. 2013 Apr 6;3(2).
169. Colman MA, Varela M, Hancox JC, Zhang H, Aslanidi O. Evolution and pharmacological modulation of the arrhythmogenic wave dynamics in canine pulmonary vein model. *Europace*. 2014 Mar;16(3):416–23.
170. Krogh-Madsen T, Abbott GW, Christini DJ. Effects of Electrical and Structural Remodeling on Atrial Fibrillation Maintenance: A Simulation Study. McCulloch AD, editor. *PLoS Comput Biol*. 2012 Feb 23;8(2):e1002390.
171. Krueger MW, Rhode KS, O’Neill M, Rinaldi CA, Gill J, Razavi R, et al. Patient-specific modeling of atrial fibrosis increases the accuracy of sinus rhythm simulations and may explain maintenance of atrial fibrillation. *J Electrocardiol*. 2014;47(3):324–8.
172. McDowell KS, Vadakkumpadan F, Blake R, Blauer J, Plank G, MacLeod RS, et al. Mechanistic Inquiry into the Role of Tissue Remodeling in Fibrotic Lesions in Human Atrial Fibrillation. *Biophys J*. 2013 Jun 18;104(12):2764–73.
173. Zhao J, Hansen B, Wang Y, Csepe TA, Sul L V, Tang A, et al. Three-dimensional integrated functional, structural, and computational mapping to define the structural “fingerprints” of heart-specific atrial fibrillation drivers in human heart ex vivo. *J Am Heart Assoc*. 2017 Aug 22;6(8):e005922.

174. Morgan R, Colman MA, Chubb H, Seemann G, Aslanidi O. Slow conduction in the border zones of patchy fibrosis stabilizes the drivers for atrial fibrillation: Insights from multi-scale human atrial modeling. *Front Physiol.* 2016;7(OCT):1–15.
175. Chrispin J, Gucuk Ipek E, Zahid S, Prakosa A, Habibi M, Spragg D, et al. Lack of regional association between atrial late gadolinium enhancement on cardiac magnetic resonance and atrial fibrillation rotors. *Hear Rhythm.* 2016 Mar 1;13(3):654–60.
176. Sohns C, Lemes C, Metzner A, Fink T, Chmelevsky M, Maurer T, et al. First-in-Man Analysis of the Relationship between Electrical Rotors from Noninvasive Panoramic Mapping and Atrial Fibrosis from Magnetic Resonance Imaging in Patients with Persistent Atrial Fibrillation. *Circ Arrhythmia Electrophysiol.* 2017 Aug 1;10(8):e004419.
177. Fukumoto K, Habibi M, Ipek EG, Zahid S, Khurram IM, Zimmerman SL, et al. Association of Left Atrial Local Conduction Velocity With Late Gadolinium Enhancement on Cardiac Magnetic Resonance in Patients With Atrial Fibrillation. *Circ Arrhythmia Electrophysiol.* 2016 Mar 25;9(3):e002897.
178. Spach MS, Heidlage JF, Dolber PC, Barr RC. Electrophysiological effects of remodeling cardiac gap junctions and cell size. Experimental and model studies of normal cardiac growth. *Circ Res.* 2000 Feb 18;86(3):302–11.
179. Jacquemet V, Henriquez CS. Genesis of complex fractionated atrial electrograms in zones of slow conduction: A computer model of microfibrosis. *Hear Rhythm.* 2009 Jun;6(6):803–10.
180. Costa CM, Campos FO, Prassl AJ, Dos Santos RW, Sanchez-Quintana D, Ahammer H, et al. An efficient finite element approach for modeling fibrotic clefts in the heart. *IEEE Trans Biomed Eng.* 2014 Mar;61(3):900–10.
181. Vigmond E, Pashaei A, Amraoui S, Cochet H, Hassaguerre M. Percolation as a mechanism to explain atrial fractionated electrograms and reentry in a fibrosis model based on imaging data. *Hear Rhythm.* 2016 Jul 1;13(7):1536–43.
182. Tanaka K, Zlochiver S, Vikstrom KL, Yamazaki M, Moreno J, Klos M, et al. Spatial distribution of fibrosis governs fibrillation wave dynamics in the posterior left atrium during heart failure. *Circ Res.* 2007;101(8):839–47.
183. Karamitsos TD, Neubauer S. Detecting diffuse myocardial fibrosis with CMR: The future has only just begun. *JACC Cardiovasc Imaging.* 2013;6(6):684–6.
184. Camelliti P, Green CR, LeGrice I, Kohl P. Fibroblast Network in Rabbit Sinoatrial Node: Structural and Functional Identification of Homogeneous and Heterogeneous Cell Coupling. *Circ Res.* 2004 Apr 2;94(6):828–35.
185. Maleckar MM, Greenstein JL, Giles WR, Trayanova N. Electrotonic Coupling between Human Atrial Myocytes and Fibroblasts Alters Myocyte Excitability and Repolarization. *Biophys J.* 2009 Oct;97(8):2179–90.
186. Ashihara T, Haraguchi R, Nakazawa K, Namba T, Ikeda T, Nakazawa Y, et al. The role of fibroblasts in complex fractionated electrograms during persistent/permanent atrial fibrillation: Implications for electrogram-based catheter ablation. *Circ Res.* 2012 Jan 20;110(2):275–84.

187. Roney CH, Bayer JD, Zahid S, Meo M, Boyle PM, Trayanova N, et al. Modelling methodology of atrial fibrosis affects rotor dynamics and electrograms. *Europace*. 2016;18:iv146–55.
188. Whitaker J, Rajani R, Chubb H, Gabrawi M, Varela M, Wright M, et al. The role of myocardial wall thickness in atrial arrhythmogenesis. *Europace*. 2016;i:euw014.
189. Yamazaki M, Mironov S, Taravant C, Brec J, Vaquero LM, Bandaru K, et al. Heterogeneous atrial wall thickness and stretch promote scroll waves anchoring during atrial fibrillation. *Cardiovasc Res*. 2012;94(1):48–57.
190. Biktasheva I V., Dierckx H, Biktashev VN. Drift of scroll waves in thin layers caused by thickness features: Asymptotic theory and numerical simulations. *Phys Rev Lett*. 2015;114(6):1–12.
191. Krul SPJ, Berger WR, Smit NW, Van Amersfoorth SCM, Driessen AHG, Van Boven WJ, et al. Atrial fibrosis and conduction slowing in the left atrial appendage of patients undergoing thoracoscopic surgical pulmonary vein isolation for atrial fibrillation. *Circ Arrhythmia Electrophysiol*. 2015;8(2):288–95.
192. Zheng Y, Xia Y, Carlson J, Kongstad O, Yuan S. Atrial average conduction velocity in patients with and without paroxysmal atrial fibrillation. *Clin Physiol Funct Imaging*. 2017 Nov;37(6):596–601.
193. Varela M, Bisbal F, Zacur E, Berruezo A, Aslanidi O, Mont L, et al. Novel computational analysis of left atrial anatomy improves prediction of atrial fibrillation recurrence after ablation. *Front Physiol*. 2017 Feb 14;8(FEB):68.
194. Sánchez-Quintana D, Anderson RH, Cabrera JA, Climent V, Martin R, Farré J, et al. The terminal crest: morphological features relevant to electrophysiology. *Heart*. 2002 Oct;88(4):406–11.
195. Varela M, Morgan R, Theron A, Dillon-Murphy D, Chubb H, Whitaker J, et al. Novel MRI Technique Enables Non-Invasive Measurement of Atrial Wall Thickness. *IEEE Trans Med Imaging*. 2017 Apr 13;36(8):1607–14.
196. Wang Y, Rudy Y. Action potential propagation in inhomogeneous cardiac tissue: safety factor considerations and ionic mechanism. *Am J Physiol Circ Physiol*. 2000 Apr;278(4):H1019–29.
197. Cherry EM, Fenton FH. Effects of boundaries and geometry on the spatial distribution of action potential duration in cardiac tissue. *J Theor Biol*. 2011 Sep 21;285(1):164–76.
198. Connolly A, Trew ML, Smaill BH, Plank G, Bishop M. Local Gradients in Electrotonic Loading Modulate the Local Effective Refractory Period: Implications for Arrhythmogenesis in the Infarct Border Zone. *IEEE Trans Biomed Eng*. 2015 Sep;62(9):2251–9.
199. Walton RD, Benson AP, Hardy MEL, White E, Bernus O. Electrophysiological and structural determinants of electrotonic modulation of repolarization by the activation sequence. *Front Physiol*. 2013 Oct 8;4:281.
200. Calvo CJ, Deo M, Zlochiver S, Millet J, Berenfeld O. Attraction of rotors to the pulmonary veins in paroxysmal atrial fibrillation: A modeling study. *Biophys J*. 2014 Apr 15;106(8):1811–21.

201. Fast VG, Pertsov AM. Drift of vortex in the myocardium. *Biofizika*. 35(3):478–82.
202. Olmos-Liceaga D. Spiral Waves, Obstacles and Cardiac Arrhythmias. In: *Cardiac Arrhythmias - New Considerations*. 2012.
203. Zuo K, Li K, Liu M, Li J, Liu X, Liu X, et al. Correlation of left atrial wall thickness and atrial remodeling in atrial fibrillation. *Medicine (Baltimore)*. 2019 Apr;98(15):e15170.
204. Thomsen AF. Left Atrial Wall Thickness and Pulmonary Vein Size are Increased in Patients with Atrial Fibrillation Compared to Healthy Controls - A Multidetector Computed Tomography Study. *Int J Clin Cardiol*. 2017 Jun 30;4(2).
205. Nakatani Y, Sakamoto T, Yamaguchi Y, Tsujino Y, Kataoka N, Kinugawa K. Heterogeneity in the left atrial wall thickness contributes to atrial fibrillation recurrence after catheter ablation. *Heart Vessels*. 2018 Dec 5;33(12):1549–58.
206. Park J, Park CH, Lee HJ, Wi J, Uhm JS, Pak HN, et al. Left atrial wall thickness rather than epicardial fat thickness is related to complex fractionated atrial electrogram. *Int J Cardiol*. 2014;172(3):e411–3.
207. Bishop M, Rajani R, Plank G, Gaddum N, Carr-White G, Wright M, et al. Three-dimensional atrial wall thickness maps to inform catheter ablation procedures for atrial fibrillation. *Europace*. 2016 Mar;18(3):376–83.
208. Fedorov A, Beichel R, Kalpathy-Cramer J, Finet J, Fillion-Robin J-C, Pujol S, et al. 3D Slicer as an image computing platform for the Quantitative Imaging Network. *Magn Reson Imaging*. 2012 Nov;30(9):1323–41.
209. Fischl B, Dale AM. Measuring the thickness of the human cerebral cortex from magnetic resonance images. *Proc Natl Acad Sci*. 2000 Sep 26;97(20):11050–5.
210. Lerch JP, Evans AC. Cortical thickness analysis examined through power analysis and a population simulation. *Neuroimage*. 2005 Jan 1;24(1):163–73.
211. Rueckert D. Nonrigid registration using free-form deformations: Application to breast mr images. *IEEE Trans Med Imaging*. 1999;18(8):712–21.
212. Kalman JM, Olgin JE, Karch MR, Hamdan MH, Lee RJ, Lesh MD. “Cristal tachycardias”: Origin of right atrial tachycardias from the crista terminalis identified by intracardiac echocardiography. *J Am Coll Cardiol*. 1998;31(2):451–9.
213. Gonzales MJ, Vincent KP, Rappel WJ, Narayan SM, McCulloch AD. Structural contributions to fibrillatory rotors in a patient-derived computational model of the atria. *Europace*. 2014;16:iv3–10.
214. Tobón C, Ruiz-Villa CA, Heidenreich E, Romero L, Hornero F, Saiz J. A Three-Dimensional Human Atrial Model with Fiber Orientation. Electrograms and Arrhythmic Activation Patterns Relationship. *Kabla AJ*, editor. *PLoS One*. 2013 Feb 11;8(2):e50883.
215. García-Cosío F, Pastor Fuentes A, Núñez Angulo A. Clinical Approach to Atrial Tachycardia and Atrial Flutter From an Understanding of the Mechanisms. *Electrophysiology Based on Anatomy*. *Rev Española Cardiol (English Ed)*. 2012;65(4):363–75.
216. Morita N, Kobayashi Y, Horie T, Iwasaki YK, Hayashi M, Miyauchi Y, et al. The

- undetermined geometrical factors contributing to the transverse conduction block of the crista terminalis. *PACE - Pacing Clin Electrophysiol.* 2009 Jul 1;32(7):868–78.
217. Ohkubo K, Watanabe I, Okumura Y, Ashino S, Kofune M, Kawauchi K, et al. Anatomic and electrophysiologic differences between chronic and paroxysmal atrial flutter: Intracardiac echocardiographic analysis. *PACE - Pacing Clin Electrophysiol.* 2008 Apr;31(4):432–7.
218. Otani NF. A primary mechanism for spiral wave meandering. *Chaos.* 2002;12(3):829–42.
219. Akoum N, Daccarett M, McGann C, Segerson N, Vergara G, Kuppahally S, et al. Atrial fibrosis helps select the appropriate patient and strategy in catheter ablation of atrial fibrillation: a DE-MRI guided approach. *J Cardiovasc Electrophysiol.* 2011 Jan;22(1):16–22.
220. Narayan SM, Krummen DE, Clopton P, Shivkumar K, Miller JM. Direct or Coincidental Elimination of Stable Rotors or Focal Sources May Explain Successful Atrial Fibrillation Ablation: On-Treatment Analysis of the CONFIRM Trial (Conventional Ablation for AF With or Without Focal Impulse and Rotor Modulation). *J Am Coll Cardiol.* 2013 Jul 9;62(2):138–47.
221. Hansen BJ, Zhao J, Csepe TA, Moore BT, Li N, Jayne LA, et al. Atrial fibrillation driven by micro-anatomic intramural re-entry revealed by simultaneous sub-epicardial and sub-endocardial optical mapping in explanted human hearts. *Eur Heart J.* 2015 Sep 14;36(35):2390–401.
222. De Groot N, Houben RPM, Smeets JL, Boersma E, Schotten U, Schalij MJ, et al. Electropathological substrate of longstanding persistent atrial fibrillation in patients with structural heart disease: Epicardial breakthrough. *Circulation.* 2010 Oct 26;122(17):1674–82.
223. Martins RP, Kaur K, Hwang E, Ramirez RJ, Willis BC, Filgueiras-Rama D, et al. Dominant frequency increase rate predicts transition from paroxysmal to long-term persistent atrial fibrillation. *Circulation.* 2014 Apr 8;129(14):1472–82.
224. Li D, Fareh S, Leung TK, Nattel S. Promotion of atrial fibrillation by heart failure in dogs: Atrial remodeling of a different sort. *Circulation.* 1999 Jul 6;100(1):87–95.
225. Boyle PM, Zghaib T, Zahid S, Ali RL, Deng D, Franceschi WH, et al. Computationally guided personalized targeted ablation of persistent atrial fibrillation. *Nat Biomed Eng.* 2019;3(11):870–9.
226. Boyle PM, Hakim JB, Zahid S, Franceschi WH, Murphy MJ, Vigmond EJ, et al. Comparing reentrant drivers predicted by image-based computational modeling and mapped by electrocardiographic imaging in persistent atrial fibrillation. *Front Physiol.* 2018 Apr 19;9:414.
227. Boyle PM, Hakim JB, Zahid S, Franceschi WH, Murphy MJ, Prakosa A, et al. The Fibrotic Substrate in Persistent Atrial Fibrillation Patients: Comparison Between Predictions From Computational Modeling and Measurements From Focal Impulse and Rotor Mapping. *Front Physiol.* 2018 Aug 29;9:1151.
228. Okamura T, Nishizaki T, Ikeda N, Nakano S, Sakakura T, Fujii N, et al. Diagnosis of

- cochleovestibular neurovascular compression syndrome: A scoring system based on five clinical characteristics. *Neurol Surg.* 2017 Feb;45(2):117–25.
229. Chubb H, Karim R, Mukherjee R, Williams SE, Whitaker J, Harrison J, et al. A comprehensive multi-index cardiac magnetic resonance-guided assessment of atrial fibrillation substrate prior to ablation: Prediction of long-term outcomes. *J Cardiovasc Electrophysiol.* 2019;30(10):1894–903.
230. Wolf I, Vetter M, Wegner I, Böttger T, Nolden M, Schöbinger M, et al. The medical imaging interaction toolkit. *Med Image Anal.* 2005 Dec;9(6):594–604.
231. Dice LR. Measures of the Amount of Ecologic Association Between Species. *Ecology.* 1945 Jul;26(3):297–302.
232. Akoum N, Wilber D, Hindricks G, Jais P, Cates J, Marchlinski F, et al. MRI assessment of ablation-induced scarring in atrial fibrillation: Analysis from the DECAAF study. *J Cardiovasc Electrophysiol.* 2015 May;26(5):473–80.
233. Saha M, Roney CH, Bayer JD, Meo M, Cochet H, Dubois R, et al. Wavelength and fibrosis affect phase singularity locations during atrial fibrillation. *Front Physiol.* 2018 Sep 10;9:1207.
234. Deng D, Murphy MJ, Hakim JB, Franceschi WH, Zahid S, Pashakhanloo F, et al. Sensitivity of reentrant driver localization to electrophysiological parameter variability in image-based computational models of persistent atrial fibrillation sustained by a fibrotic substrate. *Chaos An Interdiscip J Nonlinear Sci.* 2017 Sep 19;27(9):093932.
235. Bayer JD, Roney CH, Pashaei A, Jais P, Vigmond EJ. Novel Radiofrequency Ablation Strategies for Terminating Atrial Fibrillation in the Left Atrium: A Simulation Study. *Front Physiol.* 2016 Apr 12;7:108.
236. Wilhelms M, Hettmann H, Maleckar MM, Koivumäki JT, Dössel O, Seemann G. Benchmarking electrophysiological models of human atrial myocytes. *Front Physiol.* 2013;3:487.
237. Cherry EM, Evans SJ. Properties of two human atrial cell models in tissue: Restitution, memory, propagation, and reentry. *J Theor Biol.* 2008;254(3):674–90.
238. Krummen DE, Bayer JD, Ho J, Ho G, Smetak MR, Clopton P, et al. Mechanisms of human atrial fibrillation initiation: clinical and computational studies of repolarization restitution and activation latency. *Circ Arrhythm Electrophysiol.* 2012 Dec;5(6):1149–59.
239. Tsai WC, Chen YC, Kao YH, Lu YY, Chen SA, Chen YJ. Distinctive sodium and calcium regulation associated with sex differences in atrial electrophysiology of rabbits. *Int J Cardiol.* 2013 Oct 12;168(5):4658–66.
240. Maceira AM, Cosin-Sales J, Prasad SK, Pennell DJ. Characterization of left and right atrial function in healthy volunteers by cardiovascular magnetic resonance. *J Cardiovasc Magn Reson.* 2016 Oct 10;18(1):1–16.
241. Giraud GD, Morton MJ, Davis LE, Paul MS, Thornburg KL. Estrogen-induced left ventricular chamber enlargement in ewes. *Am J Physiol - Endocrinol Metab.* 1993;264(4 27-4).

242. Odening KE, Deiß S, Dilling-Boer D, Didenko M, Eriksson U, Nedios S, et al. Mechanisms of sex differences in atrial fibrillation: Role of hormones and differences in electrophysiology, structure, function, and remodelling. Vol. 21, *Europace*. Oxford University Press; 2019. p. 366–76.
243. Liu XK, Katchman A, Whitfield BH, Wan G, Janowski EM, Woosley RL, et al. In vivo androgen treatment shortens the QT interval and increases the densities of inward and delayed rectifier potassium currents in orchietomized male rabbits. *Cardiovasc Res*. 2003 Jan 1;57(1):28–36.
244. Ho SY, Sánchez-Quintana D. The importance of atrial structure and fibers. *Clin Anat*. 2009 Jan;22(1):52–63.
245. Hocini M, Ho SY, Kawara T, Linnenbank AC, Potse M, Shah D, et al. Electrical conduction in canine pulmonary veins: Electrophysiological and anatomic correlation. *Circulation*. 2002 May 21;105(20):2442–8.
246. Kumagai K, Ogawa M, Noguchi H, Yasuda T, Nakashima H, Saku K. Electrophysiologic properties of pulmonary veins assessed using a multielectrode basket catheter. *J Am Coll Cardiol*. 2004 Jun 16;43(12):2281–9.
247. Guillem MS, Climent AM, Rodrigo M, Fernández-Aviles F, Atienza F, Berenfeld O. Presence and stability of rotors in atrial fibrillation: Evidence and therapeutic implications. *Cardiovasc Res*. 2016 Apr 1;109(4):480–92.
248. Lee S-H, Tai C-T, Hsieh M-H, Tsao H-M, Lin Y-J, Chang S-L, et al. Predictors of Non-Pulmonary Vein Ectopic Beats Initiating Paroxysmal Atrial Fibrillation: Implication for Catheter Ablation. *J Am Coll Cardiol*. 2005 Sep 20;46(6):1054–9.
249. Calkins H, Brugada J, Packer DL, Cappato R, Chen S-A, Crijns HJG, et al. HRS/EHRA/ECAS Expert Consensus Statement on Catheter and Surgical Ablation of Atrial Fibrillation: Recommendations for Personnel, Policy, Procedures and Follow-Up: A report of the Heart Rhythm Society (HRS) Task Force on Catheter and Surgical Ablation of . *Europace*. 2007 Jun;9(6):335–79.
250. Boyle PM, Zahid S, Trayanova NA. Using personalized computer models to custom-tailor ablation procedures for atrial fibrillation patients: are we there yet? *Expert Rev Cardiovasc Ther*. 2017 May 4;15(5):339–41.
251. Jacquemet V. Lessons from computer simulations of ablation of atrial fibrillation. *J Physiol*. 2016;594(9):2417–30.
252. Shim J, Hwang M, Song J-S, Lim B, Kim T-H, Joung B, et al. Virtual In-Silico Modeling Guided Catheter Ablation Predicts Effective Linear Ablation Lesion Set for Longstanding Persistent Atrial Fibrillation: Multicenter Prospective Randomized Study. *Front Physiol*. 2017 Oct 11;8:792.
253. Rotter M, Dang L, Jacquemet V, Virag N, Kappenberger L, Haïssaguerre M. Impact of varying ablation patterns in a simulation model of persistent atrial fibrillation. *PACE - Pacing Clin Electrophysiol*. 2007 Mar 1;30(3):314–21.
254. Heijman J, Guichard JB, Dobrev D, Nattel S. Translational challenges in atrial fibrillation. *Circ Res*. 2018 Mar 1;122(5):752–3.
255. Prakosa A, Arevalo HJ, Deng D, Boyle PM, Nikolov PP, Ashikaga H, et al. Personalized

- virtual-heart technology for guiding the ablation of infarct-related ventricular tachycardia. *Nat Biomed Eng.* 2018;2(10):732–40.
256. Reumann M, Bohnert J, Seemann G, Osswald B, Doessel O. Preventive Ablation Strategies in a Biophysical Model of Atrial Fibrillation Based on Realistic Anatomical Data. *IEEE Trans Biomed Eng.* 2008 Feb;55(2):399–406.
257. Haïssaguerre M, Sanders P, Hocini M, Hsu LF, Shah DC, Scavée C, et al. Changes in atrial fibrillation cycle length and inducibility during catheter ablation and their relation to outcome. *Circulation.* 2004 Jun 22;109(24):3007–13.
258. Gaita F, Caponi D, Scaglione M, Montefusco A, Corleto A, Di Monte F, et al. Long-Term Clinical Results of 2 Different Ablation Strategies in Patients With Paroxysmal and Persistent Atrial Fibrillation. *Circ Arrhythmia Electrophysiol.* 2008 Oct;1(4):269–75.
259. Calvo D, Rubín J, Pérez D, Morís C. Ablation of Rotor Domains Effectively Modulates Dynamics of Human: Long-Standing Persistent Atrial Fibrillation. *Circ Arrhythmia Electrophysiol.* 2017 Dec 1;10(12).
260. Yoshida K, Chugh A, Good E, Crawford T, Myles J, Veerareddy S, et al. A critical decrease in dominant frequency and clinical outcome after catheter ablation of persistent atrial fibrillation. *Hear Rhythm.* 2010 Mar;7(3):295–302.
261. Pérez FJ, Wood MA, Schubert CM. Effects of gap geometry on conduction through discontinuous radiofrequency lesions. *Circulation.* 2006 Apr;113(14):1723–9.
262. Cappato R, Negroni S, Pecora D, Bentivegna S, Lupo PP, Carolei A, et al. Prospective assessment of late conduction recurrence across radiofrequency lesions producing electrical disconnection at the pulmonary vein ostium in patients with atrial fibrillation. *Circulation.* 2003 Sep 30;108(13):1599–604.
263. Pashakhanloo F, Herzka DA, Ashikaga H, Mori S, Gai N, Bluemke DA, et al. Myofiber architecture of the human atria as revealed by submillimeter diffusion tensor imaging. *Circ Arrhythmia Electrophysiol.* 2016 Apr 1;9(4).
264. Roney CH, Whitaker J, Sim I, O’Neill L, Mukherjee RK, Razeghi O, et al. A technique for measuring anisotropy in atrial conduction to estimate conduction velocity and atrial fibre direction. *Comput Biol Med.* 2019 Jan 1;104:278–90.
265. Sánchez C, Bueno-Orovio A, Pueyo E, Rodríguez B. Atrial Fibrillation Dynamics and Ionic Block Effects in Six Heterogeneous Human 3D Virtual Atria with Distinct Repolarization Dynamics. *Front Bioeng Biotechnol.* 2017 May 8;5:29.
266. Monaci S, Nordsletten D, Aslanidi O. Computational Modelling of Electro-Mechanical Coupling in the Atria and Its Changes During Atrial Fibrillation. In: *Lecture Notes in Computer Science (including subseries Lecture Notes in Artificial Intelligence and Lecture Notes in Bioinformatics)*. Springer Verlag; 2019. p. 103–13.
267. Muffoletto M, Fu X, Roy A, Varela M, Bates PA, Aslanidi O V. Development of a Deep Learning Method to Predict Optimal Ablation Patterns for Atrial Fibrillation. In *Institute of Electrical and Electronics Engineers (IEEE)*; 2019. p. 1–4.
268. Niederer SA, Kerfoot E, Benson AP, Bernabeu MO, Bernus O, Bradley C, et al. Verification of cardiac tissue electrophysiology simulators using an N-version

benchmark. *Philos Trans R Soc A Math Phys Eng Sci.* 2011 Nov 13;369(1954):4331–51.